APPLIED COMPUTATIONAL ELECTROMAGNETICS SOCIETY JOURNAL

November 2016
Vol. 31 No. 11
ISSN 1054-4887

The ACES Journal is abstracted in INSPEC, in Engineering Index, DTIC, Science Citation Index Expanded, the Research Alert, and to Current Contents/Engineering, Computing & Technology.

The illustrations on the front cover have been obtained from the research groups at the Department of Electrical Engineering, The University of Mississippi.

EMERITUS EDITORIAL ASSISTANTS

NOVEMBER 2016 REVIEWERS

THE APPLIED COMPUTATIONAL ELECTROMAGNETICS SOCIETY

JOURNAL

Vol. 31 No. 11 November 2016

TABLE OF CONTENTS

Approximate Calculation of the Total Attenuation Rate of Propagating Wave Inside Curved Tunnel

Hany M. El-Maghrabi [1], Ahmed M. Attiya [2], Samir F. Mahmoud [3], Mostafa El-Said [3], and Essam A. Hashish [3]

[1] Department of Electromechnical
Housing and National Research Center, Cairo, Egypt
helmaghrabi@hbrc.edu.eg

[2] Department of Microwave Engineering
Electronic Research Institute, Cairo, Egypt
attiya@eri.sci.eg

[3] Department of Electronics and Electrical Communication
Cairo University, Cairo, Egypt

Abstract ─ In this paper, a model is presented to simulate wave propagation in curved rectangular tunnels with imperfectly conducting walls. The model is based on treating the tunnel as a waveguide, which is an extension of previous proposed model by Mahmoud [3]. A new approach to calculate the total attenuation rate of the propagated wave inside tunnel is proposed. The approach is considering the effect of imperfect conductivity of the upper and lower walls of the tunnel. This approach is based on assuming that the boundaries of the tunnel section are constant impedance surfaces as the surface impedance of the wall is almost independent of the angle of the wave incidence onto the wall. A simple scenario is considered to check the accuracy of this model. This scenario is verified by comparing experimental and numerical simulation results. Good agreement between the proposed model and the experimental results is obtained.

Index Terms ─ Curved waveguide, imperfect conducting walls, wave propagation.

I. INTRODUCTION

Since the early seventies of the last century till now, there has been a continued interest in radio communication through tunnels [1-23], since signaling within working areas in mine tunnels or road tunnels was of prime importance [8–20]. A tunnel can act as a waveguide for radio waves of sufficiently high frequency, as the wavelength is much smaller than the tunnel linear dimensions, whence attenuation occurs due to the surrounding rocks [8–11]. It should be noted that at frequencies of hundred MHz, the earth rocks will act as a dielectric material with low loss tangent. In this case, the attenuation of the electromagnetic waves propagating in the tunnel occurs mainly due to leakage of waves into the rocks rather than Ohmic losses. In the presence of longitudinal conductors such as electricity cables, low frequency waves can also propagate in the form of a coaxial like mode [12–16]. Intentionally placed leaky cables have been placed inside tunnels in order to control the signal level inside the tunnel [15–19]. A typical straight tunnel with cross sectional linear dimensions of few meters can act as a waveguide to electromagnetic waves at UHF and upper VHF bands [17].

Modal propagation in curved tunnel has been considered by Mahmoud and Wait [23] and Mahmoud [3], showing a considerable increase in the attenuation due to curvature. In this paper, we review high frequency propagation in tunnels with curved rectangular cross section. We assess previously obtained closed forms of the attenuation rates of the low order modes by Mahmoud [3]. In the previous work [3], the side walls of the tunnels are considered as imperfect conducting walls, while the upper and lower walls are considered as PEC walls. So the attenuation rate is mainly due to the side walls effect. The main objective of present paper is to extend the analysis of the previous work [3] to include the effects of considering the upper and lower walls as imperfect conducting walls and to introduce the approximate total attenuation rate of the propagating signal inside tunnels due to four walls with imperfect conductivity. Also, to compare the effect of the upper and lower walls effects on the attenuation rate compared to the effects of the side walls. This approach is done by deducing the attenuation rate of the upper and lower flat walls from the analogy with rectangular waveguide analysis in [3]. Finally, experimental results are conducted

Submitted On: July 25, 2016
Accepted On: September 9, 2016

in order to verify the presented theory.

II. MODAL ANALYSIS OF CURVED TUNNEL

Following [3], let us consider a rectangular tunnel, which is curved, in the horizontal plane as shown in Fig. 1. Using a cylindrical coordinates frame with the z-axis along the vertical direction, the side surfaces of the tunnel coincide with $\rho = R - a$ and $\rho = R + a$, where R is the mean radius of curvature. The main assumptions in the analysis are [3]: (i) the frequency is high so that $k_0 a \gg 1$ and therefore the walls can be characterized by constant surface impedance and admittance Zs and Ys where their normalized values are given by [3]:

$$Y_S = (\varepsilon_r - i\sigma/\omega\varepsilon_0)/\sqrt{\varepsilon_r - 1 - i\sigma/\omega\varepsilon_0}, \quad (1)$$

and

$$Z_S = 1/\sqrt{\varepsilon_r - 1 - i\sigma/\omega\varepsilon_0}, \quad (2)$$

where ε_r is the corridor walls relative permittivity and σ is the corridor walls conductivity, and (ii) slow curvature such that $R/a \gg 1$. The waveguide modes are either TM or TE to z. Considering E_z for the low order TMz modes and ignoring field variation along z as the electric field is vertical, the field is almost constant in z-direction (since $k_z \ll k_0$), the electric field is given as [3]:

$$E_z = f_v(k_0\rho)exp(-jv\emptyset), \quad (3)$$

where $f_v(k_0\rho)$ is a linear combination of Bessel functions of first and second kind with complex order v. However, with low curvature $R \gg a$, and high frequency excitation, it is expected that v and $k_0\rho$ are both large ($\gg 1$), while their difference is much less than v. Under these conditions, the modal equations for lower order TE_z and TM_z are derived in terms of the Airy functions instead of the Bessel function of complex order v and solved numerically for the propagation constant along the ϕ-direction [3]:

$$f_v(k_0\rho) = C_1 A_i(t) + C_2 B_i(t), \quad (4)$$

with

$$t = (k_0\rho/2)^{2/3}(v^2/k_0^2\,\rho^2 - 1), \quad (5)$$

where $A_i(t)$ and $B_i(t)$ are the Airy functions as defined in [3] and C_1 and C_2 are two arbitrary constants. The mathematical reasoning behind the validity of the Airy function representation is found in [3]. It can be noted that $v/k_0\rho$ is close to 1, the argument $t \ll (k_0\rho)$ for $R - a \le \rho \le R + a$.

Applying the boundary conditions at the curved surfaces $\rho = R - a$ and $\rho = R + a$ require that $\eta_0 H_\phi = \pm Y_s\, E_z$. Where,

$$H_\emptyset = (-j/\omega\mu_0)\,\partial E_z/\partial\rho, \quad (6)$$

$$H_\rho = \left(-\frac{v}{\omega\mu_0\rho}\right) * E_z, \quad (7)$$

and that,

$$\partial/\partial k_0\rho \cong -(\partial/\partial t)\,(2/k_0\rho)^{1/3}. \quad (8)$$

The two boundary conditions lead to the two equations [3]:

$$C_1 A_i'(t_+) + C_2 B_i'(t_+) = \overline{Y_+}[C_1 A_i(t_+) + C_2 B_i(t_+)], \quad (9\text{-a})$$

$$C_1 A_i'(t_-) + C_2 B_i'(t_-) = \overline{Y_-}[C_1 A_i(t_-) + C_2 B_i(t_-)], \quad (9.b)$$

where the prime is the differentiation with respect to the argument, $t_\pm$ are given by (5) with $\rho = R \pm a$ and,

$$\bar{Y}_\pm = jY_s[k_0(R \pm a)/2]^{1/3}, \quad (10)$$

the modal equation for v is obtained by equating the determinant of the coefficient C_1 and C_2 in (9) to zero. Once v is determined, the attenuation factor along the curved axis is given by [3]:

$$\alpha = -\text{Im}\,[v/R], \quad (11)$$

and the phase constant is:

$$\beta = \text{Re}\,[v/R]. \quad (12)$$

For TE case is treated in similar fashion with H_z the terms $\bar{Y}_\pm$ are replaced by:

$$\bar{Z}_\pm = jZ_s[k_0(R \pm a)/2]^{1/3}, \quad (13)$$

where Z_s is defined by (2).

It is noted from the proposed analysis that the previous model [3] considers the upper and lower tunnel walls as Perfect Electric Conductor (PEC) [3] and the attenuation rate in (11) is due to the side walls effects while this is not the case in real environment.

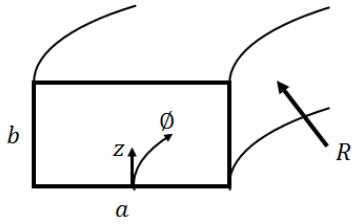

Fig. 1. Curved rectangular tunnel [3].

III. EXTRA ATTENUATION RATE DUE TO IMPERFECT CONDUCTIVITY OF THE UPPER AND LOWER

In reality, all the tunnel walls have imperfect conducting walls with low conductivity, thus for generality the attenuation rate inside the curved tunnel should be modified as to include the extra attenuation due to the imperfect conductivity of the upper and lower walls of tunnel. We can deduce the attenuation of the upper and lower flat walls of the curved tunnel with rectangular cross section from the analogy of rectangular tunnel analysis by approximating the upper and lower flat walls effect with the corresponding walls effect in the rectangular tunnel with same flat shape. We propose here, to use the attenuation of rectangular tunnel based on constant impedance walls proposed in [3]. A tunnel with rectangular cross section of dimensions a and b and the surrounding medium has a relative permittivity ε_r and conductivity σ Siemens/m. When the applied radio frequency is sufficiently high such that the tunnel dimensions are much greater than the free space wavelength λ_0, then the low order modes in the tunnel would have $k_x \ll k_0$ and $k_y \ll k_0$, where k_0 is the free space wavenumber, k_x and k_y are the wavenumbers in

the x and y directions. Under these conditions, the tunnel walls are accurately modeled by normalized constant surface impedance Zs and admittance Ys, which are obtained by (2) and (1), respectively. Following the analysis in [3], the approximate attenuation rate of the dominant mode with Vertical Polarization (VP) for rectangular tunnel is:

$$\alpha_{\text{rectangular}}^{VP} = \pi^2 Re(Y_s)/4k_0^2 b^3 + \pi^2 Re(Z_s)/4k_0^2 a^3 \quad Neper/m, \quad (14)$$

while for Horizontal Polarization (HP) is obtained by duality as:

$$\alpha_{\text{rectangular}}^{HP} = \pi^2 Re(Z_s)/4k_0^2 b^3 + \pi^2 Re(Y_s)/4k_0^2 a^3 \quad Neper/m, \quad (15)$$

where the effect of the upper and lower walls with low conductivity is approximated as the first part of (14) and (15). We use the same approach to calculate the extra attenuation in curved tunnel due to imperfect conductivity of the upper and lower walls, where the walls effect is approximated with the same corresponding effect of the upper and lower rectangular tunnel walls.

Thus, the extra attenuation is approximated for VP modes as:

$$\alpha_{extra\_atten}^{VP} = \pi^2 Re(Y_s)/4k_0^2 b^3 \quad Neper/m, \quad (16)$$

where Y_s is obtaied by (1) while for HP modes is:

$$\alpha_{extra\_atten}^{HP} = \pi^2 Re(Z_s)/4k_0^2 b^3 \quad Neper/m, \quad (17)$$

where Z_s is obtaied by (2).

Thus, the total approximate attenuation rate of wave propagating inside rectangular curved tunnel is obtained by (11) for side walls and (16) for upper and lower walls for VP modes as:

$$\alpha_{Total}^{VP} = \pi^2 Re(Y_s)/4k_0^2 b^3 + (-\text{Im}\left[\frac{v}{R}\right]), \quad (18)$$

and using same analysis, the HP total attenuation rate can be obtained.

The percentage of the extra attenuation rate due to upper and lower walls obtained by (16) and (17) compared with the side walls attenuation rate obtained by (11) is shown in Fig. 2 for HP and VP, respectively. The tunnel width a is 4.25 m while the tunnel height is $b = a/2$.

It can be noted that the VP has more attenuation than the HP, while in general it is found that the attenuation due to the side (curved) wall is much higher than the attenuation of the upper and lower flat walls.

The proposed total attenuation rate is implemented in Matlab which runs on a laptop with 8 GB of RAM, Intel 2.6 GHz processor, and operating system is Windows 10 64-bit. The tunnel width is 4.6 m while the height is 2.6 m. The tunnel radius of curvature is 20 times the tunnel width and the simulation is done in frequency range 0.2-0.8 GHz. The total program runtime for the above example is about 12 minutes. An algorithm is applied for finding the complex root of Eq. (9), which is considered the main bottleneck in the numerical calculations and the largest influence on the program speed. On the other hand, the same example is simulated using FEKO version 7.0 with the same computer resources. It is found that the simulation takes about 60 minutes using FEKO Physical Optics (PO) solver. It should be noted that the proposed model is faster than the simulation package and the differences will be increased by increasing the dimensions of the corridor or operating frequency. Figure 3 shows a comparison between the calculated normalized total attenuation rate using the proposed model and simulation results. It can be noted that good agreement is obtained and the calculated error between the model and simulation results is about 13.25%.

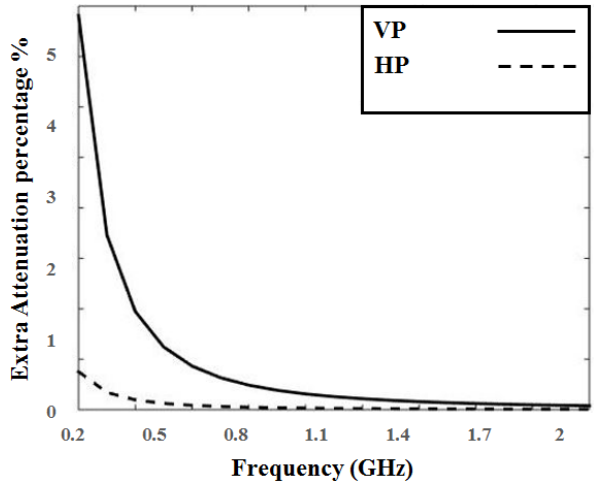

Fig. 2. Percentage of the extra attenuation due to the flat walls compared with the curved side walls attenuation.

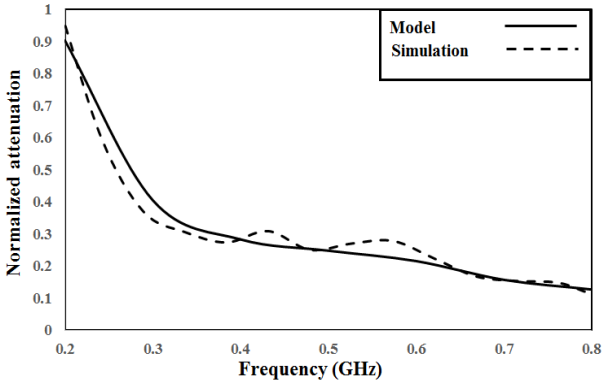

Fig. 3. Normalized attenuation in curved rectangular tunnel with VP modes, tunnel dimensions are $a = 4.6$ m, $b = 2.3$ m, and $R/a = 20$.

IV. MEASUREMENTS

In this section sample results are presented to verify the accuracy of the proposed model for the signal attenuation rate in curved tunnel. The proposed measurements are used to study the simple wave propagating inside rectangular curved tunnel for cars.

This simple scenario of a curved tunnel is verified

experimentally at frequency range 0.1-1 GHz. The scenario was done in curved tunnel for cars with concrete walls and with small metal sheets on both sides as shown in Fig. 4. The experimental setup consists of two carts. One cart is used to hold the transmitter and the other one is used to hold the receiving antenna and computer for receiving data collection and analysis as shown in Fig. 5. Handheld RF Signal Generator (RFEGEN 1.12) with dipole antenna with gain of 2.2 dBi is used as transmitter, while the receiver is RF Viewer wireless USB dongle and data is collected using computer software package RF spectrum analyzer (TOUCHSTONE PRO). The transmitting and receiving antennas are kept horizontally polarized and separated by a constant distance of 100 m. The tunnel width is 9.2 m and a length of 195 m. The height of the tunnel is 5.8 m. The height of both transmitting and receiving antennas is kept 1.3 m above the ground.

Figure 6 shows a comparison between measured total attenuation rate in dBm and the calculated one by using the proposed model. Good agreement between the measured and calculated results is obtained. The slight differences can be explained due to errors in the manual positioning of the receiving antenna and differences due to the boundary conditions of the actual tunnel and the existence of the small metal sheets. The calculated error between the model and measured results is about 12.3%.

Fig. 4. Curved rectangular tunnel for cars, width = 9.2 m, length = 195 m and height = 5.8 m.

(a)

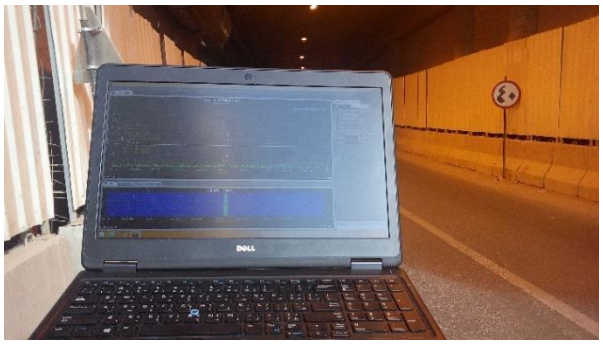

(b)

Fig. 5. Measurement setup: (a) transmitter (RF Signal Generator, and (b) receiver (computer software package RF spectrum analyzer).

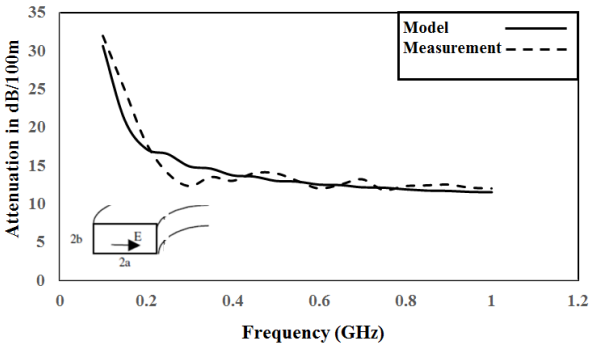

Fig. 6. Attenuation in curved rectangular tunnel with HP modes, tunnel dimensions are $a = 9.2$ m, $b = 5.8$ m, and $R/a = 56$.

V. CONCLUSION

A new approach is proposed to drive an approximate formula for the total attenuation rate in curved rectangular tunnel. The proposed model takes into consideration the attenuation effect due to imperfect conductivity of the upper and lower walls in addition to the effect of the side walls. The effect of the flat upper and lower walls are approximated by the corresponding effect of the upper and lower walls in rectangular tunnel. It is found that the attenuation due to the side (curved) wall is much higher than the attenuation of the upper and lower flat walls. The proposed total attenuation rate is verified by comparison with experimental results. Good agreements are obtained from these comparisons.

REFERENCES

[1] K. Guan, B. Ai, Z. Zhong, C. Lopez, L. Zhang, C. Briso, A. Haovat, and B. Zhang "Measurements and analysis of large-scale fading characteristics in curved subway tunnels at 920 MHz, 2400 MHz, and 5705 MHz," *IEEE Trans. on Intelligent Transportation System*, vol. 16, Oct. 2015.

[2] B. Zhang, Z. Zhong, K. Guan, R. He, and C. Briso,

"Shadow fading correlation of multi-frequencies in curved subway tunnels," *Proc. IEEE Conf. ITSC*, Qingdao, China, pp. 1111-1116, 2014.

[3] S. F. Mahmoud, "Modal propagation of high frequency electromagnetic waves in straight and curved tunnels within the earth," *J. of Electromagn. Waves and Appl.*, vol. 19, no. 12, pp. 1611-1627, 2005.

[4] M. Lienard, J. M. Molina-Garcia-Pardo, P. Laly, C. Sanchis-Borras, and P. Degauque, "Communication in tunnel: Channel characteristics and performance of diversity schemes," *General Assembly and Scientific Symposium (URSI GASS), 2014 URSI*, Aug. 2014.

[5] M. Lienard, C. Sanchis-Borras, J.-M. Molina-Garcia-Pardo, D. P. Gaillot, P. Laly, and P. Degauque, "Performance analysis of antenna arrays in tunnel environment," *IEEE Antennas and Wireless Propagation Letters*, vol. 13, pp. 12-125, 2014.

[6] M. Lienard, J.-M. Molina-Garcia-Pardo, P. Laly, C. Sanchis-Borras, and P. Degauque, "MIMO and diversity techniques in tunnels," *International Conference on Computing, Management and Telecommunications (ComManTel)*, Apr. 2014.

[7] C. Garcia-Pardo, J.-M. Molina-Garcia-Pardo, M. Lienard, D. P. Gaillot, and P. Degauque, "Double directional channel measurements in an arched tunnel and interpretation using ray tracing in a rectangular tunnel," *Progress In Electromagnetics Research M*, vol. 22, pp. 91-107, 2012.

[8] A. G. Emslie and R. L. Lagace, "Theory of the propagation of UHF radio waves in coal mine tunnels," *IEEE Trans. AP*, vol. 23, no. 2, pp. 192-205, 1975.

[9] S. F. Mahmoud and J. R. Wait, "Geometrical optical approach for electromagnetic wave propagation in rectangular mine tunnels," *Radio Science*, vol. 9, no. 12, pp. 1147-1158, 1974.

[10] P. Delogne, "Basic mechanisms of tunnel propagation," *Radio Science*, vol. 11, pp. 299-303, 1976.

[11] J. R Wait and D. A. Hill, "Guided electromagnetic waves along an axial conductor in a circular tunnel," *IEEE Trans. AP*, vol. 22, pp. 627-630, 1974.

[12] S. F Mahmoud and J. R. Wait, "Theory of wave propagation along a thin wire inside a rectangular waveguide," *Radio Science*, pp. 417-420, 1974.

[13] S. F. Mahmoud, "Characteristics of electromagnetic guided waves for communication in coal mine tunnels," *IEEE Trans. COM*, vol. 22, pp. 1547-1554, 1974.

[14] J. R. Wait and D. A. Hill, "Propagation along a braided coaxial cable in a circular tunnel," *IEEE Trans. MTT*, vol. 23, pp. 401-405, May 1975.

[15] J. R.Wait, "EM theory of the loosely braided coaxial cable: Part I," *IEEE Trans. MTT*, vol. 24, pp. 262-265, 1976.

[16] D. A. Hill and J. R. Wait, "EM theory of the loosely braided coaxial cable: Part II-Numerical results," *IEEE Trans. MTT*, vol. 28, pp. 262-265, 1980.

S. F. Mahmoud and J. R. Wait, "Calculated channel characteristics of a braided coaxial cable in a mine tunnel," *IEEE Trans. COM*, vol. 24, pp. 82-87, 1976.

[17] P. Degauque, B. Demoulin, J. Fontaine, and R. Gabillard, "Theory and experiment of a mobile communication in tunnels by means of a leaky braided coaxial cable," *Radio Science*, vol. 11, pp. 305-314, 1976.

[18] P. Delogne, *Leaky Feeders and Subsurface Radio Communication*, IEE Electromagnetic Series 14, Peter Peregrinus Ltd., 1982.

[19] M. Lienard and P. Degauque, "Propagation in wide tunnels at 2 GHz: A statistical analysis," *IEEE Trans. on Vehicular Technology*, vol. 47, no. 4, pp. 1322-1328, Nov. 1998.

[20] S. F. Mahmoud, *Wireless Transmission in Tunnels*, *Mobile and Wireless Communications Physical Layer Development and Implementatiom*. Salma Ait Fares and Fumiyuki Adachi (Ed.), InTech.

[21] M. Lienard and P. Degauque, "Natural wave propagation in mine environment," *IEEE Trans. on AP*, vol. 48, no. 9, pp. 1326-1339, 2002.

[22] S. F. Mahmoud and J. R. Wait, "Guided electromagnetic waves in a curved rectangular mine tunnel," *Radio Science*, pp. 567-572, May 1974.

Hany M. El-Maghrabi received the B.S. degree, with Honor Degree, and M.S. degree in Electrical Engineering from the Cairo University (Egypt). El-Maghrabi has received a position of Research Assistant in Housing and Building National Research Center (HBNRC), Institute of Electromechanical, Department of Communication (Egypt) in 2005. He became Assistant Researcher at HBNRC in 2011. He has co-authored technical journal articles and conference papers. El-Maghrabi has experience in electromagnetics, antennas, microstrip structures, numerical methods, wave propgation and their applications in microwave. El-Maghrabi was awarded the best paper in NRSC 2015.

Samir F. Mahmoud graduated from the Electronic Engineering Dept., Cairo University, Egypt in 1964. He received the M.Sc. and Ph.D. degrees in the Electrical Engineering Department, Queen's University, Kingston, Ontario, Canada in 1970 and 1973. During the academic year 1973-1974, he was a Visiting Research Fellow at the Cooperative Institute for Research in Environmental Sciences (CIRES), Boulder, CO, doing research on Communication in Tunnels. He spent two sabbatical years, 1980-1982, between Queen Mary College, London and the British Aerospace, Stevenage, where he was involved in design of antennas for satellite communication. He spent several years as Professor at the EE Department, Kuwait University. Currently Mahmoud is a Full Professor at the Electronic and Telecommunication Engineering Department, Cairo University. Recently, he has visited several places including Interuniversity Micro-Electronics Centre (IMEC), Leuven, Belgium and spent a sabbatical leave at Queen's University and the Royal Military College, Kingston, Ontario, Canada in 2001-2002. His research activities have been in the areas of antennas, geophysics, tunnel communication, and EM wave interaction with composite materials. Mahmoud is a Fellow of IET and one of the recipients of the Best IEEE/MTT paper for 2003.

Ahmed M. Attiya received the M.Sc. and Ph.D. degrees in Electronics and Electrical Communications, Faculty of Engineering, Cairo University in 1996 and 2001, respectively. He joined Electronics Research Institute as a Researcher Assistant in 1991. In the period from 2002 to 2004, he was a Postdoc in Bradley Department of Electrical and Computer Engineering at Virginia Tech. In the period from 2004 to 2005, he was a Visiting Scholar in Electrical Engineering Dept. at the University of Mississippi. In the period from 2008 to 2012 he was a Visiting Teaching Member in King Saud University. He is currently Full Professor and the Head of Microwave Engineering Dept. at Electronics Research Institute.

Mostafa El-Said graduated from the Electronic Engineering Dept., Cairo University, Egypt in 1963. He received the Dipl.Ing. and Dr.Ing. degrees from Karlsruhe University, West Germany, in 1970 and 1974. Since 1992, he is Professor at the Electronic Engineering and Tele-communication Department Cairo University. His research activities have been in the areas of microstrip, wave propagation and nano technology.

Essam A. Hashish (M'96) received the B.Sc., M.Sc. and Ph.D. degrees from the Electronics and Comm-unications Department, Faculty of Engineering, Cairo University, Giza, Egypt, in 1973, 1977, and 1985, respectively. He is currently a Professor with the Electromagnetics Group at the same department. His main interest is electromagnetic remote sensing, wave propagation, and microwave antennas.

Efficient Electromagnetic Scattering Analysis of Open-ended Circular Cavities with Modal MoM Method

A. Aghabarati, P. Dehkhoda, and A. Tavakoli

Department of Electrical Engineering
Amirkabir University of Technology, Tehran, Iran
aghabarati@gmail.com, pdehkhoda@aut.ac.ir, tavakoli@aut.ac.ir

Abstract ─ An efficient and accurate technique is introduced to calculate the scattered electromagnetic (EM) fields from an open-ended circular cavity (OECC). In this paper, it is assumed that the OECC is perforated in an infinite perfect electric conductor (IPEC). Then, the scattered fields are calculated using modal Method of Moments. The complexity and computational cost of the encountered quadruple integrals are addressed in detail. Here, the singularities are extracted and resolved. Next, the scattered far field of a circular PEC plate of the same size is calculated by physical optics approximation. The final OECC scattered field is the sum of these two solutions. A very good agreement is observed between the results of this method and full wave numerical simulations and measurements. The proposed approach is highly efficient and accurate over a wide range of frequencies and incidence angles, making it appealing for analysis of large frequency dispersive structures.

Index Terms ─ Electromagnetic scattering, modal moment method, open-ended circular cavity.

I. INTRODUCTION

Electromagnetic (EM) scattering from open-ended waveguides is an important and challenging problem in applied electromagnetics. Ducts and jet engine inlets that significantly contribute to the total Radar Cross Section (RCS) can be modeled by waveguide structures. The subject is also important in target recognition, object classification, and remote sensing applications.

An informative review of the existing methods for scattering analysis of open-ended cavity structures is presented by Anastassiue [1]. In this review, the methods are classified into two major categories for arbitrary shapes and canonical waveguides. For arbitrary structures, numerical techniques are reported [2-4]. In spite of their generality for handling complex geometries, these methods are computationally limited to small scatterers, particularly in wideband analysis. Various hybrid methods are developed to reduce the computational burden [5-6]. At high frequencies, where the cavity dimensions are large compared to the wavelength, asymptotic methods such as Physical Optics (PO), Soothing and Bouncing Rays (SBR) or the method of Generalized Ray Expansion (GRE) are reported [7-9].

Recently, a full wave approach by using finite-element sub-domain based scattering matrix methodology is proposed for open-ended cavities which aim to solve electrically large problem efficiently by using a reduced-order modeling technique. The efficiency in this model reduction is achieved by changing from finite element degrees of freedom to guided wave participation factors [10, 11].

For open-ended rectangular or circular waveguides, modal methods are utilized to model the wave propagation through the duct [12-14]. Modal analysis is also used to model multi-section inlets or complex terminated geometries containing hubs or straight blades [15, 16]. This efficient method is extensively used with a satisfactory level of accuracy for various cavity problems.

Here, a full wave modal moment technique (modal MoM) is offered to evaluate the scattered fields from an open-ended circular cavity (OECC). First, the modal MoM is employed to calculate the scattered field from an OECC perforated in an infinite perfect electric conductor (IPEC). In this phase, all the mutual couplings between the propagating and evanescent modes excited at the aperture are considered efficiently in the moment admittance matrix. Second, the scattered field from a PEC plate of the same shape and size of the waveguide aperture is calculated by PO method. The two solutions of the scattered fields are added to obtain the scattered field of an OECC.

The total unknown magnetic current on the aperture is represented by an entire domain vector wave function in cylindrical coordinates. The continuity of the magnetic field on the aperture is enforced and the resulted integral equation is solved by Galerkin method.

Here, the computational complexity is carefully addressed by resolving singularities and decreasing the order of integrations.

Monostatic Radar Cross Section (RSC) of various OECCs are calculated and compared with full wave numerical methods and measurements. An excellent

Submitted On: May 25, 2014
Accepted On:July 4, 2016

agreement is observed between the results for both vertical and horizontal polarizations. It is shown that adding the scattered field of the PEC to the results of the waveguide terminated by an IPEC removes the effect of IPEC presence, especially at low grazing angles. This cost effective approach could be used for wideband time-frequency dispersion analysis of open-ended circular cavities.

In Section 2, the mathematical formulation of scattering form an OECC at different polarizations is presented. Section 3 contains the comparison between the results of this approach and Finite Element-Infinite Element (FE-IE) approach [4], the Multi-Level Fast Multipole Method (MLFMM) by the commercial software FEKO and measurements. The concluding remarks are given in Section 4.

II. MATHEMATICAL FORMULATION

In this section, the scattered far field for a real OECC is formulated for an arbitrarily polarized incident plane wave based on modal Method of Moments (modal MoM).

A. Problem description and solution steps

Figure 1 shows a perfect electric conductor OECC. The waveguide is open ended at one side and shorted at the other. L is the length of the cavity and D is its diameter. The goal is the evaluation of the scattered far fields in the $z > 0$ half space, when the cylinder is obliquely illuminated by a plane wave incident at (θ_i, ϕ_i):

$$\vec{\boldsymbol{E}}_{inc} = e^{-j\vec{k}_i\cdot\vec{r}_i}\left(E^{\theta}_{inc}\hat{u}_{\theta} + E^{\phi}_{inc}\hat{u}_{\phi}\right), \quad (1)$$

where,

$$\vec{k}_i = k_0\hat{u}_i = k_0[\cos(\theta_i)\cos(\phi_i)\,\hat{u}_x + \cos(\theta_i)\sin(\phi_i)\,\hat{u}_y + \sin(\theta_i)\,\hat{u}_z], \quad (2)$$

is the wave vector and $k_0 = 2\pi/\lambda_0$ is the free space wave number. We note that the unit for all the angles in the text is radian.

Here, let $a = D/\lambda_0$ be the normalized aperture diameter, $l = L/\lambda_0$ be the normalized cavity length and also $\bar{k} = k_0/\lambda_0$ be the normalized value of wave number with respect to the wavelength.

Due to axial symmetry, one can arbitrarily set $\phi_i = 0$ and then analyze the problem for the perpendicular polarization (TM) and the parallel polarization (TE). In the following derivations, $\parallel$ and $\perp$ represent TE and TM polarizations, respectively as shown in Fig. 2. Dividing the incident wave into two polarizations leads to $E^{\theta}_{inc} = E^{\parallel}_0$ and $E^{\phi}_{inc} = E^{\perp}_0$, as well as explicit expressions for the interior EM fields in terms of modal expansions. Similarly, back scattered field can be represented by a diagonal normalized scattering matrix as in [13]. The backscattered field for the observation point $\vec{r}_s$ is:

$$\vec{\boldsymbol{E}}^{s}(\vec{r}_s) = \boldsymbol{E}^{s\parallel}(\vec{r}_s)\hat{u}_{\theta} + \boldsymbol{E}^{s\perp}(\vec{r}_s)\hat{u}_{\phi}. \quad (3)$$

Now, the problem is solved in two steps as follows:

Step 1: It is assumed that the cavity's aperture is perforated in an IPEC and then EM scattered fields are calculated. Here, applying the surface equivalence principle and enforcing the magnetic field boundary condition on the aperture results in an integral equation with unknown magnetic currents in which the dyadic Green's functions of the circular cavity and the upper half-space are utilized. The magnetic currents on the aperture ($\vec{M}_{\Gamma}$) are expanded in cylindrical entire domain basis functions for evaluation. This derivation is based on an infinite ground plane assumption and is not accurate for a real OECC [17]. However, the modification in step 2 corrects the scattered field calculations.

Step 2: Now, the scattered field of step 1 is corrected using the approach of Zdunek and Rachowicz [17]. The correction is done by adding the PO scattered field of a co-located hypothetical PEC lid of the aperture size to the previously calculated one. The simple modification provided by $\vec{\boldsymbol{E}}^{s}_{lid}(\vec{\boldsymbol{J}}_{\Gamma})$ is shown to be corrective, especially for close to normal incidence angles on the aperture.

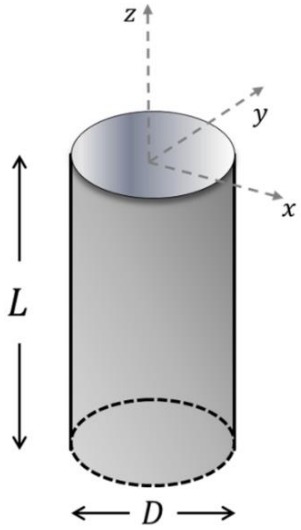

Fig. 1. Geometry of the problem.

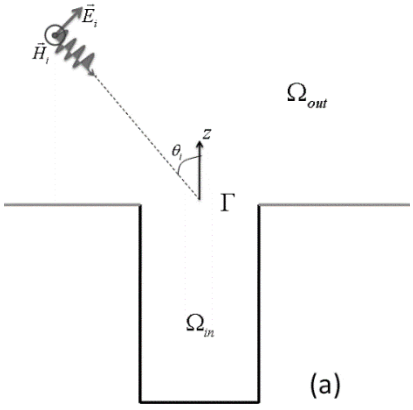

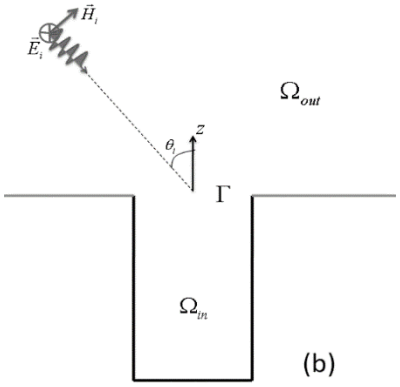

Fig. 2. Perforated OECC in an IPEC, illuminated by: (a) horizontally polarized, and (b) vertical polarized incident wave.

B. Modal MoM solution for an OECC terminated by an IPEC

Here, it is assumed that the aperture of OECC is perforated in an IPEC. This structure is analyzed by modal MoM and is called GP (Ground Plane) model. The unknown electric field on the aperture is expanded by modal functions for the TM and TE polarizations with unknown coefficients as:

$$\vec{\boldsymbol{E}}_{\Gamma}^{\parallel} = \sum_{m=0}^{M}\sum_{n=0}^{N}\left\{C_{nm}^{\mathbf{M^o}}\vec{\mathbf{M}}_{\mu_{nm}}^{\mathbf{o}} + C_{nm}^{\mathbf{N^e}}\vec{\mathbf{N}}_{\lambda_{nm}}^{\mathbf{e}}\right\}, \tag{4}$$

$$\vec{\boldsymbol{E}}_{\Gamma}^{\perp} = \sum_{m=0}^{M}\sum_{n=0}^{N}\left\{C_{nm}^{\mathbf{M^e}}\vec{\mathbf{M}}_{\mu_{nm}}^{\mathbf{e}}\right\}, \tag{5}$$

where $\Gamma = \{\mathrm{r} \in \mathbb{R}^2 : 0 < \rho < \mathrm{D},\ \mathrm{z} = 0\}$ is the domain of the aperture and nm represents the pair of indices for the considered modes [18]. $\vec{\mathbf{M}}_{\mu_{nm}}^{\mathbf{e}}$, $\vec{\mathbf{M}}_{\mu_{nm}}^{\mathbf{o}}$, $\vec{\mathbf{N}}_{\lambda_{nm}}^{\mathbf{e}}$ (and $\vec{\mathbf{N}}_{\lambda_{nm}}^{\mathbf{o}}$) are even and odd modal functions as reported in [18] and shown at the bottom of this page.

In (5), due to the orthogonality between incident wave and $\vec{\mathbf{N}}_{\lambda_{nm}}^{\mathbf{o}}$ on the aperture, all corresponding excitation coefficients are zero. In (6) and (7), $J_n(\cdot)$ and $J_n'(\cdot)$ are the Bessel function of first kind and its derivative with $\mathcal{Z}_{nm}$ and $\mathcal{Z}_{nm}'$ as their zeroes respectively. We define $\lambda_{nm} = 2\mathcal{Z}_{nm}/\mathrm{D}$ and $\mu_{nm} = 2\mathcal{Z}_{nm}'/\mathrm{D}$. In addition, Π_{nm} and Π_{nm}' are normalization factors for transverse components of nmth TE or TM mode respectively;

$$\Pi_{nm} = \left[J_n'(\mathcal{Z}_{nm})\sqrt{0.5\pi\mathcal{Z}_{nm}^2(1+\delta_n)}\right]^{-1}, \tag{8}$$

$$\Pi_{nm}' = \left[J_n(\mathcal{Z}_{nm}')\sqrt{0.5\pi(\mathcal{Z}_{nm}'^2 - n^2)(1+\delta_n)}\right]^{-1}, \tag{9}$$

where δ_n is the Dirac delta function.

The external and internal regions are separated by an equivalent magnetic currents on the aperture using the equivalence principle. The equivalent magnetic currents are:

$$\vec{\boldsymbol{M}}_{\Gamma}^{\parallel} = \hat{z} \times \vec{\boldsymbol{E}}_{\Gamma}^{\parallel} = \sum_{m=0}^{M}\sum_{n=0}^{N}\left\{C_{nm}^{\mathbf{M^o}}\vec{\mathbf{N}}_{\mu_{nm}}^{\mathbf{o}} - C_{nm}^{\mathbf{N^e}}\vec{\mathbf{M}}_{\lambda_{nm}}^{\mathbf{e}}\right\}, \tag{10}$$

$$\vec{\boldsymbol{M}}_{\Gamma}^{\perp} = \hat{z} \times \vec{\boldsymbol{E}}_{\Gamma}^{\perp} = -\sum_{m=0}^{M}\sum_{n=0}^{N}\left\{C_{nm}^{\mathbf{M^e}}\vec{\mathbf{N}}_{\mu_{nm}}^{\mathbf{e}}\right\}. \tag{11}$$

TE and TM Magnetic fields in the internal region ($\Omega_{\mathrm{in}} = \{\mathrm{r} \in \mathbb{R}^3 : 0 < \rho < \mathrm{D}, -\mathrm{L} < \mathrm{z} < 0\}$) are calculated from the sources in (10) and (11) using $\overline{\overline{\mathrm{G}}}_{\mathrm{E}'}$, which is the circular cavity dyadic Green's function of the second kind [18]. The Dyadic Green's function can be used to calculate the magnetic fields due to arbitrary oriented magnetic current source inside the cavity. It is obtained from the solution of vector eigenfunctions in cylindrical coordinate system satisfying the boundary conditions of the cylindrical cavity and provides the basic mathematical tool for numerical study of the cylindrical cavities by MoM. The resultant magnetic fields at $\mathrm{z} = 0$ are:

$$\vec{\boldsymbol{H}}_{\mathrm{in}}^{\parallel}\big|_{z=0} = -\sum_{m=0}^{M}\sum_{n=0}^{N}\left\{\frac{\bar{h}_{nm}^{\mu}\cot(\bar{h}_{nm}^{\mu}l/a)}{\bar{k}^2}C_{nm}^{\mathbf{M^o}}\vec{\mathbf{N}}_{\mu_{nm}}^{\mathbf{e}} - \frac{\cot(\bar{h}_{nm}^{\lambda}l/a)}{\bar{h}_{nm}^{\lambda}}C_{nm}^{\mathbf{N^e}}\vec{\mathbf{M}}_{\lambda_{nm}}^{\mathbf{e}}\right\}, \tag{12}$$

$$\vec{\boldsymbol{H}}_{\mathrm{in}}^{\perp}\big|_{z=0} = -\sum_{m=0}^{M}\sum_{n=0}^{N}\left\{\frac{\bar{h}_{nm}^{\mu}\cot(\bar{h}_{nm}^{\mu}l/a)}{\bar{k}^2}C_{nm}^{\mathbf{M^e}}\vec{\mathbf{N}}_{\mu_{nm}}^{\mathbf{e}}\right\}, \tag{13}$$

where $\bar{h}_{nm}^{\mu} = \sqrt{\bar{\mathrm{k}}^2 - \mathcal{Z}_{nm}'^2}$, $\bar{h}_{nm}^{\lambda} = \sqrt{\bar{\mathrm{k}}^2 - \mathcal{Z}_{nm}^2}$ and $\vec{\mathbf{N}}_{\mu_{nm}}^{\mathbf{e}} = \begin{Bmatrix}\vec{\mathbf{N}}_{\mu_{nm}}^{\mathbf{e}} \\ \vec{\mathbf{N}}_{\mu_{nm}}^{\mathbf{o}}\end{Bmatrix}$ stands for simultaneous inclusion of both even and odd functions.

The magnetic current for the external region ($\Omega_{\mathrm{in}} = \{\mathrm{r} \in \mathbb{R}^3 : \mathrm{z} > 0\}$) is the negative of (10) and (11) due to the continuity of the tangential electric field. Addition of IPEC to the problem allows the application of the half-space Green's function. Magnetic fields at $\mathrm{z} = 0$ become:

$$\vec{\boldsymbol{H}}_{\mathrm{out}}^{\parallel}\big|_{z=0} = \frac{-2}{a}\iint_{\Gamma}\left(1 + \frac{1}{k_0^2}\nabla\nabla\cdot\right)\vec{\boldsymbol{M}}_{\Gamma}^{\parallel}\,\mathbf{G}_0(\vec{\boldsymbol{r}},\vec{\boldsymbol{r}}')\mathrm{d}s', \tag{14}$$

$$\vec{\boldsymbol{H}}_{\mathrm{out}}^{\perp}\big|_{z=0} = \frac{2}{a}\iint_{\Gamma}\left(1 + \frac{1}{k_0^2}\nabla\nabla\cdot\right)\vec{\boldsymbol{M}}_{\Gamma}^{\perp}\,\mathbf{G}_0(\vec{\boldsymbol{r}},\vec{\boldsymbol{r}}')\mathrm{d}s', \tag{15}$$

where $\mathrm{G}_0(\vec{\mathrm{r}},\vec{\mathrm{r}}') = \frac{\mathrm{e}^{\mathrm{j}\mathrm{k}|\vec{\mathrm{r}}-\vec{\mathrm{r}}'|}}{4\pi|\vec{\mathrm{r}}-\vec{\mathrm{r}}'|}$, and the surface integral is

$$\begin{Bmatrix}\vec{\mathbf{M}}_{\mu_{nm}}^{\mathbf{e}} \\ \vec{\mathbf{M}}_{\mu_{nm}}^{\mathbf{o}}\end{Bmatrix} = \Pi_{nm}'\left[\frac{n}{\rho}J_n(\mu_{nm}\rho)\begin{Bmatrix}-\sin(n\phi) \\ \cos(n\phi)\end{Bmatrix}\hat{u}_{\rho} - \mu_{nm}J_n'(\mu_{nm}\rho)\begin{Bmatrix}\cos(n\phi) \\ \sin(n\phi)\end{Bmatrix}\hat{u}_{\phi}\right], \tag{6}$$

$$\begin{Bmatrix}\vec{\mathbf{N}}_{\lambda_{nm}}^{\mathbf{e}} \\ \vec{\mathbf{N}}_{\lambda_{nm}}^{\mathbf{o}}\end{Bmatrix} = \Pi_{nm}\left[\lambda_{nm}J_n'(\lambda_{nm}\rho)\begin{Bmatrix}\cos(n\phi) \\ \sin(n\phi)\end{Bmatrix}\hat{u}_{\rho} - \frac{n}{\rho}J_n(\lambda_{nm}\rho)\begin{Bmatrix}\sin(n\phi) \\ -\cos(n\phi)\end{Bmatrix}\hat{u}_{\phi}\right]. \tag{7}$$

taken over the aperture.

The continuity of the tangential magnetic field at $z = 0$ leads to:

$$\vec{H}^{\parallel,\perp}_{\text{in}}\big|_{z=0} - \vec{H}^{\parallel,\perp}_{\text{out}}\big|_{z=0} = 2\vec{H}^{\parallel,\perp}_{\text{inc}}\big|_{z=0}. \quad (16)$$

Factor 2 in (16) comes from the summation of the incident and reflected fields in the external region. Equation (16) is a Magnetic Field Integral Equation (MFIE) and can be converted to matrix equations using the Galerkin method. The matrix equations have the form $[K]^{\parallel}[C]^{\parallel} = [B]^{\parallel}$ and $[K]^{\perp}[C]^{\perp} = [B]^{\perp}$, where $[K]^{\parallel}$ and $[K]^{\perp}$ are the moment admittance matrices and $[B]^{\parallel}$ and $[B]^{\perp}$ are the excitation matrices. Also, $[C]^{\parallel}$ and $[C]^{\perp}$ consist of the unknown modal amplitudes for the two polarizations that depend on the incident wave angle.

C. Mathematical consideration in admittance and excitation matrices

The above matrices have the following general forms for the two polarizations:

$$\begin{bmatrix} K^{\langle \mathbf{M^e},\mathbf{M^e}\rangle} & K^{\langle \mathbf{M^e},\mathbf{N^o}\rangle} \\ K^{\langle \mathbf{N^o},\mathbf{M^e}\rangle} & K^{\langle \mathbf{N^o},\mathbf{N^o}\rangle} \end{bmatrix} \begin{bmatrix} C^{\mathbf{N^e}} \\ C^{\mathbf{M^o}} \end{bmatrix} = \begin{bmatrix} B^{\langle \mathbf{N^e},\vec{H}^{\parallel}_{\text{inc}}\rangle} \\ B^{\langle \mathbf{N^o},\vec{H}^{\parallel}_{\text{inc}}\rangle} \end{bmatrix}, \quad (17)$$

$$\left[K^{\langle \mathbf{N^o},\mathbf{N^o}\rangle}\right]\left[C^{\mathbf{M^e}}\right] = \left[B^{\langle \mathbf{N^e},\vec{H}^{\perp}_{\text{inc}}\rangle}\right]. \quad (18)$$

Since computing admittance and excitation matrix for the entire domain moment method can impose large computational burden, it is necessary to evaluate them efficiently. The admittance matrices in TE polarization is a block structured matrix. The elements in $[K]^{\parallel}$ and $[K]^{\perp}$ correspond to different interactions between expansion and weighting functions in Galerkin method. Hence, if $W_{pq}(\rho,\phi)$ and $E_{nm}(\rho',\phi')$ are the pqth weighting coefficient and nmth expansion functions, each element of admittance matrices in $[K]^{\parallel}$ or $[K]^{\perp}$ will have the following form:

$$K^{\langle \mathbf{W}_{pq},\mathbf{E}_{nm}\rangle} = V^{\langle \mathbf{W}_{pq},\mathbf{E}_{nm}\rangle} + Z^{\langle \mathbf{W}_{pq},\mathbf{E}_{nm}\rangle}, \quad (19)$$

where $V^{\langle \mathbf{W}_{pq},\mathbf{E}_{nm}\rangle}$ and $Z^{\langle \mathbf{W}_{pq},\mathbf{E}_{nm}\rangle}$ are related to inside and outside field contributions, respectively. Then,

$$V^{\langle \mathbf{W}_{pq},\mathbf{E}_{nm}\rangle} = \iint_{\Gamma}\iint_{\Gamma'} \mathbf{W}_{pq}\cdot\mathbf{E}_{nm}\,ds'\,ds, \quad (20)$$

$$Z^{\langle \mathbf{W}_{pq},\mathbf{E}_{nm}\rangle} = \frac{2}{a}\iint_{\Gamma}\iint_{\Gamma'}\left\{\mathbf{W}_{pq}\cdot\mathbf{E}_{nm} - \frac{1}{k_0^2}\left[\nabla\cdot\mathbf{W}_{pq}\right]\cdot\left[\nabla'\cdot\mathbf{E}_{nm}\right]\right\}\mathbf{G}_0\,ds'ds, \quad (21)$$

where,

$$\langle \mathbf{W}_{pq},\mathbf{E}_{nm}\rangle \in \left\{\begin{matrix}\langle \vec{\mathbf{M}}^{\mathbf{e}}_{\lambda_{pq}},\vec{\mathbf{M}}^{\mathbf{e}}_{\lambda_{nm}}\rangle, \langle \vec{\mathbf{M}}^{\mathbf{e}}_{\lambda_{pq}},\vec{\mathbf{N}}^{\mathbf{o}}_{\mu_{nm}}\rangle, \langle \vec{\mathbf{N}}^{\mathbf{o}}_{\mu_{pq}},\vec{\mathbf{M}}^{\mathbf{e}}_{\lambda_{nm}}\rangle \\ \langle \vec{\mathbf{N}}^{\mathbf{o}}_{\mu_{pq}},\vec{\mathbf{N}}^{\mathbf{o}}_{\mu_{nm}}\rangle, \langle \vec{\mathbf{N}}^{\mathbf{e}}_{\mu_{pq}},\vec{\mathbf{N}}^{\mathbf{e}}_{\mu_{nm}}\rangle\end{matrix}\right\}. \quad (22)$$

While numerical evaluation of (20) is straight forward, evaluation of (21) is complicated due to a singularity at $\vec{r} = \vec{r}'$ in $G_0(\vec{r},\vec{r}')$. By applying the following modifications, the singularity in (21) is removed and the integrations are computed efficiently.

First, at each integration point (ρ,ϕ) in (21), a change of variables $x' - \rho\cos(\phi) = \rho'\cos(\phi')$ and $y' - \rho\sin(\phi) = \rho'\sin(\phi')$ is done in prime coordinates in order to shift the origin into the point (ρ,ϕ). Even though this makes the prime variable integration dependent on ρ and ϕ, but removes the singularity. Next, the integration on ϕ is simply carried out analytically and hence, the order of integration is decreased by one. In addition, orthogonality of the functions with unequal p and n, which leads to zero entries in most of the elements in $[K]^{\parallel}$ and $[K]^{\perp}$, is employed. For instance, outside field contributions of a single element in $K^{\langle \mathbf{N^o},\mathbf{N^o}\rangle}$ can be reduced to the triple integral as follows:

$$Z^{\langle \vec{\mathbf{N}}^{\mathbf{o}}_{\mu_{pq}},\vec{\mathbf{N}}^{\mathbf{o}}_{\mu_{nm}}\rangle} = \delta(p-n)\Pi'_{pq}\Pi'_{nm}\int_{\rho=0}^{1} d\rho \int_{\phi'=0}^{\pi} d\,\phi' \int_{\rho=0}^{\Upsilon} \{[-Z'_{pq}Z'_{pm}J_{p-1}(Z'_{pq}\rho) + \frac{pZ'_{pm}}{\rho}J_p(Z'_{pq}\rho)]J_{p+1}(Z'_{pm}|X|) + [\frac{pZ'_{pq}}{|X|}J_{p-1}(Z'_{pq}\rho) - \left(\frac{Z'_{pq}Z'_{pm}}{2\pi\rho}\right)^2 J_p(Z'_{pq}\rho)]J_p(Z'_{pm}|X|)\} \cos(px)\, e^{j2\pi a\rho'} d\rho', \quad (23)$$

where, $X = \rho + \rho' e^{j\phi'} = |X|e^{jx}$ and $\Upsilon = -\rho\cos(\phi') + \sqrt{1-\rho^2\sin(\phi')}$ are defined variables that appear in the evaluation of non-zero entries for all blocks of admittance matrices. The adaptive quadrature integration method of [19] is used to compute integrations similar to (23) for $[K]^{\parallel}$ and $[K]^{\perp}$.

Here we note that mentioned modifications to the integrals of form (21) extensively reduce the computational cost in modal MoM solution. In contrast to other numerical methods (e.g., sub-domain MoM), this technique deals with a fairly small, sparse, symmetric and well-conditioned matrices. Furthermore, most of the computational cost in this method is due to the calculation of the wave coupling through the aperture, which is independent of the cavity depth or the incident wave direction. Thus, the method is very efficient even for very long dispersive OECCs.

Finally, elements of the excitation matrices are:

$$B^{\langle \mathbf{W}_{pq},\vec{H}^{\parallel}_{\text{inc}}\rangle} = \iint_{\Gamma} \mathbf{W}_{pq}\cdot\vec{H}^{\parallel}_{\text{inc}}\,ds, \quad (24)$$

$$B^{\langle \mathbf{W}_{pq},\vec{H}^{\perp}_{\text{inc}}\rangle} = \iint_{\Gamma} \mathbf{W}_{pq}\cdot\vec{H}^{\perp}_{\text{inc}}\,ds. \quad (25)$$

Integrals in (24) and (25) are analytically evaluated. In horizontal illumination where,

$$\vec{H}^{\parallel}_{\text{inc}} = \frac{-E_0^{\parallel}}{\eta_0}\left(\sin(\phi)\hat{u}_{\rho} + \cos(\phi)\hat{u}_{\phi}\right). \quad (26)$$

The excitation vector is:

$$B^{\langle \vec{\mathbf{N}}^{\mathbf{o}}_{\mu_{pq}},\vec{H}^{\parallel}_{\text{inc}}\rangle} = -4\pi E_0^{\parallel}\Pi'_{pq}(-j)^{p-1}\frac{pJ_p(Z'_{pq})J_p(2\pi a\sin\theta_i)}{2\pi a\sin\theta_i}. \quad (27)$$

D. Evaluation of the scattered field

By solving the matrix equation of (17) and (18), unknown equivalent magnetic currents are obtained. Using the image theory and the free half space Green's function, the total backscattered fields for both polarizations at distance $\bar{r}_s = r/\lambda_0$ and direction of θ_s are:

$$\vec{E}^{s\parallel}_{cavity}(\vec{M}_\Gamma) = -E_0^{\parallel}\frac{ae^{2\pi\bar{r}_s}}{\bar{r}_s} \times \sum_{m=0}^{M}\sum_{n=0}^{N}\left\{\begin{array}{l} C^{\mathbf{M^o}}_{nm}\Pi'_{nm}(-j)^{n-1}\dfrac{nJ_n(\mathcal{Z}'_{nm})J_n(\bar{k}\sin\theta_s)}{\bar{k}\sin\theta_s} \\ +C^{\mathbf{N^e}}_{nm}\Pi_{nm}(-j)^{n-1}\dfrac{I_n(\mathcal{Z}_{nm},\bar{k}\sin\theta_s)}{\bar{k}\sin\theta_s}\end{array}\right\}, \quad (28)$$

$$\vec{E}^{s\perp}_{cavity}(\vec{M}_\Gamma) = E_0^{\perp}\frac{ae^{2\pi\bar{r}_s}}{\bar{r}_s} \times \sum_{m=0}^{M}\sum_{n=0}^{N}\left\{C^{\mathbf{M^e}}_{nm}\Pi'_{nm}(-j)^{n-1}\cos\theta_s\frac{I_n(\mathcal{Z}'_{nm},\bar{k}\sin\theta_s)}{\bar{k}\sin\theta_s}\right\}, \quad (29)$$

where $I_n(\cdot,\cdot)$ is a frequently encountered integral in the equations, defied as:

$$I_n(x,y) = \int_0^1 \left\{\left(n/\rho\right)^2 J_n(x\rho)J_n(y\rho) + xyJ'_n(x\rho)J'_n(y\rho)\right\}\rho d\rho. \quad (30)$$

E. Scattered field of a real OECC

The interior scattered fields computed from (28) and (29) are the dominant part of the total scattered signal [9]. Even though assumption of an IPEC simplifies the analysis, but it degrades the results, especially at grazing angles [13]. The results could be corrected by adding the PO solution of the scattered field from a hypothetical PEC plate at the aperture:

$$\vec{E}^{s\parallel,\perp}_{total} = \vec{E}^{s\parallel,\perp}_{cavity}(\vec{M}_\Gamma) + \vec{E}^{s\parallel,\perp}_{lid}(\vec{J}_\Gamma), \quad (31)$$

where

$$\begin{Bmatrix}\vec{E}^{s\parallel}_{lid}(\vec{J}_\Gamma)\\ \vec{E}^{s\perp}_{lid}(\vec{J}_\Gamma)\end{Bmatrix} = \frac{jke^{2\pi\bar{r}_s}J_1[\bar{k}(\sin\theta_i+\sin\theta_s)]}{2\pi\bar{r}_s\bar{k}(\sin\theta_i+\sin\theta_s)}\begin{Bmatrix}E_0^{\parallel}\cos\theta_s\\ E_0^{\perp}\cos\theta_s\end{Bmatrix}. \quad (32)$$

From now, $\vec{E}^{s\parallel,\perp}_{\text{total}}$ is referred to modal MoM3D model in the text.

III. NUMERICAL RESULTS

In this section, the monostatic RCS of various targets are evaluated for horizontal and vertical polarizations. The results are compared with Finite Element Method (FEM) [13], Multi-Level Fast Multi-pole Method (MLFMM) generated by the commercial software FEKO and measurements [20], [21] as well. Generally, measurements are conducted in the anechoic chamber by placing the OECC as a target in front of the standard gain horn antenna, while absorbing materials are used to diminish scattering from the exterior of the cavity to reduce its contribution in the total scattering.

In large waveguides, shooting and bouncing rays method [13] is used for validation. For large apertures or low grazing angles, the field modes m and n should be large enough to assure convergence.

First, a circular cavity with $D = 2\lambda$, $L = 4\lambda$ and $\lambda = 3$ cm is analyzed. Figure 3 shows the monostatic RCS for horizontal illumination as a function of θ_i for $m = 8$ and $n = 10$. The result of modal MoM without correction (GP model) is also shown in Fig. 3. The correction is effective at all incidence angles. Please note that the presence of IPEC underestimates the RCS. The results of FEM [15], FEKO and measurements [20] show a very good agreement with this efficient method.

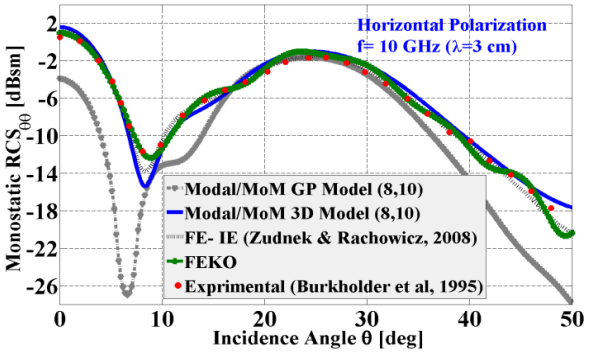

Fig. 3. Horizontal polarization monostatic RCS (dB/m^2) of an OECC with $D = 2\lambda$, $L = 4\lambda$ versus incidence angle.

Figure 4 depicts the convergence of RCS results for various modes for vertical polarization at 10 GHz as a function of incidence angle. As expected, as incidence angle increases, a larger number of modes are needed for convergence. Considering the hierarchy of the moment matrix, as the number of modes increase, we only need to add the computations of the new modes because previously computed and stored entries are still valid.

Monostatic RCS for the same OECC for vertical polarization is compared to reference methods in Fig. 5. A good agreement between these methods is observed.

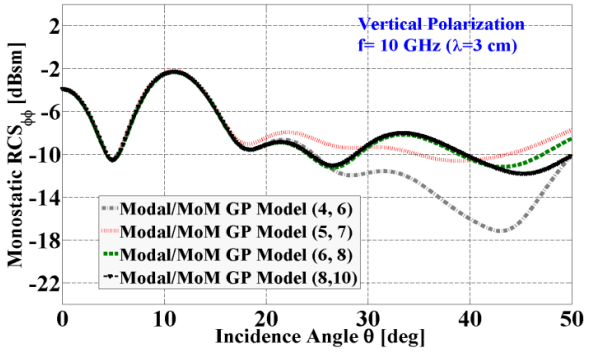

Fig. 4. Convergence of RCS with increasing the number of modes for an OECC with $D = 2\lambda$, $L = 4\lambda$ illuminated by a vertically polarized incident wave.

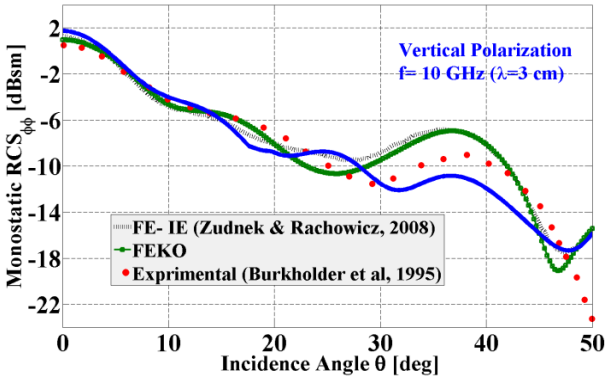

Fig. 5. Vertical polarization monostatic RCS (dB/m^2) of an OECC with $D = 2\lambda$, $L = 4\lambda$ versus incidence angle.

It should be noted that modal MoM is highly accurate and computationally efficient. Due to the similarity of formulations of the two polarizations, entries of matrices could be evaluated at the same time.

For example, $Z^{\langle \vec{N}^e_{\mu pq}, \vec{N}^e_{\mu nm} \rangle}$ and $Z^{\langle \vec{N}^o_{\mu pq}, \vec{N}^o_{\mu nm} \rangle}$ in corresponding blocks of $K^{\langle N^e, N^e \rangle}$ and $K^{\langle N^o, N^o \rangle}$ can be computed simultaneously. This significantly reduces the computational time. CPU time for the RCS calculation of the above OECC for both polarizations is 84.22 sec, while the same simulation with FEKO using MLFMM is about 28 minutes on an Acer Aspire 1.66 GHz laptop with 2GB of RAM.

As a second example, a straight circular cylindrical air-intake channel with $D = 6.274$ cm and $L = 21.59$ cm is analyzed. Convergence is achieved by 54 modes ($m = 4$ and $n = 6$) of horizontal and 56 modes ($m = 6$ and $n = 8$) of vertical polarizations. The same problem is studied in [17] by FE-IE and in [21] with internal irradiation and diffraction model. Measurements are also reported in [17]. Figure 6 shows comparisons of RCS at 15.2 GHz. A very good agreement is observed between these methods at both polarizations.

For the above OECC, the relative amplitude of various modes in horizontal polarization is plotted in Fig. 7.

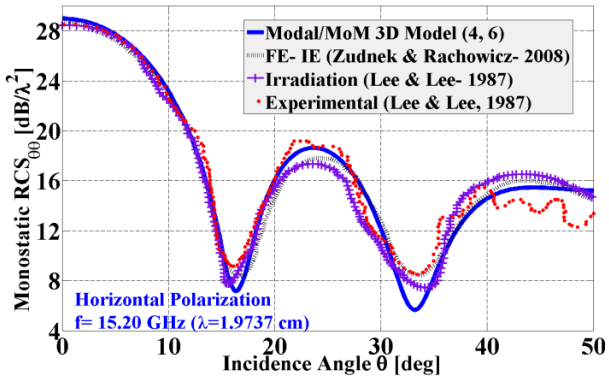

(a)

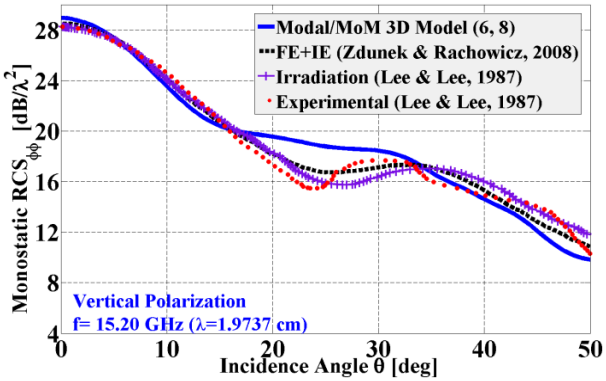

(b)

Fig. 6. Monostatic RCS versus incidence angle for a cylindrical PEC cavity $D = 6.274\ cm$ and $L = 21.59\ cm$: (a) horizontal polarization, and (b) vertical polarization.

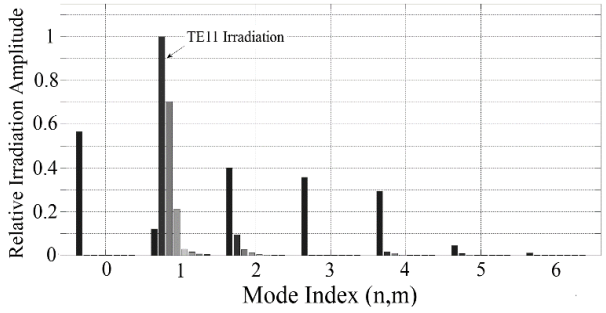

Fig. 7. Comparison of the relative amplitude of irradiating modes in vertical polarization.

Irradiation amplitude of each component is normalized to the dominant propagating mode value, TE_{11}. As observed, higher order vanescent modes might even have some contributions in the total scattered field. Sparsity pattern (non-zero element plot) of moment matrix for vertical polarization is depicted in Fig. 8. For this problem, $[K]^{\|}$ is a 54×54 sparse matrix with 612 non-zeros (%21), while the condition number is 34.9902. As mentioned before, the modal MoM admittance matrix is symmetrical and well-conditioned. Even though the size of $[K]^{\|}$ is favourably small, the above mentioned properties further expedites the numerical solution by using direct or iterative methods.

As another example, a cylindrical large cavity with $D = 10\lambda$ and $D = 30\lambda$ at 10 GHz is considered. This structure is also studied by Ling et al. with SBR method [13]. RCS results are shown in Figs. 9 and 10 at both polarizations. For this large structure, the modes corresponding to $m = 10$ and $n = 14$ yield convergent results. As mentioned before, the computational burden for this long cavity is mainly due to computing the coupling on the aperture and not the cavity length.

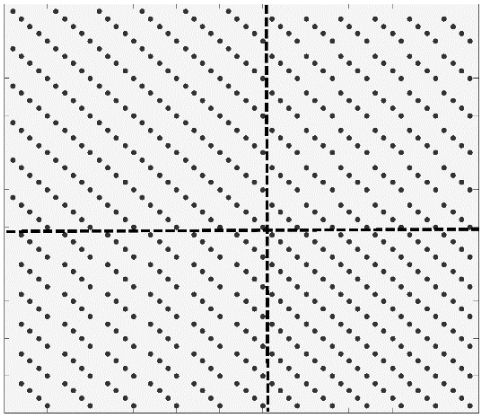

Fig. 8. Sparsity pattern of admittance matrix in modal MoM solution for horizontal polarization.

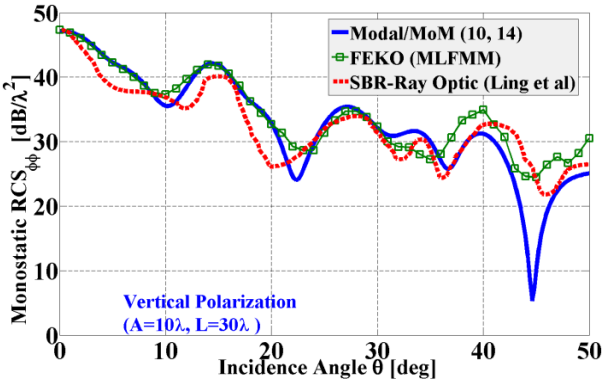

Fig. 9. Monostatic RCS of an OECC with $D = 10\lambda$ and $L = 30\lambda$ versus incidence angle for horizontal polarization.

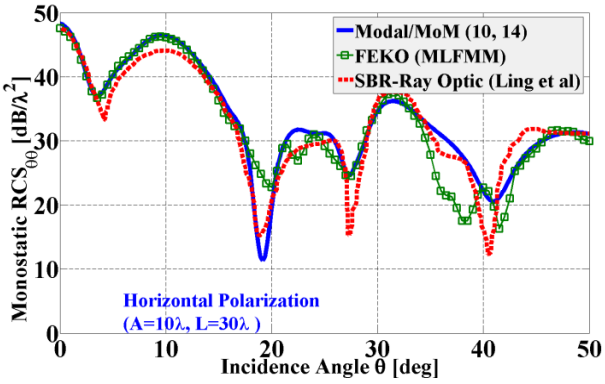

Fig. 10. Monostatic RCS of an OECC with $D = 10\lambda$ and $L = 30\lambda$ versus incidence angle for vertical polarization.

IV. CONCLUSION

Here, an efficient technique is introduced to analyze the scattered field from an open ended circular cavity (OECC) based on modal Method of Moments. Entire domain cylindrical vector wave functions are employed to express the fields on the cavity aperture and the dyadic Green's functions of the circular cavity is used to formulate the fields inside OECC. At first, scattered field from a perforated OECC in an infinite PEC is calculated by applying the surface equivalence theorem and Galerkin method for solving the resultant integral equation. Then, the scattered field from a hypothetically PEC plate with the size and shape of the circular aperture is added to the previously calculated scattered field to compensate the effect of the infinite PEC assumption. This addition corrects the monostatic RCS results, particularly at close to grazing incident angles.

Monostatic RCS of different size OECCs is calculated and compared with other numerical techniques and measurements. Different sizes are selected in order to demonstrate the capability of the proposed method to evaluate cavities with sizes including resonant size up to several wavelengths. Excellent agreement between the results proves the accuracy of the presented method. Since the method is based on the full wave modal MoM approach, the technique is very efficient for large structures compared to other numerical methods. In addition, further numerical considerations in the formulations have increased the efficiency of the method.

REFERENCES

[1] H. T. Anastassiu, "A review of electromagnetic scattering analysis for inlets, cavities, and open ducts," *IEEE Trans. Antennas Propagat*., vol. 45, no. 6, pp. 27-40, 2003.

[2] J. M. Jin and J. L. Volakis, "A finite element boundary integral formulation for scattering by three dimensional cavity-backed apertures," *IEEE Trans. Antennas Propagat*., vol. 39, no. 1, pp. 97-104, 1991.

[3] J. Liu and J. M. Jin, "A special higher order finite element method for scattering by deep cavities," *IEEE Trans. Antennas Propagat*., vol. 48, no. 5, pp. 694-703, 2000.

[4] W. Rachowicz and A. Zdunek, "An *hp*-adaptive finite element method for scattering problems in electromagnetics," *International Journal of Numerical Methods in Engineering*, vol. 62, no. 9, pp. 1226-1249, 2005.

[5] H. Ling, "RCS of waveguide cavities: A hybrid boundary integral/modal approach," *IEEE Trans. Antennas Propagat*., vol. 38, no. 9, pp. 1413-1420, 1990.

[6] T. T. Chia, R. J. Burkholder, and R. Lee, "The application of FDTD in hybrid methods for cavity scattering analysis," *IEEE Trans. Antennas Propagat*., vol. 43, no. 10, pp. 1082-1090, 1995.

[7] C. A. Chuang and P. H. Pathak, "Ray analysis of modal reflection for three dimensional open-ended

cavities," *IEEE Trans. Antennas Propagat*., vol. 37, pp. 339-346, 1989.

[8] H. S. Ling, W. Lee, and R. C. Chou, "High frequency RCS of open cavities with rectangular and circular cross sections," *IEEE Trans. Antennas Propagat*., vol. 37, no. 5, pp. 648-654, 1989.

[9] A. G. Pino, F. Obelleiro, and J. L. Rodriguez, "Scattering from conducting open cavities by generalized ray expansion (GRE)," *IEEE Trans. Antennas Propagat*., vol. 41, no. 7, pp. 989-992, 1993.

[10] A. Zdunek and W. Rachowicz, "hp-adaptive CEM in practical applications," In Spectral and High Order Methods for Partial Differential Equations, *Springer Berlin Heidelberg*, pp. 339-346, 2011.

[11] A. Zdunek and W. Rachowicz, "Efficient jet-engine inlet radar cross-section prediction using higher-order finite-element method and reduced-order modeling," *Electromagnetics*, vol. 34, pp. 345-362, 2014.

[12] H. R. Witt and E. L. Price, "Scattering from hollow conducting cylinders," *IEE Proceedings*, vol. 115, pp. 94-99, 1968.

[13] H. S. Ling, W. Lee, and R. C. Chou, "High frequency RCS of open cavities with rectangular and circular cross sections," *IEEE Trans. Antennas Propagat*., vol. 37, no. 5, pp. 648-654, 1989.

[14] P. H. Patbak, C. W. Chuang, and M. C. Liang, "Inlet Modeling Studies," Technical Report no. 717674-1, *The Ohio State University Electro Science Laboratory*, Columbus, OH, 1986.

[15] A. Altintas, P. H. Pathak, and M. C. Liang, "A selective modal scheme for the analysis of EM coupling into or radiation from large open-ended waveguides," *IEEE Trans. Antennas Propagat*., vol. 36, pp. 84-96, 1988.

[16] K. K. Chan and F. Tremblay, "Mode matching analysis of metallic blades in a cylinder," *IEEE International Symposium on Antennas and Propagation*, Newport Beach, CA, pp. 38-41, June 18-23, 1995.

[17] A. Zdunek and W. Rachowicz. "Cavity radar cross section prediction," *IEEE Trans. Antennas Propagat*., vol. 56, no. 6, 2008.

[18] C. T. Tai, *Dyadic Green Function in Electro-magnetic Theory*. 2nd edition, New York: IEEE Press, 1994.

[19] L. F. Shampine, "Vectorized adaptive quadrature in MATLAB," *Journal of Computational and Applied Mathematics*, 211, pp. 131-140, 2008.

[20] R. J. Burkholder, P. H. Pathak, and H. T. Chou, "New Ray and Physical Optics Based Methods for Modeling Duct Propagation in the Hybrid Analysis of EM Scattering by Jet Inlets," Technical Report no. 729526–1, *The Ohio State University Electro-Science Laboratory*, Columbus, Ohio, 1995.

[21] C. S. Lee and S. W. Lee, "RCS of a coated circular waveguide terminated by a perfect conductor," *IEEE Trans. Antennas Propagat*., vol. 35, no. 4, pp. 391-398, 1987.

Ali Aghabarati received the B.Sc. degree in Electrical Engineering from Iran University of Science and Technology, Tehran, Iran, in 2008, and the M.Sc. degree in Electrical Engineering from Amirkabir University of Technology, Tehran, Iran, in 2010. He obtained the Ph.D. degree in Computational Electromagnetics from McGill University, Montreal, QC, Canada in 2014. His main research interest is numerical techniques in electro-magnetic computation.

Parisa Dehkhoda was born in Tabriz, Iran, on August 16, 1978. She received the B.S. degree from University of Tehran, Iran, in 2000 and the M.S. and Ph.D. degrees from Amirkabir University of Technology, Tehran, Iran, in 2004 and 2009 respectively, all in Electrical Engineering. She is now an Assistant Professor in Electrical Engineering Department, in Amirkabir University of Technology. Her research interests are EMC, Scattering, and microstrip antennas.

Ahad Tavakoli was born in Tehran, Iran, on March 8, 1959. He received the B.S. and M.S. degrees from the University of Kansas, Lawrence, and the Ph.D. degree from the University of Michigan, Ann Arbor, all in Electrical Engineering, in 1982, 1984, and 1991, respectively.

He is currently a Professor in the Department of Electrical Engineering at Amirkabir University of Technology. His research interests include EMC, scattering of electromagnetic waves and microstrip antennas.

Fast Monostatic Scattering Analysis Based on Bayesian Compressive Sensing

Huan-Huan Zhang [1], Xun-Wang Zhao [1], Zhong-Chao Lin [1], and Wei E. I. Sha [2]

[1] The School of Electronic Engineering
Xidian University, Xi'an, 710071, China
zhanghuanajkd@outlook.com

[2] The Department of Electrical and Electronic Engineering
The University of Hong Kong, Hong Kong, China

Abstract ─ The Bayesian compressive sensing algorithm is utilized together with the method of moments to fast analyze the monostatic electromagnetic scattering problem. Different from the traditional compressive sensing based fast monostatic scattering analysis method which cannot determine the required measurement times, the proposed method adopts the Bayesian framework to recover the underlying signal. Error bars of the signal can be obtained in the recovery procedure, which provides a means to adaptively determine the number of compressive-sensing measurements. Numerical results are given to demonstrate the accuracy and effectiveness of proposed method.

Index Terms ─ Bayesian compressive sensing, method of moments, monostatic, scattering.

I. INTRODUCTION

Electromagnetic scattering simulation has been widely applied to the area of non-cooperative radar target identification and radar imaging to get the echo signal of radar target without measurement. Among various electromagnetic scattering analysis methods, the method of moments (MoM) has drawn great interests in the past several decades [1-3]. The MoM is particularly advantageous for the analysis of exterior open-region scattering problems duo to its inherent capability for simulating unbounded domains.

When utilizing MoM to acquire echo signals from a large amount of aspect angles, one has to run the simulation code equal times with the number of aspect angles to obtain all the echo signals. For instance, to obtain the inverse synthetic aperture radar (ISAR) image of the B2 model as shown in Fig. 1, one has to get the wideband scattered field data from 720 aspect angles of the model. Actually, it takes much time to analyze the electrically large objects only once, let alone many times. So there is an urgent demand to accelerate the simulation process of monostatic scattering.

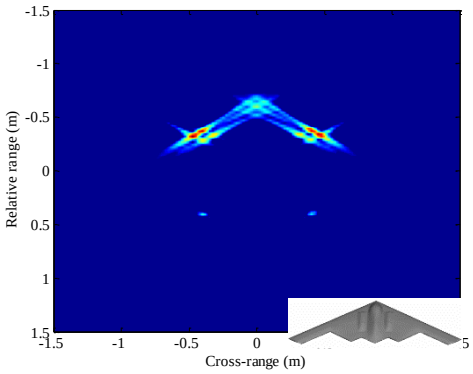

Fig. 1. Inverse synthetic aperture radar (ISAR) image of the B2 model based on the wideband scattered field data from 720 aspect angles of the target.

Two kinds of effort have been done to achieve this goal. One is to speed up the single simulation by using fast algorithms to accelerate the method of moments. The existing fast algorithms can mainly be classified into three categories: fast multipole method (FMM) [4-6], FFT-based methods [7-9], and low rank matrix based methods [10-12]. The alternative way is to reduce the total number of simulations using algorithms like asymptotic waveform evaluation (AWE) [13, 14], model-based parameter estimation (MBPE) [15], excitation matrix compression methods [16, 17], etc. But these algorithms show some shortcomings. For AWE and MBPE, a multi-point expansion or interpolation is needed for wide-angle problems. The major technical challenge is to adaptively choose the expansion points or interpolation points. The excitation matrix compression methods compress the excitation matrix and remove redundancies in the initial excitation assembly. The considered full right-hand-side (RHS) matrix has to be stored explicitly. Moreover, a SVD-based compression is restricted to comparatively small matrices due to the high computational complexity.

Submitted On: June 30, 2016
Accepted On: September 11, 2016

Compressive sensing (CS) is a rapidly emerging signal processing technique and has already been applied to electromagnetics [18-20]. A CS based method is proposed in [20] for fast analysis of wide-angle monostatic scattering problems, which falls into the second category fast algorithm described above. This method uses CS to construct a new set of right-hand-side vectors for MoM, where the number of constructed right-hand-side vectors is much less than the original ones. But it is found that orthogonal matching pursuit (OMP) algorithm [21] is adopted to solve the CS optimization problem and the number of measurement cannot be determined adaptively, just like that the number of expansion or interpolation points is unknown in [13-15]. This sets up a limit for the practical applications of this technique.

Recently, more and more researchers focus on the study of Bayesian compressive sensing (BCS) method [22-25], which adopts the Bayesian framework to recover the underlying signals. Error bars of the signal can be obtained in the recovery procedure, leading to an effective strategy for adaptively determining the number of compressive-sensing measurements. The BCS method is used for coherent fusion of multi-band radar data from multiple spatially collocated radars in [24]. In [25], the BCS method is applied for estimation of the directions of arrival (DoAs) of narrow-band signals impinging on a linear antenna array. In this paper, we utilize the BCS for fast monostatic scattering calculation. Numerical results show the proposed method can determine the number of compressive-sensing measurements in an adaptive manner.

The rest of this paper is organized as follows. Section II describes the detailed theory and formulation of the proposed Bayesian compressive sensing based fast monostatic scattering analysis method. Section III demonstrates the accuracy and effectiveness of the proposed method through several numerical results. Section IV presents our conclusions.

II. THEORY AND FORMULATION

A. Review of MoM for electromagnetic scattering problems

For the analysis of electromagnetic scattering from perfect electrical conductor (PEC), the Maxwell's equations can be recast in the form of surface integral equations, including electric field integral equation (EFIE), magnetic field integral equation (MFIE) and combined field integral equations (CFIE). Take the following EFIE as an example:

$$\int_S \hat{t}\cdot[\,j\omega\mu J_s(\mathbf{r}')G(\mathbf{r},\mathbf{r}') - \frac{j}{\omega\varepsilon}(\nabla'\cdot J_s(\mathbf{r}'))(\nabla' G(\mathbf{r},\mathbf{r}'))]dS' = \hat{t}\cdot\mathbf{E}^i(\mathbf{r}). \quad (1)$$

Here, $G(\mathbf{r},\mathbf{r}')$ refers to the Green's function in free space. $\mathbf{r}$ and $\mathbf{r}'$ denote the observation and source point locations. $\mathbf{E}^i(\mathbf{r})$ is the incident excitation plane wave. ε and μ are the permittivity and permeability, respectively. ω is the angular frequency. $J_s(\mathbf{r}')$ is the unknown surface current. $\hat{t}$ refers to the tangential direction of the surface.

Equation (1) can be discretized by using MoM with planar Rao-Wilton-Glisson (RWG) basis functions [26]. The linear system of equations after Galerkin's testing is briefly outlined as follows:

$$\sum_{n=1}^{N} Z_{mn} I_n = V_m, \qquad \mathrm{m} = 1,2,...,N, \quad (2)$$

where

$$Z_{mn} = \int_s \Lambda_m(\mathbf{r})\cdot\int_{s'} j\omega\mu\Lambda_n(\mathbf{r}')G(\mathbf{r},\mathbf{r}')dS'dS - \int_s \frac{j}{\omega\varepsilon}\nabla\cdot\Lambda_m(\mathbf{r})\int_{s'}\nabla'\cdot\Lambda_n(\mathbf{r}')G(\mathbf{r},\mathbf{r}')dS'dS, \quad (3)$$

$$V_m = \int_s \Lambda_m(\mathbf{r})\cdot\mathbf{E}^i(\mathbf{r})dS. \quad (4)$$

Here, I_n represents the unknown current coefficients. Equation (2) can be written as:

$$\mathbf{ZI}(\theta)=\mathbf{V}(\theta), \quad (5)$$

where $\mathbf{Z}$ is the impedance matrix with its elements given in (3), $\mathbf{V}(\theta)$ is the right-hand-side vector related to the (4), $\mathbf{I}(\theta)$ is a vector containing the unknown current coefficients. Both the right-hand-side vector and the unknown current coefficients will change with the incident angle θ.

B. Basic principle of using CS for fast monostatic scattering analysis

Suppose that multiple monostatic scattering problem with the incident angles $\theta_1,\theta_2,\cdots\theta_M$ is analyzed, then the following M matrix equations need to be solved:

$$\mathbf{ZI}(\theta_i)=\mathbf{V}(\theta_i),\ i=1,2,\cdots,M. \quad (6)$$

Use $\mathrm{I}_n(\theta_i)$ to represent the current coefficient of the n-th element in $\mathbf{I}(\theta_i)$ and $n=1,2,\cdots,N$. Based on the CS theory, a measurement matrix $\boldsymbol{\Phi}=\left[c_{ij}\,\middle|\,i=1,2,\cdots,M';\ j=1,2,\cdots,M\right]$ with its elements i.i.d. Gaussian can be constructed. The measurement value of $\{I_n(\theta_1),\ I_n(\theta_2),\cdots,\ I_n(\theta_M)\}$ can be written as:

$$\begin{pmatrix} I_{n1}^{CS} \\ I_{n2}^{CS} \\ \vdots \\ I_{nM'}^{CS} \end{pmatrix} = \begin{pmatrix} c_{11} & c_{12} & c_{13} & \cdots & c_{1M} \\ c_{21} & c_{22} & c_{23} & \cdots & c_{2M} \\ \vdots & \vdots & \vdots & \ddots & \vdots \\ c_{M'1} & c_{M'2} & c_{M'3} & \cdots & c_{MM} \end{pmatrix} \begin{pmatrix} I_n(\theta_1) \\ I_n(\theta_2) \\ \vdots \\ \vdots \\ I_n(\theta_M) \end{pmatrix}. \quad (7)$$

It is worth mentioning that the number of measurement values M' is much less than M. Obviously, the m-th measurement can be expressed as:

$$I_{nm}^{CS}=\sum_{i=1}^{M}c_{mi}I_n(\theta_i). \tag{8}$$

Let $\mathbf{I}_m^{CS}=\left\{I_{1m}^{CS},I_{2m}^{CS},\cdots,I_{Nm}^{CS}\right\}$, then we have:

$$\begin{aligned}\mathbf{Z}\mathbf{I}_m^{CS}&=\mathbf{Z}\begin{pmatrix}\mathrm{I}_{1m}^{CS}\\ \mathrm{I}_{2m}^{CS}\\ \vdots\\ \mathrm{I}_{Nm}^{CS}\end{pmatrix}=\mathbf{Z}\begin{pmatrix}\sum_{i=1}^{M}c_{mi}I_1(\theta_i)\\ \sum_{i=1}^{M}c_{mi}I_2(\theta_i)\\ \vdots\\ \sum_{i=1}^{M}c_{mi}I_N(\theta_i)\end{pmatrix}\\ &=\sum_{i=1}^{M}c_{mi}\mathbf{Z}\mathbf{I}(\theta_i)=\sum_{i=1}^{M}c_{mi}\mathbf{V}(\theta_i).\end{aligned} \tag{9}$$

The right hand side of (9) is a random superposition of M right-hand-side vectors related to different incident angles and the weights are the m-th row elements of $\boldsymbol{\phi}$. So the M' measurement values of each current coefficient can be obtained by changing the subscript m in (9) from 1 to M'. In such a manner, the number of equations to be solved can be greatly reduced.

According to the theory of CS [27], if the unknown vector $\left\{I_n(\theta_1),\ I_n(\theta_2),\cdots,\ I_n(\theta_M)\right\}$ is compressible in terms of a orthonormal basis $\boldsymbol{\Psi}$, i.e.,

$$\begin{pmatrix}I_n(\theta_1)\\ I_n(\theta_2)\\ \vdots\\ \vdots\\ I_n(\theta_M)\end{pmatrix}=\boldsymbol{\Psi}\boldsymbol{\omega}, \tag{10}$$

where $\boldsymbol{\Psi}$ is a $M\times M$ matrix, $\boldsymbol{\omega}=\left\{\omega_1,\omega_2,\cdots,\omega_M\right\}$ has just a few of large coefficients and many small coefficients. Substitute (10) into (7), $\boldsymbol{\omega}$ can be obtained by solving the following matrix equation:

$$\begin{pmatrix}I_{n1}^{CS}\\ I_{n2}^{CS}\\ \vdots\\ I_{nM'}^{CS}\end{pmatrix}=\boldsymbol{\phi}\boldsymbol{\Psi}\boldsymbol{\omega}=\boldsymbol{\Phi}\boldsymbol{\omega}, \tag{11}$$

where $\boldsymbol{\Phi}=\boldsymbol{\phi}\boldsymbol{\Psi}$ is a $M\times M$ sensing matrix. M' is much smaller than M. Hence, (11) is an underdetermined equation which is a nondeterministic polynomial time (NP)-hard problem. A reconstruction algorithm is required to recover $\boldsymbol{\omega}$ from M' measurements. After $\boldsymbol{\omega}$ is solved, we can adopt (10) to obtain the original current coefficient vector.

C. Bayesian compressive sensing method

To solve (11), the reconstruction algorithm in [20] is the orthogonal matching pursuit (OMP) algorithm [21]. However, the OMP algorithm is a greedy algorithm and it frequently converges to local optimal. Moreover, the number of measurement cannot be predefined adaptively and one has to try several times to find the optimized values for the number of measurements.

In the Bayesian compressive sensing method, the solution of the NP-hard problem in (11) can be rewritten into the following form:

$$\mathbf{t}=\boldsymbol{\Phi}\boldsymbol{\omega}+\boldsymbol{\varepsilon}, \tag{12}$$

where $\mathbf{t}$ is the vector of measurement values, $\boldsymbol{\varepsilon}$ is the expansion error and it is assumed to be zero-mean Gaussian distribution with variance σ^2. Then the vector $\mathbf{t}$ obeys a multivariate Gaussian distribution,

$$p\left(\mathbf{t}\middle|\boldsymbol{\omega},\sigma^2\right)=\left(2\pi\sigma^2\right)^{-\frac{M'}{2}}\exp\left(-\frac{1}{2\sigma^2}\left\|\mathbf{t}-\boldsymbol{\Phi}\boldsymbol{\omega}\right\|^2\right). \tag{13}$$

A zero-mean Gaussian prior is defined over $\boldsymbol{\omega}$:

$$p(\boldsymbol{\omega}|\mathbf{a})=\prod_{i=1}^{M}N(\omega_i|0,a_i^{-1}), \tag{14}$$

where $\mathbf{a}=\left[a_1,a_2,\cdots,a_M\right]^T$ is a vector of M independent hyperparameters and a_i is the precision (reciprocal of variance) of a Gaussian distribution.

For the fixed values of hyperparameters controlling the prior, the posterior probability density of the weights can be obtained:

$$p(\boldsymbol{\omega}|\mathbf{t};\mathbf{a},\sigma^2)=N(\boldsymbol{\omega}|\boldsymbol{\mu},\boldsymbol{\Sigma}), \tag{15}$$

where its mean and covariance are:

$$\boldsymbol{\mu}=\sigma^{-2}\boldsymbol{\Sigma}\boldsymbol{\Phi}^T\mathbf{t}, \tag{16}$$

$$\boldsymbol{\Sigma}=(\mathbf{A}+\sigma^{-2}\boldsymbol{\Phi}^T\boldsymbol{\Phi})^{-1}, \tag{17}$$

with $\mathbf{A}=diag\left(a_1,a_2,\cdots,a_M\right)$.

According to (13) and (14), the marginal distribution of $\mathbf{t}$ can be computed as:

$$p(\mathbf{t}|\mathbf{a},\sigma^2)=(2\pi)^{-M'/2}|\mathbf{C}|^{-1/2}\exp\left(-\frac{1}{2}\mathbf{t}^{\mathrm{T}}\mathbf{C}^{-1}\mathbf{t}\right), \tag{18}$$

where

$$\mathbf{C}=\sigma^2\mathbf{I}+\boldsymbol{\Phi}\mathbf{A}^{-1}\boldsymbol{\Phi}^T. \tag{19}$$

In the sparse Bayesian learning method, the maximization of $p(\mathbf{t}|\mathbf{a},\sigma^2)$ is termed as type-II maximum likelihood method. The hyperparameters $\mathbf{a}$ and σ^{-2} are estimated through computing the derivatives of (18) with respect to $\mathbf{a}$ and σ^{-2}:

$$a_i^{new}=\frac{\gamma_i}{\mu_i^2}, \tag{20}$$

$$\left(\sigma^2\right)^{new}=\frac{\left\|\mathbf{t}-\boldsymbol{\Phi}\boldsymbol{\mu}\right\|^2}{M'-\sum_{i=1}^{M}\gamma_i}, \tag{21}$$

where $\gamma_i = 1 - a_i \Sigma_{ii}$, Σ_{ii} is the i th diagonal element of the covariance in (17).

The formulas (16) and (17) coupled with (20) and (21) lead to an iterative learning process, which updates the corresponding quantity until a convergence criterion is satisfied. Many elements of $\mathbf{a}$ tend to infinity during the iteration with the consequence that $\boldsymbol{\mu}$ contains very few non-zero elements. After the convergence of the iterative learning process, $\boldsymbol{\mu}$ is used to approximate $\boldsymbol{\omega}$.

Since the diagonal elements of the covariance matrix $\boldsymbol{\Sigma}$ correspond to the variance of each element in $\boldsymbol{\omega}$, they provide error bars on the accuracy of $\boldsymbol{\omega}$. When the number of measurement is sufficiently large, the variance of each element in $\boldsymbol{\omega}$ should be small. If the diagonal elements of the covariance matrix $\boldsymbol{\Sigma}$ is $\Sigma_{ii}, i = 1, 2, \cdots, M$, the number of measurement times M' is enough when,

$$\frac{\Sigma_{11} + \Sigma_{22} + \cdots + \Sigma_{MM}}{M} < \delta, \tag{22}$$

where δ is a small value and $\delta = 10^{-3}$ in this paper. If (22) is not satisfied, more measurement will be added. In such a manner, the proposed method can adaptively determine the number of measurement.

III. NUMERICAL RESULTS

The effectiveness and accuracy of the proposed method are demonstrated through several numerical results. All results are generated on a personal PC with 2.83 GHz CPU and 8 GHz RAM. The flexible general minimal residual (FGMRES) algorithm is adopted to solve the matrix equation and the iteration process is terminated when the 2-norm residual error is reduced by 10^{-3}. Multilevel fast multipole method (MLFMM) is utilized to accelerate the matrix vector product process.

A. Almond

The NASA almond model is analyzed as the first example as shown in Fig. 2 [28]. It is discretized with 3290 triangular patches with 4935 unknowns. The tip of the almond points to the x-axis. The elevation angle of the incident wave is fixed to be 90°, while the aspect angle ranges from 0° to 63° with a 1° increment. Since the basis matrix $\boldsymbol{\Psi}$ has an important effect on the measurement number, we compare three different bases in this example including Hermite basis, discrete cosine transformation (DCT) basis and Haar wavelet basis. All these basis are adopted to analyze the monostatic scattering problem and their results are compared with the result of MLFMM. The real parts of current coefficients at a randomly chosen edge under different incident angles are shown in Fig. 3. It can be observed that the results obtained by Hermite and DCT basis agree well with that of MLFMM. The result obtained by using Haar basis is comparable to that of MLFMM. The numbers in the brackets means the corresponding measurement times. Note that the measurement number corresponds to the number of MoM solutions. Obviously, the measurement times after adopting Hermite basis achieve its minimum. So the basis function is fixed to be the Hermite basis in the following two examples. Figure 4 demonstrates the current magnitude distributions obtained by MLFMM and the proposed method with different basis. Good agreement can be achieved.

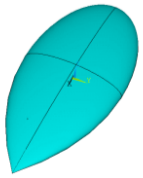

Fig. 2. Almond model.

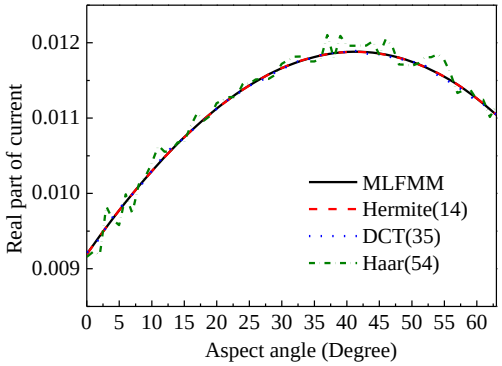

Fig. 3. Real parts of current coefficients at a randomly chosen edge under different incident angles obtained by using three kinds of basis. The numbers in the brackets represent the number of measurement.

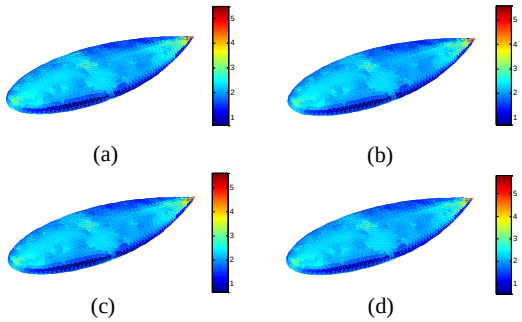

Fig. 4. The current magnitude distributions obtained by MLFMM and the proposed method with different basis when the aspect angle is 0°: (a) MLFMM, (b) Hermite, (c) DCT, and (d) Haar.

B. Missile model

A PEC missile model as shown in Fig. 5 is analyzed as the second example. The model is created based on

the picture of Tomahawk missile in Wikipedia [29]. The maximum size in the x, y and z directions are 1.4 m, 0.62 m and 0.25 m. It is discretized into 6792 unknowns at 1.5 GHz. The warhead is towards the positive direction of x-axis. The elevation angle of the incident wave is fixed to be 90° while the aspect angle ranges from 0° to 180° with 0.5° increment. Both the proposed method (BCS) and the method in [20] (CS_OMP) are adopted to analyze the monostatic scattering problem and their results are compared with that of MLFMM as shown in Fig. 6. Table 1 lists the measurement number and CPU time for different methods. The number of measurement of the proposed method is determined to be 63 adaptively, and the result match well with that of MLFMM. Since the CS_OMP method cannot determine the number of measurement, we try several different measurement number and select the smallest one giving the similar level of accuracy with the proposed method. The measurement number determined in such a manner for CS_OMP method is 71. Although the measurement time of the proposed method is less than the CS_OMP method, their CPU time is similar since the computational cost of BCS algorithm is larger than OMP algorithm.

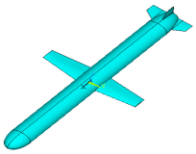

Fig. 5. Missile model.

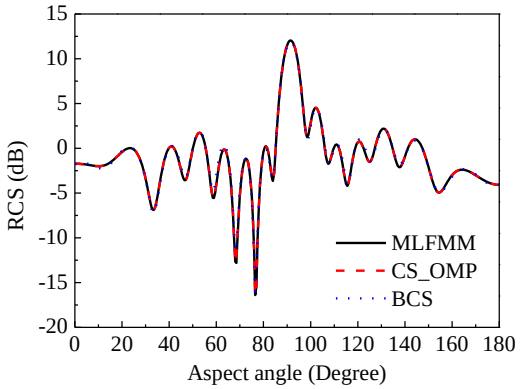

Fig. 6. Monostatic RCS of the missile model obtained by MLFMM, CS_OMP and BCS.

Table 1: Measurement number and CPU time of three kinds of methods for the missile model

Method	Measurement Number	CPU Time (s)
MLFMM	360	5527
CS_OMP	71	1272
BCS	63	1295

C. Aircraft model

A scaled aircraft model shown in Fig. 7 is analyzed as the third example. The model is created based on the picture of F15 fighter plane in Wikipedia [30]. The maximum size in the x, y and z directions are 1.9 m, 1.2 m and 0.4 m. It is discretized into 6741 unknowns at 600 MHz. The nose of the aircraft is towards the positive direction of x-axis. The elevation angle of the incident wave is fixed to be 90° while the aspect angle ranges from 0° to 360° with 1° increment. Figure 8 demonstrates the monostatic RCS computed by the MLFMM, CS_OMP and BCS method. Table 2 lists the measurement number and CPU time for different methods. Similar conclusions can be drawn with the second numerical example.

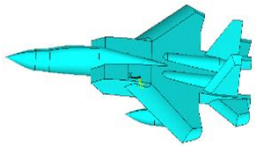

Fig. 7. Aircraft model.

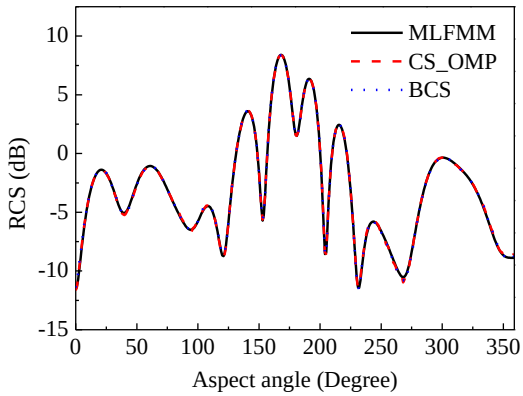

Fig. 8. Monostatic RCS of the aircraft model obtained by MLFMM, CS_OMP and BCS.

Table 2: Measurement number and CPU time of three kinds of methods for the aircraft model

Method	Measurement Number	CPU Time (s)
MLFMM	360	15817
CS_OMP	80	3534
BCS	69	3505

IV. CONCLUSION

The Bayesian compressive sensing method is applied to the fast monostatic scattering analysis. Compared with the traditional CS based method, the proposed method adopts the Bayesian framework and can adaptively determine the number of compressive-sensing measurements. Moreover, the proposed method

needs less measurements than OMP method with the similar level of accuracy.

ACKNOWLEDGMENT

This work is supported by the Fundamental Research Funds for the Central Universities JB160218, XJS16048 and the NSFC 61301069.

REFERENCES

[1] R. F. Harrington, *Field Computation by Moment Methods*. Oxford University Press, 1996.

[2] J. J. Bai, G. Zhang, L. X. Wang, and T. H. Wang, "Uncertainty analysis in EMC simulation based on improved method of moments," *Appl. Comput. Electromagn. Soc. J.*, vol. 31, no. 1, pp. 66-71, 2016.

[3] G. Apaydin and L. Sevgi, "A novel wedge diffraction modeling using method of moments (MoM)," *Appl. Comput. Electromagn. Soc. J.*, vol. 30, no. 10, pp. 1053-1058, 2015.

[4] J. M. Song, C. C. Lu, and W. C. Chew, "Multilevel fast multipole algorithm for electromagnetic scattering by large complex objects," *IEEE Trans. Antennas Propagat.*, vol. 45, no. 10, pp. 1488-1493, 1997.

[5] J. Song and W. C. Chew. "The fast Illinois solver code: Requirements and scaling properties," *IEEE Comput. Sci. Eng.*, vol. 5, no. 3, pp. 19-23, 1998.

[6] J. Song and W. C. Chew., "Multilevel fast-multipole algorithm for solving combined field integral equations of electromagnetic scattering," *Microw. Opt. Technol. Lett.*, vol. 10, no. 1, pp. 14-19, 1995.

[7] E. Bleszynski, M. Bleszynski, and T. Jaroszewicz, "AIM: Adaptive integral method for solving large-scale electromagnetic scattering and radiation problems," *Radio Science*, vol. 31, no. 5, pp. 1225-1251, 1996.

[8] J. R. Phillips and J. K. White, "A precorrected-FFT method for electrostatic analysis of complicated 3-D structures," *IEEE Trans. Comput.-Aided Des. Integr. Circuits Syst.*, vol. 16, no. 10, pp. 1059-1072, 1997.

[9] S. M. Seo and J. F. Lee, "A fast IE-FFT algorithm for solving PEC scattering problems," *IEEE Trans. Magn.*, vol. 41, no. 5, pp. 1476-1479, 2005.

[10] W. Chai and D. Jiao, "An-matrix-based integral-equation solver of reduced complexity and controlled accuracy for solving electrodynamic problems," *IEEE Trans. Antennas Propagat.*, vol. 57, no. 10, pp. 3147-3159, 2009.

[11] K. Zhao, M. N. Vouvakis, and J. F. Lee, "The adaptive cross approximation algorithm for accelerated method of moments computations of EMC problems," *IEEE Trans. Electromagn. Compat.*, vol. 47, no. 4, pp. 763-773, 2005.

[12] J. M. Rius, J. Parron, A. Heldring, J. M. Tamayo, and E. Ubeda, "Fast iterative solution of integral equations with method of moments and matrix decomposition algorithm-singular value decomposition," *IEEE Trans. Antennas Propagat.*, vol. 56, no. 8, pp. 2314-2324, 2008.

[13] Y. E. Erdemli, J. Gong, C. J. Reddy, and J. L. Volakis, "Fast RCS pattern fill using AWE technique," *IEEE Trans. Antennas Propagat.*, vol. 46, no. 11, pp. 1752-1753, 1998.

[14] M. S. Chen, X. L. Wu, and W. Sha, "Asymptotic waveform evaluation technique based on fast lifting wavelet transform," *Appl. Comput. Electromagn. Soc. J.*, vol. 21, no. 1, pp. 99-104, 2006.

[15] E. K. Miller, "Model-based parameter estimation in electromagnetic III: Applications to EM integral equations," *IEEE Antennas Propag. Mag.*, vol. 40, no. 3, pp. 49-66, 1998.

[16] Z. Peng, M. Stephanson, and J. F. Lee, "Fast computation of angular responses of large-scale three-dimensional electromagnetic wave scattering," *IEEE Trans. Antennas Propag.*, vol. 58, no. 9, pp. 3004-3012, 2010.

[17] A. Schröder, H.-D. Brüns, and C. Schuster, "A hybrid approach for rapid computation of two-dimensional monostatic radar cross section problems with the multilevel fast multipole algorithm," *IEEE Trans. Antennas Propag.*, vol. 60, no. 12, pp. 6058-6061, 2012.

[18] A. Massa, P. Rocca, and G. Oliveri, "Compressive sensing in electromagnetics - A review," *IEEE Antennas Propag. Mag.*, vol. 57, no. 1, pp. 224-238, 2015.

[19] A. F. Morabito, A. R. Laganà, G. Sorbello, and T. Isernia, "Mask-constrained power synthesis of maximally sparse linear arrays through a compressive-sensing-driven strategy," *Journal of Electromagnetic Waves and Applications*, vol. 29, no. 10, pp. 1384-1396, 2015.

[20] M. S. Chen, F. L. Liu, H. M. Du, and X. L. Wu, "Compressive sensing for fast analysis of wide-angle monostatic scattering problems," *IEEE Antennas Wirel. Propag. Lett.*, vol. 10, pp. 1243-1246, 2011.

[21] J. A. Tropp and A. Gilbert, "Signal recovery from partial information by orthogonal matching pursuit," *IEEE Trans. Inf. Theory*, vol. 53, no. 12, pp. 4655-4667, 2007.

[22] S. H. Ji, Y. Xue, and L. Carin, "Bayesian compressive sensing," *IEEE Trans. Signal Process.*, vol. 56, no. 6, pp. 2346-2356, 2008.

[23] D. Baron, S. Sarvotham, and R. G. Baraniuk, "Bayesian compressive sensing via belief propagation," *IEEE Trans. Signal Process.*, vol. 58, no. 1, pp. 269-280, 2010.

[24] H. H. Zhang and R. S. Chen, "Coherent processing

and superresolution technique of multi-band radar data based on fast sparse Bayesian learning algorithm," *IEEE Trans. Antennas Propag.*, vol. 62, no. 12, pp. 6217-6227, 2014.

[25] M. Carlin, P. Rocca, G. Oliveri, F. Viani, and A. Massa, "Directions-of-arrival estimation through Bayesian compressive sensing strategies," *IEEE Trans. Antennas Propag.*, vol. 61, no. 7, pp. 3828-3838, 2013.

[26] S. M. Rao, D. R. Wilton, and A. W. Glisson, "Electromagnetic scattering by surfaces of arbitrary shape," *IEEE Trans. Antennas Propagat*, vol. 30, no. 3, pp. 409-418, 1982.

[27] E. J. Candes and M. B. Wakin, "An introduction to compressive sampling," *IEEE Signal Process. Mag.*, vol. 25, no. 2, pp. 21-30, 2008.

[28] A. C. Woo, H. T. G. Wang, M. J. Schuh, and M. L. Sanders, "Benchmark radar targets for the validation of computational electromagnetics programs," *IEEE Trans. Antennas Propagat*, vol. 35, no.1, pp. 84-89, 1993.

[29] https://en.wikipedia.org/wiki/Tomahawk_(missile)

[30] https://en.wikipedia.org/wiki/McDonnell_Douglas_F-15_Eagle

Huan Huan Zhang received the Ph.D. degree in Electromagnetic Fields and Microwave Technology from Nanjing University of Science and Technology in 2015. He was a Postdoctoral Research Fellow with the Center of Electromagnetics and Optics, the University of Hong Kong, Hong Kong, from 2015 to 2016. He is currently a Lecturer with The School of Electronic Engineering, Xidian University, Xi'an, China.

Zhang serves as the Reviewer of the IEEE Transactions on Antenna and Propagation, Communications in Computational Physics, IET Radar, Sonar & Navigation, etc. His current research interests include computational electromagnetics, IC signal integrity, EMC/EMI and radar signal processing.

Xun Wang Zhao received the B.S. and Ph.D. degrees from Xidian University, Xi'an, China, in 2004, and 2008, respectively. He joined Xidian University as a Faculty Member in 2008. As principal Investigator, he is doing or has completed some projects including project of NSFC.

Zhong Chao Lin received the B.S. degree from Xidian University, Xi'an, China, in 2011, and is currently working toward the Ph.D. degree at the School of Electronic and Engineering, Xidian University, Xi'an, China. His current research interests is computational electromagnetic.

Wei E. I. Sha has co-authored two books respectively on wavelet theory and finite-difference time-domain method. He has published 72 peer-reviewed journal papers included in Web of Science Core Collection. He also contributed four book chapters at Springer, CRC Press and InTech Publishers and 13 invited talks at international conferences. Sha is an IEEE Member and an OSA Member. He has served as the Onsite Award Committee, Technical Program Committee or Session Chair of several international conferences including ICCEM 2017/2016, PIERS 2016, IMWS-AMP 2015, EICT 2015, ICSPS 2011, etc. He has been serving as the Invited Referees of IEEE, OSA, AIP, APS and Nature Publishing Group journals. He also served as the Book Proposal Reviewers for CRC Press and Bentham Science publishers.

He received the Second Prize and First Prize of National Postgraduates Mathematical Contest in Modeling, respectively in 2006 and 2007. He was awarded Chinese Youth Science and Technology Innovation Prize in 2007. He and his collaborators received Research Output Prize at the University of Hong Kong in 2013. In 2014, he was awarded Outstanding Reviewer of Journal of Computational Physics. In 2015, he was awarded Second Prize of Natural Science from Anhui Province Government, China. Sha also received three Best Student Paper Prizes and one Young Scientist Award with his students.

He engages in theoretical and computational research in electromagnetics and optics, focusing on the multiphysics and interdisciplinary research. The research topics are inspired by applications in several areas including solar energy, microwave/optical communication, sensing/detection, and quantum information. His research involves fundamental and applied aspects in plasmonics, emerging photovoltaics, metasurfaces, quantum electrodynamics, and computational electromagnetics.

Moving Targets Imaging in Spaceborne TOPS SAR

Hongbo Mo [1], Wei Xu [2], and Zhimin Zeng [1]

[1] School of Information and Communication Engineering and Beijing Key Laboratory of Network System Architecture and Convergence
Beijing University of Posts and Telecommunications, Beijing, 100876, China
mohongbo@bupt.edu.cn, zengzm@bupt.edu.cn

[2] Spaceborne Microwave Remote Sensing System Department
Institute of Electronics, Chinese Academy of Sciences (IECAS), Beijing, 100190, China
iecasxuwei@163.com

Abstract ─ Terrain Observation by Progressive Scans (TOPS) is the spaceborne wide swath synthetic aperture radar (SAR) imaging mode and attractive for ocean remote sensing. Its imaging processors are quite different from the one of the conventional stripmap mode due to antenna beam progressive scanning. This paper proposes a new imaging processor in TOPS for moving targets especially for moving ships in ocean. In addition to resolving the azimuth aliasing problem in TOPS, the Doppler parameter estimation is the key point of the proposed processor. According to the estimated Doppler parameters, some transfer functions of the processor should be updated. Simulation results on point and distributed targets validate the proposed imaging processor.

Index Terms ─ Doppler parameter estimation, moving target imaging, Synthetic Aperture Radar (SAR), Terrain Observation by Progressive Scans (TOPS).

I. INTRODUCTION

The terrain observation by progressive scans (TOPS) mode achieves the wide swath coverage by progressive steering the antenna beam in both azimuth and elevation, and it was first successfully achieved by the TerraSAR-X (TSX) in 2008 [1, 2]. Although the wide swath coverage of the TOPS is exchanged by the impaired azimuth resolution compared with the stripmap case, the TOPS imaging scheme is the attractive spaceborne synthetic aperture radar (SAR) imaging mode for multiple applications, especially for ocean observation and ships detection due to its wide swath coverage with better system performances than conventional ScanSAR [2]. Therefore, most of future spaceborne microwave remote sensing missions would adopt this wide swath imaging mode for ocean remote sensing [2].

Since the azimuth antenna beam is steered from aft to fore during the whole raw data acquisition duration, the raw data of the TOPS mode couldn't be well handled by conventional stripmap processors. Up to now, multiple imaging efficient processors are proposed for the TOPS mode [1, 3-7]. However, little work about moving targets focusing in TOPS could be found. In this paper, a new imaging processor to handle the raw data of moving targets especially for moving ships in ocean in TOPS is proposed. In addition to resolve both Doppler spectra and azimuth output SAR image back folding problems, the key point of the proposed imaging processor is the Doppler parameters estimation in TOPS. With the estimated Doppler parameters, the processor is modified to be fit for the signal mode of the moving target.

This paper is arranged as follows. The echo model of moving targets in TOPS is established in Section II. The proposed imaging processor for moving targets in TOPS is presented in detail in Section III. To validate the proposed imaging algorithm, a simulation experiment on point targets is carried out. Finally, this paper is concluded in section V.

II. ECHO PROPERTIES OF MOVING TARGETS IN TOPS

In TOPS, the elevation antenna beam is periodically scanned from sub-swath to sub-swath to obtain the wide swath coverage similar to ScanSAR, while the azimuth antenna beam is actively steered from aft to fore during the whole SAR raw data acquisition time as shown in Fig. 1. In Fig. 1, v_s is the velocity of the sensor, and ω_r is the azimuth beam rotation rate. In addition to making sure azimuth continuous imaging in each sub-swath, the azimuth beam progressive scanning is adopted to reduce the effect of the scalloping phenomenon in the burst imaging mode, since each target is illuminated by the whole 3dB azimuth antenna pattern in TOPS. The better image quality in TOPS than in ScanSAR is very attractive, especially for ocean remote sensing applications, as the

Submitted On: May 29, 2016
Accepted On: September 9, 2016

scalloping effect of SAR images of ocean is hard to correct by existing radiometric calibration algorithms [2].

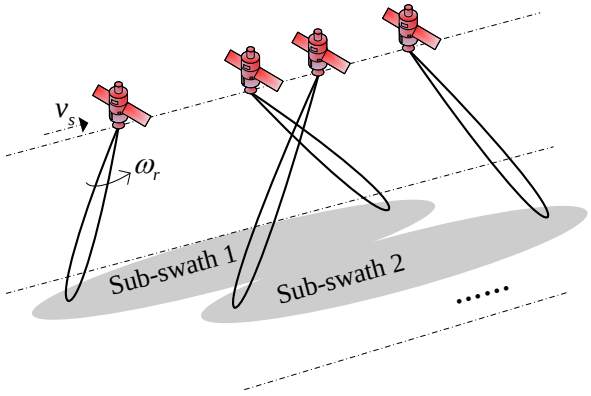

Fig. 1. TOPS SAR acquisition geometry.

The planar imaging geometry of the TOPS mode in a sub-swath is shown in Fig. 2, which indicates that the azimuth beam is electronically steered from aft to fore. As show in Fig. 2, there is a fixed virtual rotation center on the imaging plane, and the rotation center is farther away from the imaged scene than the SAR sensor. The rotation range r_{rot} has negative sign, and v_r is the effective velocity of the sensor in the planar imaging geometry. Assuming that there is a moving target P with the azimuth location x and the slant range r in the scene, and the moving target velocity is u. Furthermore, the moving target velocity is divided into two components: the azimuth velocity component u_a and the range velocity component u_r, as shown in Fig. 2.

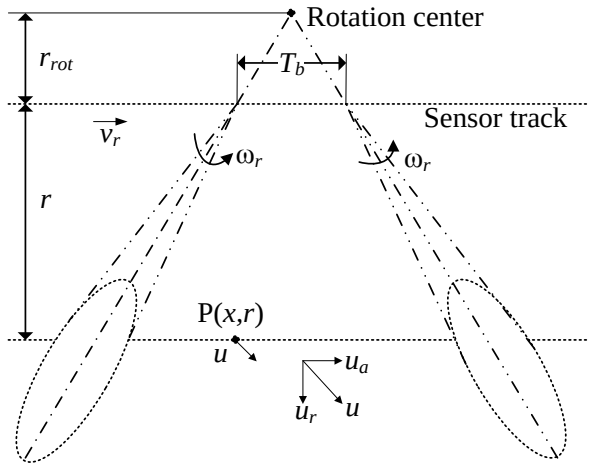

Fig. 2. Planar TOPS SAR geometry in a sub-swath.

The echo signal of a point moving target P as shown in Fig. 2 can be expressed as [8-10]:

$$s(\tau,t;x,r)=C_0\cdot\exp\left(-j\frac{4\pi}{\lambda}R(t)\right)\cdot\mathrm{rect}\left[\frac{\tau-2R(t)/c}{\tau_p}\right]\cdot\exp\left[-jK_r\left(\tau-\frac{2R(t)}{c}\right)^2\right]\cdot\mathrm{rect}\left[\frac{A(r)\cdot t-x/(v_r-u_a)}{T_f}\right], \quad (1)$$

with

$$R(t)=\sqrt{(v_r t-u_a t-x)^2+(r+u_r t)^2}, \quad (2)$$

$$A(r)=1+\frac{\omega_r\cdot r}{v_r-u_a}, \quad (3)$$

where τ and t are the range time and the azimuth time, respectively, C_0 is a complex constant, λ is the wavelength, K_r is the chirp rate of the transmitted pulse, c is the light speed, τ_p is the transmitted pulse duration, and T_f is the synthetic aperture time in the stripmap mode determined by the exploited azimuth beam angular interval. Compared to echoes of moving targets in the conventional stripmap mode, the major difference in TOPS is the azimuth signal component. Therefore, we just need to focus on analyzing the properties of the azimuth signal, and the simplified expression of the azimuth signal component of point target P(x, r) is expressed as follows:

$$\begin{aligned}s_a(t;x,r)&=C_1\cdot\exp\left(-j\frac{4\pi}{\lambda}R(t)\right)\cdot\mathrm{rect}\left[\frac{A(r)\cdot t-x/v}{T_f}\right]\\&\approx C_2\cdot\exp\left(-j\frac{4\pi r}{\lambda}\right)\cdot\mathrm{rect}\left[\frac{A(r)\cdot t-x/v}{T_f}\right]\\&\quad\cdot\exp\left[-j\pi\frac{2(v^2+u_r^2)t^2}{\lambda r}+j\frac{4\pi}{\lambda}\left(\frac{vx}{r}-u_r\right)t\right]\end{aligned}, \quad (4)$$

where both C_1 and C_2 are complex constants, while $v=v_r-u_a$ is the relative azimuth velocity between the SAR sensor and the moving target. According to (4), the instantaneous Doppler frequency $f_a(t;x,r)$ of the moving target P could be obtained as follows:

$$\begin{aligned}f_a(t;x,r)&=\frac{1}{2\pi}\cdot\frac{\partial\varphi(t)}{\partial t}\\&=-\frac{2(v^2+u_r^2)}{\lambda r}t+\frac{2}{\lambda}\left(\frac{vx}{r}-u_r\right)\end{aligned}. \quad (5)$$

Furthermore, according to the last component of (1), the azimuth beam illumination center time for the moving target P is:

$$t_x=\frac{x}{A(r)\cdot v}. \quad (6)$$

Consequently, the Doppler centroid of the moving target could be obtained as:

$$f_{dc}(x,r) = f_a(t_x;x,r) = \frac{2v^2}{\lambda r}\cdot\frac{x}{v}\cdot\frac{A(r)-1}{A(r)} - \frac{2u_r^2}{\lambda r}\cdot\frac{x}{A(r)\cdot v} - \frac{2u_r}{\lambda} = \frac{2v^2}{\lambda r_{rot}}\cdot\frac{x}{A(r)\cdot v} - \frac{2u_r^2}{\lambda r}\cdot\frac{x}{A(r)\cdot v} - \frac{2u_r}{\lambda}. \quad (7)$$

The Doppler centroid $f_{dc}(x,r)$ of the moving target P includes three parts. The first part is almost the same as the fixed target in TOPS; the second part due to the range velocity u_r of the moving target is very small and could be neglected; the third part is also caused by the velocity u_r but much larger than the second part. From (5), the Doppler modulation rate of the moving target P is:

$$k_{am}(x,r) = \frac{\partial f_a(t;x,r)}{\partial t} \approx -\frac{2(v^2+u_r^2)}{\lambda r}. \quad (8)$$

Figure 3 shows the azimuth time frequency diagram (TFD) in TOPS for both fixed and moving targets, the thick solid and the thick dash lines indicates fixed and moving targets, respectively. As shown in Fig. 3, the fixed target Q and the moving target P are with the same azimuth location at the moment of the azimuth beam center time, and the Doppler frequency difference Δf_a between their Doppler centroids is expressed as follows:

$$\Delta f_{ac}(x,r) = f_{dc}(x,r) - f_{ac}(x,r) \approx -\frac{2u_a}{\lambda r_{rot}}\cdot\frac{x}{A(r)} - \frac{2u_r}{\lambda} \approx -\frac{2u_r}{\lambda}, \quad (9)$$

where $f_{ac}(x,r)$ is the Doppler centroid of the fixed target with the location of (x, r). Therefore, the Doppler frequency difference Δf_a is mainly determined by the range velocity component u_r of the moving target.

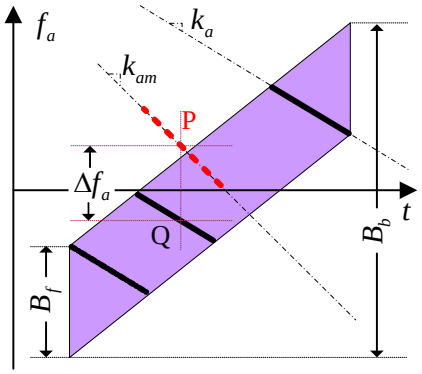

Fig. 3. The azimuth time frequency diagram in TOPS for both fixed and moving targets.

III. NEW IMAGING PROCESSOR FOR MOVING TARGETS IN TOPS

In the TOPS mode, the Doppler bandwidth of the whole burst may span over several pulse repetition frequency (PRF) intervals, multiple approaches to overcome this problem have been proposed in recent years [3-7]. Among them, the azimuth pre-filtering based on the two step focusing technique is one of most efficient approaches, which introduces an azimuth involution between the SAR raw data and the selected chirp signal and is implemented by two complex multiplications and an azimuth Fourier transform (FT). In this paper, we extend the azimuth pre-filtering approach based on the two step focusing technique to handle the raw data of moving targets in TOPS. The key point of the extended imaging algorithm is the updated selected transfer functions for SAR focusing according to the target velocity estimation results. The block diagram of the proposed is shown in Fig. 4.

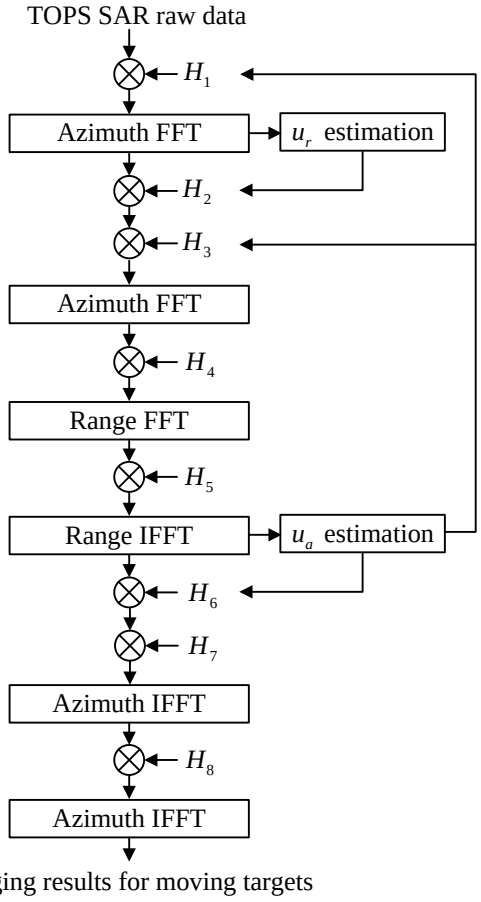

Fig. 4. Block diagram of the proposed imaging approach.

According to the signal model of the moving target, the first multiplied function for moving targets in azimuth pre-filtering is given as follows:

$$H_1(n\cdot\Delta t) = \exp\left[j\pi \frac{2(v_r-u_a)\omega_r}{\lambda}(n\cdot\Delta t)^2 \right], \quad (10)$$

where $n = -I/2,...,0,...,I/2-1$, $\Delta t = 1/\text{PRF}$ is the azimuth time sampling interval, PRF is the pulse

repetition frequency, and I is the number of azimuth samples. As the velocity component u_a is usually unknown before Doppler parameters estimation, $u_a = 0$ is assumed and the value would be updated after the velocity u_a estimation as shown in Fig. 4. After azimuth FT, the Doppler centroid estimation would be taken. As the azimuth time variant Doppler centroid component is removed after multiplying H_1, the Doppler centroid estimation for the resulting raw data of the TOPS mode is the same as the conventional stripmap mode and multiple approaches for the Doppler centroid estimation could be found in [11]. Due to $v_r \gg u_a$, the effect of the unknown velocity u_a on the estimated Doppler centroid of the azimuth center time for SAR raw data collection could be neglected and the estimated velocity $\tilde{u}_r$ could be computed as follows:

$$\tilde{u}_r = -\frac{\lambda \tilde{f}_{ac}}{2}, \tag{11}$$

where $\tilde{f}_{ac}$ is the estimated Doppler center.

Consequently, the following Doppler filter as shown in Fig. 6 is taken to eliminate the out band signal component,

$$H_2(f_a) = \begin{cases} 1, & \tilde{f}_{ac} - B_f/2 \le f_a \le \tilde{f}_{ac} + B_f/2 \\ 0, & \text{otherwise} \end{cases}, \tag{12}$$

where B_f is the azimuth beam bandwidth as shown in Fig. 3. For the azimuth, the second transfer function to be multiplied is:

$$H_3(m \cdot \Delta t') = \exp\left[j\pi \frac{2(v_r - u_a)\omega_r}{\lambda} (m \cdot \Delta t')^2 \right], \tag{13}$$

where $m = -P/2, ..., 0, ..., P/2-1$, $\Delta t' = 1/B_b$ is the azimuth time sampling interval after azimuth pre-filtering, B_b is the Doppler bandwidth of the whole burst in TOPS as shown in Fig. 3, while P is the number of azimuth samples after azimuth pre-filtering and is expressed as follows:

$$P = I + \frac{\mathrm{PRF} \cdot T_f}{A-1}, \tag{14}$$

where T_f is the azimuth synthetic aperture time in the stripmap case for the same exploited azimuth beam interval. Afterwards, the conditional chirp scaling (CS) processor is adopted to implement the following range compression and range cell migration correction (RCMC) processing steps, and the transfer function H_4 and H_5 as shown in Fig. 6 are respectively expressed as follows [11, 12]:

$$H_4(f, f_a) = \exp\left[j\pi \frac{f^2}{k_r (1 + a(f_a))} \right] \cdot \exp\left[j \frac{4\pi r_{ref}}{c} a(f_a) f \right], \tag{15}$$

$$H_5(f_a, \tau; r_{ref}) = \exp\left\{ j \frac{4\pi}{\lambda} r \cdot [\beta(f_a) - 1] - j\pi \frac{f_a^2}{k_{rot}} + j\Delta\phi \right\}, \tag{16}$$

with

$$\beta(f_a) = \sqrt{1 - \left(\frac{\lambda f_a}{2v} \right)^2}, \tag{17}$$

$$a(f_a) = \frac{1}{\beta(f_a)} - 1, \tag{18}$$

$$\frac{1}{k(f_a; r_{ref})} = \frac{1}{K_r} - \frac{2\lambda r \left(\beta^2(f_a) - 1 \right)}{c^2 \cdot \beta^3(f_a)}, \tag{19}$$

$$\Delta\phi = -4\pi \frac{k(f_a; r_{ref}) \cdot [1 - \beta(f_a)]}{c^2 \cdot \beta^2(f_a)} \cdot (r - r_{ref})^2, \tag{20}$$

where f is the range frequency, and r_{ref} is the selected reference range. For the TOPS mode with low geometric resolutions, the effect of the unknown u_a on RCMC could even be neglected. However, the unknown u_a on azimuth compression could not be neglected and would result in the reduced imaging quality. The estimated velocity component $\tilde{u}_a$ is obtained as follows:

$$\tilde{u}_a = \sqrt{ -\frac{\lambda r \tilde{k}_{am}(x, r)}{2} - u_r^2 } - v_r, \tag{21}$$

with

$$\tilde{k}_{am}(x, r) = \left(\frac{\lambda}{2 v_r \omega_r} - \frac{1}{\tilde{k}_a(x, r)} \right)^{-1}, \tag{22}$$

where $\tilde{k}_a(x, r)$ is the estimated Doppler modulation rate after range IFFT. The Doppler modulation rate estimation of the resulting raw data after range IFFT is the same as the one in the stripmap mode. After obtaining the estimated velocity $\tilde{u}_a$, the transfer functions H_1 and H_3 in Fig. 4 should be updated. The azimuth scaling phase function H_6 removes the hyperbolic azimuth phase history for the azimuth data compression, and it is expressed as follows:

$$H_6(r, f_a) = \exp\left[\frac{j4\pi r}{\lambda} \left(\beta(f_a) - 1 \right) \right] \exp\left[j\pi \frac{\lambda}{2v\omega_r} f_a^2 \right]. \tag{23}$$

The multiplied transfer functions H_7 and H_8 with

an azimuth inverse fast Fourier transform (IFFT) step are introduced to implement the azimuth convolution between the compressed azimuth signal and the selected chirp signal to resolve the output back folding in the focused TOPS SAR images. According to (10), the multiplied transfer functions H_7 is expressed as [5, 7]:

$$H_7(f_a) = \exp\left[j\pi \left(n \cdot \Delta f_a\right)^2 / k_d \right], \tag{24}$$

with

$$k_d = \frac{A(r)-1}{A(r)} \cdot \frac{2\left(v_r - u_a\right)^2}{\lambda r}, \tag{25}$$

where $n = -P/2, ..., 0, ..., P/2-1$, $\Delta f_a = 1/T$ is the azimuth time sampling interval, T is the azimuth time duration after azimuth pre-filtering. The final multiplied phase function H_8 in Fig. 4 is easily obtained as follows:

$$H_8(f_a) = \exp\left[j\pi \left(n \cdot \Delta f_a'\right)^2 / k_d \right], \tag{26}$$

with

$$\Delta f_a' = \left| \frac{P \cdot k_d}{\Delta f_a} \right| \tag{27}$$

IV. SIMULATION EXPERIMENT

To validate the proposed imaging approach, simulation experiment on point and distributed targets are carried out and simulation parameters are listed in Table 1.

Table 1: Simulation parameters

Parameters	Value
Carrier frequency	9.65 GHz
Azimuth beam width	0.4º
System PRF	4000Hz
Transmitted pulse duration	20μs
Transmitted pulse bandwidth	20MHz
Sampling frequency	24MHz
Effective velocity	7200m
Burst duration	0.4s
Slant range of imaging center	600km
Azimuth beam rotation rate	2.06º/s

The designed scene including three point targets is shown in Fig. 5, and point target P2 is located at the scene center. Azimuth velocity components u_a of point targets P1, P2 and P3 are 0m/s, 5m/s and 10m/s, respectively, while their range velocity components u_r are 5m/s, 0m/s and 10m/s, respectively.

Figure 6 (a) shows the imaging result of the designed scene, and point targets P1 and P3 are not located at their actual positions due to the range velocity component, which results in an azimuth position shift. Figures 6 (b)~(d) show contour plots of three point targets, which show the well-focused behavior and structure. Resolution, Peak Side Lobe Ratio (PSLR) and Integrated Side Lobe Ratio (ISLR) of three point targets are summarized and listed in Table 2. Both imaging results in Fig. 6 and imaging parameters in Table 2 validate the proposed imaging approach.

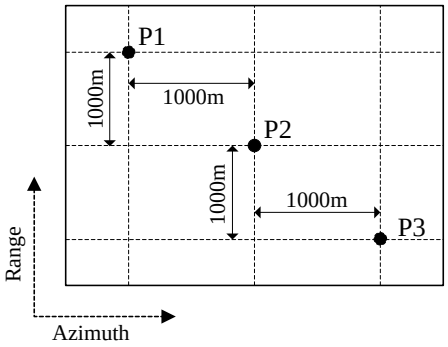

Fig. 5. The designed imaged scene.

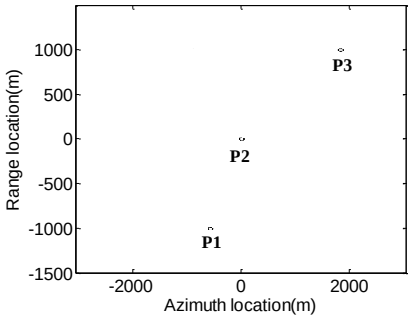

(a) The imaging result

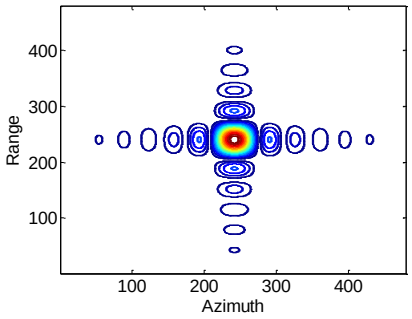

(b) Point target P1

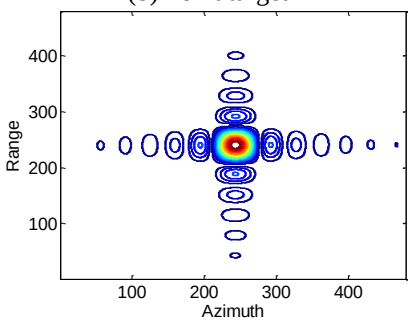

(c) Point target P2

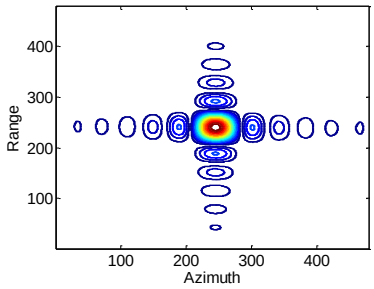

(d) Point target P3

Fig. 6. The imaging results of the designed scene with point targets.

Table 2: Imaging parameters of point targets

		Res (m)	PSLR (dB)	ISLR (dB)
P1	Range	6.65	-13.24	-10.02
	Azimuth	8.02	-13.22	-9.93
P2	Range	6.65	-13.28	-10.10
	Azimuth	8.04	-13.18	-9.96
P3	Range	6.65	-13.23	6.65
	Azimuth	8.04	-13.16	-9.91

To further validate the proposed imaging approach, a simulation experiment on a distributed target is carried out. An electromagnetic modeling of the ship consisting of 45 independent points is designed as shown in Fig. 7 (a), while the velocity components in the range direction and azimuth direction of the designed moving ship are 6m/s and 5m/s, respectively. The raw data of the designed moving ship in TOPS is handled by both the conventional imaging processor in TOPS and the proposed imaging processor. The imaging result handled by the conventional processor shows the defocusing phenomenon as shown in Fig. 7 (b), while it is well focused by the proposed imaging approach as shown in Fig. 7 (c).

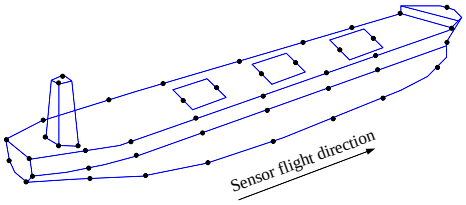

(a) The designed moving ship

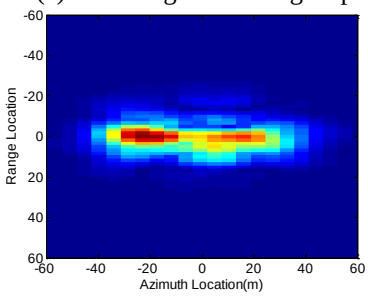

(b) The result by the conventional processor

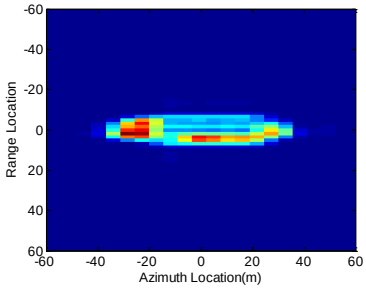

(c) The result by the proposed processor

Fig. 7. The imaging results of the designed moving ship.

V. CONCLUSION

The TOPS mode achieves the wide swath coverage and is attractive for ocean remote sensing. Due to azimuth beam progressive scanning, imaging processors of the TOPS mode are different from other modes. Although multiple TOPS SAR imaging algorithms for fixed targets are proposed in recent years, these algorithms are not very suitable for moving ships in ocean in TOPS. According to the signal model of the moving target in TOPS, we extend the processing ability of the classic TOPS SAR processor to handle the raw data of moving ships. The key points of the proposed imaging approach are the moving target velocity estimation and updating the transfer functions for focusing. Simulation results on both point and distributed targets validate the proposed imaging approach. However, in windy weather conditions, ship motions of roll, yaw, and pitch should be considered during its focusing, and this case requires a more complex imaging processor for moving ships focusing.

ACKNOWLEDGMENT

This work is supported in part by NSF of China (No. 61271177) and in part by the high resolution earth observation system major special project youth innovation foundation of China.

REFERENCE

[1] F. De Zan and A. Monti Guarnieri, "TOPSAR: Terrain observation by progressive scans," *IEEE Trans. Geosci. Remote Sens*., vol. 44, no. 9, pp. 2352-2360, Sep. 2006.

[2] A. Meta, J. Mittermayer, P. Prats, R. Scheiber, and U. Steinbrecher, "TOPS imaging with TerraSAR-X: Mode design and perfomance analysis," *IEEE Trans. Geosci. Remote Sens*., vol. 48, no. 2, pp. 759-769, Feb. 2010.

[3] W Xu, P. Huang, and Y. Deng, "An efficient imaging approach with scaling factors for TOPS mode SAR data focusing," *IEEE Geosci Remote Sens Lett*., vol. 8, no. 5, pp. 929-933, Oct. 2011.

[4] P. Prats, R. Scheiber, J. Mittermayer, A. Meta, and A. Moreira, "Processing of sliding spotlight and

TOPS SAR data using baseband azimuth scaling," *IEEE Trans. Geosci. Remote Sens*., vol. 48, no. 2, pp. 770-780, Feb. 2010.

[5] W Xu, P. Huang, and Y. Deng, "TOPSAR data focusing based on azimuth scaling preprocessing," *Adv. Space Res*., vol. 48, no. 2, pp. 270-277, 2011.

[6] W. Xu, Y. Deng, and R. Wang, "Imaging processor for different spacebarne SAR imaging modes," *IET Elect. Lett*., vol. 48, no. 6, pp. 340-342, Mar. 2012.

[7] W. Xu, P. Huang, Y. Deng, and R. Wang, "TOPS-mode raw data processing using chirp scaling algorithm," *IEEE Journal of Selected Topics in Applied Earth Observations and Remote Sensing*, vol. 7, no. 1, pp. 235-246, 2014.

[8] S. Zhu, G. Liao, Y. Qu, Z. Zhou, and X. Liu, "Ground moving targets imaging algorithm for synthetic aperture radar," *IEEE Trans. Geosci. Remote Sens*., vol. 49, no. 1, pp. 462-477, Jan. 2011.

[9] J. K. Jao, "Theory of synthetic aperture radar imaging of a moving target," *IEEE Trans. Geosci. Remote Sens*., vol. 39, no. 9, pp. 1984-1992, Sep. 2001.

[10] W. Zhou, J.-T. Wang, H. W. Chen, and X. Li, "Signal model and moving target detection based on MIMO synthetic aperture radar," *Progress In Electromagnetics Research*, vol. 131, pp. 311-329, 2012.

[11] I. G. Cumming and F. H. Wong, *Digital Processing of Synthetic Aperture Radar Data: Algorithms and Implementation*, Artech House, Norwood, MA, 2005.

[12] A. Moreira, J. Mittermayer, and R. Scheiber, "Extended chirp scaling algorithm for air- and spaceborne SAR data processing in stripmap and ScanSAR imaging modes," *IEEE Trans. Geosci. Remote Sens*., vol. 34, no. 5, pp. 1123-1136, Sep. 1996.

Hongbo Mo, Ph.D. student of Beijing University of Posts and Telecommunications. His research interests include signal processing, wireless telecommunication and Internet of Things.

Using a Radial, Switchable, Sector Ground Screen to Produce Azimuthal Directivity for a Monopole Antenna

Edmund K. Miller

Los Alamos National Laboratory (retired), 597 Rustic Ranch Lane, Lincoln, CA USA
e.miller@ieee.org

Abstract ─ Ground-mounted monopole antennas are usually driven against a radial-wire ground system to control their input impedance and to improve their radiation efficiency. This results in a radiation pattern that is uniform in azimuth angle with a front-to-back ratio of 1, or 0 dB. The use of a sectorial ground screen, one whose radial or angular extent is varied to produce a radiation pattern having azimuthal directivity has received some attention. An alternate approach also is explored in this discussion. It involves exploring the effect of varying the number of "active" radials in an otherwise uniform ground system of radial wires, an active radial being one that is electrically connected to the base of the monopole. A "passive" radial on the other hand is one that is separated from the monopole by a switch. By varying the number and angular locations of the active and passive ground wires, the resulting azimuth pattern can be varied in angle and directive gain. This arrangement makes possible a steerable pattern, something not usually associated with ground-mounted monopoles. The antenna and ground screen are modeled using the well-known NEC package. For convenience in modeling, active radials are made into passive ones by adding a large resistance between the base of the monopole and a given radial. Directive gains of more than 5 dB are found to be possible.

Index Terms ─ Directivity, ground screen, monopole antenna, steerable pattern, switching radials.

I. INTRODUCTION

Sectorized ground screens have been examined previously using either a disk [1] or an arrangement of radial wires that are limited to a specified angular sector [2,3]. The approach taken here is to generalize [2] to a ground screen comprised of uniformly spaced wires that cover 360 degrees around the base of the monopole. This is illustrated in Fig. 1 for the 30 radial-wire system used to obtain the results presented below.

A sectorized ground screen is made here by inserting a 10-MOhm resistor at the connection points of one or more radials to the base of the monopole to create a passive, or loaded, radial. The unloaded radials are denoted as active radials. The resultant pattern can be steered in azimuth by rotating the loading arrangement in angle. The number of passive radials is varied from 0 to 30, with 0 loads denoted as the reference case. The input powers are normalized in the pattern comparisons that follow.

Some more recent publications somewhat related to this general problem are [4-6]. A comprehensive review of ground screens can be found in a book devoted to monopole antennas [7]. A discussion on the effects of elevated and buried ground screens on monopole-antenna performance can be found in [8]. The results presented in [2], [8] and here have been obtained using NEC, the Numerical Electromagnetics Code [9].

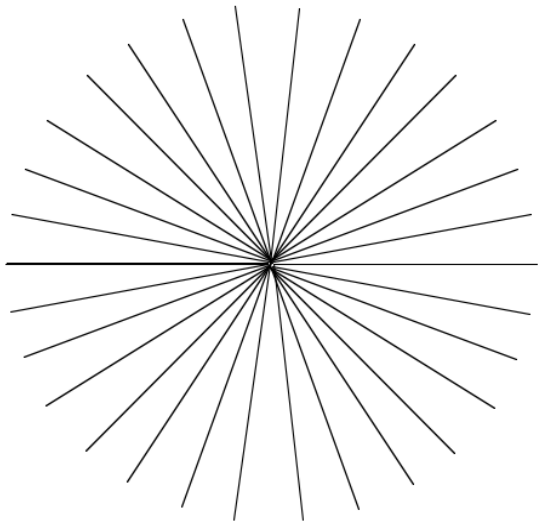

Fig. 1. A 30-wire radial ground screen.

The nominal model parameters are:
-- Operating frequency of 10 MHz (30-m wavelength).
-- Wire radius of 0.001 m (3.33x10-5 wavelengths).
-- Monopole height of 7.5 m (¼ wavelength).
-- Radials are 9-m long (0.3 wavelengths), and are 0.1 m (3.333x10-3 wavelengths) above the interface.

Submitted On: June 15, 2016
Accepted On: September 9, 2016

-- A ground conductivity of 10-3 mhos/m and relative dielectric constant of 4.
-- Segment lengths throughout are 0.75 m (0.025 wavelengths).

II. REPRESENTATIVE RESULTS

Varying the number of loaded radials from 0 to 29 yields the elevation-pattern peak plotted in Fig. 2. The elevation pattern in Fig. 3 is obtained using 13 active radials whose effect is to provide a peak at about 5.7 dB at an elevation angle of about 35 degrees.

The azimuth pattern for 13 active radials is plotted at 35 degrees of the elevation pattern in dB in Fig. 4 and on a linear scale in Fig. 5, where the latter plot deemphasizes the sharpness of the pattern minimum.

The input and radiated powers for a 1-V source are plotted in Fig. 6 as a function of the number of loaded radials. Both the radiated and input powers monotonically decrease as the number of active radials is reduced from 30 to 1. The radiation efficiency also decreases from about 52% of 0.0115 w to 37% of 0.0052 w when the number of active radials is reduced from 30 to 12, as exhibited in Fig. 7.

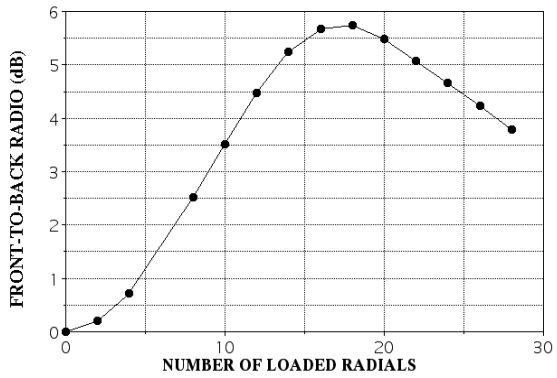

Fig. 2. The directive elevation gain as a function of the number of loaded radial wires.

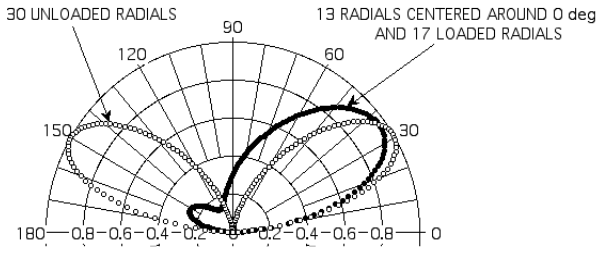

Fig. 3. The elevation patterns for 30 and 13 active radials respectively for equal input powers normalized to the reference pattern of 30 active radials.

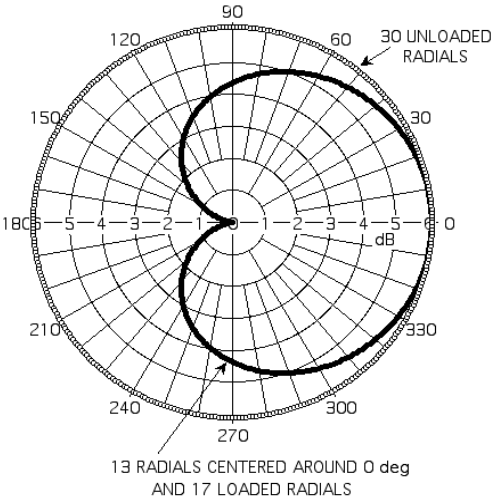

Fig. 4. The azimuthal pattern in dB for 30 and 13 active radials respectively, at the peak of their respective elevation patterns for equal input powers.

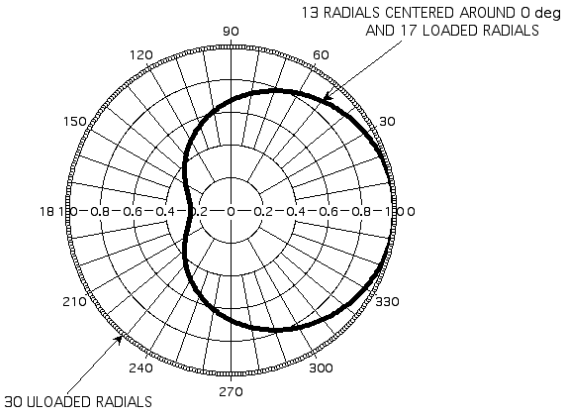

Fig. 5. The patterns of Fig. 4 plotted on a linear scale.

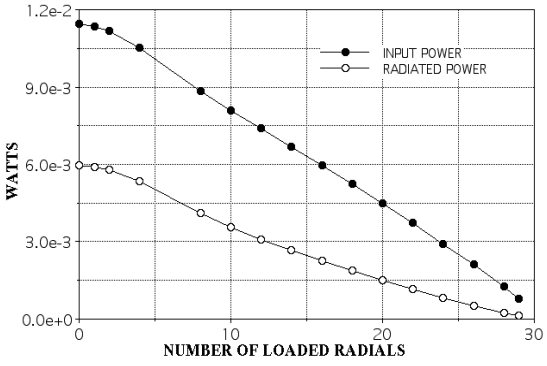

Fig. 6. Input and radiated power variation as a function of the number of loaded radials.

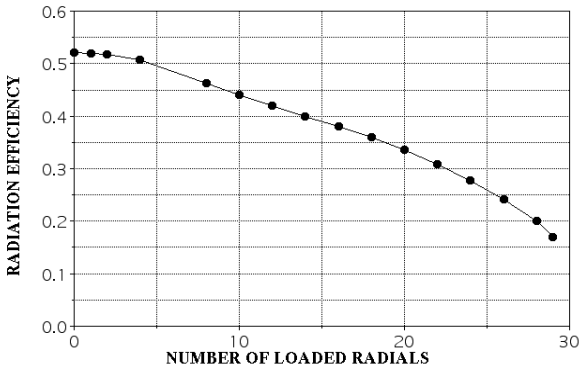

Fig. 7. Radiation efficiency as a function of the number of loaded radials.

The monopole and total ground-wire currents are shown as a function of position in Fig. 8 for case of 30 active ground wires. While the currents are equal at the base of the monopole it is interesting to see that the sum of the ground-screen currents otherwise exceeds that on the monopole.

The spatial distribution of power radiated by the monopole and 30 active radials as obtained from FARS [10] is shown in Fig. 9. More than 90% of the radiated power comes from the monopole in spite of the sum of the current on the 30 active radials exceeding that of the monopole. The total power coming from the monopole and radials is 4.53×10^{-3} w and 3.44×10^{-4} w respectively.

The monopole admittance is found to vary monotonically as the number of loaded radials is increased as shown in Fig. 10. The directivity is plotted as a function of the ground-wire lengths in Fig. 11 for the nominal case of 17 loaded radials and maximizes at about the length of 0.3 wavelengths used in this study.

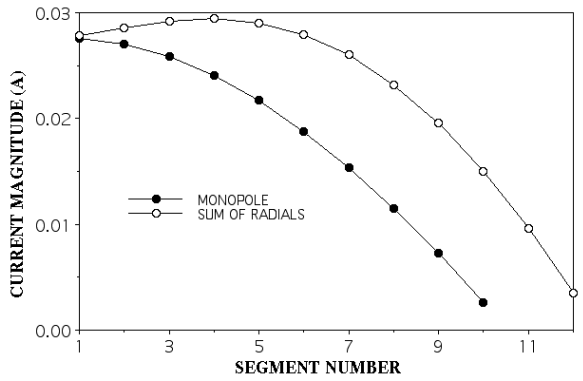

Fig 8. The current magnitudes on the monopole and sum on the 30 active radials.

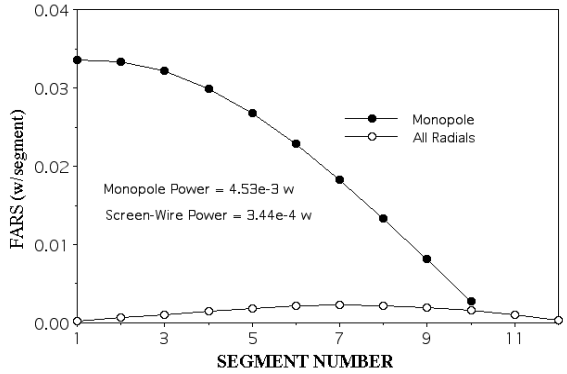

Fig. 9. The distribution of the radiated power from the monopole and 30 active radials.

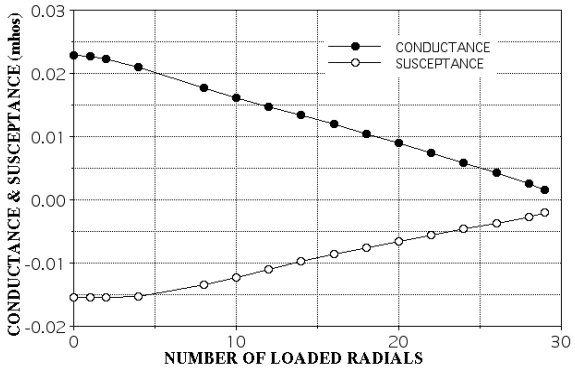

Fig. 10. The conductance and susceptance of the monopole as a function of the number of loaded radials.

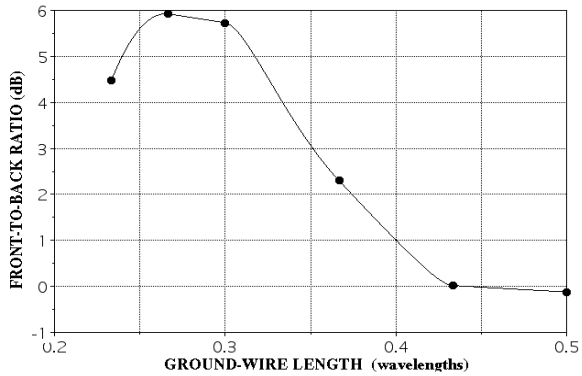

Fig. 11. The dependence of the directivity on the length of the ground wires.

III. CONCLUDING COMMENTS

The sectorized ground system has some interesting

properties:

1) It maintains approximately the same far-field power flow in the direction of the unloaded radials.
2) It reduces the far-field power flow in the direction of the loaded radials due to increased ground loss.
3) It permits the pattern to be rotated in azimuth by switching the loaded sector.
4) However, loading the radials to produce directivity does reduce the overall radiation efficiency.

Other arrangement might be worth exploring. One possibility is to vary the lengths of some of the radials in a fashion similar to what is done above at the base of the monopole. Another would be to connect the ends of the radials to grounding stakes. In addition to providing more pattern control, such arrangements might also improve the radiation efficiency.

REFERENCES

[1] J. R. Wait, et al., "Antenna performance influenced by the finite extent and conductivity of ground planes: A collection of reprints," *Mitre Corporation, M90-79, AD-A232 132*, September 1990, including: James R. Wait and Lillie C. Walters, "Influence of a sector ground screen on the field of a vertical antenna," *U. S. National Bureau of Standards*, Monograph 60, April 1963.

[2] E. K. Miller, J. N. Brittingham, and J. T. Okada, "Explicit modeling of antennas with sparse ground screens," *Electronics Letters*, vol. 14, no. 19, pp. 627-629, 1978.

[3] J. R. Hallas, "Vertical monopoles can indeed be directive," *American Radio Relay League QST*, pp. 59-60, April 2015.

[4] M. Hirose and M. Miyake, "Pattern control of a 1/4 λ monopole antenna on a handset by passive loading," *Universal Personal Communications: Gateway to the 21st Century, Conference Record*, vol. 1, pp. 44-48, October 1993.

[5] J. F. Janek and J. J. Evans, "Predicting ground effects of omnidirectional antennas in wireless sensor networks," *Wireless Sensor Network*, vol. 2, pp. 879-890, 2010.

[6] L. Kibona, "Analysis of the effects of rectangular ground plane on radiation pattern of the monopole antenna," *Int. J. of Scientific and Research Publications*, vol. 3, no. 11, November 2013.

[7] M. M. Weiner, *Monopole Antennas*. Marcel Dekker, Inc., 2003.

[8] G. J. Burke and E. K. Miller, "Numerical modeling of monopoles on radial-wire ground screens," *IEEE Ant. and Propagat. Society Int. Symp.*, vol. 1, pp. 244-247, 1989.

[9] G. J. Burke, E. K. Miller, and A. J. Poggio, "The numerical electromagnetics code (NEC) – A brief history," *IEEE AP-S Int. Symp. and USNC/URSI National Radio Science*, Monterey, California, June 20-25, 2004.

[10] E. K. Miller, "Development of the incremental IEMF method as an analytical proof for the validity of FARS (far-field analysis of radiation sources)," *IEEE Ant. and Propagat. Society Magazine*, vol. 52, no. 6, pp. 46-54, December 2010.

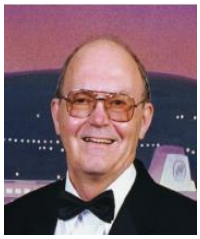

Edmund K. Miller earned his Ph.D. in Electrical Engineering at the University of Michigan, and since has held a variety of government, academic and industrial positions. These include 15 years at Lawrence Livermore National Laboratory and 4+ years at Los Alamos National Laboratory His academic experience includes holding a position as Regents-Distinguished Professor at Kansas University, Stocker Visiting Professor at Ohio University, Physics Instructor at Michigan Technological University and Research Engineer at the University of Michigan. Miller has been appointed as an AP Distinguished Lecturer for 2014-2016, and wrote the columns "PCs for AP and Other EM Reflections" from 1984 to 2000 for the Magazine of the Antennas and Propagation Society. He received (with others) a Certificate of Achievement from the IEEE Electromagnetic Compatibility Society for Contributions to Development of NEC (Numerical Electromagnetics Code) and was a recipient (with others) in 1989 of the Best Paper Award given by the Education Society for "Computer Movies for Education." He is a Life Fellow of the IEEE and an ACES Fellow.

Arbitrary Shaped Homogeneous Invisible Ground Cloak

Mohamad Fazeli [1], Seyed Hassan Sedighy [2*], and Hamid Reza Hassani [1]

[1] Department of Electrical Engineering
Shahed University, Tehran, Iran
mohamadfu@gmail.com, hassani@shahed.ac.ir

[*2] School of New Technologies
Iran University of Science and Technology, Tehran, Iran
sedighy@iust.ac.ir

Abstract ─ A general approach is introduced to design an arbitrary shaped invisible ground cloak with homogeneous constitutive parameters. The proposed homogenous ground cloak design method facilitates the fabrication process and achieves a variety of choices for choosing the cloak shape. In this approach, an arbitrary polygonal 2D cloak with any number of sides can be designed by dividing the polygonal cloak cross section into triangular segments and applying the proposed method on each one. The full wave simulations results confirm the idea performance, properly. Finally, a homogeneous ground invisible cloak for an object, which its contour is very similar to the lateral cross section of a car is designed and simulated to validate the capability and generality of the proposed idea.

Index Terms ─ Cloak, coordinate transformation, invisible.

I. INTRODUCTION

Although invisibility used to be deemed as a merely unattainable dream of mankind for years, invisibility cloaks have attracted intense attention, lately [1-6]. The coordinate transformation which is based on form invariant of Maxwell's equations has been widely used to design these invisibility cloaks [7, 8]. Free space and carpet cloaks are two kinds of invisibility cloaks. The free space cloaks hide the objects in free space. Narrow bandwidth and high loss are these cloak serious problems to achieve perfect invisibility which are mainly caused by resonant metamaterials needed for their implementations [9]. The ground cloaks or carpet cloaks are the second group of the invisible cloaks where the cloaked object lies on the flat ground reflects the wave without scattering and the observer perceives a flat ground plane, consequently [10]. Moreover, it has this advantage that its constitutive parameters are not singular and can even be made by isotropic medium [9-11]. The ground cloaks as the second proposed cloak groups have attracted a lot of researcher attentions [9-15]. Also, some demonstrations of the both free space and ground invisible cloaks in different frequency ranges have been presented in [16-19] to show the realized cloaks performances.

The coordinate transformations which are the bases of the cloak design, affect the homogeneity [20-22], order of the anisotropy [22-24] and shape of the cloak [25-28] that are the realization bottlenecks of an invisible cloak. Therefore using a set of proper transformation relations can considerably improve the cloak design approach and facilitates its realization process, consequently.

In many researches, a particular case of transformation relations for a special cloak structure has been used. For example, a triangular ground cloak has been implemented in [12] by using oblique multilayer dielectrics. A 2D triangular ground cloak has been proposed in [13] by using straightforward linear coordinate transformation. A three dimensional ground cloak with conical structure has been discussed in [14] by a rotation of the 2D cloak. An acoustic ground cloak has been proposed in [15] with pyramidal configuration for control of sound propagation and reflection, also.

In this paper, a general approach to extract the coordinate transformations for an arbitrary polygonal shaped ground cloak is proposed which results in homogeneous constitutive parameters. This approach is based on finding the suitable location to place point *N*, the vertex of a 2D triangular cloak. The simulation results verify the designed cloak performance, also. Afterwards, a simplifying assumption is performed that makes the proposed relations simpler. To show the capability and power of the proposed design method, a ground cloak for a schematic car cross section is designed and simulated. Moreover, homogeneity of the required materials for the proposed cloak facilitates the fabrication process and applications of the proposed cloak.

Submitted On: August 19, 2015
Accepted On: July 24, 2016

II. TRIANGULAR CLOAKS DESIGNING PROCEDURE

Under the coordinate transformations between so-called real and virtual spaces, Maxwell's equations remain unchanged in form, which is referred as form-invariant of Maxwell's equations property [1-6]. In other words, the coordinate transformation is a consequence of form-invariant of Maxwell's equations and provides the constitutive parameters of the transformed medium. The relative permittivity and permeability of the transformed medium can be expressed by $\varepsilon'_r = \varepsilon_r AA^T / \det(A)$ and $\mu'_r = \mu_r AA^T / \det(A)$, respectively where **A** is the Jacobian matrix associated with the transformation established between the above-mentioned spaces, ε_r and μ_r denote the relative permittivity and permeability of the background (host medium). Notice that the structure background is considered as free space in this research.

In the mapping procedure of a virtual space into a real space in a 2D regime, the relations between Cartesian coordinates of two spaces are generally defined in the form of Eq. (1a) and (1b) as:

$$x' = f(x, y), \tag{1a}$$

$$y' = g(x, y), \tag{1b}$$

where f and g are functions of x and y, and (x', y') and (x, y) are associated with real and virtual spaces coordinates, respectively. Notice that since the cloak is considered uniformly along the z axis which is the cylindrical axis, it suffices to consider the coordinate transformation in 2D regime and achieves simplicity in the design procedure. One of the critical effective factors in the invisible cloak realization process is the medium homogeneity. Clearly, the homogeneous media is easier to realize rather than the inhomogeneous ones. Therefore, finding the proper relations that result in a homogeneous media facilitates the cloaks realization process, considerably. Since the components of Jacobian matrix **A**, are the first-order partial derivatives ($A_{ij} = \partial X'_i / \partial X_j$), the real space coordinates (x' and y') should be written in terms of a linear combination of virtual space coordinates (x and y) to achieve a transformed homogeneous media. For this purpose, at the first step we assume two linear relations between real and virtual coordinate spaces as:

$$x' = \alpha_1 x + \beta_1 y + \gamma_1, \tag{2a}$$

$$y' = \alpha_2 x + \beta_2 y + \gamma_2, \tag{2b}$$

where $\alpha_1, \beta_1, \gamma_1$ and $\alpha_2, \beta_2, \gamma_2$ are unknown coefficients in these linear relations. On the other hand, to design an invisibility cloak for the triangular bump in a 2D geometry depicted in Fig. 1 (a), the point *N* as the vertex of a triangle shaped cloak should be located in an area with possibility triangle side vertices connection by using straight lines without crossing the ΔAMB sides. In other words, we are searching for a point above the ground (X axis) in the exterior area of ΔAMB with possibility to simultaneously connect it with straight lines to side vertices *A* and *B* with no crossing of $\overline{AM}$ and $\overline{BM}$ sides. Obviously, such area is located above the extensions of two sides $\overline{AM}$ and $\overline{BM}$ which is shaded in Fig. 1 (a).

Figure 1 (b) shows the cross section of the triangular bump (ΔAMB) and the ground invisibility cloak consist of two triangular parts, ΔANM and ΔBNM, which are created by finding the suitable region to locate the point *N* and connecting it to vertices of ΔAMB by using straight lines. As it is shown in this figure, the extension of $\overline{NM}$ crosses the line segment $\overline{BA}$ is considered as the coordinate system origin, *O*. Notice that the extensions of $\overline{AM}$ and $\overline{BM}$ sides (dot-dashed lines) are not suitable places for the point *N* to lie on, because it results in a zero area for at least one of the left or right parts of the cloak.

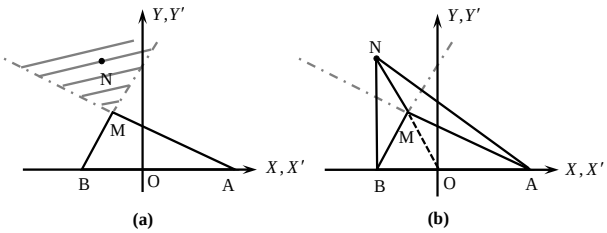

Fig. 1. A lateral view of the design process of an invisibility cloak for a triangular bump. (a) A triangular bump on the flat ground plane. The suitable area for the point *N* is dashed between dot-dashed extensions of the sides. (b) A 2D geometry of the triangular bump covered with a cloak, after choosing the place for *N*. The origin *O* is considered to be positioned at intersection of $\overline{NM}$ and $\overline{BA}$.

By considering of Fig. 1 (b), mapping of $\measuredangle OAN$ vertices, $A(x_A, y_A)$, $N(x_N, y_N)$ and $O(x_O, y_O)$ in the virtual space into ΔMAN vertices, $A(x'_A, y'_A)$, $N(x'_N, y'_N)$ and $M(x'_M, y'_N)$ in the real space, and substituting coordinates of the mentioned points in both spaces in Eqs. (2a) and (2b) result in six linear equations in terms of six unknown aforementioned coefficients. Having this in mind that points *A*, *N* and *B* should have the same coordinates in both virtual and real spaces. Therefore the coefficients associated with the right side part of the cloak (ΔANM) can be obtained as:

$$\alpha_1 = \frac{x_A - x_M}{x_A}, \quad \beta_1 = \frac{x_M (x_N - x_A)}{x_A y_N}, \quad \gamma_1 = x_M, \tag{3a}$$

$$\alpha_2 = -\frac{y_M}{x_A}, \beta_2 = \frac{x_A y_N + \{y_M (x_N - x_A)\}}{x_A y_N}, \gamma_2 = y_M. \tag{3b}$$

In a same way, mapping the ΔOBN vertices, $B(x_B, y_B)$, $N(x_N, y_N)$, and $O(x_O, y_O)$ in the virtual space into the ΔMBN vertices, $B(x'_B, y'_B)$, $N(x'_N, y'_N)$ and $M(x'_M, y'_M)$ in the real space result in the coefficients of linear Eqs. (2a) and (2b) correspond to the left side part of the cloak (ΔBNM) as:

$$\alpha_1 = \frac{x_B - x_M}{x_B}, \quad \beta_1 = \frac{x_M (x_N - x_B)}{x_B y_N}, \quad \gamma_1 = x_M, \quad (4a)$$

$$\alpha_2 = -\frac{y_M}{x_B}, \beta_2 = \frac{x_B y_N + \{y_M (x_N - x_B)\}}{x_B y_N}, \gamma_2 = y_M \quad (4b)$$

Substituting coefficients of the linear equations (Eqs. 2) with obtained values from Eq. (3) and Eq. (4), results in design of two individually homogeneous media for the right and left side parts of the cloak.

The finite element method (FEM) simulations performed with COMSOL Multiphysics software are used to validate the proposed approach. As shown in Fig. 2, a triangular PEC bump with 0.25 m height and 0.5 m long base, covered with a 0.7 m height triangular invisible cloak is designed and simulated. The working frequency is set as 2 GHz and the simulations are performed under TE polarization of a Gaussian beam incident incoming from left with 45° azimuth angle. The direction of E_Z the only component of the electric field depicted in the simulation results is normal to the 2D geometry plane of the problem. Figure 2 (a) illustrates the electric field distribution by the illumination of a perfect reflective flat ground plane with a TE-polarized Gaussian beam electromagnetic wave. Figure 2 (b) demonstrates the response of a triangular perfect electric conductor (PEC) bump lied on the ground to the Gaussian beam incidence. The protrusion of the ground surface performs some irregular scattering in the electric field such that the triangular PEC bump is detectable. Figures 2 (c) and 2 (d) show the performance of ground plane invisible cloak designed by the proposed approach. The electric field distribution of the TE-polarized Gaussian beam on the structure in Figs. 2 (c) and 2 (d) shows that the triangular bump covered with the designed invisible cloaks mimics the response of a flat PEC ground plane. Therefore the designed invisible cloak performs the triangular PEC bump perfectly undetectable. Normalized average scattering power outflows corresponding to Figs. 2 (a)-(d), have been illustrated in Fig. 2 (e), which are in good agreement with the simulations ones.

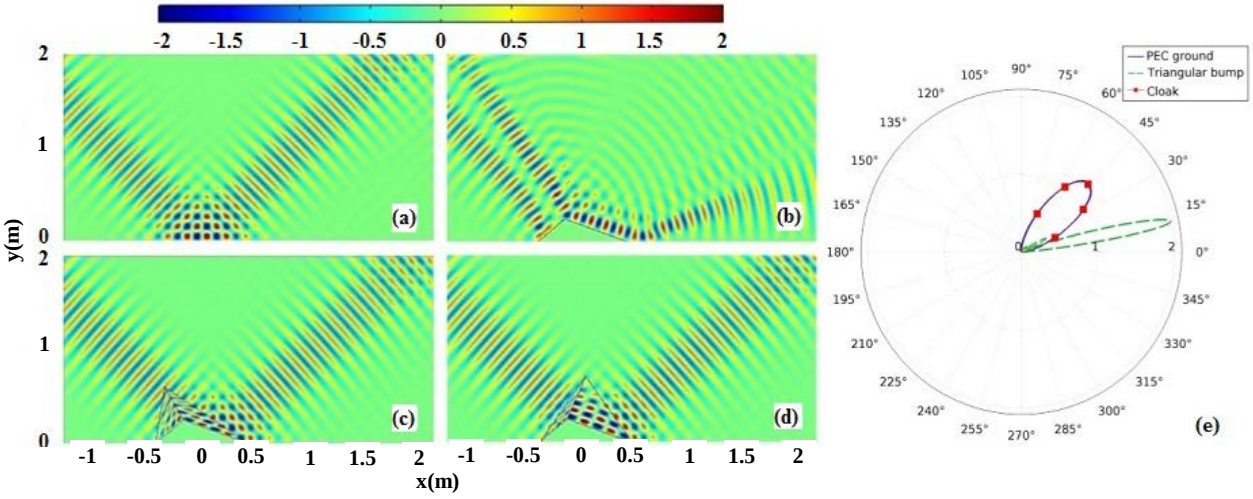

Fig. 2. The electric field distribution of a TE-polarized Gaussian beam incident from the left with *45°* azimuth angle on: (a) flat PEC ground plane, (b) triangular PEC bump with *0.25 m* height and *0.5 m* base, (c) and (d) *0.5 m* height designed cloaks for the triangular bump depicted in Fig. 2 (b), (e) Normalized average power outflows corresponding to Figs. 2 (a)-(d).

As it was mentioned previously, the proposed triangular ground cloak consists of two parts which are homogeneous. Figure 3 represents the constitutive parameters corresponding to the proposed cloak in Fig. 2 (c). Notice that choosing different places for point *N* results in different values for constitutive parameters which can create some options in the realization of the constitutive parameters. The components of the relative permittivity tensor possess a range of -0.85~3.57. It should be noted that ε_{yx} is equal to ε_{xy}, and by considering the 2D geometry of the problem, the rest of the components (ε_{xz} and ε_{yz}) are equal to zero.

According to Fig. 4 (a), choosing the point *N* to lie

on a vertical straight line which crosses the vertex *M* ($x_N = x_M$), results in a set of simpler relations for α, β and γ coefficients for both cloak parts. By connecting vertices *B* and *A* to *N* with $\overline{BN}$ and $\overline{AN}$ line segments, and mapping the points *o*, *A* and *B* into *M*, *A* and *B*, the design process can be simplified as below for the right side part of the cloak:

$$\alpha_1 = 1, \qquad \beta_1 = 0, \qquad \gamma_1 = 0, \quad (5a)$$

$$\alpha_2 = -\frac{y_M}{x_A}, \qquad \beta_2 = \frac{y_N - y_M}{y_N}, \qquad \gamma_2 = y_M. \quad (5b)$$

Also, all coefficients except α_2 can be calculated by using these equations for the left side part of the cloak while α_2 for this side is:

$$\alpha_2 = -\frac{y_M}{x_B}. \quad (6)$$

As is represented in Fig. 4 (b), the triangular PEC bump depicted in Fig. 2 covered with a triangular invisibility cloak designed by using this simplifying assumption, is ideally hided from the incidence of the Gaussian beam of TE-polarized electric field. Although various positions for the point *N* can be chosen, here *N* is placed at (0, 0.7). As an inherent part of this approach, both left and right side parts of this cloak have homogeneous constitutive parameters which are very important to facilitate the realization process.

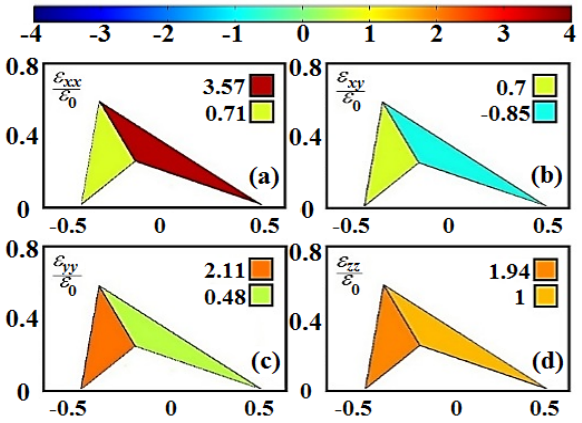

Fig. 3. The relative permittivity tensor components corresponding to the left and right side parts of the designed invisible cloak depicted in Fig. 2 (c).

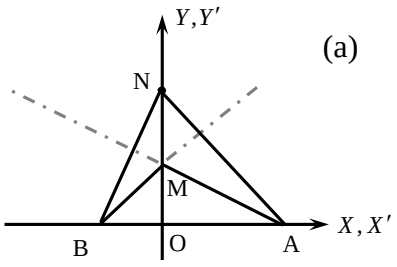

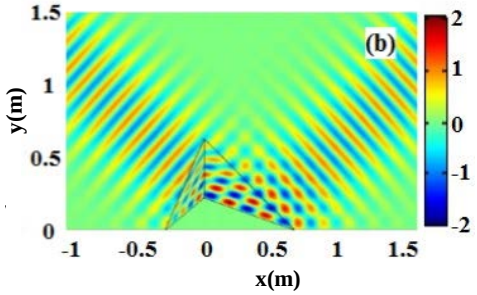

Fig. 4. A lateral view of the invisibility cloak designing procedure corresponding to the particular case in which $x_N = x_M$. (a) 2D design of triangular bump covered with the ground cloak of simpler designing relations. (b) Electric field distribution of a TE-polarized Gaussian beam incident incoming from left at an azimuth angle of *45°* on the cloaked bump at the frequency of 2 GHz.

III. HOMOGENEOUS CLOCK OF ARBITRARY SHAPE

Arbitrary shaped polygonal ground cloaks can be designed by using the proposed approach. For this purpose, the cloak is considered as a set of incomplete triangular segments as shown in Fig. 5. In this figure, a geometric lateral view of the ground cloak designing process is presented for an arbitrary polygonal shaped bump. The presented approach in the previous section can be used to design the segments of the arbitrary polygonal cloak, separately. In this way, a complete triangular cloak is considered in each segment, such that point *N* is laid on the *y* axis and $\overline{AB'C'D'E}$ path remains continuous.

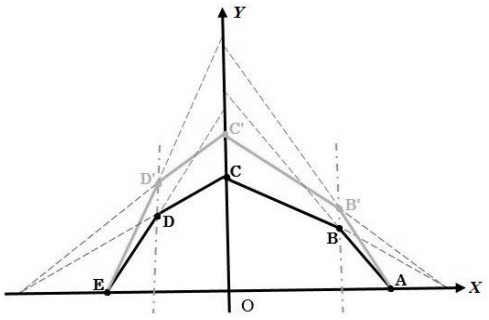

Fig. 5. A lateral view corresponding to design process of an arbitrary shaped polygonal ground plane cloak.

As an example of the cloak design for an arbitrary shaped polygonal bump, we present a 2D ground invisible cloak that its contour is very similar to lateral cross section of a car lied on a flat PEC ground surface in a free space background as shown in Fig. 6 (b). The cross section of the schematic car with 1.5 *m* length and 0.5 *m* height with outer PEC surface is illuminated by an

oblique Gaussian beam which caused irregular wave scattering compared with the PEC ground plane as a highly reflective surface in Fig. 6 (a). The FEM simulation results depicted in Figs. 6 (c) and (d) verify that the designed ground cloak perfectly mimics the response of a flat ground plane to the incident wave at two arbitrary frequencies, 2 and 5 GHz, and the car is undetectable, consequently. It should be mentioned that this schematic car designed invisible cloak is consisted of homogeneous parts.

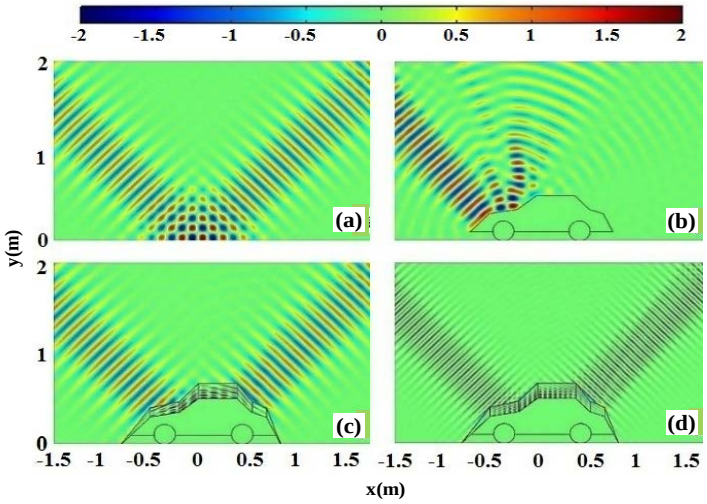

Fig. 6. The electric field distribution of a Gaussian beam incident under TE-polarization incoming from left at an azimuth angle of *45*° on: (a) flat PEC ground plane, (b) contour cross section of a schematic car (0.5 m height and 1.5 m length) with the PEC outer surface, (c) and (d) the 2D designed ground invisibility cloak for the schematic car contour of Fig. 6 (b), at 2 GHz and 5 GHz, respectively.

IV. CONCLUSION

A general approach was introduced to design arbitrary shaped invisible cloaks. By considering the problem geometry, coefficients of a linear system transformation which describes the relations between the real and virtual spaces were obtained. By using this method, the different triangular shape homogeneous cloaks for a triangular bump can be designed. By employing the mentioned relations and using the homogeneous triangular cloak segments, a homogeneous polygonal arbitrary shaped cloak has been achieved. As an example, a 2D homogeneous ground plane invisible cloak for an object where its contour is very close to the cross section of a car was designed and simulated. The FEM simulation results verify that when an oblique Gaussian beam illuminates the cloaked car, it mimics the response of a flat ground plane perfectly and renders the car undetectable, consequently.

REFERENCES

[1] N. Landy and D. R. Smith, "A full-parameter unidirectional metamaterial cloak for microwaves," *Nature Materials*, vol. 12, no. 1, pp. 25-28, 2013.

[2] J. S. McGuirk, P. J. Collins, M. J. Havrilla, and A. W. Wood, "A Green's function approach to calculate scattering width for cylindrical cloaks," *ACES Journal*, vol. 25, no. 2, February 2010.

[3] A. Shahzad, S. Ahmed, A. Ghaffar, and Q. A. Naqvi, "Incorporation of the Nihility medium to improve the cylindrical invisibility cloak," *ACES Journal*, vol. 29, no. 1, January 2014.

[4] Y. Shi, W. Tang, and C.-H. Liang, "A minimized invisibility complementary cloak with a composite Shape," *IEEE Antennas and Wireless Propagation Letters*, vol. 13, pp. 1800-1803, 2014.

[5] N. Landy and D. R. Smith, "A full-parameter unidirectional metamaterial cloak for microwaves," *Nature Materials*, vol. 12, no. 1, pp. 25-28, 2013.

[6] X. Zhu, et al., "One-way invisible cloak using parity-time symmetric transformation optics," *Optics Letters*, vol. 38, no. 15, pp. 2821-2824, 2013.

[7] L. Xu and H. Chen, "Conformal transformation optics," *Nature Photonics*, vol. 9, no. 1, pp. 15-23, 2015.

[8] H. Chen, C. Chan, and P. Sheng, "Transformation optics and metamaterials," *Nature Materials*, vol. 9, pp. 387-396, 2010.

[9] H. Ma, W. Jiang, X. Yang, X. Zhou, and T. Cui, "Compact-sized and broadband carpet cloak and free-space cloak," *Optics Express*, vol. 17, p. 19947, 2009.

[10] J. Li and J. Pendry, "Hiding under the carpet: A new strategy for cloaking," *Physical Review Letters*, vol. 101, p. 203901, 2008.

[11] R. Liu, C. Ji, J. Mock, J. Chin, T. Cui, and D. Smith, "Broadband ground-plane cloak," *Science*, vol. 323, pp. 366-369, 2009.
[12] W. Shen-Yun and L. Shao-Bin, "Simplified triangular ground plane cloak by oblique multilayer dielectrics," *Chinese Physics B*, vol. 21, p. 044102, 2012.
[13] X. Xu, Y. Feng, S. Xiong, J. Fan, J.-M. Zhao, and T. Jiang, "Broad band invisibility cloak made of normal dielectric multilayer," *Applied Physics Letters*, vol. 99, p. 154104, 2011.
[14] N. Wang, Y. Ma, R. Huang, and C. Ong, "Far field free-space measurement of three dimensional hole–in–Teflon invisibility cloak," *Optics Express*, vol. 21, pp. 5941-5948, 2013.
[15] L. Zigoneanu, B.-I. Popa, and S. A. Cummer, "Three-dimensional broadband omnidirectional acoustic ground cloak," *Nat. Mater*., vol. 13, pp. 352-355, 2014.
[16] Y. Ma, Y. Liu, L. Lan, T. Wu, W. Jiang, C. Ong, et al., "First experimental demonstration of an isotropic electromagnetic cloak with strict conformal mapping," *Scientific Reports*, vol. 3, pp. 2182-2182, 2012.
[17] N. Wang, M. Mukhtar, Y. Ma, R. Huang, and C. Ong, "Homogeneous anisotropic dielectric invisibility carpet cloak made of Al2O3 plates," *EPL (Europhysics Letters)*, vol. 104, p. 14003, 2013.
[18] M. Gharghi, C. Gladden, T. Zentgraf, Y. Liu, X. Yin, J. Valentine, et al., "A carpet cloak for visible light," *Nano Letters*, vol. 11, pp. 2825-2828, 2011.
[19] J. Valentine, J. Li, T. Zentgraf, G. Bartal, and X. Zhang, "An optical cloak made of dielectrics," *Nature Materials*, vol. 8, pp. 568-571, 2009.
[20] S. Xi, H. Chen, B.-I. Wu, and J. A. Kong, "One-directional perfect cloak created with homogeneous material," *IEEE Microwave and Wireless Components Letters*, vol. 19, pp. 131-133, 2009.
[21] T. Han and C.-W. Qiu, "Isotropic nonmagnetic flat cloaks degenerated from homogeneous anisotropic trapeziform cloaks," *Opt. Express*, vol. 18, pp. 13038-13043, 2010.
[22] B. Zhang, Y. Luo, X. Liu, and G. Barbastathis, "Macroscopic invisibility cloak for visible light," *Physical Review Letters*, vol. 106, p. 033901, 2011.
[23] X. Chen, Y. Luo, J. Zhang, K. Jiang, J. B. Pendry, and S. Zhang, "Macroscopic invisibility cloaking of visible light," *Nature Communications*, 2, 176, 2011.
[24] S. H. Sedighy and M. Khalaj-Amirhosseini, "Effect of optical transformation order on design of arbitrary polygonal invisible cloak," JOSA A, vol. 29, pp. 2638-2642, 2012.
[25] J. Hu, X. Zhou, and G. Hu, "Design method for electromagnetic cloak with arbitrary shapes based on Laplace's equation," *Optics Express*, vol. 17, pp. 1308-1320, 2009.
[26] S. Hasan Sedighy and M. Khalaj-Amirhosseini, "Arbitrary n-sided irregular polygonal electromagnetic transformed media," JOSA A, vol. 29, pp. 1549-1555, 2012.
[27] J. Zhang, Y. Luo, H. Chen, and B.-I. Wu, "Cloak of arbitrary shape," JOSA B, vol. 25, pp. 1776-1779, 2008.
[28] J. Hu, X. Zhou, and G. Hu, "Nonsingular two dimensional cloak of arbitrary shape," *Applied Physics Letters*, vol. 95, p. 011107, 2009.

Mohamad Fazeli received the M.Sc. degree in Electrical Engineering, at Shahed University, Tehran, Iran, in 2014. His current research areas of interest include EM theory, EM wave propagation and scattering in complex media and NRI metamaterials.

Seyed Hassan Sedighy was born in Qaen, South Khorasan, Iran, in 1983. He received his B.Sc., M.Sc. and Ph.D. degrees all in Electrical Engineering from Iran University of Science and Technology (IUST), in 2006, 2008 and 2013, respectively. From December 2011 to July 2012, he was with the University of California, Irvine as a Visiting Scholar. He joined the School of New Technologies at IUST, as an Assistant Professor in 2013.

Hamid Reza Hassani was born in Tehran, Iran. He received his B.Sc. in Communication Engineering from Queen Mary College of London in 1984, the M.Sc. degree in Microwave and Modern Optics from University College London in 1985, and the Ph.D. degree in Electrical Engineering from University of Essex, UK, in 1990. In 1991, he joined the Department of Electrical Engineering, Shahed University, Tehran, Iran, where he is currently a Professor.

Efficient Analysis of Object with Fine Structures by Combined MLSSM/MLFMA via Compressed Block Decomposition Preconditioner

Zhao N. Jiang [1,3], Fei Shen [1], Yuan Xu [2], and Xiao Y. Yang [1]

[1] Department of Information Engineering
Hefei University of Technology, Hefei, 230009, China
jiangzhaoneng@hfut.edu.cn

[2] Department of Applied Mathematics
Nanjing University of Science and Technology, Nanjing, 210094, China
xuyuan650708@hotmail.com

[3] State Key Laboratory of Millimeter Waves, Nanjing, 210096, China

Abstract ─ A large dense fine mesh is used to model object with fine structures to guarantee good solution accuracy, and this in turn places an inordinately heavy burden on the CPU in terms of both memory requirement and computational complexity. To analyze the large dense complex linear system efficiently, the combined MLSSM/MLFMA is used to accelerate the matrix-vector multiplication. Multilevel fast multipole algorithm (MLFMA) cannot be used to analyze the box's size of tree structure below 0.2 wavelength, because the "low frequency breakdown" phenomenon would happen. For the large-scale problems, the matrix assembly time of multilevel simply sparse method (MLSSM) is much longer than that of MLFMA. This combined method takes advantage of the virtues of both MLFMA and MLSSM, which is more efficient than either conventional MLFMA or conventional MLSSM. An efficient preconditioning technique based on compressed block decomposition (CBD) is applied to speed up the convergence rate. Numerical results are presented to demonstrate the accuracy and efficiency of the proposed method.

Index Terms ─ Compressed Block Decomposition (CBD) preconditioner, Multilevel Simply Sparse Method (MLSSM), object with fine structures.

I. INTRODUCTION

The increased power and availability of computational resources and acceleration schemes have enabled solution of problems with very large number of unknowns, varying from few thousands to few millions [1]. Another class of problems arises when analyzing structures which require a high local density of unknowns to accurately capture geometric features. This class of problems is referred to as object with fine structures problems exhibit multiple scales in length. For example, small length scale discretizations are required to capture sharp or fine geometric features that are embedded within large and smooth geometries discretized at a coarser length scale. Generally, the characteristic of an object with fine structures problem is the concentration of large number of unknowns in electrically small domains. All these simulations require fast and efficient numerical methods to compute an approximate solution of Maxwell's equations. Numerous authors have derived a variety of methods that are used for computing the electromagnetic problems. The method of moments (MoM) [2-4] is one of the most widely used techniques for electromagnetic problems. However, for large-scale problems, a great number of unknowns are required for modeling objects, which always leads to intensive computation and unaffordable CPU time.

The fast algorithms are developed to reduce computational cost. The most popular fast solution include the multilevel fast multipole algorithm (MLFMA) [5-6], has $O(N\log N)$ (where N denotes the number of unknowns) complexity for a given accuracy. Though efficient and accurate, this algorithm is highly technical. It utilizes a large number of tools, such as partial wave expansion, exponential expansion, filtering, and interpolation of spherical harmonics. However, MLFMA becomes numerically unstable and inefficient when applied to object with fine structures problems. This is a consequence of the fact that Helmholtz MLFMA does not smoothly transition to Laplace MLFMA as frequency tends to zero. Therefore, when the finest level box's size is below 0.2λ (λ indicates the incident wavelength), MLFMA will suffer from "low frequency breakdown" phenomenon [1]. As a result, it cannot be easily applied to analyze the object with fine structures problems.

Submitted On: September 4, 2015
Accepted On: September 9, 2016

In recent years, the matrix decomposition technique has been introduced to analyze the electromagnetic problems, which exploits the well-known fact that for well separated sub-scatterers, the corresponding sub-matrices are low rank and can be compressed [7-8]. In contrast with MLFMA, it is purely algebraic and can be easily interfaced to existing MOM codes. MLSSM is a popular matrix decomposition technique, which has been successfully applied in [9-14] to electromagnetic problems. It has no limit of the box's size and has a memory requirement of $O(N)$ and computational complexity is proportional to $O(N\log N)$. However, for the large-scale problems, the matrix filling time of MLSSM is much longer than that of MLFMA.

In this paper, a hybrid method called combined MLSSM/MLFMA is proposed, which uses the main framework of MLFMA but adopts the MLSSM to deal with the box's size is below 0.2λ. This method takes advantage of both MLFMA and MLSSM and is more efficient than either conventional MLFMA or conventional MLSSM for analyzing the multi-scale problems. For the object with fine structures problems, the matrix condition number is very large due to the mixed discretization. Therefore, the system has poor convergence history and requires urgently a good solver or preconditioner. In this paper, an efficient preconditioning technique based on CBD algorithm [15-17] is applied to improve the property of electric field integral equation (EFIE) formulation.

II. MLSSM ALGORITHM

The impedance matrix filled by MLSSM is carried out based on the same multilevel spatial decomposition of MLFMA. The single level of SSM is presented in [18] and the MLSSM is shown in [9-14]. The structure of the MLSSM representation is given in a multilevel recursion manner [9-14]:

$$Z_l = \hat{Z}_l + U_l Z_{l-1} V_l^H , \tag{1}$$

where Z_l is the reduced order impedance matrix and consists of only far interactions at level l+1, which will be compressed in the coarser levels recursively up to level-3. There is no level L+1 near interactions at the finest level L (where L denotes the number of the levels). Thus, Z_L is the impedance matrix Z. In (1), $\hat{Z}_l$ is the sparse matrix containing all near-neighbor interactions at level l of the oct-tree which were not represented at finer level of the oct-tree. U_l and V_l are the new basis and testing function matrices, respectively, which are block diagonal unitary matrices that compress interaction between sources in non-touching groups at level l. The following is the procedure in details. Suppose that the object is decomposed in 4-level oct-tree, the impedance matrix can be expressed as:

$$Z = \hat{Z}_4 + Z_4^{far} = \hat{Z}_4 + U_4 Z_3 V_4^H , \tag{2}$$

where

$$Z_3 = \hat{Z}_3 + Z_3^{far} = \hat{Z}_3 + U_3 Z_2 V_3^H . \tag{3}$$

The forms of matrices U_l, Z_{l-1} and V_l^H are shown in Figs. 1 and 2 at levels 4 and 3, respectively.

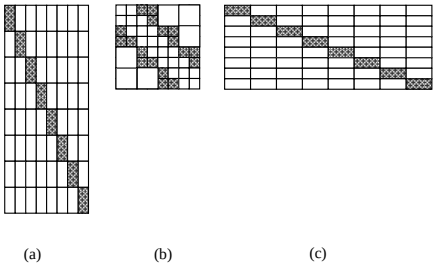

Fig. 1. Level 4 SSM matrices: (a): U_4, (b): $\hat{Z}_3$, and (c): V_4^H.

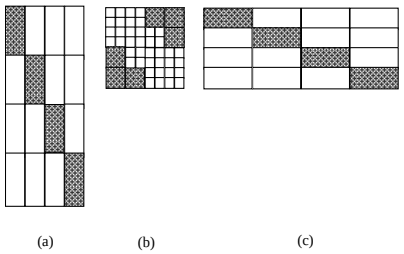

Fig. 2. Level 3 SSM matrices: (a): U_3, (b): $\hat{Z}_2$, and (c): V_3^H.

The major requirements of the MLSSM memory is to store the matrices $\hat{Z}_l$, U_l, and V_l^H at all levels. The matrix-vector multiplication of MLSSM is very similar to MLFMA in manner, which has $O(N\log N)$ complexity for a given accuracy.

III. COMBINED MLSSM/MLFMA ALGORITHM

A. MLSSM/MLFMA algorithm

MLFMA [5-6] has been widely used to solve the electromagnetic scattering of complex object with the surface integral equation approach. When it is applied to analyze the scattering from the multi-scale objects where dense discretization is necessary to capture geometric features accurately, the memory usage of MLFMA is very large. It is because of that the box's size of tree structure cannot be set to less than 0.2λ, the number of unknowns in the near-field boxes is very large. The near-field matrices of MLFMA is filled by direct method. Therefore, the near-field of MLFMA needs large memory requirement for large-scale problems.

In this section, a hybrid method called combined MLSSM/MLFMA algorithm is proposed, which uses the

main framework of MLFMA. The framework of the hybrid method is shown in the Fig. 3, the box's sizes below the dotted line are less than 0.2λ and are filled by MLSSM algorithm, the box's sizes up the dotted line are larger than 0.2λ and are filled by MLFMA.

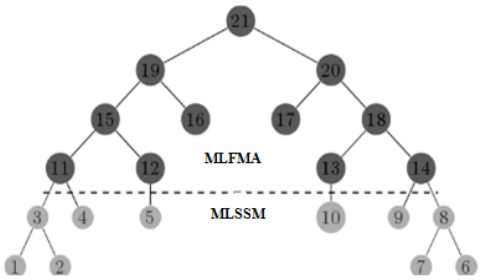

Fig. 3. The framework of combined MLSSM/MLFMA algorithm.

Using the combined MLSSM/MLFMA for filling the impedance matrix *Z*, a fast matrix-vector production algorithm (MVP) can be obtained as follows:
Subroutine MVP,
(1) The direct MVP algorithm is used to the near interaction impedance matrix;
Begin $l = L:3:-1$,
(2) From $l = L : L_{\mathrm{MLFMA}}+1$,
MLSSM is applied to speed up MVP;
End.
(3) From $l = L_{\mathrm{MLFMA}}: 3$,
MLFMA is used to speed up MVP;
End.
End.

This new method takes advantages of the virtues of both MLFMA and MLSSM, which uses MLFMA to reduce the matrix assembly time of MLSSM and utilizes MLSSM to alleviate the near-field pressure of MLFMA. The efficiency of the method is demonstrated by the numerical results.

B. CBD preconditioner

In order to accelerate the convergence rate of the Krylov iteration, the linear system is transformed into an equivalent one:

$$[M][Z][I]=[M][V], \tag{4}$$

where $[M]$ referred as the preconditioner for the impedance matrix $[Z]$. The product matrix $[M][Z]$ has much better spectral property than original matrix $[Z]$, which leads to a greatly reduced number of iterations. Since the sparse near-field matrix is the best available approximation to the coefficient matrix $[Z]$, it makes sense to use near-field matrix to construct a preconditioner. In this paper, an efficient CBD preconditioner [19] is applied to form the matrix $[M]$.

IV. NUMERICAL RESULTS

In this section, a number of numerical examples are presented to demonstrate the efficiency of the proposed method for analyzing the object with fine structures. All the computations are carried out on a Core-i5 3350P with 3.1 GHz CPU and 4GB RAM in single precision and the MLSSM truncating tolerance is 10^{-3} relative to the largest singular value. In the implementation of the combined MLSSM/MLFMA algorithm, the restarted version of GMRES algorithm [20] is used as the iterative method. The iteration process is terminated when the normalized backward error is reduced by 10^{-3} for all examples.

A. A metal helicopter model

A metal helicopter model with many fine structures is considered in the first example in Fig. 4, which needs large number of unknowns to accurately capture fine structures of the helicopter model. The dimension of the structure is $20.48\,m\times12.37\,m\times6.2\,m$. The incident and scattered angles are $(\theta_i=0^\circ,\phi_i=0^\circ)$ and $(0^\circ\le\phi_s\le180^\circ,\theta_s=0^\circ)$, respectively. The maximum dimension of the structure is 10.24λ at 150 MHz and the number of unknowns is 74913. The number of the octrees for the combined MLSSM/MLFMA algorithm is $L = 5$, and $L = 4$ for the MLFMA. The finest level box's sizes of combined MLSSM/MLFMA algorithm and MLFMA are 0.16λ and 0.32λ, respectively. The bistatic RCS of the proposed method is shown in Fig. 5, and is agreed well with that of FEKO. Table 1 shows the memory storages and the MVP times of the MLSSM/MLFMA and MLFMA. "MVP time" in the table indicates the time of one matrix-vector production. The near-field memory of MLSSM/MLFMA is much less than that of MLFMA, while the total memory consumption of MLSSM/MLFMA is half less than that of MLFMA. The MVP time of MLSSM/MLFMA is also much less than that of MLFMA. The convergence history curves of the MLSSM/MLFMA solved with CBD preconditioner are shown in Fig. 6. It can be found that the proposed method has a much better convergence properties by using the CBD preconditioner.

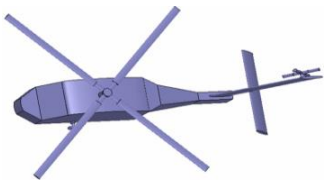

Fig. 4. The configuration of the metal helicopter model.

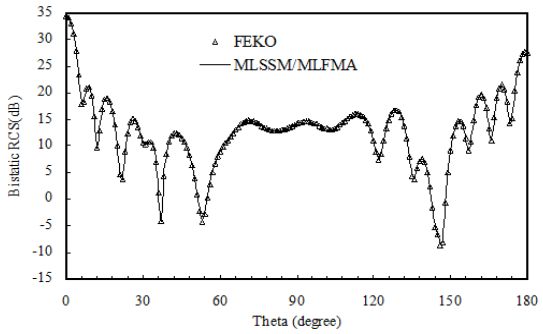

Fig. 5. Bistatic scattering cross section of metal helicopter model.

Table 1: The memory requirements and the MVP times of the proposed method for the metal helicopter model

Algorithms	Near-Field (MB)	Total (MB)	MVP Time (s)
MLFMA	1097	1209	6.07
MLSSM/MLFMA	273	465	2.96

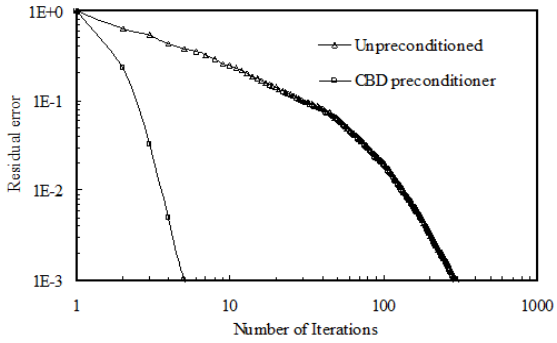

Fig. 6. Convergence histories of the MLSSM/MLFMA solved with CBD preconditioner.

B. A metal missile model

The second multi-scale example is a complex metal missile structure and is analyzed shown in Fig. 7. The dimension of the structure is $6\,m \times 2.56\,m \times 1.32\,m$. The incident and scattered angles are $(\theta_i = 0^\circ, \phi_i = 0^\circ)$ and $(0^\circ \le \phi_s \le 180^\circ, \theta_s = 0^\circ)$, respectively. The maximum dimension of the structure is 6λ at 300 MHz and the number of unknowns is 67420. The number of the octrees for the MLSSM/MLFMA algorithm is L = 4, and L = 3 for the MLFMA. The finest level box's sizes of combined MLSSM/MLFMA algorithm and MLFMA are 0.18λ and 0.37λ, respectively. The bistatic RCS of the metal missile structure is analyzed by the proposed method shown in Fig. 8. It can be observed that the result of the proposed method is agreed well with that of FEKO. The efficiency of the proposed method is analyzed in this example shown in Table 2. It can be found that the memory storage and the MVP time of the MLSSM/MLFMA are both much less than that of the conventional MLFMA. The convergence rate of the CBD preconditioner is shown in Fig. 9. It can be found that the CBD preconditioner is much more efficient than the unpreconditioned GMRES algorithm.

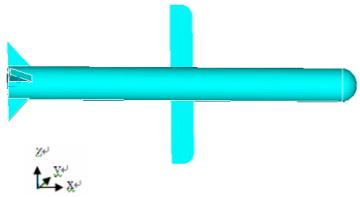

Fig. 7. The configuration of the metal missile model.

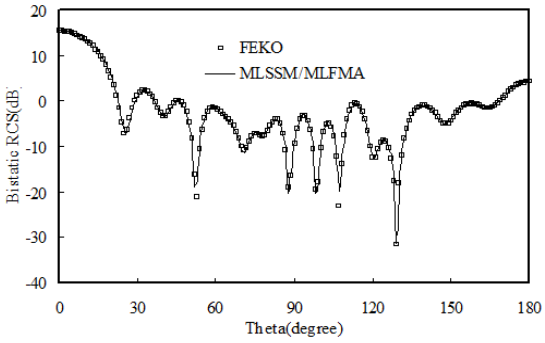

Fig. 8. Bistatic scattering cross section of metal missile model.

Table 2: The memory requirements and the MVP times of the proposed method for the metal missile model

Algorithms	Near-Field (MB)	Total (MB)	MVP Time (s)
MLFMA	871	1045	4.52
MLSSM/MLFMA	209	362	1.67

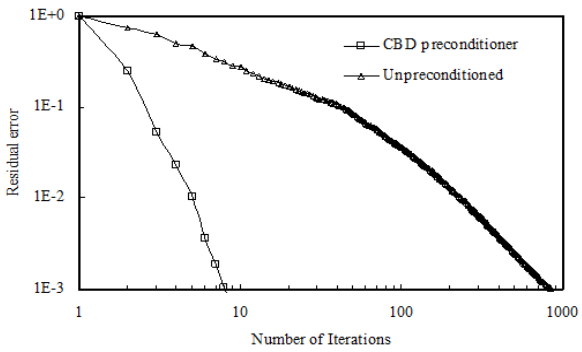

Fig. 9. Convergence histories of the MLSSM/MLFMA solved with CBD preconditioner.

VI. CONCLUSION

In this paper, a novel combined MLSSM/MLFMA algorithm is proposed to solve the electromagnetic scattering of object with fine structures. It takes advantage of the virtues of both MLFMA and MLSSM, which uses MLFMA to reduce the matrix assembly time of MLSSM and utilizes MLSSM to alleviate the near interaction pressure of MLFMA. Since compression of near interactions,the matrix-vector multiplication of MLSSM/ MLFMA is more efficient than that of MLFMA. The CBD preconditioner is used to further speed up the convergence. It can be found that MLSSM/MLFMA combined with CBD preconditioner is very efficient for analyzing the object with fine structures problems.

ACKNOWLEDGMENT

This work is sponsored by Natural Science Foundation of China (61501159), Open Research Program Foundation of State Key Laboratory of Millimeter Waves (K201602), Natural Science Foundation of Anhui Province (1608085MF124).

REFERENCES

[1] W. C. Chew, J. M. Jin, E. Michielssen, and J. Song, *Fast Efficient Algorithms in Computational Electromagnetics*. Boston, MA: Artech House, 2001.

[2] A. F. Peterson, "Accuracy of currents produced by the locally-corrected Nystrom method and the method of moments when used with higher-order representations," *ACES Journal*, vol. 17, no. 1, pp. 74-83, 2002.

[3] S. M. Rao, D. R. Wilton, and A. W. Glisson, "Electromagnetic scattering by surfaces of arbitrary shape," *IEEE Trans. Antennas Propagat.*, vol. AP-30, pp. 409-418, May 1982.

[4] D. Colak, R. J. Burkholder, and E. H. Newman, "On the convergence properties of the multiple sweep method of moments," *ACES Journal*, vol. 22, no. 2, pp. 207-218, 2007.

[5] R. Coifman, V. Rokhlin, and S. Wandzura, "The fast multipole method for the wave equation: A pedestrian prescription," *IEEE Antennas Propag. Mag.*, vol. 35, no. 6, pp. 7-12, June 1993.

[6] M. Vikram and B. Shanker,"An incomplete review of fast multipole methods–from static to wideband–as applied to problems in computational electromagnetics," *ACES Journal*, vol. 24, no. 2, pp. 79-108, 2009.

[7] Z. Jiang, R. Chen, Z. Fan, Y. An, M. Zhu, and K. W. Leung, "Modified adaptive cross approximation algorithm for analysis of electromagnetic problems," *ACES Journal*, vol. 26, no. 2, pp. 160-169, 2011.

[8] F. Canning and J. Shaeffer, "Adaptive cross approximation for MoM matrix fill for PC problem sizes to 157000 unknowns," *ACES International Conference on Wireless Communications & Applied Computational Electromagnetics*, pp. 748-753, 2005.

[9] A. Zhu, R. J. Adams, and F. X. Canning, "Modified simply sparse method for electromagnetic scattering by PEC," *in Proc. IEEE Antennas and Propagation Society Int. Symp*, Washington, DC, vol. 4, pp. 427-430, 2005.

[10] J. Cheng, S. A. Maloney, R. J. Adams, and F. X. Canning, "Efficient fill of a nested representation of the EFIE at low frequencies," *IEEE Antennas and Propagation Society Int. Symp*., pp. 1-4, 2008.

[11] R. J. Adams, A. Zhu, and F. X. Canning, "Sparse factorization of the TMz impedance matrix in an overlapped localizing basis," *Progress in Electromagnetics Research*, *PIER*, 61, pp. 291-322, 2006.

[12] Y. Xu, X. Xu, and R. J. Adams, "A sparse factorization for fast computation of localizing modes," *IEEE Trans. Antennas Propagat.*, vol. 58, no. 9, pp. 3044-3049, 2010.

[13] X. Xu, "Modular Fast Direct Analysis Using Non-Radiating Local-Global Solution Modes," *Ph.D. Dissertation*, Electrical and Computer Engineering, University of Kentucky, 2009.

[14] Z. Jiang, Y. Xu, R. Chen, Z. Fan, and D. Ding, "Efficient matrix filling of multilevel simply sparse method via multilevel fast multipole algorithm," *Radio Science*, 46, RS5011, doi:10.1029/2010RS 004549, 2011.

[15] A. Heldring, J. M. Rius, J. M. Tamayo, and J. Parron, "Compressed block-decomposition algorithm for fast capacitance extraction," *IEEE Transactions on Computer-Aided Design of Integrated Circuits and Systems*, vol. 27, no. 2, pp. 265-271, Feb. 2008.

[16] A. Heldring, J. M. Tamayo, J. M. Rius, J. Parron, and E. Ubeda, "Multiscale CBD for fast direct solution of MoM linear system," *IEEE Antennas & Propagation Society International Symposium*, pp. 1-4, 2008.

[17] A. Heldring, J. M. Rius, J. M. Tamayo, J. Parron, and E. Ubeda, "Fast direct solution of method of moments linear system," *IEEE Trans. Antennas Propag*, vol. 55, no. 11, pp. 3220-3228, Nov. 2007.

[18] F. X. Canning and K. Rogovin, "A universal matrix solver for integral equation-based problems," *IEEE Antennas Propag. Mag.*, vol. 45, pp. 19-26, 2003.

[19] Z. Jiang, R. Chen, Z. Fan, and Y. An, "Modified compressed block decomposition preconditioner for electromagnetic problems," *Microwave and Optical Technology Letters*, vol. 53, no. 8, pp. 1915-1919, Aug. 2011.

[20] Y. Saad, "Iterative methods for sparse linear system," *Studies in Computational Mathematics*, vol. 8, pp. 423-440, 2001.

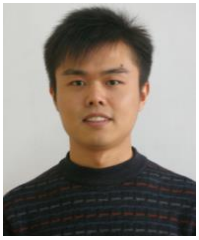

Zhao Neng Jiang received the B.S. degree in Physics from Huaiyin Normal College, Huaian, China, in 2007, and the Ph.D. degree in Electrical Engineering from Nanjing University of Science and Technology (NJUST), Nanjing, China, in 2013. He worked as a Teacher at the Hefei University of Technology, Hefei, China. His current research interests include computational electromagnetics, antennas and electromagnetic scattering and propagation, electromagnetic modeling of microwave integrated circuits.

Fei Shen received the Ph.D. degree from the University of Electronic Science and Technology of China (UESTC), Chengdu, China, in 2012. He worked as a Teacher at the Hefei University of Technology, Hefei, China. His current research interests include antennas, microwave & millimeter wave devices and techniques

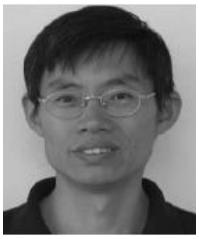

Yuan Xu received the B.S. and M.S. degrees in Mathematics from Suzhou University, Suzhou, China, in 1988 and 1991, respectively, and the Ph.D. degree in Electrical Engineering from Nanjing University of Science and Technology (NJUST), Nanjing, China, in 2001. He worked as a Postdoctoral Scholar at the University of Kentucky, Lexington, in 2006 and 2010. He is currently an Associated Professor with the Electronic Engineering Department, NJUST. His research interests include computational electromagnetics, integral equation methods, and the analysis of large-scale electromagnetics problems.

Xiao Yu Yang received the B.S. degree in Physics from Harbin Normal University, Harbin, China, in 2005, the M.S. degree in Physics from Northeast Normal University, Changchun, China, in 2008, and the Ph.D. degree in Physics from Harbin Institute of Technology, Harbin, China, in 2014. She worked as a Teacher at the Hefei University of Technology, Hefei, China. Her current research interests include properties and device of electromagnetic metamaterials.

Novel UWB Trapezoidal and Butterfly Shaped Microstrip Phase Shifters Using Multilayered PCB Technology

Osama M. Haraz [1] and Abdel-Razik Sebak [1,2]

[1] Electrical Engineering Department
Faculty of Engineering, Assiut University, Assiut 71516, Egypt
o_haraz@aun.edu.eg

[2] Department of Electrical and Computer Engineering
Concordia University, Montreal, Quebec H3G 1M8, Canada
abdo@ece.concordia.ca

Abstract ─ In this paper, design of two different aperture-coupled phase shifters for ultra-wideband (UWB) multilayer microwave circuits are introduced. The proposed phase shifters use broadside coupling between microstrip patches at the top and the bottom layers via a rectangular-shaped slot in the common ground plane (mid-layer). The proposed patch shapes are trapezoidal and butterfly shapes which are capable of achieving broadband characteristics for UWB operation. The reference transmission line is installed on the top layer. The numerical calculated results using two simulation programs using two different numerical techniques show that the proposed phase shifters have good phase characteristics with high return losses and good insertion losses over most of the 3.1–10.6 GHz frequency band. The phase characteristics for the proposed phase shifters can be easily controlled by proper adjusting the physical dimensions. Two 45° phase shifters prototypes are fabricated and then tested experimentally using Agilent E8364B PNA Network Analyzer. Experimental results are in good agreement with the calculated ones.

Index Terms ─ Beam-forming, microstrip phase shifters, microstrip printed circuit board (PCB) technology, multi-layer technology, ultra-wideband (UWB).

I. INTRODUCTION

There is a big need for phase shifters due to their consideration as important microwave devices widely used in different applications such as electronic beam scanning phased arrays, phase modulators, etc. Conventional phase shifters have narrowband characteristics and the phase changes linearly with increasing the frequency. For wideband applications, phase shifters should be implemented using printed circuit board (PCB) technology because of the non-dispersive characteristic and broadband propagation properties of microstrip PCB. The original Schiffman phase shifter [1] which is considered one of the early designs based on using sections of coupled-strip transmission lines operating in the transverse electromagnetic (TEM) mode and a reference transmission line. The constant broadband phase difference between these lines can be achieved by controlling the degree of coupling between lines and the length of those coupled lines. However, the bandwidth of the original Schiffman phase shifter does not cover the desired UWB frequency range. Recently, researchers have tried to improve the original Schiffman phase shifter to achieve the desired broadband phase response [2]-[6]. This can be achieved by using cascade of multiple coupled parallel transmission line sections connected to each other as in [4]. These designs have large size and some limitations in PCB manufacturing because of narrow gaps for tight coupling. Another approach is achieved by using dumb-bell-shaped phase shifter using multi-section stubs, but the bandwidth achieved does not cover the whole UWB frequency range [2]. In [3], an improved wideband Schiffman phase shifter is proposed by modifying the ground plane underneath the microstrip coupled lines to form a defected ground structure (DGS), while the achieved bandwidth is from 1 GHz to 3.5 GHz which is not enough for UWB operation. Another approach to design a broadband phase shifter in multi-layer PCB technology is achieved by using the multi-layer vertical elliptical transition and a microstrip reference line as in [5].

The problem with the conventional narrowband phase shifters that the phase changes linearly with the frequency. To design a broadband phase shifter where the phase is almost constant with frequency, we exploit the broadband characteristics of the designed trapezoidal and butterfly shaped transitions and the conventional transmission lines. In this paper, two aperture-coupled microstrip 45° phase shifters with different patch shapes

Submitted On: April 10, 2014
Accepted On:May 30, 2016

are presented. In the first design, the microstrip coupling patches have trapezoidal structure while the coupling slot has rectangular structure. The second proposed transition has butterfly shaped microstrip coupling patches with rectangular coupling slot. The trapezoidal-shaped UWB phase shifter is presented in Section II. In Section III, the design and results of the butterfly-shaped phase shifters are investigated and discussed. Finally, conclusions are given in Section IV.

II. TRAPEZOIDAL-SHAPED UWB PHASE SHIFTERS

A. Geometrical configuration

The configuration of the proposed trapezoidal shaped 45° microstrip phase shifter is shown in Fig. 1. It is simply consists of the designed trapezoidal shaped transition connected to port #1 and port #2. The reference transmission line is installed on the top layer between port #3 and port #4. By controlling the transition parameters (W_{p1}, W_{p2}, W_s, L_s) and the length of the reference transmission line l, the suitable phase shift can be achieved over the desired bandwidth. All proposed phase shifter designs are built using two RT Duroid 5880 substrates with thickness of 0.508 mm, relative permittivity of ε_r = 2.2 and loss tangent of $tan\delta$ = 0.0009. The overall dimensions of proposed phase shifters are 20 mm × 40 mm. The width of the microstrip feed line is set to be W_m = 1.3 mm for 50 Ω characteristic impedance.

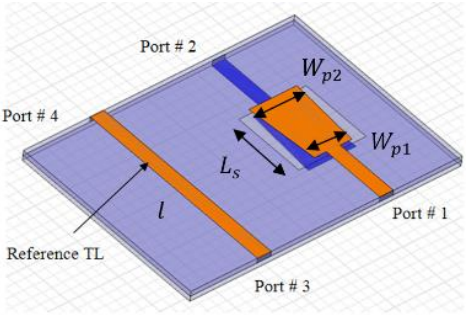

(a)

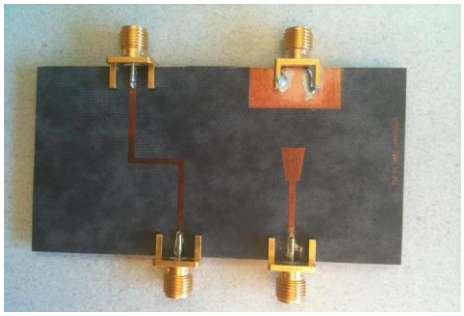

(b)

Fig. 1. Configuration of the proposed trapezoidal shaped UWB 45° phase shifter. (a) The whole structure and (b) photograph of fabricated phase shifter prototype.

B. Parametric study and design

Parametric studies have been carried out to address the effect of phase shifter physical parameters on the phase characteristics and the operational bandwidth but not shown here because of limited space.

C. Simulation and experimental results

Figure 2 shows the calculated phase shift $\angle S_{43} - \angle S_{21}$ for different phase shift values, i.e., 22.5°, 45° and 67.5° versus frequency.

It can be seen that the proposed phase shifters have good phase characteristic across the whole UWB frequency range. The achieved phases are 22.5°±5.5°, 45°±7° and 67.5°±6.5° through the desired UWB frequency band from 3.1 to 10.6 GHz. The optimized trapezoidal phase shifter parameters for different phase shift values of 22.5°, 45° and 67.5° are calculated numerically using simulations programs and tabulated in Table 1. The simulated and measured return and insertion losses for the 45° trapezoidal phase shifter are illustrated in Figs. 3 (a) & (b), respectively.

It can be seen that the simulated return and insertion losses are better than 10 dB and 1.2 dB in the 3.1-10.6 GHz band, respectively. There is a good agreement between both HFSS and CST simulation results. The measured return and insertion losses are good in the lower frequency band from 3.3 GHz to 9.6 GHz.

The phase difference ($\angle S_{43} - \angle S_{21}$) has been simulated and plotted in Fig. 4 (a). The simulated achieved phase difference is almost 45° with phase error of less than ±7° across the whole UWB frequency band. Also, the measured phases and phase difference between the ports (1, 2) and ports (3, 4) are shown in Fig. 4 (b). It can be noticed that phases are almost linear as a function of frequency and the measured phase difference achieved is varying around 45°, but it deteriorated at higher frequencies above 8.0 GHz.

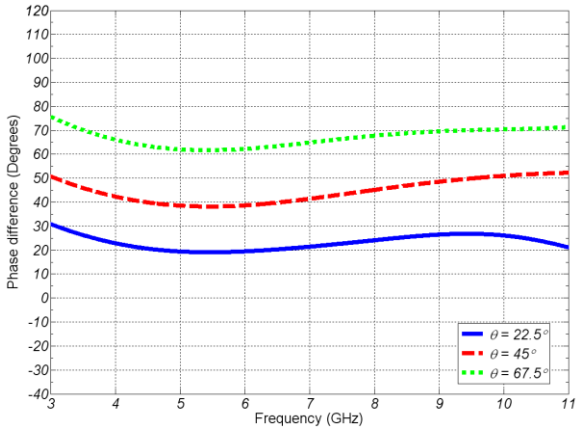

Fig. 2. Calculated phase shift $\angle S_{43} - \angle S_{21}$ of the trapezoidal phase shifter for different phase shift values, i.e., 22.5°, 45° and 67.5°.

Table 1: Parameters of the trapezoidal phase shifter for different phase shift values

Parameters (mm)	Phase Shift Values		
	22.5°	45°	67.5°
W_{p1}	5.2	3.7	2.0
W_{p2}	6.3	4.5	3.1
W_s	8.2	7.2	5.0
$L_s\ (=L_p)$	8.2	7.7	7.2
l	29.3	29.5	30.0

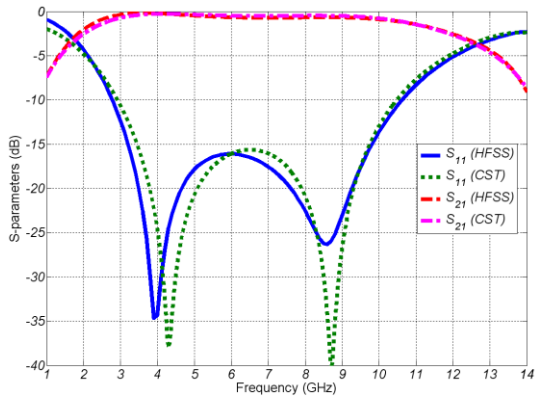

(a)

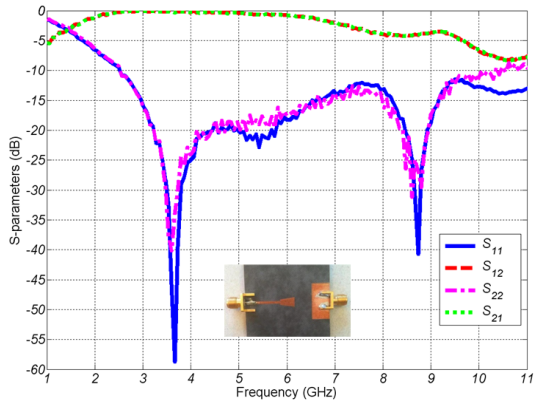

(b)

Fig. 3. (a) Simulated and (b) measured return and insertion losses of the proposed UWB 45° trapezoidal phase shifter.

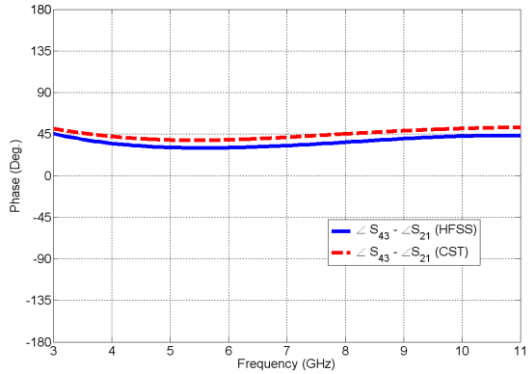

(a)

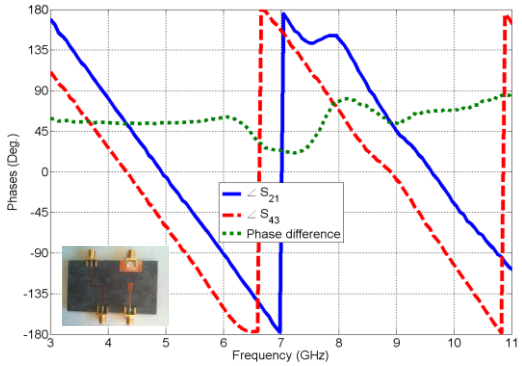

(b)

Fig. 4. (a) Simulated phase difference and (b) measured $\angle S_{21}$ & $\angle S_{43}$ phases and phase difference ($\angle S_{43} - \angle S_{21}$) of the proposed 45° trapezoidal phase shifter.

III. BUTTERFLY-SHAPED UWB PHASE SHIFTERS

A. Geometrical configuration

The configuration of the proposed butterfly shaped 45° microstrip phase shifter is shown in Fig. 5. It simply consists of the designed butterfly shaped transition connected to port #1 and port #2. The reference transmission line is installed on the top layer between port #3 and port #4. By controlling the transition parameters: radius R, angle θ, open-circuit stub length d, rectangular coupling slot width W_s, rectangular coupling slot length L_s and the length of the reference transmission line l, the suitable phase shift can be achieved over the desired bandwidth.

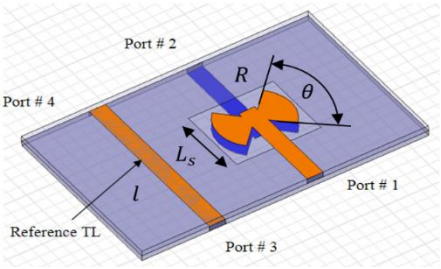

(a)

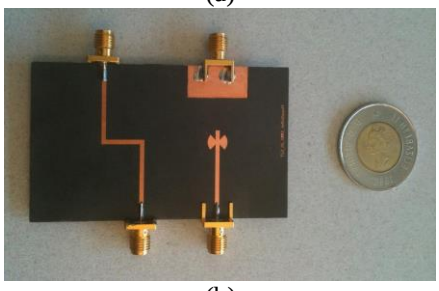

(b)

Fig. 5. Configuration of the proposed 45° phase shifter. (a) The whole structure and (b) photograph of fabricated phase shifter prototype.

B. Parametric study and design

Based on parametric studies, the optimized 45° butterfly phase shifter parameters are found to be: R = 2.2 mm, θ = 90°, d = 3.5 mm, W_s = 7.3 mm, L_s = 6.0 mm and l = 32 mm.

The calculated phase shift $\angle S_{43} - \angle S_{21}$ for different phase shift values, i.e., 22.5°, 45° and 67.5° versus frequency are shown in Fig. 6. It can be noticed that the proposed phase shifters have good phase characteristic across the whole UWB frequency range. The achieved phases are 22.5°±6°, 45°±9° and 67.5°±8.5° through the desired UWB frequency band from 3.1 to 10.6 GHz. The optimized parameters for the butterfly phase shifter for different phase values are calculated numerically using simulation programs and summarized in Table 2.

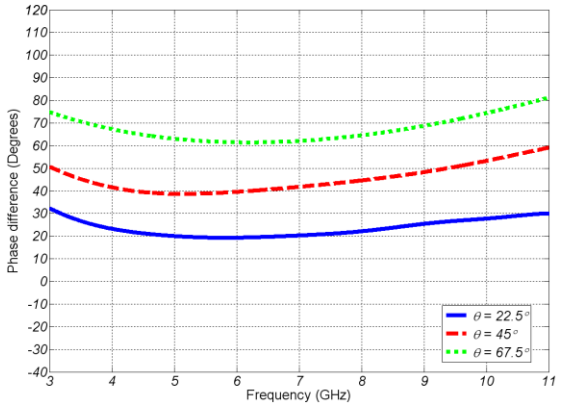

Fig. 6. The calculated phase shift $\angle S_{43} - \angle S_{21}$ of the butterfly phase shifter for different phase shift values, i.e., 22.5°, 45° and 67.5°.

Table 2: Parameters of the butterfly phase shifter for different phase shift values

Parameters	Phase Shift Values		
	22.5°	45°	67.5°
R (mm)	2.9	2.2	1.7
θ°	100°	90°	80°
d (mm)	3.7	3.5	3.0
W_s (mm)	8.5	7.3	5.3
L_s (mm)	6.2	6.0	5.0
l (mm)	33	32	31

C. Simulation and experimental results

The simulated return and insertion losses for the 45° butterfly phase shifter are illustrated in Fig. 7 (a). Because of the symmetry of the butterfly transition, only return loss at port #1 is shown, i.e., $S_{11} = S_{22}$. It can be seen that the return loss (S_{11}) using both Ansoft HFSS and CST Microwave Studio is better than 13 dB across the whole UWB band. The simulated insertion loss between port #1 and port #2 (S_{21}) is better than 0.8 dB in the 3.1-10.6 GHz band. There is a good agreement between HFSS and CST results.

The measured S-parameters for the butterfly phase shifter are also shown in Fig. 7 (b). The measured results show good return losses and insertion losses, especially at low frequencies; i.e., below 7 GHz. The discrepancies in measured results may be due to the misalignment between the two layers and any other fabrication errors.

The phase difference between ports (1, 2) and ports (3, 4) has been calculated and plotted in Fig. 8 (a). It can be noticed that the phase is almost linear as a function of frequency.

The achieved phase difference ($\angle S_{43} - \angle S_{21}$) is almost 45° with phase error of less than ±7° across the 7.5 GHz UWB frequency bandwidth from 3.1 to 10.6 GHz. The measured phases and phase difference between the ports (1, 2) and ports (3, 4) are shown in Fig. 8 (b). It can be seen that the measured phase difference achieved is varying around 45° but it deteriorated at higher frequencies after 8 GHz.

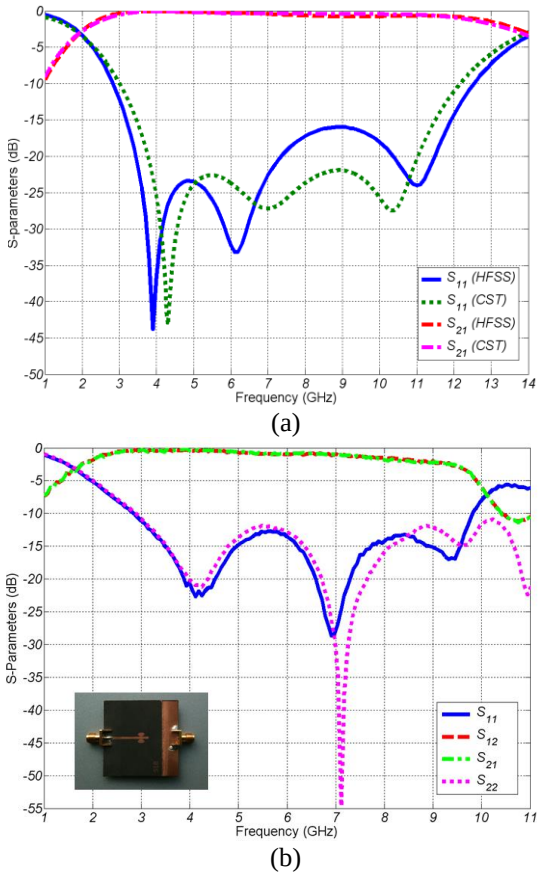

Fig. 7. (a) Simulated and (b) measured return and insertion losses of the proposed UWB 45° butterfly phase shifter.

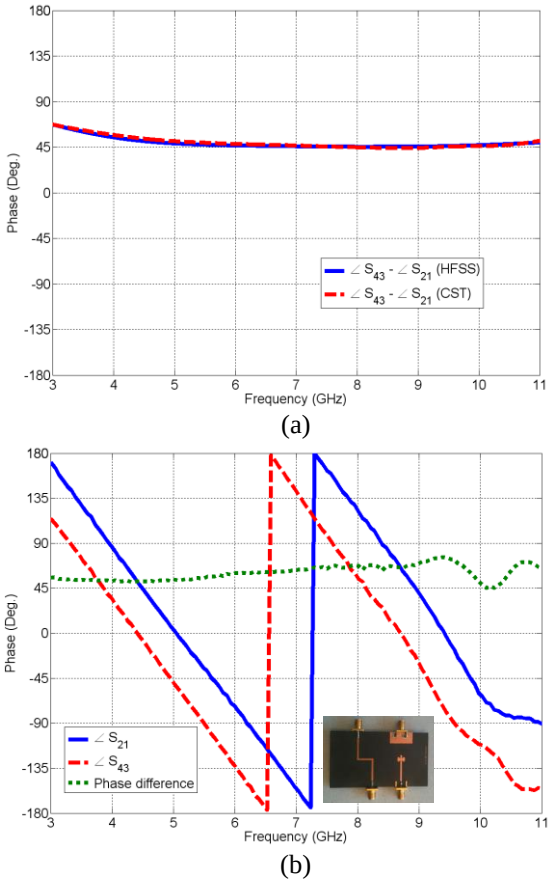

Fig. 8. (a) Simulated phase difference and (b) measured $\angle S_{21}$ & $\angle S_{43}$ phases and phase difference ($\angle S_{43} - \angle S_{21}$) of the proposed 45° butterfly phase shifter.

IV. CONCLUSION

The design of two different slot-coupled phase shifters for UWB applications has been presented. The proposed phase shifters utilize broadside coupling between trapezoidal and butterfly shaped microstrip patches at the top and bottom layers. Three different phase shift values for both phase shifter designs are proposed 22.5°, 45° and 67.5° to show the possibility to achieve wide range of phase shift values by proper adjusting their physical parameters. Two different 45° trapezoidal and butterfly prototypes have been fabricated and tested experimentally.

REFERENCES

[1] R. C. Hansen, *Chapter Ten—Multiple-Beam Antennas*, in Phased Array Antennas, ser. Wiley Series in Microwave and Optical Engineering, K. Chang, Ed., New York: Wiley, 1998.

[2] J. Butler and R. Lowe, "Beam-forming matrix simplifies design of electronically scanned antennas," *Electron. Design*, pp. 170-173, Apr. 1961.

[3] J. Blass, "Multidirectionnal antenna, a new approach to stacked beams," *IRE Int. Conf. Record*, vol. 8, pt. 1, pp. 48-50, 1960.

[4] J. Nolen, "Synthesis of multiple beam networks for arbitrary illuminations," *Ph.D. Dissertation*, Baltimore, MD, Radio Division, Bendix Corp, Apr. 1965.

[5] Y. T. Lo and S.W. Lee, *Antenna Handbook.* New York: Van Nostrand Reinhold, 1988.

[6] O. M Haraz and A. R. Sebak, "Two-layer butterfly-shaped microstrip 4×4 Butler matrix for ultra-wideband beam-forming applications," *Ultra-Wideband (ICUWB), 2013 IEEE International Conference on*, pp. 1,6, 15-18 Sept. 2013.

Osama Haraz received the B.S. (with honors) and M.S. degree in Electrical Engineering from Assiut University, Egypt, in 1999 and 2004, respectively and the Ph.D. degree from Concordia University, Montreal, QC, Canada, in 2011.

From 1999 to 2000 he worked with Nuclear Material Authority, Cairo, Egypt as an Electronic Engineer. Between 2000 and 2006 he was with the Electrical Engineering Department of Faculty of Engineering, Assiut University as Assistant Lecturer. He is currently an Assistant Professor of Electrical Engineering (Electronics & Communication Section), Assiut University. His current research interests include small antennas, microwave circuits for UWB and MMW applications, phased array antennas, interaction of EM waves with new advanced materials.

Haraz received the 2010 Concordia Ph.D. Thesis Completion Award, Concordia University, Montreal, Canada. He has also received the Scholarship of the Egyptian Ministry of Higher Education (2006-2010), the 2000 MobiNil Communication Company Excellence Award and the 6th October University Academic Distinction Award (1997-1998), Cairo, Egypt.

Abdel-Razik Sebak received the B.Sc. degree in Electrical Engineering from Cairo University in 1976 and the M.Eng. and Ph.D. degrees from the University of Manitoba in 1982 and 1984, respectively.

From 1984 to 1986, he was with the Canadian Marconi Company. From 1987 to 2002, he was a Professor of Electrical and Computer Engineering, University of Manitoba. He is currently a Professor of Electrical and Computer Engineering, Concordia University. His current research interests include phased array antennas, computational

electromagnetics, integrated antennas, electromagnetic theory, interaction of EM waves with new materials and bio electromagnetics.

Sebak received the 2000 and 1992 University of Manitoba Merit Award for Outstanding Teaching and Research, the 1994 Rh Award for Outstanding Contributions to Scholarship and Research in the Applied Sciences category, and the 1996 Faculty of Engineering Superior Academic Performance. He has served as Chair for the IEEE Canada Awards and Recognition Committee (2002-2004).

A Quadruple Band-Notched UWB Antenna by Using Arc-Shaped Slot and Rotated E-shaped Resonator

Yuanyuan Kong [1], Yingsong Li [1], Wenhua Yu [2], and Kai Yu [1]

[1] College of Information and Communications Engineering
Harbin Engineering University, Harbin 150001, China
liyingsong@ieee.org

[2] 2COMU, Inc.
4031 University Drive, Suite 100, Fairfax, VA 22030, USA
wenyu@2comu.com

Abstract ─ A simple quadruple band-notched ultra-wideband (UWB) antenna is proposed and its performance is investigated both numerically and experimentally. The proposed quadruple band-notched UWB antenna is realized based on an asymmetric planar monopole antenna which consists of a fan-shaped radiation patch, a microstrip feeding line and a trapezoidal ground plane. By etching an arc-shaped slot with a gap and adding a rotated E-shaped resonator beside the microstrip feeding line, four notched bands are achieved to suppress potential interferences from WiMAX (3.3-3.6 GHz), WLAN (5.15-5.35 GHz, 5.725-5.825 GHz) and uplink of X-band satellite communication system (7.9-8.4 GHz). The proposed monopole antenna can operate over 2.94-12 GHz band with VSWR<2 except these notch bands. Simulation and measurement results of the fabricated prototype demonstrate that the proposed antenna has quadruple band-notched characteristics and near-omnidirectional radiation patterns, making it suitable for UWB communication applications.

Index Terms ─ Arc-shaped slot, monopole antenna, quadruple notch bands, rotated E-shaped resonator, UWB antenna.

I. INTRODUCTION

UWB system is famous for its excellent characteristics of high transmission rate, high safety for its low transmitting power, low interception rate and amazing performance of anti-multipath attenuation [1]. Furthermore, the UWB system has a bandwidth of 7.5 GHz (FCC defined UWB band from 3.1 GHz to 10.6 GHz). Thus, it has more advantage to transmit signals than conventional narrow-band communication system. As an important component of the UWB system, UWB antennas have attracted more attention and have potential applications in medical imaging and indoor communication applications.

In order to cover the entire UWB band, a UWB antenna should have wide bandwidth, and hence, it will overlap with existing narrowband communication systems. In sequel, band-notched UWB antennas have been proposed to filter out potential interference bands to address this problem. Recently, various slots have been used to achieve the desired notch bands, including the modified shovel-shaped defected ground structure (DGS) [2], U-shaped and H-shaped slots on the radiation patch and ground plane [3], split-ring resonator (SRR) on the patch [4-7], and so on. Furthermore, parasitic strips or stubs have been used as resonators to produce stop-band filters to suppress the unwanted narrowband signal interferences [8-12], which include the SIR resonators [11], crescent-shaped resonator [12]. In [13], Che et al. designed a UWB antenna with a T-shaped stub embedded in the square slot shaped radiation patch and a pair of U-shaped parasitic strips along the feeding line to create the designated dual band notched characteristics. To enhance the notched performance of the UWB antennas, many double and multiple band-notched UWB antennas are investigated in recent years [14-19]. Moreover, several quadruple band-notched UWB antennas are designed [15-16]. Although they can achieve quadruple notch characteristics, each notched is implemented corresponding to a band-notched structure, which may increase the complexity of the antenna. In [17], a rectangular tuning stub and a tapered-shape slot are used to achieve dual-notched bands. In [18], multilayered resonators are used to achieve four notch bands, which increase the complexity of the antenna fabrication. Thus, we should design a UWB antenna with multi-band-notched function and simple structures to expand the application of the UWB antennas.

In this paper, a quadruple band-notched UWB antenna is proposed to reduce the potential interferences with the narrowband signals and to expand the applications of the band-notched UWB antenna. The

Submitted On: April 4, 2016
Accepted On: September 25, 2016

proposed UWB antenna can operate from 2.94 GHz to 12 GHz to cover the entire UWB band, which provides a bandwidth of 121.2% with respect to VSWR<2. By using etching arc-shaped slots on the radiation patch and adding a rotating E-shaped resonator beside the microstrip feeding line, the proposed UWB antenna can produce four notched bands to give resistance to the interferences from WiMAX (3.3-3.6 GHz), WLAN (5.15-5.35 GHz and 5.725-5.825 GHz) and the uplink of the X-band satellite communications (7.9-8.4 GHz). Furthermore, the proposed antenna has nearly omnidirectional radiation patterns and a good impedance matching characteristic, which has very broad prospects for modern UWB communication systems.

II. ANTENNA DESIGN

In this section, we will introduce geometry and the design procedure of the proposed quadruple band-notched UWB antenna.

A. Antenna schematic and dimensions

The proposed quadruple band-notched UWB antenna is designed based on the monopole UWB antenna [20-21]. Figure 1 depicts the configuration and the fabrication prototype of the proposed antenna. From Fig. 1, we can see that the proposed antenna consists of fan-shaped radiation patch with arc-shaped slots (ASS), 50-Ohm microstrip feeding transmission line and rotated E-shaped resonator (RESR) printed on the top layer of the proposed antenna. On the back layer, there is a trapezoidal ground plane. The antenna is printed on a substrate with a dielectric constant of 2.65 and thickness of 0.5 mm. The total size of the antenna is 35.6×20 mm^2. A slit divides the ASS into two segments (upper segment and lower segment) to implement the dual notch bands, which are located at WiMAX and the uplink of the X-band satellite communication bands. Additionally, the RESR is used for achieving another two narrow notch bands operated at WLAN bands. On the basis of the principle of the proposed quadruple band-notched UWB antenna, the proposed antenna is optimized by the Ansoft HFSS Ver. 13 and the optimized dimensions are listed as follows: w1=1.05 mm, h=21 mm, g=-0.4 mm, rf=15 mm, a=16 mm, b=20 mm, w2=6 mm, hs=1 mm, wc=3 mm, hc=1.2 mm. The dimensions of the designed two notch structures, including ASS and RESR, are given by c1=7.6 mm, cd=0.3 mm, hu=6 mm, uw=6.1 mm, ug=0.45 mm, ul=6.9 mm, ul1=8.4 mm, ud=0.5 mm. The angle of the ASS is 66°, and it is divided into two segments at an angle of 40°. Herein, the optimized parameters are obtained by using the HFSS and are rendered to meet both the desired UWB bandwidth and the designated notch bands referred to the VSWR.

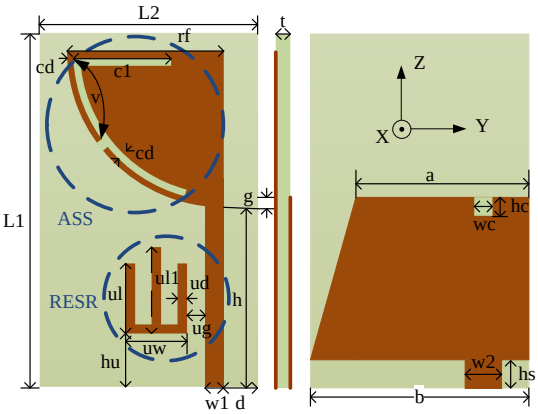

(a) Configuration of the proposed antenna

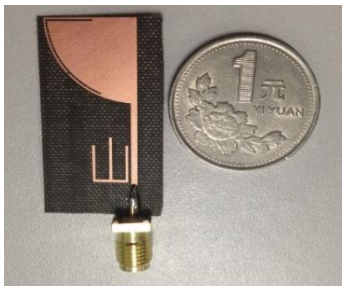

(b) Fabricated antenna

Fig. 1. Schematic and the prototype of the proposed UWB antenna.

B. Design procedure of the proposed antenna

The design procedure of the proposed quadruple band-notched UWB antenna is depicted in Fig. 2. Here, we will introduce how to design the proposed antenna step by step. Also, the dimensions of the corresponded notched structures, namely the arc-shaped slot and the RESR, are given by:

$$L_{notch} = \frac{c}{2 f_{notch} \sqrt{\frac{\varepsilon_r + 1}{2}}},$$

where ε_r is the dielectric constant of the substrate, c is the speed of the light, f_{notch} is the center frequency of the notch, and L_{notch} is the resonance length of the notch structure.

Firstly, a UWB antenna is used to design the proposed antenna, which is denoted as Antenna 1. Antenna 1 has a wide bandwidth, covering UWB band 3.1-10.6 GHz, and it has small size and good omnidirectional radiation characteristic [20-21]. Then, an ASS with a slit is etched on the fan-shaped radiation patch to create the Antenna 2 which is to design dual notch bands at WiMAX and X-band satellite communication band. Finally, a RESR is set along the

feed transmission line of the Antenna 2 to construct the proposed antenna which is named as Antenna 3. Antenna 3 is the proposed antenna, which is designed for providing four designated notch bands and suppressing unwanted interference signals from the above narrowband systems.

To verify the effectiveness and feasibility of the proposed antenna, the proposed antenna is investigated by using the HFSS based on the finite element method (FEM) and its performance is shown in Fig. 3. From Fig. 3, we can see that the frequency band of the Antenna 1 is 2.94-12 GHz with VSWR<2, which covers the entire UWB frequency band. Also, we can see that the Antenna 2 is also a UWB antenna which has two notch bands at 3.4 GHz and 7.32-9.07 GHz to suppress the potential narrowband interferences. In this case, the dual notch bands can be controlled by adjusting the dimensions of the ASS. Antenna 3 is our proposed quadruple band-notched UWB antenna. It is obvious that Antenna 3 has four notch bands located at 3.4 GHz, 7.32-9.07 GHz, 5.25 GHz and 5.75 GHz, which can be used for filter out potential interferences from WiMAX, WLAN, the uplink of the X-band satellite communications and 8 GHz ITU band. Thus, we can say that the four notch bands are generated by the ASS and RESR. Thus, we can design the dimensions of the ASS and RESR to create the desired notch bands.

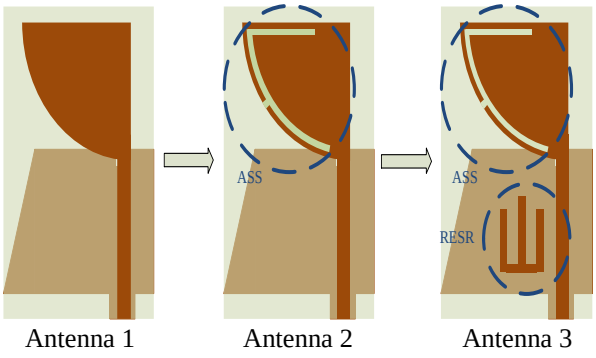

Fig. 2. Design procedure of the proposed antenna.

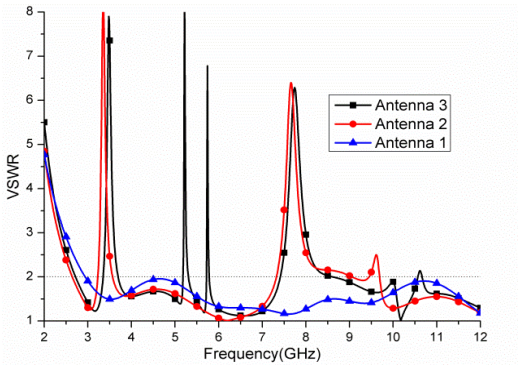

Fig. 3. Performance of the design procedure of the proposed antenna.

III. PERFORMANCE OF THE PROPOSED ANTENNA

In this section, we will discuss the performance of the proposed antenna by using the HFSS, which includes the impedance characteristic, current distribution and radiation patterns.

A. Impedance characteristic and parameter performance

Here, the quadruple band-notched UWB antenna is optimized by using the HFSS, and the optimized S11 and VSWR are shown in Fig. 4. We can see that the antenna operates from 2.94 GHz to 12 GHz which can cover the entire UWB band. Also, it has four notch bands with respect to S11>-10 dB or VSWR>2 to filter out the potential interferences from the WiMAX system ranging from 3.3 to 3.6 GHz, WLAN frequency band 5.25-5.35 GHz and 5.725-5.825 GHz, and the uplink of the X-band satellite systems ranging from 7.9 to 8.4 GHz. The input impedance of the proposed antenna is given in Fig. 5. It is found that the real part is around 50-Ohm and the imaginary part is about 0 ohm at operating frequency range, which indicates the antenna has a good matching with 50-Ohm terminals. In addition, the real part and the imaginary part changes very quickly in the notch bands, which result in no resonance, and hence, the desired notch characteristics has been produced.

Next, we will investigate the parameter effects on the VSWR. Here, the parameters v and ul are selected for evaluating the effects on the proposed quadruple band-notched UWB antenna and the results are demonstrated in Fig. 6 and Fig. 7, respectively. It is found from Fig. 6 that v has important effects on the notch band at uplink of X-band satellite communication. The degree of v controls the lower resonator of ASS. By adjusting the degree of v from 65 degree to 67 degree, the center frequency of 8 GHz notch band moves from high frequency to low frequency. This is caused by the increased resonance length of the lower ASS. In this paper, the optimized value of v is 66 degree referred to Fig. 6, which can be used for producing a notch to cover 7.9-8.4 GHz for uplink band of X-band satellite communication.

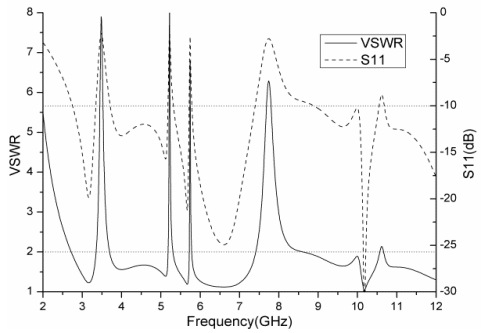

Fig. 4. S11 and VSWR of the proposed quadruple band-notched UWB antenna.

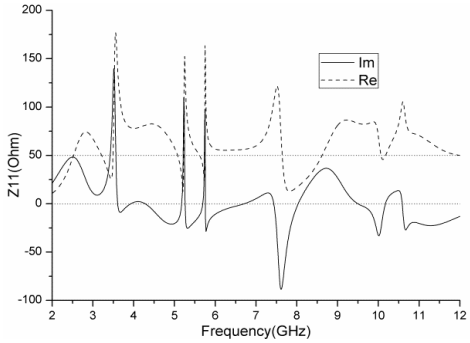

Fig. 5. Z11 of the proposed quadruple band-notched UWB antenna.

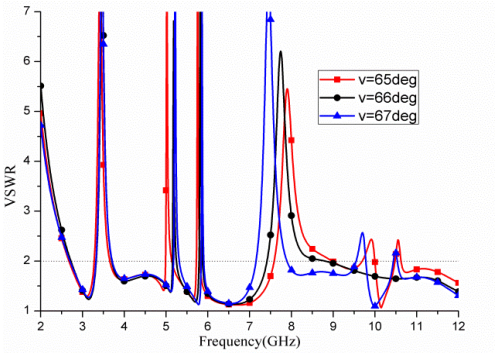

Fig. 6. VSWR of the proposed quadruple band-notched UWB antenna with varying v.

The parameter ul can control the resonance length of the RESR, which is depicted in Fig. 7. When ul increases from 6.8 mm to 7 mm, the center frequencies of the two WLAN notch bands all move from high frequency to low frequency. This is because the resonance lengths of RESR become larger with an increasing ul.

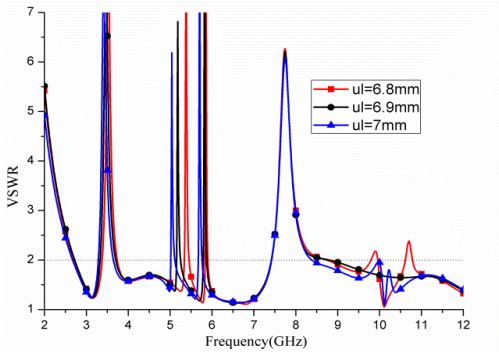

Fig. 7. VSWR of the proposed quadruple band-notched UWB antenna with varying ul.

B. Measured S11, radiation patterns, gain and current distributions

To verify the effectiveness of the proposed antenna, the optimized antenna is fabricated and its S11 is measured by using Agilent N5224A vector network analyzer. The comparisons of the simulated and measured S11 are shown in Fig. 8. It can be seen that the measurement results agree well with the simulation ones. It is worth noting that there are some differences between the measured and simulated results, which may be caused by fabrication tolerances and inaccuracies introduced by manual welding.

The radiation patterns of the proposed quadruple band-notched UWB antenna at 3.1 GHz, 4.5 GHz and 7 GHz are shown in Fig. 9, where we define the YOZ plane as E-plane and the XOZ plane as H-plane. From Fig. 9, we can see that the radiation plane of E-plane looks like a digit '8' and H-plane is almost omnidirectional at 3.1 GHz and 4.5 GHz. There is some distortion at 7 GHz, which may be caused by the effects of the ASS, RESR and the asymmetric antenna structure.

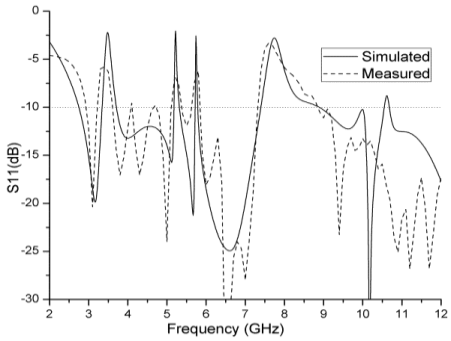

Fig. 8. S11 of the proposed antenna.

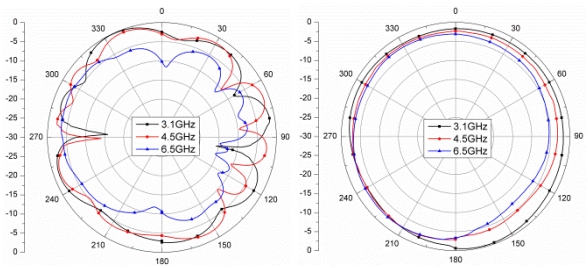

(a) E-plane (b) H-plane

Fig. 9. Measured radiation patterns of the proposed quadruple band-notched UWB antenna.

The gain of the proposed quadruple band-notched UWB antenna is given in Fig. 10. From 3.1-10.6 GHz, the value of gain ranges from 0.8-5.7 dB. At 3.4 GHz, 5.25 GHz, 5.75 GHz and 7.9 GHz, the gains drop very quickly and they are -2.8 dBi, 0.2 dBi, 0.4 dBi and 3.3 dBi, respectively. It means that the radiation ability of the antenna is strong at UWB band except four notch bands which comply with the design requirements.

To understand the principle of the designed quadruple band-notched UWB antenna, the current distribution of the proposed antenna is investigated and

is illustrated in Fig. 11. The current distribution at the notch bands 3.4 GHz, 5.25 GHz, 5.75 GHz and 7.8 GHz are discussed herein. We can clearly see that the current is focus on the upper ASS at 3.4 GHz, and the currents on the microstrip feeding line are small. At 7.8 GHz, the current is mainly on the lower ASS. Thus, we can say that the 3.4 GHz and 7.8 GHz notches are generated by the ASS. Similarly, the current distributions focus on the RESR structure at 5.25 GHz and 5.75 GHz. Thus, the RESR can provide two notch bands at WLAN bands.

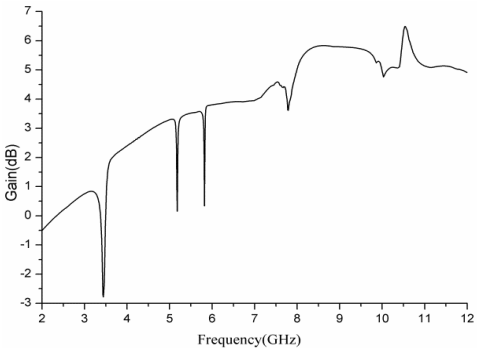

Fig. 10. Gain of the proposed quadruple band-notched UWB antenna.

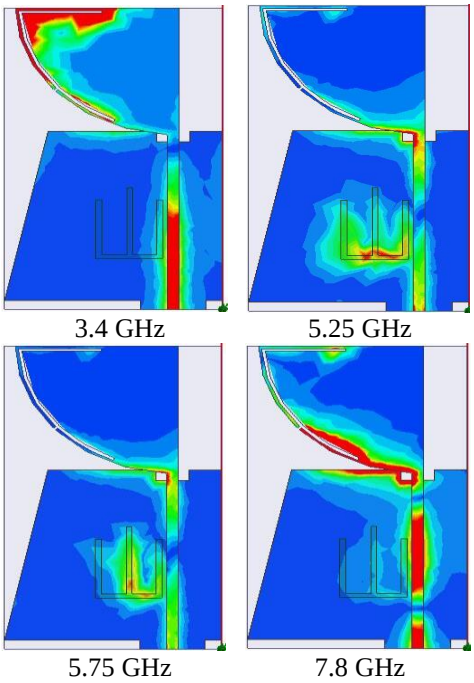

Fig. 11. Current distributions of the proposed quadruple band-notched UWB antenna.

Table 1 gives comparisons of the proposed antenna with previously reported band-notched UWB antennas with respect to the size, the number of notch bands bandwidth and gains. From Table 1, we can see that most of the antennas only have single, dual and triple notch bands. Although the references [2] and [7] have smaller size, they can only provide two stop bands. In [5] and [12], the UWB antenna can provide three notch bands. However, they are embarrassed in large size. In a word, the proposed quad notch-band UWB antenna can provide four designated notch bands and have smaller size, making it suitable to meet the requirements of ultra-wideband systems.

Table 1: Comparisons of several existing band-notched UWB antennas

References	Dimensions (mm^2)	Rejection Bands	Bandwidth	Gain (dBi) (Operating Bands)
[2]	15×18	5.13 GHz-6.1 GHz	3.1-13.4 GHz	3~5
[3]	21×28	5 GHz-6 GHz & 7.7 GHz-8.5 GHz	2.8-12 GHz	2~4
[4]	25×25	5.15 GHz-5.35 GHz	3.8-11 GHz	-1.8~4
[5]	30×26	3.3 GHz-3.6 GHz & 5.25 GHz-5.35 GHz & 7.725 GHz-7.825 GHz	3.1-12 GHz	3.8~5.6
[6]	22×26	3.8 GHz-4.28 GHz & 5.76 GHz-6.16 GHz	2.6-12 GHz	____
[7]	12×18	3.38 GHz-4.31 GHz & 5.1 GHz-5.95 GHz	3.1-13.4 GHz	2.8~5
[8]	40×31	4.1 GHz-5.8 GHz	3.1-9.9 GHz	2.7~6.2
[10]	23×28	3.5 GHz WLAN & 5.8 GHZ WLAN	2.7-11 GHz	0~5
[12]	25×28	4.94 GHz-5.52 GHz & 5.72 GHz-6.02 GHz & 7.25-7.76 GHz	3.1-12 GHz	1.9~5.8
[13]	26×32	3.3 GHz-4.0 GHz & 5.05 GHz-5.9 GHz	3.1-12 GHz	1~3.5
[17]	22×24	3.35-3.8 GHz & 5.12 GHz-5.84 GHz	3.0-10.6 GHz	-1.8~5
[21]	30×32	4.2 GHz-6.15 GHz & 6.5 GHz-7 GHz, 10 GHz-12.4 GHz	3.1-14 GHz	2~6
Proposed	20×35.6	3.3 GHz-3.6 GHz & 5.25 GHz-5.35 GHz & 5.725 GHz-5.825 GHz & 7.9 GHz-8.4 GHz	2.94-12 GHz	0.5~6

VI. CONCLUSION

In this paper, a quadruple band-notched UWB antenna has been proposed and its performance has been investigated in detail. The desired four notches are generated by ASS and RESR. The antenna can operate over the entire UWB band and can provide a good rejection function for unwanted narrowband signal interferences. Additionally, the proposed antenna only uses two notch structures to construct the desired four notch band. Also, the proposed antenna has a small size. The experiment results showed that the antenna has a good impedance match and omnidirectional radiation patterns, rendering it suitable for UWB communication applications.

ACKNOWLEDGMENT

This work was partially supported by the Natural Science Foundation of China (No. 61571149), and International Science & Technology Cooperation Program of China (2014DFR10240), Projects for the Selected Returned Overseas Chinese Scholars of Heilongjiang Province of China, the Science and Technology Innovative Talents Foundation of Harbin (2013RFXXJ083, 2016RAXXJ044) and the Foundational Research Funds for the Central Universities (HEUCFD1433, HEUCF160815).

REFERENCES

[1] I. Oppermann, M. Hamalainen, and J. Iinatti, *UWB Theory and Applications*. New York: Wiley, pp. 3-4, 2004.

[2] A. Nouri and G. R. Dadashzadeh, "A compact UWB band-notched printed monopole antenna with defected ground structure," *IEEE Antennas and Wireless Propagation Letters*, vol. 10, pp. 1178-1181, 2011.

[3] Y. S. Li, X. D. Yang, C. Y. Liu, and T. Jiang, "Compact CPW-fed ultra-wideband antenna with dual band-notched characteristics," *Electronics Letters*, vol. 46, no. 14, pp. 867-868, 2010.

[4] J. Kim, C. S. Cho, and J. W. Lee, "5.2 GHz notched ultra-wideband antenna using slot-type SRR," *Electronics Letters*, vol. 42, no. 6, pp. 315-316, 2006.

[5] M.-C. Tang, S. Xiao, T. Deng, D. Wang, J. Guan, B. Wang, and G.-D. Ge, "Compact UWB antenna with multiple band-notches for WiMAX and WLAN," *IEEE Transactions on Antennas and Propagation*, vol. 59, no. 4, pp. 1372-1376, 2011.

[6] D. Jiang, Y. Xu, R. Xu, and W. Lin, "Compact dual-band-notched UWB planar monopole antenna with modified CSRR," *Electronics Letters*, vol. 48, no. 20, pp. 1250-1252, 2012.

[7] M. Ojaroudi, N. Ojaroudi, and N. Ghadimi, "Dual band-notched small monopole antenna with novel coupled inverted U-ring strip and novel fork-shaped slit for UWB applications," *IEEE Antennas and Wireless Propagation Letters*, vol. 12, pp. 182-185, 2013.

[8] J. R. Kelly, P. S. Hall, and P. Gardner, "Band-notched UWB antenna incorporating a microstrip open-loop resonator," *IEEE Transactions on Antennas and Propagation*, vol. 59, no. 8, pp. 3048-3048, 2011.

[9] Y. Li, W. Li, and W. Yu, "A switchable UWB slot antenna using SIS-HSIR and SIS-SIR for multi-mode wireless communications applications," *Applied Computational Electromagnetics Society Journal*, vol. 27, no. 4, pp. 340-351, 2012.

[10] M. M. S. Taheri, H. R. Hassani, and S. M. A. Nezhad, "UWB printed slot antenna with Bluetooth and dual notch bands," *IEEE Antennas and Wireless Propagation Letters*, vol. 10, pp. 255-258, 2011.

[11] Y. Li, W. Li, and Q. Ye, "A reconfigurable wide slot antenna integrated with SIRs for UWB/multi-band communication applications," *Microwave and Optical Technology Letters*, vol. 55, no. 1, pp. 52-55, 2013.

[12] L. Li, Z.-L. Zhou, and J.-S. Hong, "Compact UWB antenna with four band-notches for UWB applications," *Electronics Letters*, vol. 47 no. 22, 2011.

[13] W. Jiang and W. Che, "A novel UWB antenna with dual notched bands for WIMAX and WLAN applications," *IEEE Antennas and Wireless Propagation Letters*, vol. 11, pp. 293-296, 2012.

[14] Y. Li, W. Li, and R. Mittra, "Miniaturized CPW-fed UWB antenna with dual frequency rejection bands using stepped impedance stub and arc-shaped parasitic element," *Microwave and Optical Technology Letters*, vol. 56, no. 4, pp. 783-787, 2014.

[15] Z.-H. Wu, F. Wei, X.-W. Shi, and W.-T. Li, "A compact quad band-notched UWB monopole antenna loaded one lateral l-shaped slot," *Progress in Electromagnetics Research*, vol. 139, pp. 303-315, 2013.

[16] S. H. Zainud-Deen, R. A. Al-Essa, and S. M. M. Ibrahem, "Ultrawideband printed elliptical mono-pole antenna with four band-notch characteristics," *IEEE Antennas and Propagation Society International Symposium (APSURSI)*, pp. 1-4, 2010.

[17] R. Azim, M. T. Islam, and A. T. Mobashsher, "Design of a dual band-notch UWB slot antenna by means of simple parasitic slits," *IEEE Antennas and Wireless Propagation Letters*, vol. 12, pp. 1412-1415, 2013.

[18] M. J. Almalkawi and V. K. Devabhaktuni, "Quad band-notched UWB antenna compatible with WiMAX/INSAT/lower–upper WLAN applications," *Electronics Letters*, vol. 47, no. 19, pp.

1062-1063, 2013.

[19] Y. Li, W. Li, and Q. Ye, "A reconfigurable triple notch band antenna integrated with defected microstrip structure band-stop filter for ultra-wideband cognitive radio applications," *International Journal of Antennas and Propagation*, vol. 2013, Article ID: 472645, pp. 1-13, 2013.

[20] K. Hiraguri, K. Koshiji, and F. Koshiji, "A wideband antenna with fan-shaped and trapezoidal elements on printed circuit board for ultra-wideband radio," *IEEE 2nd Global Conference on Consumer Electronics*, pp. 267-268, 2013.

[21] F. Koshiji, Y. Akiyama, S. Itaya, and K. Koshiji, "A wideband antenna with fan-shaped and trapezoidal elements for ultra-wideband radio," *2012 International Symposium on Antennas and Propagation (ISAP)*, pp. 838-841, 2012.

Ultra-Wideband Low Profile, U-Slot Microstrip Patch Antennas: L-Probe Feed Design Guidelines

Mohamed M. Elsewe, Varun K. Dandu, and Deb Chatterjee

Computer Science & Electrical Engineering Department
University of Missouri – Kansas City, Kansas City, MO 64110, USA
chatd@umkc.edu

Abstract ─ The need for low-profile and ultra-wideband (UWB) antennas is rising in wireless communication and medical applications. The method of dimensional invariance, which is a class of U-slot patch design methods, is utilized to realize an initial, low-profile, wideband design. Building on this initial wideband design, this study establishes ideal L-probe feed dimensions through extensive parametric study on ε_r = 2.2 and 4.5 substrates to propose empirical guidelines for the design of L-probe feeds which yield *first-pass* optimum impedance bandwidth. The established ideal L-probe dimensions, after further extrapolation, are used successfully on other substrates, ε_r = 3.27, 6.0 and 9.2, for the design of *first-pass* L-probe feeds which yield impedance bandwidth over 55%, 60%, and 53%, respectively. The results of three commercially available EM simulation solvers show good agreement.

Index Terms ─ FEM, L-probe, microstrip patch antenna, MoM, U-slot, UWB.

I. INTRODUCTION

Low-profile and UWB microstrip patch antennas are finding their place in many wireless communication applications like WLAN and WiMAX [1, 2], and medical applications like breast cancer detection [3].

In recent years, the U-slot patch antenna proved to be a versatile antenna that can be fine-tuned for dual-band, triple-band, and wideband operations, in addition to supporting linear and circular polarization operations [4]. Dual-band operation is particularly important in some wireless communication applications, and wideband operation is useful in UWB medical imaging and detection applications.

Several feeding structure designs for the U-slot patch antenna are proposed in the literature [4-6]. The L-shaped probe feeding method [7], in particular, has led to improved impedance bandwidth of 38% for the U-slot patch antenna [5]. Moreover, its simple structure and low production cost [6] make it an attractive feeding method for the U-slot microstrip patch antenna.

In this paper, the U-slot patch antenna design method of dimensional invariance, developed and validated in earlier work [8-11], is utilized to realize an initial, low-profile, wideband design. Building on this initial wideband design and previous work [12], this study establishes ideal L-probe feed dimensions which propose empirical guidelines for the design of L-probe feeds to yield *first-pass* optimum impedance bandwidth.

In Section II of the paper, the U-slot patch design method and CAD model are discussed. In Section III, an extensive parametric study on two substrates, ε_r = 2.2 and 4.5, is presented to find the ideal L-probe dimensions which yield optimum impedance bandwidth. In Section IV, an empirical L-probe design technique is developed using the ideal L-probe dimension information established in Section III. The new L-probe design technique is then validated on substrates with different permittivities, ε_r = 3.27, 6.0 and 9.2.

II. DESIGN METHOD AND CAD MODEL

A. Method of dimensional invariance

The method of dimensional invariance described in [8] is utilized in this paper to realize the U-slot antenna patch dimensions, shown in Fig. 1. This method relies on empirical formulas to first obtain the rectangular patch dimensions, then uses the dimensional invariance relationships in Table 1 to derive the U-slot dimensions. The method employs few criteria for substrate height, h, and patch width, W, that is $\frac{h\sqrt{\varepsilon r}}{\lambda} \approx 0.15$; $\frac{W}{L} \approx 1.385$ and ($3.5 \leq \frac{W}{h} \leq 5.5$). Once $\frac{W}{h}$ ratio is determined using the method's empirical equations, relationships in Table 1 can be used to derive the topology of the U-slot patch.

Comparative analysis between this method and another U-slot design method is presented in [9], which highlights the advantages of the method of dimensional invariance with respect to enhanced bandwidth and applicability to low and high permittivity substrates. Experimental validation of the design method of dimensional invariance in the design of U-slot microstrip patch antenna is reported from earlier work in [10], in

Submitted On: October 7, 2015
Accepted On: September 9, 2016

which HFSS simulation results agree with experimental results as shown in Fig. 2. In the absence of recent experimental results to validate our simulation results in this paper, further validation of the results presented in the published work [10] using FEKO MoM shows good agreement with the experimental data presented in Fig. 2. The discrepancy between measured and simulated MoM results is mainly due to the infinite ground plane assumption in MoM method.

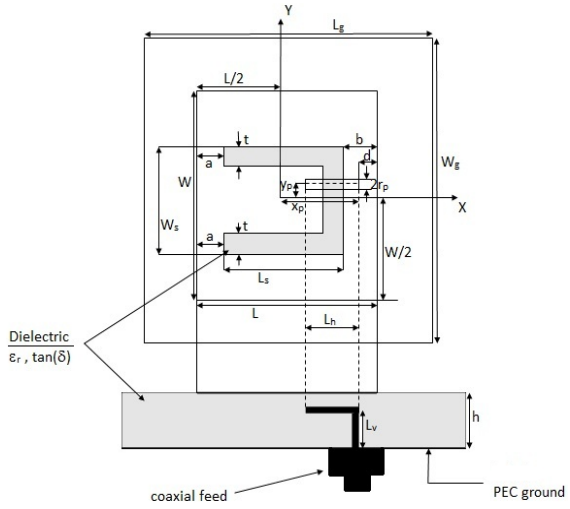

Fig. 1. Geometry of L-shaped, probe-fed, rectangular patch U-slot microstrip antenna.

Table 1: Dimensional invariance in U-slot designs for various substrates [8]

ε_r	$\frac{L}{Ls}$	$\frac{Ws}{Ls}$	$\frac{Ls}{b}$	$\frac{t}{Ws}$	$\frac{W}{Ws}$
2.33	1.445	0.777	4.5	0.144	2.573
4.0	1.443	0.776	4.51	0.144	2.573
9.8	1.442	0.777	4.48	0.144	2.574

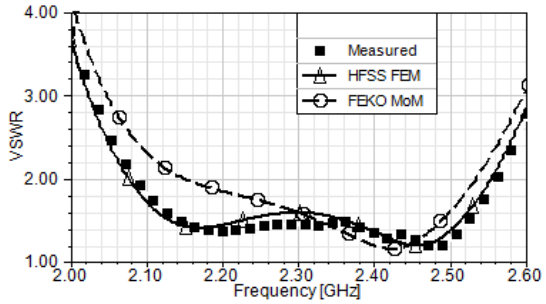

Fig. 2. Experimental [10] and simulated VSWR of a probe-fed U-slot patch antenna.

B. CAD model

The parametric studies in Section III are simulated and analyzed using the commercially available EM full-wave solvers, FEKO and HFSS, which are popular tools for analyzing microstrip patch antennas. Simulation results using the Method of Moments (MoM) and Finite Element Method (FEM) solvers within FEKO are validated with simulation results using the HFSS FEM solver. The FEKO and HFSS FEM solvers have the same underlying computational electromagnetic method and hence, are expected to produce comparable results. Table 2 shows the dimensions of the U-slot microstrip patch antenna used in the parametric study, which are derived from the aforementioned method of dimensional invariance for a 2.4 GHz design frequency. Two substrate materials are studied: the *Rogers RT/Duroid 5880* substrate material with $\varepsilon_r = 2.2$ and $\tan(\delta) = 0.0009$ and the *Rogers TMM 4* substrate material with $\varepsilon_r = 4.5$ and $\tan(\delta) = 0.002$. Further simulation optimization runs were performed to arrive at the substrate height and probe position which yield best bandwidth.

Table 2: U-slot microstrip patch antenna dimensions for various substrates

	$\varepsilon_r = 2.2$	$\varepsilon_r = 4.5$
a	5.17	3.61
b	5.17	3.61
W	46.53	32.54
L	33.6	23.49
L_s	23.26	16.27
t	2.6	1.82
W_s	18.09	12.65
r_p	1	1
x_p	13.8	8.745
y_p	1	-3
d	3	3
h	14	12

*All values are in mm.

In FEKO MoM solver, infinite substrate and ground is assumed. In FEKO FEM and HFSS FEM solvers, the substrate and ground (W_g and L_g) dimensions are extended by $\lambda/2$, where λ corresponds to the lower bandwidth frequency, from the edge of the patch to simulate an infinite substrate and ground for a more suited comparison between the FEM and MoM solvers. A radiation air box boundary which is $\lambda/4$, where λ corresponds to the lower bandwidth frequency, above the patch is used. The microstrip patch mesh size is $\lambda/20$, where λ corresponds to the upper bandwidth frequency. A 50-ohm coaxial feed line is used to feed the L-probe.

III. PARAMETRIC STUDY OF L-PROBE DIMENSIONS

In this section, parametric studies are performed on two substrates, $\varepsilon_r = 2.2$ and 4.5, in which the horizontal length, L_h, and vertical length, L_v, of the L-probe are varied to find the L-probe dimensions with the highest impedance bandwidth. VSWR results for selected L_h and

L_v variations are presented to show the results of three EM solvers on one figure for the sake of comparison and validation.

A. For ε_r = 2.2 substrate

Parametric study of horizontal length of L-probe

The horizontal length, L_h, is varied at 11 different points between 5 and 13 mm. L_v is fixed at 10 mm. As shown in the Fig. 3, a wideband behavior is observed for the L_h values equal to 11 mm and 12 mm. Figure 4 summarizes the relationship between L_h/λ_o (where λ_o is the free-space wavelength corresponding to the 2.4 GHz design frequency) and bandwidth and shows good agreement between the HFSS and FEKO results for L_h = 5-13 mm (0.04-0.11λ_o). As shown in Fig. 4, optimum bandwidth of approximately 50% is achieved when L_h is equal to 0.08-0.11λ_o.

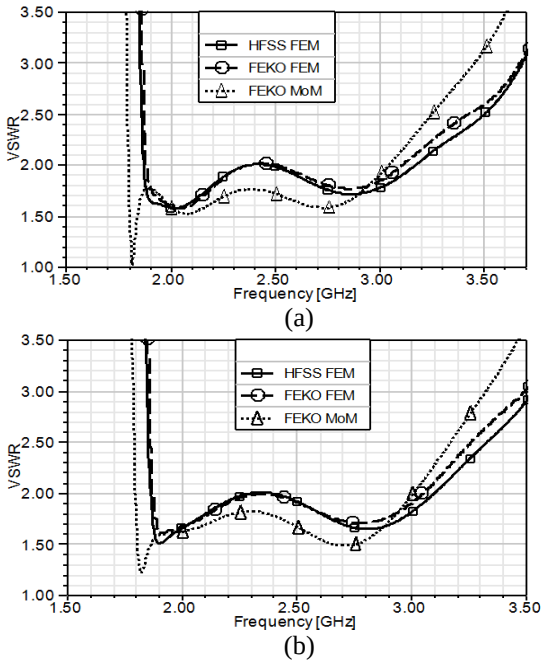

Fig. 3. VSWR for different L_h and ε_r = 2.2 substrate with fixed L_v = 10 mm. (a) L_h = 11 mm and (b) L_h = 12 mm.

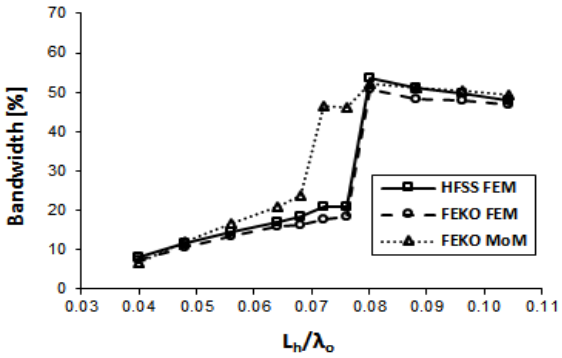

Fig. 4. Bandwidth versus L_h/λ_o for ε_r = 2.2 substrate.

Parametric study of vertical length of L-probe

The vertical length, L_v, is varied at 9 different points between 7 and 12 mm. L_h is fixed at 12 mm. As shown in the Fig. 5, a dual-band behavior is observed for the L_v values equal to 11 mm and 12 mm. Figure 6 summarizes the relationship between L_v/λ_o and bandwidth and shows good agreement between the HFSS and FEKO results for L_v = 7-12 mm (0.05-0.10λ_o). As shown in Fig. 6, optimum bandwidth of approximately 50% is achieved when L_v is equal to 10 mm (0.08λ_o). Also, wideband behavior is shown in Fig. 2 when L_v = 10 mm.

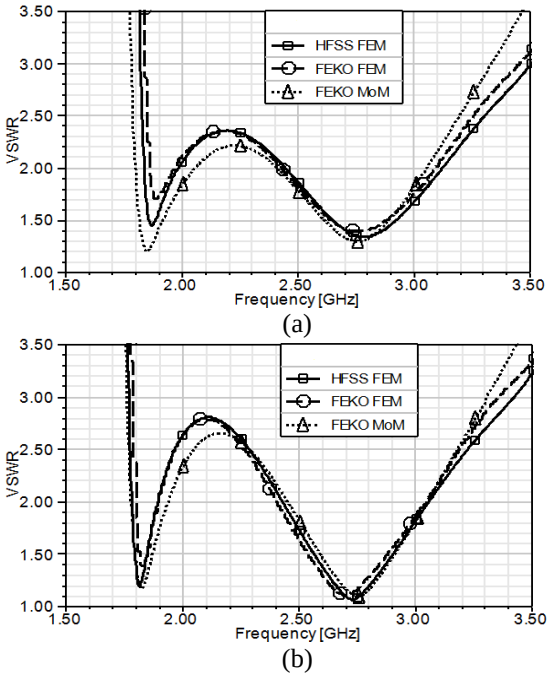

Fig. 5. VSWR for different L_v and ε_r = 2.2 substrate with fixed L_h = 12 mm. (a) L_v = 11 mm and (b) L_v = 12 mm.

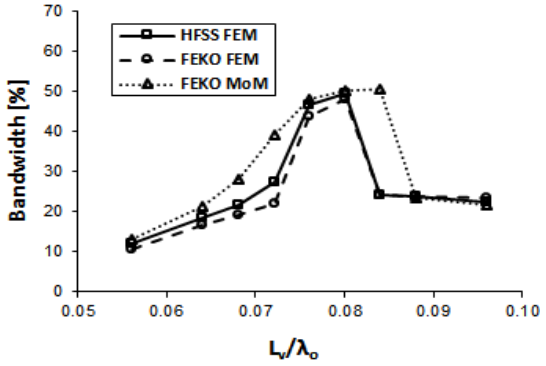

Fig. 6. Bandwidth versus L_v/λ_o for ε_r = 2.2 substrate.

The antenna gain for the wideband case of L-probe dimensions L_v = 10 mm and L_h = 12 mm is illustrated in Fig. 7. As shown in the figure, there is good agreement in the gain between the HFSS and FEKO simulation results.

Also, the antenna gain is around 5 dB for the 1.9-3.2 GHz (~50%) bandwidth achieved by these L-probe dimensions.

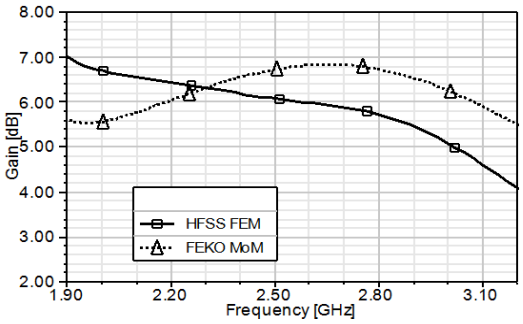

Fig. 7. Gain for L_v = 10 mm, L_h = 12 mm and ε_r = 2.2 substrate.

B. For ε_r = 4.5 substrate

Parametric study of horizontal length of L-probe

The horizontal length, L_h, is varied at 8 different points between 3 and 13 mm. L_v is fixed at 10 mm. As shown in the Fig. 8, a wideband behavior is observed for the L_h values equal to 5 mm and 9 mm. Figure 9 summarizes the relationship between L_h/λ_o (where λ_o is the free-space wavelength corresponding to the 2.4 GHz design frequency) and bandwidth and shows good agreement between the HFSS and FEKO results for L_h = 3-13 mm (0.02-0.11λ_o). As shown in Fig. 9, optimum bandwidth over 50% is achieved when L_h is equal to 0.02-0.04λ_o.

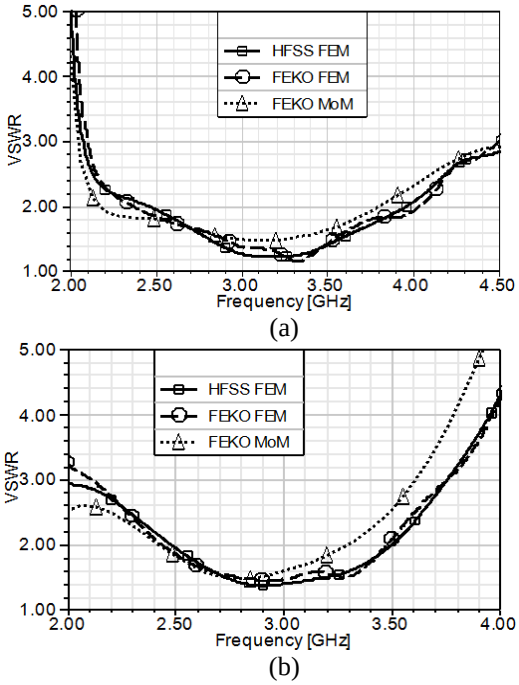

Fig. 8. VSWR for different L_h and ε_r = 4.5 substrate with fixed L_v = 10 mm. (a) L_h = 5 mm and (b) L_h = 9 mm.

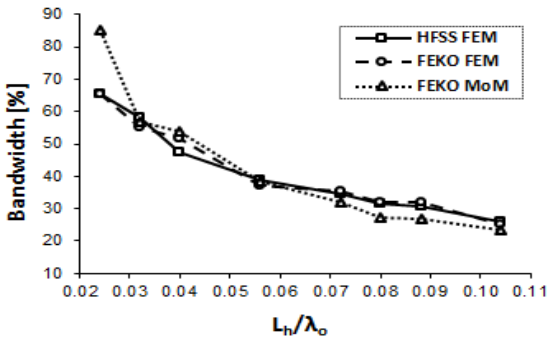

Fig. 9. Bandwidth versus L_h/λ_o for ε_r = 4.5 substrate.

Parametric study of vertical length of L-probe

The vertical length, L_v, is varied at 5 different points between 6 and 10 mm. L_h is fixed at 3 mm. As shown in Fig. 10, the wideband behavior is observed for the L_v values equal to 9 mm and 10 mm. Figure 11 summarizes the relationship between L_v/λ_o and bandwidth and shows good agreement between the HFSS and FEKO results for L_v = 6-10 mm (0.05-0.08λ_o). As shown in Fig. 11, optimum bandwidth over 50% is achieved when L_v is equal to 0.05-0.08λ_o.

The antenna gain for the wideband case of L-probe dimensions L_v = 10 mm and L_h = 3 mm in HFSS and FEKO simulations is illustrated in Fig. 12. As shown in the figure, there is good agreement in the gain between the HFSS and FEKO results. Also, the antenna gain is around 2 dB for the 2.2-2.9 GHz (~28%) bandwidth achieved by these L-probe dimensions.

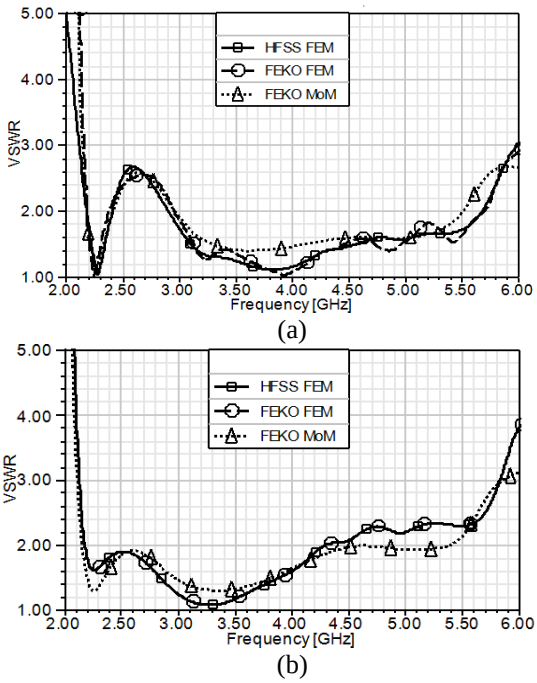

Fig. 10. VSWR for different L_v and ε_r = 4.5 substrate with fixed L_h = 3 mm. (a) L_v = 9 mm and (b) L_v = 10 mm.

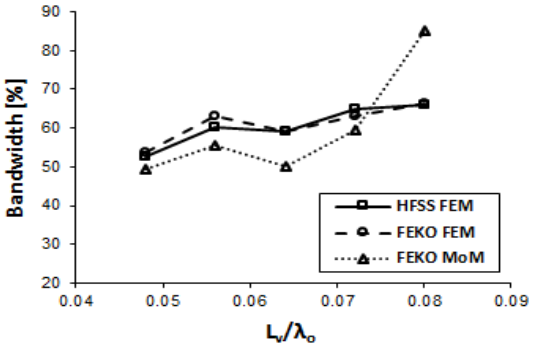

Fig. 11. Bandwidth versus L_v/λ_o for ε_r = 4.5 substrate.

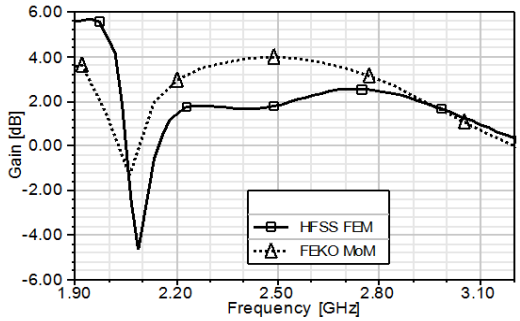

Fig. 12. Gain for L_v = 10 mm, L_h = 3 mm and ε_r = 4.5 substrate.

Comparing the results of the ε_r = 2.2 and 4.5 substrates, we note that the bandwidth is increased for the ε_r = 4.5, however, the gain is decreased. This is expected since the loss tangent of the ε_r = 4.5 substrate is higher than the loss tangent of the ε_r = 2.2 substrate. This results in more losses in the dielectric substrate, which in turn decreases the input impedance leading to increased bandwidth and decreased efficiency.

IV. EMPIRICAL DESIGN TECHNIQUE OF L-PROBE FEED

A. Development of empirical design technique for L-probe feed

In this section, the ideal L-probe dimension information presented in Figs. 4, 6, 9, and 11 is utilized to extrapolate the ideal L-probe dimensions on substrates with different dielectric constants to generate optimum impedance bandwidth. Figure 1 shows the U-slot patch antenna geometry and Table 3 shows the antenna dimensions for three substrate materials realized using the aforementioned method of dimensional invariance for a 2.4 GHz design frequency. The three substrate materials are: the *Rogers TMM 3* substrate material with ε_r = 3.27 and tan(δ) = 0.002, the *Rogers TMM 6* substrate material with ε_r = 6.0 and tan(δ) = 0.0023, and the *Rogers TMM 10* substrate material with ε_r = 9.2 and tan(δ) = 0.0022. The optimized L-probe position values, x_p and y_p, are shown in parenthesis in Table 3, and the optimized vertical probe x_p and y_p values are outside the parenthesis.

Using FEKO MoM, FEKO FEM, and HFSS FEM solvers, the three antennas are simulated with a conventional vertical probe and an L-probe feed. The horizontal length of the L-probe feed for the ε_r = 3.27 substrate is realized by taking the average of the L_h/λ_o value with maximum bandwidth for ε_r = 2.2 substrate in Fig. 4 and the L_h/λ_o value with maximum bandwidth for ε_r = 4.5 substrate in Fig. 9; which equals to approximately $0.05\lambda_o$ or 6 mm. Simulation results using the L_h/λ_o value with maximum bandwidth for ε_r = 2.2 and 4.5, instead of using the average between the two showed bandwidths of 10% and 48%, respectively, compared to over 55% when using the average value. Similarly, the vertical length of the L-probe feed for the ε_r = 3.27 substrate is realized by taking the average of the L_v/λ_o value with maximum bandwidth for ε_r = 2.2 substrate in Fig. 6 and the L_v/λ_o value with maximum bandwidth for ε_r = 4.5 substrate in Fig. 11; which equals to $0.08\lambda_o$ or 10 mm. For the ε_r = 6.0 and 9.2 substrates, the horizontal and vertical lengths of the L-probe feed are realized by taking the L_h/λ_o value with maximum bandwidth for ε_r = 4.5 substrate in Fig. 9; which equals to $0.02\lambda_o$ or 2.5 mm, and the L_v/λ_o value with maximum bandwidth for ε_r = 4.5 substrate in Fig. 11; which equals to $0.08\lambda_o$ or 10 mm.

VSWR results in Fig. 13 (a) show that, for ε_r = 3.27 substrate, using the *first-pass* L-probe design over the vertical probe, the bandwidth improved from 9% to over 55%. Similarly, VSWR results in Fig. 13 (b) show that, for ε_r = 6.0 substrate, using the designed L-probe over the vertical probe, the bandwidth improved from 13% to over 60%. VSWR results in Fig. 13 (c) show that, for ε_r = 9.2 substrate, using the designed L-probe over the vertical probe, the bandwidth improved from 33% to over 53%. FEKO FEM and HFSS FEM results for the L-probe are in agreement in the three plots.

Table 3: U-slot microstrip patch antenna dimensions for various substrates

	ε_r = 3.27	ε_r = 6.0	ε_r = 9.2
a	4.24	3.14	2.44
b	4.24	3.14	2.44
W	38.17	28.18	21.88
L	27.56	20.34	15.8
L_s	19.08	14.06	10.94
t	2.14	1.58	1.22
W_s	14.83	10.95	8.5
r_p	1	1	1
x_p	0 (10.78)	6 (7.17)	4(5.9)
y_p	0 (-2)	-3 (-3)	-5(-5)
d	3	3	3
h	13	12	12

*All values are in mm.

The antenna gain for the ε_r = 3.27, 6.0, and 9.2 substrate design examples is illustrated in Fig. 14. As expected, the antenna gain for the low permittivity 3.27 substrate is the highest with around 2-3 dB in most of the VSWR $\leq$ 2 bandwidth.

The co- and cross-polar radiation patterns in the $\phi = 0°$ and $\phi = 90°$ planes for the ε_r = 3.27 substrate design example are shown in Fig. 15. It is observed that cross-polar levels are lower in the $\phi = 0°$ plane in comparison with the $\phi = 90°$ plane. This is expected and is due to the asymmetric current distribution in the $\phi = 90°$ plane.

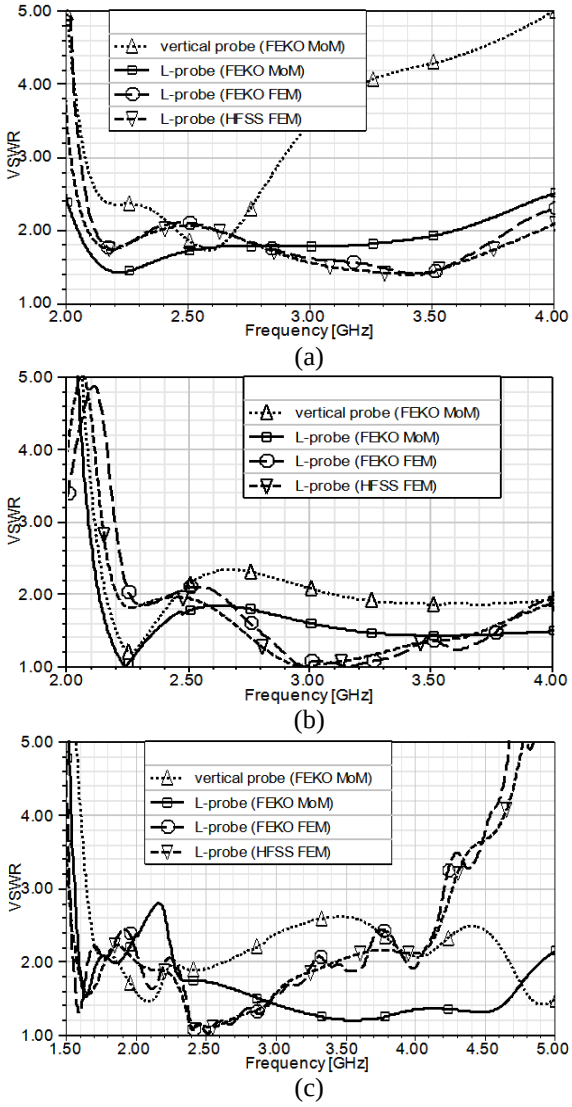

Fig. 13. VSWR with vertical probe and L-probe for substrates (a) ε_r = 3.27, (b) ε_r = 6.0, and (c) ε_r = 9.2.

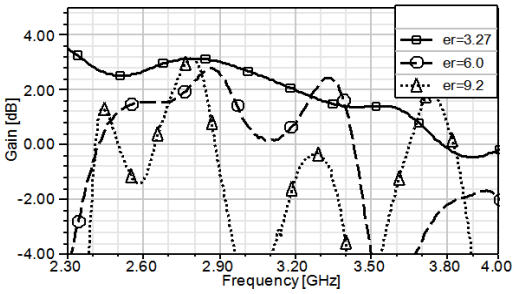

Fig. 14. FEKO FEM gain for ε_r = 3.27, 6.0, and 9.2 substrates.

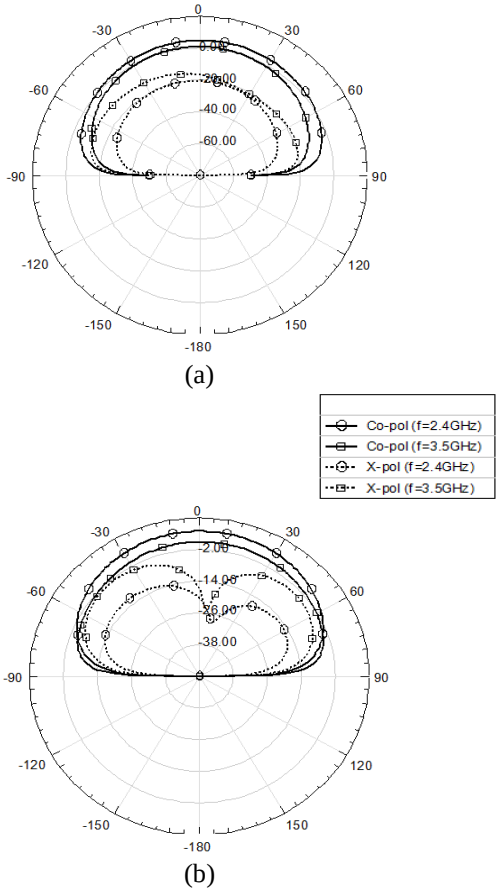

Fig. 15. FEKO MoM co-polar and cross-polar patterns for the L-probe fed U-slot patch design for ε_r = 3.27 substrate at 2.4 GHz and 3.5 GHz: (a) $\phi = 0°$ and (b) $\phi = 90°$.

B. Summary of empirical design technique for L-probe feed

The empirical design technique for the L-probe feed developed above can be summarized as follows:

(a) For $\varepsilon_r = 2.2$ substrates, use initial *first-pass* values of $L_h = 0.08\lambda_o$ and $L_v = 0.08\lambda_o$. For further optimization, use values of $0.08\lambda_o \le L_h \le 0.11\lambda_o$.

(b) For $2.2 < \varepsilon_r < 4.5$ substrates, use initial *first-pass* values of $L_h = 0.05\lambda_o$ and $L_v = 0.08\lambda_o$. For further optimization, use values of $0.05\lambda_o \le L_h \le 0.08\lambda_o$.

(c) For $4.5 \le \varepsilon_r \le 9.2$ substrates, use initial *first-pass* values of $L_h = 0.02\lambda_o$ and $L_v = 0.08\lambda_o$. For further optimization, use values of $0.02\lambda_o \le L_h \le 0.04\lambda_o$ and $0.05\lambda_o \le L_v \le 0.08\lambda_o$.

The design procedure assumes the substrate height, h, is greater than the vertical length of the L-probe, L_v, namely $0.10\lambda_o \le h \le 0.12\lambda_o$. Also, the design procedure assumes the probe diameter, $2r_p$, is less than the horizontal length of the L-probe, L_h, otherwise further optimization to either probe diameter or L_h is needed. The design procedure is applicable for $\varepsilon_r = 2.2$-9.2 substrates only.

V. CONCLUSION

In this paper, an initial, low-profile, wideband U-slot patch design is realized using the method of dimensional invariance. Ideal L-probe feed dimensions are established through extensive parametric study on $\varepsilon_r = 2.2$ and 4.5 substrates to propose empirical guidelines for the design of L-probe feeds which yield *first-pass* optimum impedance bandwidth. The established ideal L-probe dimensions, after further extrapolation, are used successfully on other substrates, $\varepsilon_r = 3.27$, 6.0 and 9.2, for the design of *first-pass* L-probe feeds which yield impedance bandwidth over 55%, 60%, and 53%, respectively.

Results show good agreement between the three EM solvers. FEKO FEM and HFSS FEM results, in particular, show closer agreement. This is to be expected since the same geometry and underlying computational electromagnetic method are used in the two solvers.

REFERENCES

[1] A. Foudazi, H. R. Hassani, and S. M. Nezhad, "Small UWB planar monopole antenna with added GPS/GSM/WLAN bands," *IEEE Transactions on Antennas and Propagation*, vol. 60, no. 6, pp. 2987-2992, June 2012.

[2] H.-D. Chen, C.-Y.-D. Sim, J.-Y. Wu, and T.-W. Chiu, "Broadband high-gain microstrip array antennas for WiMAX base station," *IEEE Transactions on Antennas and Propagation*, vol. 60, no. 8, pp. 3977-3980, August 2012.

[3] M. Bassi, M. Caruso, M. S. Khan, A. Bevilacqua, A. D. Capobianco, and A. Neviani, "An integrated microwave imaging radar with planar antennas for breast cancer detection," *IEEE Transactions on Microwave Theory and Techniques*, vol. 61, no. 5, pp. 2108-2118, May 2013.

[4] K. F. Lee, S. L. S. Yang, A. A. Kishk, and K. M. Luk, "The versatile U-slot patch antenna," *IEEE Antennas and Propagation Magazine*, vol. 52, no. 1, pp. 71-88, February 2010.

[5] Y. X. Guo, K. M. Luk, and K. F. Lee, "U-slot circular patch antennas with L-probe feeding," *Electronics Letters*, vol. 35, no. 20, pp. 1694-1695, September 1999.

[6] K. M. Luk, K. F. Lee, and H. W. Lai, "Development of wideband L-probe couple patch antenna," *Applied Computational Electromagnetics Society (ACES) Journal*, vol. 22, no. 1, pp. 88-96, March 2007.

[7] K. F. Lee and K. M. Luk, *Microstrip Patch Antennas*. Imperial College Press, pp. 255-274, 2011.

[8] V. Natarajan and D. Chatterjee, "An empirical approach for design of wideband, probe-fed, U-slot microstrip patch antennas on single-layer, infinite, grounded substrates," *Applied Computational Electromagnetics Society (ACES) Journal*, vol. 18, no. 3, pp. 191-201, November 2003.

[9] V. Natarajan and D. Chatterjee, "Comparative evaluation of some empirical design techniques for CAD optimization of wideband U-slot microstrip antennas," *Applied Computational Electromagnetics Society (ACES) Journal*, vol. 20, no. 1, pp. 50-69, March 2005.

[10] R. D. Hofer, D. E. Oliver, and D. Chatterjee, "Analysis of U-slot, microstrip phased array radiator elements on electrically thick substrates," *IEEE Antennas and Propagation Society International Symposium*, pp. 3648-3651, June 9-15, 2007.

[11] M. Khan and D. Chatterjee, "Characteristic mode analysis of a class of empirical design techniques for probe-fed, U-slot microstrip patch antennas," *IEEE Transactions on Antennas and Propagation*, vol. 64, no. 7, pp. 2758-2770, July 2016.

[12] M. M. Elsewe, V. K. Dandu, and D. Chatterjee, "Assessment of computational fidelity of MoM and FEM solvers for characterizing a class of UWB microstrip antennas: Single-element case," *29th Annual Review of Progress in Applied Computational Electromagnetics*, Monterey, CA, pp. 393-398, March 24-28, 2013.

Mohamed M. Elsewe is an Engineering Manager at Primus Diagnostics, Kansas City, Missouri. He is a Ph.D. candidate at the University of Missouri Kansas City (UMKC). He obtained his M.S. degree in Electrical Engineering from the University of Missouri, Columbia, Missouri. He has over 10 peer-reviewed articles in the IEEE and Applied Computational Electro-

magnetics Society (ACES) publications. Mohamed's research interests are in the areas of ultra-wideband microstrip patch antennas and phased arrays.

Varun K. Dandu obtained his M.S. degree in Electrical Engineering from the University of Missouri, Kansas City, Missouri. He has published in the IEEE and Applied Computational Electromagnetics Society (ACES) Conference proceedings. Dandu's research interests are focused in the area of design guidelines for ultra-wideband microstrip patch antennas.

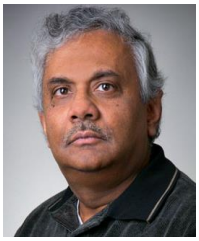

Deb Chatterjee is an Associate Professor of Electrical and Computer Engineering, with the Computer Science and Electrical Engineering (CSEE) Department at University of Missouri Kansas City (UMKC), where he joined as a Faculty in August 1999. He obtained his M.A.Sc. and Ph.D. degrees in Electrical and Computer Engineering and Electrical Engineering, from Concordia University, Montreal, Canada and University of Kansas, Lawrence, Kansas, respectively. His current research interests are in phased arrays, high-frequency scattering and propagation, miniature, ultra-wideband microstrip antennas.

Chatterjee has served as a Reviewer of technical articles for IEEE Transactions on Antennas and Propagation, IEEE Antennas and Wireless Propagation Letters, Radio Science, and the Applied Computational Electromagnetics Society (ACES) Journal. Chatterjee has published over 80 articles in peer-reviewed journals and conference proceedings, and has taught courses in the area of electromagnetics and antennas at undergraduate and graduate levels. He is a Member of the IEEE Antennas and Propagation and the Applied Computational Electromagnetics Societies.

Fully Distributed Analysis of MOS Transistor at Millimeter-Wave Band, Based on Matrix-Functions of the Three Line Active Transmission Lines Model

H. Khoshniyat, A. Abdipour, and G. Moradi

Department of Electrical Engineering, Institute of Communications Technology and Applied Electromagnetics
Amirkabir University of Technology, Tehran, 15914, Iran
hkhoshniyat@aut.ac.ir, abdipour@aut.ac.ir, ghmoradi@aut.ac.ir

Abstract ─ In this paper, distributed model of MOS transistor is presented that is based on active multi-conductor transmission line model. The analysis is done in frequency domain by considering frequency dependence of primary parameters such as series resistance caused by skin effect. The analysis is performed based on matrix function that is calculated by eigenvalue approach in the frequency domain. The scattering parameters are computed by using transmission matrix and applying boundary conditions. To investigate the analysis, the scattering parameters of a 0.13 μm transistor are calculated by proposed approach over the 1–100 GHz frequency band. They compared with the results obtained from the available lumped and distributed models and a commercial simulator that have a good agreement with each other.

Index Terms ─ Active multi transmission lines, distributed analysis, matrix function, MOS transistor, skin effect.

I. INTRODUCTION

Nowadays, the demand for low cost implementation of monolithic microwave integrated circuits leads to considerable progress in CMOS technology [1, 2]. Modern CMOS technologies have been matured enough for using in mm-wave applications. An accurate modeling of high frequency effect in millimeter wave is required for successful design of integrated CMOS circuits [3, 4]. By increasing the operating frequency of MOSFET to mm-wave band, the width of transistor becomes comparable to the wavelength. In such cases, the wave propagation through transistor's electrodes and distributed transmission line effects need to be studied accurately, in device modeling.

In [5], [6] and [7] the distributed transmission line effect along the gate width has been investigated. In these models, the gate electrode is divided into finite number of segments that are connected together by using of series of scaled gate resistor. In [8], the distributed transmission line signal and noise modeling of millimeter wave CMOS transistor is studied. The MOSFET transistor is considered as coupled active transmission lines structure, exciting by the noise equivalent sources distributed on its conductors.

In [9], distributed modeling of field effect transistors in the case of GaAs MESFET is studied. The transistor is considered as a multi-conductor active transmission line and the equations are solved by the Finite-Difference Time-Domain (FDTD) technique. According to this approach, the fully distributed analysis of CMOS transistor in the time domain has been studied in [10], based on the active multi-conductor transmission lines model.

In this paper, distributed model of MOS transistor based on active multi-conductor transmission line is presented. The analysis is performed in the frequency domain by considering frequency dependence of primary parameters such as series resistance that caused by skin effect. Based on matrix function calculated by eigenvalue approach, the analysis is done in the frequency domain. The scattering parameters are computed by using transmission matrix and applying boundary conditions. To verify the analysis, the scattering parameters of a 0.13 μm transistor are calculated by proposed approach over the 1–100 GHz frequency band and compared with the results obtained from the available lumped and distributed models and Cadence SpectreRF simulator that shown a good agreement with each other.

II. DISTRIBUTED MODEL OF TRANSISTOR

The schematic of MOSFET, is shown in Fig. 1. At high frequencies, the wavelength becomes comparable to the width of transistor and wave propagation through transistor's electrodes must be assumed. To consider this distributed effect, MOSFET can be modeled as three coupled transmission lines.

Submitted On: May 30, 2016
Accepted On: September 9, 2016

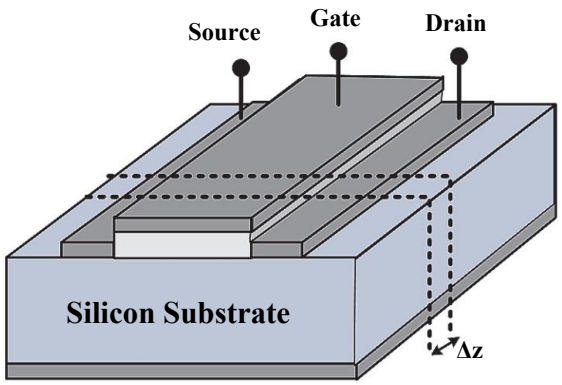

Fig. 1. The schematic of MOSFET as three coupled transmission lines on silicon substrate.

A. Transmission line model and equations

By considering the differential width of Δz (Δz << $\lambda_g(f_{max})$), the partial equivalent model of MOSFET is obtained as shown in Fig. 2. The equivalent model of MOSFET is combination of active and passive parts. Active part explains the behavior of intrinsic device while the passive part shows electromagnetic interaction between electrodes.

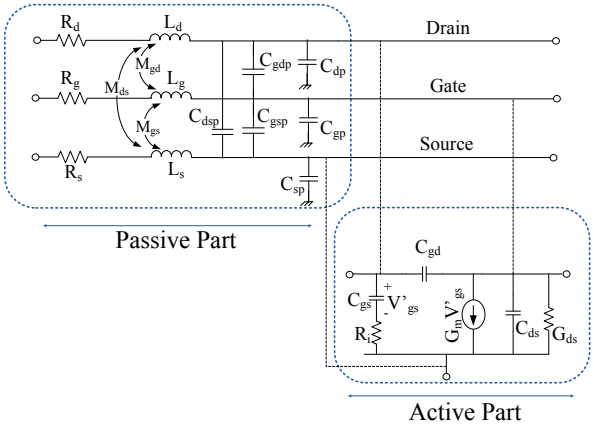

Fig. 2. The equivalent model of MOSFET.

By using of Kirchhoff's circuit laws, the matrix equations are achieved in the phasor domain as [11]:

$$\frac{d\mathbf{V}(z,\omega)}{dz} = -\mathbf{Z}_s(\omega)\mathbf{I}(z,\omega), \tag{1}$$

$$\frac{d\mathbf{I}(z,\omega)}{dz} = -\mathbf{Y}_p(\omega)\mathbf{V}(z,\omega). \tag{2}$$

The voltage and current matrices are defined as:

$$\mathbf{V}(z,\omega) = \begin{bmatrix} V_d & V_g & V_s \end{bmatrix}^T (z,\omega), \tag{3}$$

$$\mathbf{I}(z,\omega) = \begin{bmatrix} I_d & I_g & I_s \end{bmatrix}^T (z,\omega). \tag{4}$$

The series impedance and parallel admittance matrices are defined as:

$$\mathbf{Z}_s = \mathbf{R} + j\omega\mathbf{L}, \tag{5}$$

$$\mathbf{Y}_p = \mathbf{Y}_{TL} + \mathbf{Y}_{FET} = j\omega\mathbf{C} + \mathbf{Y}_{FET}. \tag{6}$$

Based on equivalent model, the primary matrices $(\mathbf{R},\mathbf{L},\mathbf{C})$ and $\mathbf{Y}_{FET}$ are obtained as shown in equations (7-10):

$$\mathbf{R} = \begin{bmatrix} R_d & 0 & 0 \\ 0 & R_g & 0 \\ 0 & 0 & R_s \end{bmatrix}, \tag{7}$$

$$\mathbf{L} = \begin{bmatrix} L_d & M_{gd} & M_{ds} \\ M_{gd} & L_g & M_{gs} \\ M_{ds} & M_{gs} & L_s \end{bmatrix}, \tag{8}$$

$$\mathbf{C} = \begin{bmatrix} C_{dp}+C_{gdp}+C_{dsp} & -C_{gdp} & -C_{dsp} \\ -C_{gdp} & C_{gp}+C_{gdp}+C_{gsp} & -C_{gsp} \\ -C_{dsp} & -C_{gsp} & C_{sp}+C_{dsp}+C_{gsp} \end{bmatrix}, \tag{9}$$

$$\mathbf{Y}_{FET} = \begin{bmatrix} Y_{11} & Y_{12} & Y_{13} \\ Y_{21} & Y_{22} & Y_{23} \\ Y_{31} & Y_{32} & Y_{33} \end{bmatrix},$$

$$Y_{11} = G_{ds} + j\omega(C_{gd}+C_{ds}), Y_{12} = -j\omega C_{gd} + G_m \frac{1}{1+j\omega R_i C_{gs}},$$

$$Y_{13} = -G_{ds} - j\omega C_{ds} - G_m \frac{1}{1+j\omega R_i C_{gs}}, Y_{21} = -j\omega C_{gd},$$

$$Y_{22} = j\omega C_{gd} + \frac{j\omega C_{gs}}{1+j\omega R_i C_{gs}}, Y_{23} = -\frac{j\omega C_{gs}}{1+j\omega R_i C_{gs}},$$

$$Y_{31} = -G_{ds} - j\omega C_{ds}, Y_{32} = -\frac{G_m + j\omega C_{gs}}{1+j\omega R_i C_{gs}},$$

$$Y_{33} = \frac{G_m + j\omega C_{gs}}{1+j\omega R_i C_{gs}} + G_{ds} + j\omega C_{ds}. \tag{10}$$

By considering the skin effect, the series resistance is proportional to the square of frequency and can be represented as:

$$R_i = \chi_i \sqrt{f} \qquad i = g,d,s\ . \tag{11}$$

In Fig. 3, the schematic of simulated MOSFET is shown. Based on chain matrix, the $\mathbf{V}$ and $\mathbf{I}$ matrices at $z=0$ are calculated from the $\mathbf{V}$ and $\mathbf{I}$ matrices at $z=l$. This is expressed with matrix-functions as [11]:

$$\begin{bmatrix} \mathbf{V}(0) \\ \mathbf{I}(0) \end{bmatrix} = \begin{bmatrix} \cosh(\sqrt{\mathbf{Z}_s\mathbf{Y}_p}\,l) & \sinh(\sqrt{\mathbf{Z}_s\mathbf{Y}_p}\,l)\mathbf{Z}_C \\ \mathbf{Z}_C^{-1}\sinh(\sqrt{\mathbf{Z}_s\mathbf{Y}_p}\,l) & \mathbf{Y}_p\cosh(\sqrt{\mathbf{Z}_s\mathbf{Y}_p}\,l)\mathbf{Y}_p^{-1} \end{bmatrix} \begin{bmatrix} \mathbf{V}(l) \\ \mathbf{I}(l) \end{bmatrix}. \tag{12}$$

The characteristic impedance matrix ($\mathbf{Z}_C$) can be written as [11]:

$$\mathbf{Z}_C = \mathbf{Y}_P^{-1}\sqrt{\mathbf{Y}_P\mathbf{Z}_s} = \mathbf{Z}_s\left(\sqrt{\mathbf{Y}_P\mathbf{Z}_s}\right)^{-1}. \tag{13}$$

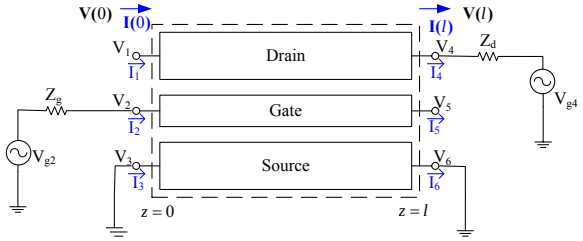

Fig. 3. The schematic of simulated MOSFET.

B. Intrinsic parameters of MOSFET

The intrinsic parameters of MOS transistor including G_m, C_{gs}, C_{ds}, C_{gd}, R_i, and G_{ds} (active part parameters) are calculated based on the accurate physical model of the MOSFET, BSIM3v3. The drain-source current by using a complete single equation for both linear and saturation regions is expressed as:

$$I_{ds} = \frac{I_{ds0}(V_{dseff})}{1+\dfrac{R_{ds}I_{ds0}(V_{dseff})}{V_{dseff}}}\left(1+\frac{V_{ds}-V_{dseff}}{V_A}\right) \cdot\left(1+\frac{V_{ds}-V_{dseff}}{V_{ASCBE}}\right). \tag{14}$$

The transistor conductance G_m can be obtained as:

$$G_m = \left.\frac{\partial I_{ds}}{\partial V_{gs}}\right|_{V_{ds=Const.}} . \tag{15}$$

Also, all capacitances are derived from the charges to ensure charge conservation as:

$$C_{ij} = \frac{\partial Q_i}{\partial V_j};\ \ i,j = g,d,s,b\ \ , \tag{16}$$

where the terminal charges Q_g, Q_b, Q_s, and Q_s are the charges associated with the gate, bulk, source, and drain terminals, respectively. The details of this model containing other equations and the parameters description are given in [12].

C. Solving equations

As shown in Fig. 3, the chain matrix can be assumed as a six-port network that ports 1, 2 and 3 are inputs ($z=0$) and ports 4, 5 and 6 are outputs ($z=l$). The six-port matrix ($\mathbf{T}$) equation is shown as:

$$\begin{bmatrix} V_1 \\ V_2 \\ V_3 \\ I_1 \\ I_2 \\ I_3 \end{bmatrix} = \begin{bmatrix} T_{11} & T_{12} & T_{13} & T_{14} & T_{15} & T_{16} \\ T_{21} & T_{22} & T_{23} & T_{24} & T_{25} & T_{26} \\ T_{31} & T_{32} & T_{33} & T_{34} & T_{35} & T_{36} \\ T_{41} & T_{42} & T_{43} & T_{44} & T_{45} & T_{46} \\ T_{51} & T_{52} & T_{53} & T_{54} & T_{55} & T_{56} \\ T_{61} & T_{62} & T_{63} & T_{64} & T_{65} & T_{66} \end{bmatrix} \begin{bmatrix} V_4 \\ V_5 \\ V_6 \\ I_4 \\ I_5 \\ I_6 \end{bmatrix}. \tag{17}$$

Based on Fig. 3, the boundary conditions are applied to matrix equation that is shown as:

$$\begin{bmatrix} V_1 \\ V_2 \\ 0 \\ 0 \\ \dfrac{V_{g2}-V_2}{Z_g} \\ I_3 \end{bmatrix} = \begin{bmatrix} T_{11} & T_{12} & T_{13} & T_{14} & T_{15} & T_{16} \\ T_{21} & T_{22} & T_{23} & T_{24} & T_{25} & T_{26} \\ T_{31} & T_{32} & T_{33} & T_{34} & T_{35} & T_{36} \\ T_{41} & T_{42} & T_{43} & T_{44} & T_{45} & T_{46} \\ T_{51} & T_{52} & T_{53} & T_{54} & T_{55} & T_{56} \\ T_{61} & T_{62} & T_{63} & T_{64} & T_{65} & T_{66} \end{bmatrix} \begin{bmatrix} V_4 \\ V_5 \\ 0 \\ \dfrac{V_4-V_{g4}}{Z_d} \\ 0 \\ I_6 \end{bmatrix}. \tag{18}$$

In Equation (18), V_1, V_2, V_4, V_5, I_3 and I_6 are unknowns while the elements of $\mathbf{T}$ (T_{ij}), Z_g and Z_d are knowns; V_{g2} and V_{g4} are input voltages for calculating scattering parameters. The unknowns ($\mathbf{X}$) and input voltages ($\mathbf{V_g}$) are considered as:

$$\mathbf{X} = \begin{bmatrix} V_1 & V_2 & V_4 & V_5 & I_3 & I_6 \end{bmatrix}^T, \tag{19}$$

$$\mathbf{V_g} = \begin{bmatrix} 0 & V_{g2} & 0 & V_{g4} & 0 & 0 \end{bmatrix}^T. \tag{20}$$

By arranging Equation (18) based on unknowns ($\mathbf{X}$) and input voltages ($\mathbf{V_g}$), the matrix equation with coefficient matrices ($\mathbf{A}$ and $\mathbf{B}$) is obtained as:

$$\mathbf{AX} = \mathbf{BV_g}, \tag{21}$$

$$\mathbf{X} = \mathbf{A}^{-1}\mathbf{BV_g}. \tag{22}$$

For example, by sorting the first row of Equation (18), the first row of $\mathbf{A}$ and $\mathbf{B}$ are achieved as:

$$\begin{aligned} V_1 &= T_{11}V_4 + T_{12}V_5 + T_{14}\frac{V_4 - V_{g4}}{Z_d} + T_{16}I_6, \\ \frac{T_{14}}{Z_d}V_{g4} &= -V_1 + \left(T_{11} + \frac{T_{14}}{Z_d}\right)V_4 + T_{12}V_5 + T_{16}I_6. \end{aligned} \tag{23}$$

By arranging the other rows of Equation (18), the coefficient matrices ($\mathbf{A}$ and $\mathbf{B}$) are obtained as:

$$\mathbf{A} = \begin{bmatrix} -1 & 0 & T_{11}+\dfrac{T_{14}}{Z_d} & T_{12} & 0 & T_{16} \\ 0 & -1 & T_{21}+\dfrac{T_{24}}{Z_d} & T_{22} & 0 & T_{26} \\ 0 & 0 & T_{31}+\dfrac{T_{34}}{Z_d} & T_{32} & 0 & T_{36} \\ 0 & 0 & T_{41}+\dfrac{T_{44}}{Z_d} & T_{42} & 0 & T_{46} \\ 0 & \dfrac{1}{Z_g} & T_{51}+\dfrac{T_{54}}{Z_d} & T_{52} & 0 & T_{56} \\ 0 & 0 & T_{61}+\dfrac{T_{64}}{Z_d} & T_{62} & -1 & T_{66} \end{bmatrix}, \tag{24}$$

$$\mathbf{B}=\begin{bmatrix} 0 & 0 & 0 & \frac{T_{14}}{Z_d} & 0 & 0 \\ 0 & 0 & 0 & \frac{T_{24}}{Z_d} & 0 & 0 \\ 0 & 0 & 0 & \frac{T_{34}}{Z_d} & 0 & 0 \\ 0 & 0 & 0 & \frac{T_{44}}{Z_d} & 0 & 0 \\ 0 & \frac{1}{Z_g} & 0 & \frac{T_{54}}{Z_d} & 0 & 0 \\ 0 & 0 & 0 & \frac{T_{64}}{Z_d} & 0 & 0 \end{bmatrix}. \quad (25)$$

D. Computing scattering parameters

Based on scattering matrix definition, by assuming port 2 as input port and port 4 as output port, the scattering parameters are obtained as:

$$S_{11}, S_{21}\Big|_{V_{gi}=V_{g2}=V_g \;\&\; V_{go}=V_{g4}=0}, \quad (26)$$

$$\mathbf{V_g}=\begin{bmatrix}0 & V_g & 0 & 0 & 0 & 0\end{bmatrix}^T. \quad (27)$$

By considering $\mathbf{V_g}$ as was defined in (27), the unknown matrix ($\mathbf{X}$) is computed from (22) and input and output voltages are extracted as:

$$V_i=V_2=X(2)\ ,\ V_o=V_4=X(3). \quad (28)$$

The forward and backward voltage wave at input and output ports are defined as:

$$I_2=\frac{V_{g2}-V_2}{Z_g},$$

$$V_i^+=V_2^+=\frac{1}{2}\left(V_2+Z_gI_2\right)=\frac{V_{g2}}{2}, \quad (29)$$

$$V_i^-=V_2^-=\frac{1}{2}\left(V_2-Z_gI_2\right)=V_2-\frac{V_{g2}}{2},$$

$$I_4=\frac{V_4-V_{g4}}{Z_d},$$

$$V_o^+=V_4^+=\frac{1}{2}\left(V_4-Z_dI_4\right)=\frac{V_{g4}}{2}, \quad (30)$$

$$V_o^-=V_4^-=\frac{1}{2}\left(V_4+Z_dI_4\right)=V_4-\frac{V_{g4}}{2}.$$

The S_{11} and S_{21} are calculated as:

$$S_{11}=\frac{V_i^-}{V_i^+}\Big|_{V_{g4}=0}, \quad (31)$$

$$S_{21}=\frac{V_o^-}{V_i^+}\Big|_{V_{g4}=0}. \quad (32)$$

Similarly when $V_{gi}=V_{g2}=0$ and $V_{go}=V_{g4}=V_g$, the S_{12} and S_{22} are computed as:

$$S_{12}=\frac{V_i^-}{V_o^+}\Big|_{V_{g2}=0}, \quad (33)$$

$$S_{22}=\frac{V_o^-}{V_o^+}\Big|_{V_{g2}=0}. \quad (34)$$

The step by step procedure of fully distributed analysis in the frequency domain is shown in Fig. 4.

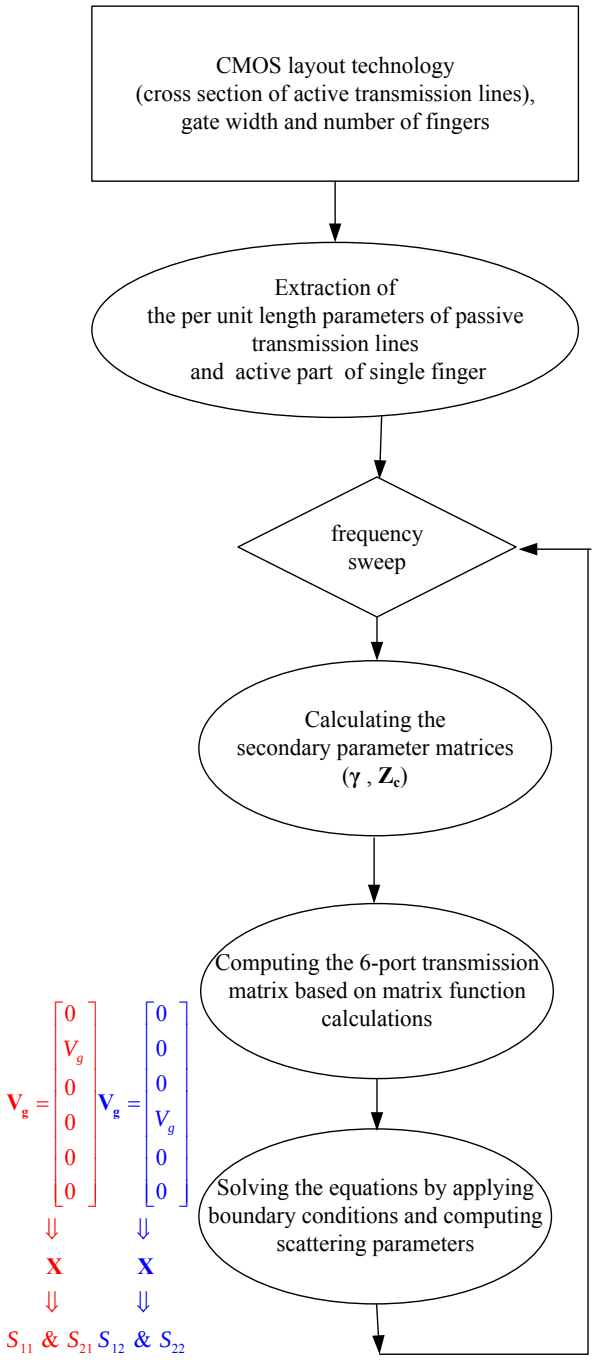

Fig. 4. The step by step flowchart of the proposed fully distributed method.

III. REULTS AND DISCUSSION

In order to analyze the MOS transistor with the proposed method, a single finger MOSFET with gate dimension of 0.13×10 μm is studied as shown in Fig. 3. In this example, both R_g and R_d are assumed to be 50 Ω. The end of gate electrode and the beginning of drain electrode are open, while both sides of the source electrode are grounded.

The per-unit-length parameters of the intrinsic MOSFET (active parameters) are achieved by using the BSIM3v3 model at the V_{gs}=1.2 V and V_{ds}=1.2 V bias point, with applying scaling technique. The per-unit-length capacitance and inductance matrixes of the passive part of the transistor are numerically specified by solving the two-dimensional electrostatic field problem in the cross section of each transmission lines. The per-unit-length resistances of the passive part of the MOSFET are obtained by considering the skin effect of the transistor electrodes. The achieved parameters are shown in Table 1 [10].

Table 1: The parameters of the passive part of distributed model [10]

Parameter	Value
L_d	1.919 μH/m
L_s	1.919 μH/m
L_g	1.95 μH/m
M_{gd}	1.54 μH/m
M_{gs}	1.54 μH/m
M_{ds}	1.407 μH/m
χ_d	3.2255 Ω. Hz $^{-0.5}$/m
χ_s	3.9781 Ω. Hz $^{-0.5}$/m
χ_g	3.2255 Ω. Hz $^{-0.5}$/m
C_{gp}	136.75 pF/m
C_{dp}	110.5 pF/m
C_{sp}	110.5 pF/m
C_{gdp}	63.07 pF/m
C_{gsp}	63.07 pF/m
C_{dsp}	29.65 pF/m

The scattering parameters of the transistor are obtained by the proposed approach at 1-100 GHz and compared with those of achieved by lumped model of the MOS transistor, distributed gate model [7], distributed time domain analysis [10] and also Cadence simulator. The scattering parameters are shown in Fig. 5. It seems that the results of all methods are in good agreement at low frequencies. But, the difference between the results becomes larger by increasing the frequency. Especially at higher frequencies, the results of proposed distributed approach are closer to the Cadence SpectreRF simulator results. At high frequencies the transistor width become order of the wavelength and this justified difference between various modeling approaches obviously. In such cases, the distributed analysis of the transistor based on multi conductor transmission lines can explain the behavior of the device at high frequencies more precise than others. Also, the frequency dependence of series resistance that caused by skin effect is considered by using the frequency domain approach based on transmission matrix equation.

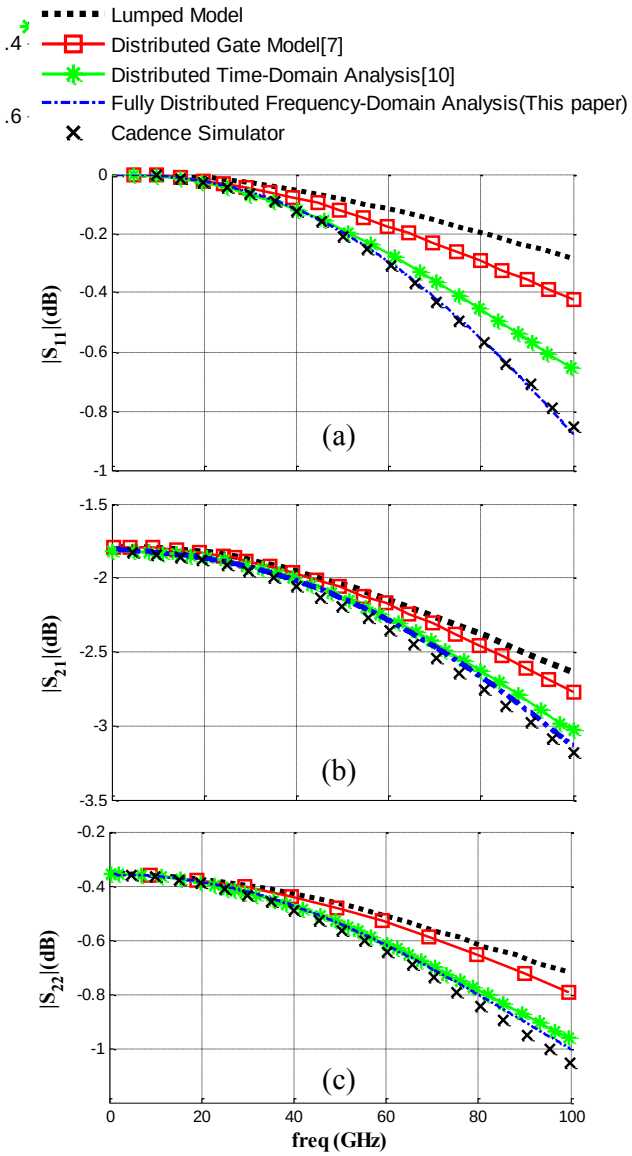

Fig. 5. The scattering parameters of the MOSFET: (a) S_{11}, (b) S_{21}, and (c) S_{22}.

The G_{MAX} versus frequency is one of the behavioral parameters of transistor that defined based on scattering parameters as [13]:

$$G_{MAX} = \begin{cases} MAG = (K - \sqrt{K^2 - 1}) \dfrac{|S_{21}|}{|S_{12}|} & K > 1 \\ \\ MSG = \dfrac{|S_{21}|}{|S_{12}|} & K < 1 \end{cases}, \quad (35)$$

where K (Rollet stability factor) is defined as:

$$K = \frac{1 - |S_{11}|^2 - |S_{22}|^2 + |\Delta|^2}{2|S_{21}S_{12}|}, \quad (36)$$

$$\Delta = S_{11}S_{22} - S_{12}S_{21}. \quad (37)$$

In Fig. 6, maximum gain versus frequency is shown for the 8-finger 0.13µm×50µm MOSFET. The behavior of transistor is analyzed with different methods (lumped model, semi distributed (5 and 50 slices) and fully distributed methods). Results of semi distributed model with the large number of sections have a good agreement with that of fully distributed model. Based on this graph, the f_{max} of transistor was extracted around 60 GHz.

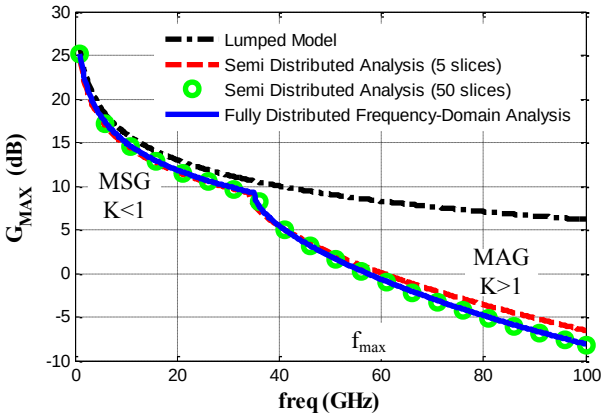

Fig. 6. Gmax (Maximum Available Gain (MAG) and Maximum Stable Gain (MSG)) versus frequency with lumped, semi and fully distributed analysis.

IV. CONCLUSION

The fully distributed analysis for high frequency MOSFETs based on three coupled transmission lines structure has been proposed. The matrix-based equations of that structure are extracted and solved using the frequency domain matrix function with applying boundary conditions and considering the frequency dependence of series resistance. By using the proposed method for a 0.13 µm MOS transistor, the small signal parameters have been obtained at 1–100 GHz and compared with the conventional models. Results of the proposed method present a good agreement with other models at low frequencies. But for the higher frequencies the differences become considerable and the calculated result of proposed approach is closer to the commercial simulator. Thus, the three-conductor transmission line modeling of MOS transistors in the frequency domain is more accurate than other conventional methods.

APPENDIX A. FUNCTIONS OF MATRICES

Computing a function $f(\mathbf{A})$ of an n-by-n matrix $\mathbf{A}$ is a popular problem in many application domains. If $\mathbf{A} \in \mathbb{C}^{n \times n}$ is diagonalizable, then it is particularly easy to specify $f(\mathbf{A})$ in terms of $\mathbf{A}$'s eigenvalues and eigenvectors [14].

If $\mathbf{A} \in \mathbb{C}^{n \times n}$, $\mathbf{A} = \mathbf{X}.diag(\lambda_1,...,\lambda_n).\mathbf{X}^{-1}$, and $f(\mathbf{A})$ is defined, then

$$f(\mathbf{A}) = \mathbf{X}.diag(f(\lambda_1),..., f(\lambda_n)).\mathbf{X}^{-1} \quad . \quad (A\text{-}1)$$

By using of matrix relations, the matrix function can be represented easily as:

$$f(\mathbf{A}) = \mathbf{X}.f(\mathbf{X}^{-1}.\mathbf{A}.\mathbf{X}).\mathbf{X}^{-1} \quad . \quad (A\text{-}2)$$

REFERENCES

[1] Z. Y. Cui, J. W. Park, C. S. Lee, and N. S. Kim, "Integration of CMOS logic circuits with lateral power MOSFET," *2013 4th International Conference on Intelligent Systems Modelling & Simulation (ISMS)*, pp. 615-618, Jan. 2013.

[2] A. M. Niknejad and H. Hashemi, *mm-Wave Silicon Technology 60 GHz and Beyond*. Springer Science+Business Media, LLC, 2008.

[3] S. Ma, J. Ren, and H. Yu, "An overview of new design techniques for high performance CMOS millimeter-wave circuits," in Proc. 14th Int. Symp. Integrated Circuits (ISIC), pp. 292-295, Dec. 2014.

[4] A. A. Abidi, "CMOS microwave and millimeter-wave ICs: The historical background," *in Proc. IEEE Int. Symp. Radio-Frequency Integrated Technology (RFIT)*, pp. 1-5, Aug. 2014.

[5] B. Razavi, R.-H. Yan, and K. F. Lee, "Impact of distributed gate resistance on the performance of MOS devices," *IEEE Trans. Circuits Syst. I*, vol. 41, pp. 750-754, Nov. 1994.

[6] E. Abou-Allam and T. Manku, "A small signal MOSFET model for radio frequency IC applications," *IEEE Trans. Computer-Aided Design*, vol. 16, pp. 437-447, May 1997.

[7] E. Abou-Allam and T. Manku, "An improved transmission-line model for MOS transistors," *IEEE Transaction on Circuits and Systems*, vol. 46, pp. 1380-1387, May 1999.

[8] Z. Seifi, A. Abdipour, and R. Mirzavand, "Distributed signal and noise modeling of millimeter wave transistor based on CMOS technology," *Applied Computational Electro-magnetics Society (ACES) Journal*, vol. 30, no. 8, pp. 915-921, Aug. 2015.

[9] K. Afrooz, A. Abdipour, A. Tavakoli, and Movahhedi, "FDTD analysis of small signal model for GaAs MESFETs based on three line structure,"

Asia-Pacific Microwave Conference APMC, pp. 1-4, 2007.
[10] F. Daneshmandian, A. Abdipour, and R. Mirzavand, "A three-conductor transmission line model for MOS transistors," *Applied Computational Electromagnetics Society (ACES) Journal*, vol. 30, no. 6, pp. 670-676, June 2015.
[11] C. R. Paul, *Analysis of Multiconductor Transmission Lines*. 2nd edition, John Wiley & Sons, Inc., Hoboken, New Jersey, 2008.
[12] C. Yuhua, et al., "*BSIM3v3 Manual: Final version*," University of California, Berkeley, 1996.
[13] J. Rollett, "Stability and power-gain invariants of linear two ports," *in IRE Transactions on Circuit Theory*, vol. 9, no. 1, pp. 29-32, Mar. 1962.
[14] G. H. Golub and C. F. Van Loan, *Matrix Computations*. 4th edition, The Johns Hopkins University Press, Baltimore, 2013.

Hamed Khoshniyat was born in Karaj, Iran, in 1985. He received the B.Sc. and M.Sc. degrees from the Amirkabir University of Technology (Tehran Polytechnic), Tehran, Iran, both in Electrical Engineering, in 2008 and 2010 respectively. He is currently working toward the Ph.D. degree in "Fields and Waves" and a Research Assistant in the Wave Propagation and Microwave Measurement Laboratory (WPMML) in Electrical Engineering at Amirkabir University of Technology (Tehran Polytechnic). His current research interests include analysis and modeling of distributed amplifiers and switches, non-Foster elements, active and passive microwave device and circuits and microwave measurement.

Abdolali Abdipour was born in Alashtar, Iran, in 1966. He received his B.Sc. degree in Electrical Engineering from Tehran University, Tehran, Iran, in 1989, his M.Sc. degree in Electronics from Limoges University, Limoges, France, in 1992, and his Ph.D. degree in Electronic Engineering from Paris XI University, Paris, France, in 1996. He is currently a Professor with the Electrical Engineering Department, Amirkabir University of Technology (Tehran Polytechnic), Tehran, Iran. He has authored 5 books and has authored or co-authored over 300 papers in refereed journals and local and international conferences. His research areas include wireless communication systems (RF technology and transceivers), RF/microwave/millimeter-wave/THz circuit and system design, electromagnetic (EM) modeling of active devices and circuits, high-frequency electronics (signal and noise), nonlinear modeling, and analysis of microwave devices and circuits.

Gholamreza Moradi was born in Shahriar, Iran in 1966. He received his B.Sc. in Electrical Communication Engineering from Tehran University, Tehran, Iran in 1989, and the M.Sc. in the same field from Iran University of Science and Technology in 1993. Then he received his Ph.D. degree in Electrical Engineering from Tehran Polytechnic University, Tehran, Iran in 2002. His research areas include applied and numerical Electromagnetics, Microwave measurement and antenna. He has published more than fifty journal papers and has authored/co-authored five books in his major. He is currently an Associate Professor with the Electrical Engineering Department, Amirkabir University of Technology (Tehran Polytechnic), Tehran, Iran. He is now a Visiting Professor at the University of Alberta.

An Efficient Spectral Element Method for Semiconductor Transient Simulation

Huaguang Bao [1], Dazhi Ding [1], Junjian Bi [2], WenYang Gu [1], and Rushan Chen [1]

[1] Department of Communication Engineering
Nanjing University of Science and Technology, Nanjing, 210094, China
dzding@njust.edu.cn

[2] Key Laboratory of Electromagnetic Environment Effect
Ordnance Engineering College, Shijiazhuang, 05003, China

Abstract ─ An efficient spectral element method (SEM) based on Gauss-Lobatto-Legendre (GLL) polynomials is proposed for the semiconductor transient simulation. The fully coupled Newton iteration method is employed to solve the nonlinear drift-diffusion model. The mix-order basis functions with different variables and domains are employed to give a full play to the superiority of the proposed SEM. The PIN diode with quasi one-dimensional structure has been analyzed, and the numerical results have demonstrated the efficiency and accuracy of the proposed method.

Index Terms ─ Gauss-Lobatto-Legendre (GLL) polynomials, mix-order basis function, PIN diode, Spectral Element Method (SEM).

I. INTRODUCTION

The drift-diffusion model is a common way to describe the interior carrier behavior of semiconductor devices, and it is a directly-coupled system of three nonlinear partial differential equations [1]. During the past few decades, numerical methods such as finite element method (FEM) and finite difference method (FDM) have been employed to solve the equations [1, 2]. In consideration of the efficiency and accuracy, several adaptive grid refinement strategies have been proposed [3, 4], but the implementation is relatively cumbersome. Recently, the spectral element method (SEM) has shown its higher accuracy and lower computation cost than FEM or FDM [5, 6, 10, 11]. The efficient SEM has been proposed to solve the Schrödinger's equation in nanodevice simulation [7] and the high power microwave propagation problems [8].

In this paper, the spectral element method based on the drift-diffusion model has been developed for semiconductor transient simulation. The Gauss-Lobatto-Legendre (GLL) polynomials are used as the basis function to expand the variables, and it gets the advantage that the error decreases exponentially with the polynomial order increases, called spectral accuracy [8]. To minimize the unknowns, different orders of the basis function can be selected with the following criterion: the higher order of the basis function for the variables with larger range of values such as electron concentration and hole concentration, and the higher order of the basis function for the domain with rapid changing values for the same variable.

The organizations of this article are as follows. In Section II, the basic theory of SEM based on GLL polynomials has been described briefly. Then, the detailed process about how to solve the drift-diffusion model with the spectral element method, and the two strategies that the different orders of the basis function are selected according to the different variables and domains has been introduced specifically. Next, in Section III, the overshoot phenomena in PIN diode with quasi one-dimensional structure has been analyzed to demonstrate the efficiency and accuracy with the proposed method.

II. FORMULATION

The drift-diffusion model is composed of three nonlinear differential equations, the electronic and hole current continuity equations and Poisson equation [2], described as:

$$\begin{aligned} \frac{\partial n}{\partial t} &= \frac{1}{q}\nabla\cdot\mathbf{J}_n + G - R \\ \frac{\partial p}{\partial t} &= -\frac{1}{q}\nabla\cdot\mathbf{J}_p + G - R \\ \nabla^2\varphi &= -\frac{q}{\varepsilon}(N_0 + p - n) \end{aligned}, \tag{1}$$

where φ is the electrostatic potential, q is the electric charge, N_0 is the electrically active net impurity

Submitted On: December 31, 2015
Accepted On: July 27, 2016

concentration, ε is the permittivity, and n and p are the electron and hole carrier densities. G and R describe the generation phenomena and recombination processes. The electron and hole current densities symbolized by $\mathbf{J}_n$ and $\mathbf{J}_p$ are given by:

$$\begin{aligned}\mathbf{J}_n &= qD_n\nabla n - q\mu_n n\nabla\varphi \\ \mathbf{J}_p &= -qD_p\nabla p - q\mu_p p\nabla\varphi,\end{aligned} \tag{2}$$

where D_n and D_p are the corresponding diffusion coefficients, and μ_n and μ_p are the electron and hole mobility.

A. Basis functions

The difference between SEM and FEM lies in the choice of the expansion basis. In order to achieve the high accuracy, the GLL basis functions are employed throughout this article. A rough introduction is shown as follows, and more details can be found in the reference [7].

The Nth order GLL basis functions in a 3-D cubic element $(\xi,\eta,\zeta)\in[-1,1]\times[-1,1]\times[-1,1]$ can be written as:

$$\Phi_{rst}(\xi,\eta,\zeta)=\phi_r^{(N_\xi)}(\xi)\phi_s^{(N_\eta)}(\eta)\phi_t^{(N_\zeta)}(\zeta), \tag{3}$$

for $r=0,1,...,N_\xi; s=0,1,...,N_\eta; t=0,1,...,N_\zeta$. Here, $\phi_r^{(N_\xi)}(\xi)$, $\phi_s^{(N_\eta)}(\eta)$ and $\phi_t^{(N_\zeta)}(\zeta)$ represent the basis functions with three directions and have the following definition:

$$\phi_j^{(\mathrm{N})}=\frac{-1}{N(\mathrm{N}+1)\mathrm{L}_N(\xi_j)}\frac{(1-\xi^2)\mathrm{L}_N'(\xi)}{(\xi-\xi_j)}, \tag{4}$$

Here, $\mathrm{L}_N(\xi)$ and $\mathrm{L}_N'(\xi)$ are the Legendre polynomial of Nth order and its derivative. The points $\{\xi_j, \mathrm{j}=0,1,...,\mathrm{N}\}$ are the zeros of $(1-\xi^2)\mathrm{L}_N'(\xi_j)=0$.

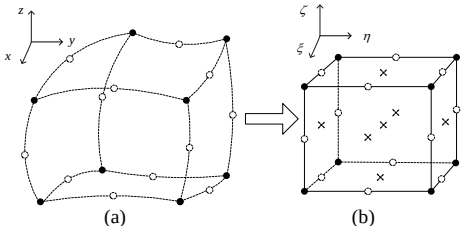

Fig. 1. The mapping from the: (a) physical to the (b) reference domain.

Because of the basis functions definition on the standard cubic element, the mapping from the physical to the reference domain is essential for general meshes as shown in Fig. 1. The basis functions below the physical coordinate and reference one have the following relationship:

$$\begin{cases}N_i=\Phi_i \\ \nabla N_i=\mathbf{J}^{-1}\nabla\Phi_i\end{cases}, \tag{5}$$

where N_i and Φ_i represent the basis functions for the physical and reference coordinate, and $\mathbf{J}$ is the Jacobian matrix.

B. SEM for semiconductor simulation

Here, the electron and hole concentrations and electric potential are selected as the unknown variables. The fully coupled Newton iteration method is employed to solve the nonlinear equations.

Taking electronic current continuity equation for an example, the specific derivation process is introduced here. Firstly, the equation should be normalized into dimensionless form and the factors can be found in [2]. For the time partial derivative, the backward difference operator is employed to achieve the unconditional stability with a large time step represented by Δt:

$$\frac{n^{\mathrm{m}}-n^{m-1}}{\Delta t}=f_n(n^m,p^m,\varphi^m), \tag{6}$$

where $f_n(n,p,\varphi)=\nabla\cdot(\mu_n\nabla n-\mu_n n\nabla\varphi)-(R-G)$, and n^{m} represents the electron carrier densities at the time of $m\Delta t$. The Equation (6) is equivalent to the following form:

$$F_n(n^m,p^m,\varphi^m)=f_n(n^m,p^m,\varphi^m)\cdot\Delta t-\left(n^m-n^{m-1}\right)=0. \tag{7}$$

Expand the formula (7) using the Taylor series and just retain the first order item. Then, the Newton iterative formula can be obtained finally:

$$\begin{aligned}&F_n\left(n^{m,l},p^{m,l},\varphi^{m,l}\right)+\left.\frac{\partial F_n(n,p,\varphi)}{\partial n}\right|_{\substack{n=n^{m,l}\\p=p^{m,l}\\\varphi=\varphi^{m,l}}}\left(n^{m,l+1}-n^{m,l}\right)+\\ &\left.\frac{\partial F_n(n,p,\varphi)}{\partial p}\right|_{\substack{n=n^{m,l}\\p=p^{m,l}\\\varphi=\varphi^{m,l}}}\left(p^{m,l+1}-p^{m,l}\right)+\left.\frac{\partial F_n(n,p,\varphi)}{\partial\varphi}\right|_{\substack{n=n^{m,l}\\p=p^{m,l}\\\varphi=\varphi^{m,l}}}\left(\varphi^{m,l+1}-\varphi^{m,l}\right)=0.\end{aligned} \tag{8}$$

Here, the (n^l,p^l,φ^l) represents the results obtained by the l th Newton iteration. By applying the Galerkin weighted-residual method to (8), the following form (9) can be obtained:

$$\begin{aligned}&\oint_V N_i\cdot F_n\left(n^{m,l},p^{m,l},\varphi^{m,l}\right)dv+\\ &\oint_V N_i\cdot\left.\frac{\partial F_n(n,p,\varphi)}{\partial n}\right|_{\substack{n=n^{m,l}\\p=p^{m,l}\\\varphi=\varphi^{m,l}}}\left(n^{m,l+1}-n^{m,l}\right)dv+\\ &\oint_V N_i\cdot\left.\frac{\partial F_n(n,p,\varphi)}{\partial p}\right|_{\substack{n=n^{m,l}\\p=p^{m,l}\\\varphi=\varphi^{m,l}}}\left(p^{m,l+1}-p^{m,l}\right)dv+\\ &\oint_V N_i\cdot\left.\frac{\partial F_n(n,p,\varphi)}{\partial\varphi}\right|_{\substack{n=n^{m,l}\\p=p^{m,l}\\\varphi=\varphi^{m,l}}}\left(\varphi^{m,l+1}-\varphi^{m,l}\right)dv=0\end{aligned}. \tag{9}$$

Using the GLL basis functions, the variables can be

expanded as follows:

$$n=\sum_{j=1}^{N_{total}} n_j N_j,\ \ p=\sum_{j=1}^{N_{total}} p_j N_j,\ \varphi=\sum_{j=1}^{N_{total}} \varphi_j N_j, \quad (10)$$

where $N_{total}=(N_\xi+1)(N_\eta+1)(N_\varsigma+1)$ represents the total number of basis functions. Substituting (10) into (9) and simplifying the resulting equation, we have the final form of equation system (11):

$$[\mathbf{EN}]\boldsymbol{\delta}_n^{m,l+1}+[\mathbf{EP}]\boldsymbol{\delta}_p^{m,l+1}+[\mathbf{EF}]\boldsymbol{\delta}_\varphi^{m,l+1}=\mathbf{BE}, \quad (11)$$

where $\mathbf{EN}$, $\mathbf{EP}$ and $\mathbf{EF}$ are the matrices, $\mathbf{BE}$ is the vector, and $\boldsymbol{\delta}_n^{m,l+1}$, $\boldsymbol{\delta}_p^{m,l+1}$ and $\boldsymbol{\delta}_\varphi^{m,l+1}$ are differences between the two values of variables obtained by the l+1th and l th Newton iteration at the time of $m\Delta t$. The elemental matrices are defined as:

$$[\mathbf{EN}]_{ij}=-\Delta t\int\nabla N_i\cdot(-\mu_n(\nabla\varphi^{m,l}\cdot N_j-\nabla N_j))dV - \Delta t\int N_i\cdot N_j\frac{\partial(R-G)^{m,l}}{\partial n}dV-\int N_i\cdot N_j dV, \quad (12)$$

$$[\mathbf{EP}]_{ij}=-\Delta t\int N_i\cdot N_j\frac{\partial(R-G)^{m,l}}{\partial p}dV, \quad (13)$$

$$[\mathbf{EF}]_{ij}=\Delta t\int\mu_n n^{m,l}\nabla N_i\cdot\nabla N_j dV, \quad (14)$$

$$[\mathbf{BE}]_i=\Delta t\int\nabla N_i\cdot(-\mu_n(\nabla\varphi^{m,l}\cdot n^{m,l}-\nabla n^{m,l}))dV+ \Delta t\int N_i\cdot(R-G)^{m,l}dV+\int N_i\cdot(n^{m,l}-n^{m-1})dV. \quad (15)$$

Repeat the above operations for the hole current continuity equation and Poisson equation, then the fully-coupled system can be described by the following matrix form:

$$\begin{pmatrix}\mathbf{EN}&\mathbf{EP}&\mathbf{EF}\\ \mathbf{HN}&\mathbf{HP}&\mathbf{HF}\\ \mathbf{PN}&\mathbf{PP}&\mathbf{PF}\end{pmatrix}\begin{pmatrix}\boldsymbol{\delta}_n^{m,l+1}\\ \boldsymbol{\delta}_p^{m,l+1}\\ \boldsymbol{\delta}_\varphi^{m,l+1}\end{pmatrix}=\begin{pmatrix}\mathbf{BE}\\ \mathbf{BH}\\ \mathbf{BP}\end{pmatrix}. \quad (16)$$

The remaining elemental matrices are defined as:

$$[\mathbf{HN}]_{ij}=-\Delta t\int N_i\cdot N_j\frac{\partial(R-G)^{m,l}}{\partial n}dV, \quad (17)$$

$$[\mathbf{HP}]_{ij}=\Delta t\int\nabla N_i\cdot(-\mu_p(\nabla\varphi^{m,l}\cdot N_j+\nabla N_j))dV- \Delta t\int N_i\cdot N_j\frac{\partial(R-G)^{m,l}}{\partial p}dV-\int N_i\cdot N_j dV, \quad (18)$$

$$[\mathbf{HF}]_{ij}=-\Delta t\int\mu_p p^{m,l}\nabla N_i\cdot\nabla N_j dV, \quad (19)$$

$$[\mathbf{BH}]_i=-\Delta t\int\nabla N_i\cdot(-\mu_p(\nabla\varphi^{m,l}\cdot p^{m,l}+\nabla p^{m,l}))dV+ \Delta t\int N_i\cdot(R-G)^{m,l}dV+\int N_i\cdot(p^{m,l}-p^{m-1})dV, \quad (20)$$

$$[\mathbf{PN}]_{ij}=\int N_i\cdot N_j dV, \quad (21)$$

$$[\mathbf{PP}]_{ij}=\int N_i\cdot N_j dV, \quad (22)$$

$$[\mathbf{PF}]_{ij}=\int\nabla N_i\cdot\nabla N_j dV, \quad (23)$$

$$[\mathbf{BP}]_i=-\int\nabla N_i\cdot\nabla\varphi^{m,l}dV-\int N_i\cdot(n^{m,l}-p^{m,l}-N_0)dV. \quad (24)$$

When the norm of $(\boldsymbol{\delta}_n^{m,l+1},\boldsymbol{\delta}_p^{m,l+1},\boldsymbol{\delta}_\varphi^{m,l+1})^T$ is less than the setting of tolerance, $(\mathbf{n}^{m,l+1},\mathbf{p}^{m,l+1},\boldsymbol{\varphi}^{m,l+1})^T$ can be account as the approximate solution of the original nonlinear system.

Particularly, it may suffer from instability when a simple finite difference scheme is employed as mentioned in [12]. The numerical error is caused by the hyperbolic and convection dominated equations. The stability of the model can be improved by employing proper discretization method. In this paper, the backward Euler scheme in time and GLL basis functions in space are employed. The backward Euler scheme is implicit and unconditionally stable with large time steps. As a specific finite element method, the SEM with GLL basis functions also satisfies the discrete maximum principle [13]. Therefore, the proposed method can yield a reasonable degree of accuracy independent of perturbations.

C. Mix-order basis function

Here, the electron and hole concentrations and electric potential are selected as the unknown variables. The fully coupled Newton iteration method is employed to solve the nonlinear equations. The variation range of the electron and hole carrier densities is still larger than electrostatic potential by expressing all densities in units of n_i and all potential in units of kT/q, where n_i is the intrinsic density, k is the Boltzmann's constant and T is the carrier temperature [2]. To capture the density gradient, the fine meshes or the higher order basis function is necessary. Based on the above consideration, different orders of the basis function can be selected by the range and the changing domain of the three variables. Here, we employ higher order for the electron and hole carrier densities and higher order for the rapid changing domain with the same variable. Because of using different orders of basis function for carrier densities and potential, the following integration is needed to fill the above matrices, taking the $[\mathbf{T}]_{ij}$ for example:

$$\begin{aligned}&\int_{\Omega_e}N_iN_j dV\\ &=\int_{-1}^{1}\int_{-1}^{1}\int_{-1}^{1}\Phi_i\Phi_j|\mathbf{J}|d\xi d\eta d\zeta\\ &=\int_{-1}^{1}\int_{-1}^{1}\int_{-1}^{1}\phi_m^{(N_\xi)}(\xi)\phi_n^{(N_\eta)}(\eta)\phi_p^{(N_\varsigma)}(\zeta)\cdot\phi_{m'}^{(N'_\xi)}(\xi)\phi_{n'}^{(N'_\eta)}(\eta)\phi_{p'}^{(N'_\varsigma)}(\zeta)|\mathbf{J}|d\xi d\eta d\zeta\\ &=\sum_{r=0}^{N_\xi}\sum_{s=0}^{N_\eta}\sum_{t=0}^{N_\varsigma}|J_{rst}|w_r w_s w_t\phi_m^{(N_\xi)}(\xi_r)\phi_n^{(N_\eta)}(\eta_s)\phi_p^{(N_\varsigma)}(\zeta_t)\cdot\phi_{m'}^{(N'_\xi)}(\xi_r)\phi_{n'}^{(N'_\eta)}(\eta_s)\phi_{p'}^{(N'_\varsigma)}(\zeta_t),\end{aligned} \quad (25)$$

N_i and N_j have different orders and the high order integration is employed with $(N_\xi>N'_\xi, N_\eta>N'_\eta, N_\varsigma>N'_\varsigma)$.

Due to the fact that different domain has different order of basis functions, the continuity at the interface between two domains must be handled properly. Considering that the quasi one-dimensional structure is analyzed in this paper, the different orders basis functions are only applied at the direction with changing variables. Therefore, the continuity can be enforced easily.

III. NUMERICAL EXAMPLES AND DISCUSSIONS

In order to verify the accuracy and efficiency of the proposed method, the quasi one-dimensional PIN diode with the p^+nn^+ doping is selected as the numerical model [9]. As shown in Fig. 2, the cross section area of the diode is $10^{-8}cm^2$, and the length is 10 μm. The distribution of doping concentration is displayed by Fig. 3.

Here, it should be indicated that all the numerical examples are computed on an Intel(R) Core(TM)2 with 2.83 GHz CPU (the results are computed by only one processor) and 8 GB RAM. The tolerance is set to be 10^{-6}.

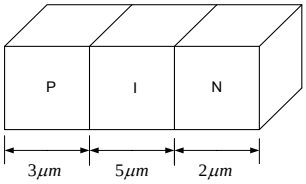

Fig. 2. The model of PIN diode.

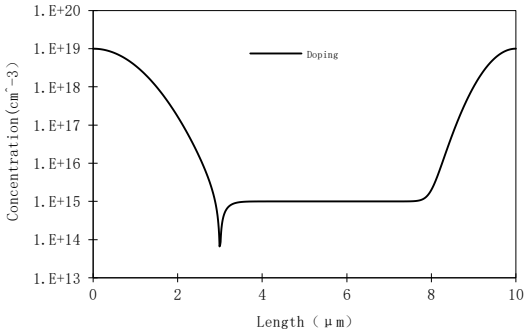

Fig. 3. The doping concentration of PIN diode.

A. Basic simulation

In order to verify the validity of the proposed SEM for transient semiconductor simulation, a sine-wave voltage is imposed on the anode of the PIN diode. The mesh size is 0.01 μm, and the order of the basis functions is set to be 1. The time step size is 1 *ns*. Figure 4 shows the transient current flowing through the diode, and it is in good agreement with the result obtained by COMSOL software.

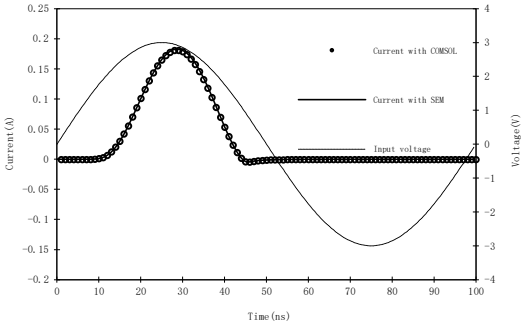

Fig. 4. The distribution of transient current.

Figure 5 shows the distribution of variables at the time of 20 *ns*, and the results of the comparison with COMSOL demonstrate the validity of the SEM for transient semiconductor simulation.

B. Mix-order with variables and domains

It can be found that the electron and hole carrier densities have a faster change than the electric potential from Fig. 5. Therefore, it is reasonable to use high order basis function for densities and low one for potential. As can be seen in Fig. 5, the densities in P domain and N domain have larger gradient than I domain. So, the high order basis functions are employed for the variables in P domain and N domain.

To verify the efficiency of the mix-order basis function with different variables and domains, the transient response under the electromagnetic pulse with fast rise time has been simulated. Figure 6 shows the input voltage imposed on the anode of the diode, and gives the transient current densities obtained by SEM with 1st order and 5th order basis function. The mesh size for 1st order basis function is 0.01 μm and 0.2 μm for 5th order basis function. The time step size is 1 ps. The overshoot current shown in Fig. 6 is due to the capacitive performance of PIN diode under high frequency.

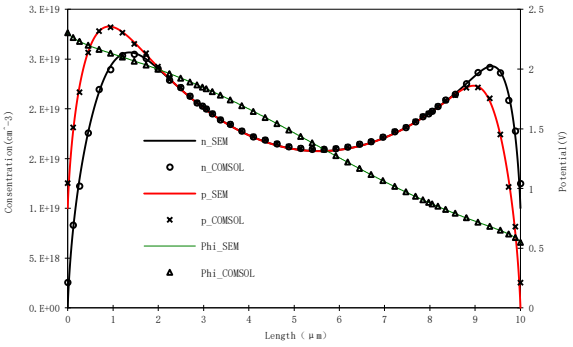

Fig. 5. The distribution of variables at the time of 20 ns.

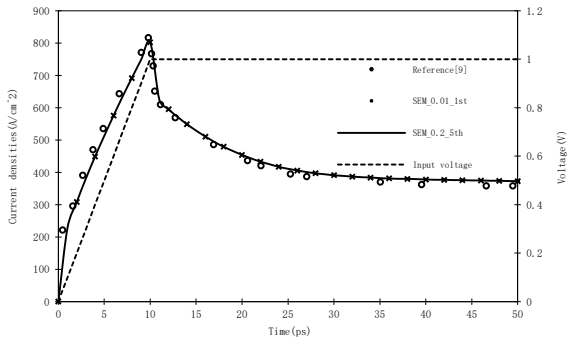

Fig. 6. The distribution of transient current densities.

Table 1 shows the compute time using the mix-order basis functions with different variables. The same high order basis functions for the electron and hole carrier densities, and low order basis functions for electric potential. Table 2 shows the compute time using the mix-order basis functions with different variables and different domains. The same high order basis functions for the P and N domain, and low order basis functions for I domain. As can be seen in Table 2, the case with standard 1st order of basis function takes 3.32 times CPU time than the proposed mix-order method. The proposed mix-order SEM exhibits a good efficiency in semiconductor transient simulation.

Table 1: Comparison of computation Efficiency

Mesh Size (μm)	Order of Basis Function		Number of Unknowns	CPU Time (s)
	n, *p*	φ		
0.01	1st	1st	11988	206
0.1	4th	4th	4788	177
	4th	1st	3588	132
0.2	5th	5th	2988	148
	5th	2nd	2388	112

Table 2: Comparison of computation efficiency

Mesh Size (μm)	Order of Basis Function		Number of Unknowns	CPU Time (s)
	n, *p*	φ		
0.01	1st	1st	11988	206
0.1	4th	1st	3588	132
	4th (2nd)	1st	2788	88
0.2	5th	2nd	2388	112
	5th (2nd)	2nd (1st)	1688	62

The numbers in the bracket represent the orders of basis functions for I domain. The default represents the same order of basis function for the whole domain.

VI. CONCLUSION

In this paper, the spectral element method (SEM) is proposed for the semiconductor transient simulation. The Gauss-Lobatto-Legendre (GLL) polynomials are used as the basis function to expand the variables. The fully coupled Newton iteration method is employed to solve the nonlinear drift-diffusion model. The mix-order basis functions with different variables and domains are employed to improve the compute efficiency. The PIN diode with quasi one-dimensional structure has been analyzed, and the numerical results demonstrate the accuracy and efficiency with the proposed method.

ACKNOWLEDGMENT

This work was supported in part by Natural Science Foundation of 61522108, 61171041.

REFERENCES

[1] R. E. Bank, D. J. Rose, and W. Fichtner, "Numerical methods for semiconductor device simulation," *IEEE Trans. Electron Devices*, vol. 30, no. 9, pp. 1031-1041, Sep. 1983.

[2] W. Fichtner, D. J. Rose, and R. E. Bank, "Semiconductor device simulation," *IEEE Trans. Electron Devices*, vol. 30, no. 9, pp. 1018-1030, Sep. 1983.

[3] S. Goasguen, M. M. Tomeh, and S. M. El-Ghazaly, "Electromagnetic and semiconductor device simulation using interpolating wavelets," *IEEE Trans. Microw Theory Tech*, vol. 49, no. 12, pp. 2258-2265, Dec. 2001.

[4] J. F. Burgler, W. Coughran, and W. Fichtner, "An adaptive grid refinement strategy for the drift-diffusion equations," *IEEE Trans. Computer Aided Design of Integrated Circuits and Systems*, vol. 10, no. 10, pp. 1251-1258, Sep. 1991.

[5] J.-H. Lee and Q. H. Liu, "A 3-D spectral-element time-domain method for electromagnetic simulation," *IEEE Trans. Microw Theory Tech*, vol. 55, no. 5, pp. 983-991, May 2007.

[6] I. Mahariq, M. Kuzuoglu, I. H. Tarman, and H. Kurt, "Photonic nanojet analysis by spectral element method," *IEEE Photonics Journal*, vol. 6, no. 5, pp. 85-90, Oct. 2014.

[7] J. Lee and Q. H. Liu, "An efficient 3-D spectral-element method for Schrödinger equation in nanodevice simulation," *IEEE Trans. Computer Aided Design of Integrated Circuits and Systems*, vol. 24, no. 12, pp. 1848-1858, Dec. 2005.

[8] C. Cheng, Q. H. Liu, and H. Z. Massoud, "Spectral element method for the Schrödinger-equation system," *IEEE. International Workshop on Computational Electronics*, pp. 221-222, 2004.

[9] H. Zhou, Z. W. Du, and K. Gong, "Overshoot phenomena in PIN diode under EMP with fast rise time," *High Power Laser and Particle Beams*, vol. 17, no. 5, pp. 783-787, May 2005.

[10] I. Mahariq, M. Kuzuolu, and H. I. Tarman, "On the attenuation of perfectly matched layer in electromagnetic scattering problems with spectral element method," *Appl. Comput. Electromagn. Soc. J*., vol. 29, no. 9, pp. 701-710, 2014.

[11] H. Xu, D. Z. Ding, and R. S. Chen, "A hybrid explicit-implicit scheme for spectral-element time-domain analysis of multiscale simulation," *Appl. Comput. Electromagn. Society J*., vol. 31, no. 4, pp. 444-449, Apr. 2016.

[12] N. Bushyager, B. McGarvey, and E. M. Tentzeris, "Introduction of an adaptive modeling technique for the simulation of RF structures requiring the coupling of Maxwell's, mechanical, and solid-state equations," *Appl. Comput. Electromagn. Soc. J*., vol. 17, no. 1, pp. 104-111, 2002.

[13] J. Miller, W. Schilders, and S. Wang, "Application of finite element method to the simulation of semiconductor devices," *Rep. Prog. Phys*., vol. 62, pp. 277-353, 1999.

Huaguang Bao received the B.Sc. degree in Communication Engineering from the School of Electrical Engineering and Optical Technique, Nanjing University of Science and Technology, Nanjing, China, in 2011. He is currently working towards the Ph.D. degree in Electromagnetic Fields and Microwave Technology at the School of Electrical Engineering and Optical Technique, Nanjing University of Science and Technology. His research interests include semiconductor simulation, RF-integrated circuits, and computational electromagnetics.

Dazhi Ding was born in Jiangsu, China, in 1979. He received the B.S. and Ph.D. degrees in Electromagnetic Field and Microwave Technique from Nanjing University of Science and Technology (NUST), Nanjing, China, in 2002 and 2007, respectively.

During 2005, he was with the Center of Wireless Communication in the City University of Hong Kong, Kowloon, as a Research Assistant. He is currently an Associate Professor with the Electronic Engineering of NJUST. He is the author or co-author of over 30 technical papers. His current research interests include computational electromagnetics, electromagnetic scattering, and radiation.

Rushan Chen (M'01) was born in Jiangsu, China. He received the B.Sc. and M.Sc. degrees from the Department of Radio Engineering, Southeast University, China, in 1987 and 1990, respectively, and the Ph.D. degree from the Department of Electronic Engineering, City University of Hong Kong, in 2001.

He joined the Department of Electrical Engineering, Nanjing University of Science and Technology (NJUST), China, where he became a Teaching Assistant in 1990 and a Lecturer in 1992. Since September 1996, he has been a Visiting Scholar with the Department of Electronic Engineering, City University of Hong Kong, first as Research Associate, then as a Senior Research Associate in July 1997, a Research Fellow in April 1998, and a Senior Research Fellow in 1999. From June to September 1999, he was also a Visiting Scholar at Montreal University, Canada. In September 1999, he was promoted to Full Professor and Associate Director of the Microwave and Communication Research Center in NJUST, and in 2007, he was appointed Head of the Department of Communication Engineering, NJUST. He was appointed as the Dean in the School of Communication and Information Engineering, Nanjing Post and Communications University in 2009. And in 2011 he was appointed as Vice Dean of the School of Electrical Engineering and Optical Technique, Nanjing University of Science and Technology. His research interests mainly include microwave millimeter-wave systems, measurements, antenna, RF-integrated circuits, and computational electromagnetics. He has authored or co-authored more than 200 papers, including over 140 papers in international journals.

Chen received the Science and Technology Advance Prize several times given by the National Military Industry Department of China, the National Education Committee of China, and Jiangsu Province. He is the recipient of the Foundation for China Distinguished Young Investigators presented by the National Science Foundation (NSF) of China in 2003. In 2008, he became a Chang-Jiang Professor under the Cheung Kong Scholar Program awarded by the Ministry of Education, China. Besides, he was selected as a Member of Electronic Science and Technology Group by Academic Degree Commission of the State Council in 2009. Chen is a Fellow of the Chinese Institute of Electronics (CIE), Vice-Presidents of Microwave Society of CIE and IEEE MTT/APS/EMC Nanjing Chapter. He serves as the Reviewer for many technical journals such as IEEE Trans. on AP and MTT, Chinese Physics etc., and now serves as an Associate Editor for the International Journal of Electronics.

A Design of Low-pass Filter with Wide Stopband and Sharp Roll-off Rate Using Series LC Tanks Resonator

A. R. Nouritabar, Ashkan Abdipour, and Arash Abdipour

Young Researchers and Elite Club, Kermanshah Branch, Islamic Azad University, Kermanshah, Iran
Alireza.Nouritabar@yahoo.com, Ashkan_Abdipour@yahoo.com, Arash.Abdipour@yahoo.com

Abstract ─ In this letter, a lowpass filter (LPF) using resonators synthesized with series LC tank patches has been proposed. Each of the employed LC tank is composed of a high-low impedance lines, which have been mirrored to create the patches of the main resonance cells. Using this kind of resonator combining with eight suppressing cells leads to designing a LPF with specifications such as ultra-wide stopband, sharp cut-off and an acceptable return loss in the pass band. The -3 dB cut-off frequency of the proposed LPF is located in 2.4 GHz. The spurious frequencies have been suppressed in the stop-band region from 2.66 up to 23 GHz with a suppression level of -35 dB. Moreover, the transition band has been measured from 2.4 to 2.67 GHz with corresponding attenuation levels of -3 and -40 dB, respectively. To clarify the performance of each section and how they affect the frequency response the equivalent LC circuit of resonators and the final design have been obtained, separately.

Index Terms ─ High-low impedance lines, LC tank patches, Lowpass Filter (LPF).

I. INTRODUCTION

Microstrip LPFs are one of the most important components that have been utilized widely in wireless communication systems and played a key role for many years. So far, several compact LPFs have been proposed to achieve a desired frequency response such as wide stopband with high rejection level and sharp roll-off. For example, in [1], a microstrip lowpass filter with quasi-elliptic response using both loaded radial-shape patches and meandered main transmission line has been proposed. However, it suffers from a gradual transition band and low level of stopband rejection. To expand the stopband region in the frequency response of LPFs, hairpin resonators can be useful [2-6]. By utilizing this unit in [2], the stopband has been expanded. However, the overall circuit size is relatively large and the skirt performance is not desired. A method to design a LPF with wide stopband is using stepped impedance hairpin resonator with radial stubs, which has been done in [3], but this design has been failed to achieve a sharp roll-off rate. In [4], by employing stepped impedance hairpin units a compact LPF has been proposed. However, this filter has a narrow stopband. In [5], another method to propose a LPF based on an application of shunt open-stubs coupled-line in the structure of hairpin unit has been introduced. It has retained a wide stopband as the main characteristic of hairpin resonators. A gradual transition band and large circuit size have been remained significant challenges, though. In [6], defected ground structure (DGS) as a popular method is applied to design a LPF with sharp rejection. However, DGS increases the complexity of design procedure and the proposed circuit using this method cannot be utilized on metal surfaces. To design a LPF rat-race directional couplers have been used to operate as bandstop transversal filtering sections (TFSs), in [7]. However, by adopting this method the occupied area has been significantly increased and also the rejection band has not been adequately widened. In [8], a quasi-π-slot resonator and open stubs is employed and a LPF with sharp transition band is proposed, but the occupied area is relatively large. A microstrip LPF by using triangular and radial patch resonators has been designed [9], but this filter suffers from gradual transition band. In this letter, a lowpass filter (LPF) with -3 dB cut-off frequency located on 2.4 GHz has been proposed. The designed LPF is composed of a main resonator with series LC tank patches and completive resonance cells having the same structure as the main one to omit the aforementioned defects of the frequency response. To expand the stopband more, eight suppressing cells have been employed in both sides of the proposed LPF.

II. THE PROCEDURE OF DESIGNING THE PROPOSED LPF

To define the basic structure of series LC tanks configuration, Fig. 1 (a) shows the primary resonance cell using these patches. As it is observed, the designed resonator consists of two high-low impedance transmission lines standing for LC tank patches. The dimensions of the implemented resonator are as follows: L1 = 2.9, L2 = 3.1, L3 = 0.75, W1 = W2 = W3 = 0.1,

Submitted On: March 26, 2015
Accepted On: November 8, 2015

W4 = 21.5, W5 = 20.5, S1 = 0.3 (all in millimetre). In Fig. 1 (b) the frequency response of the resonator has been shown. For the simulation, Agilent Advanced Design System (ADS) is used.

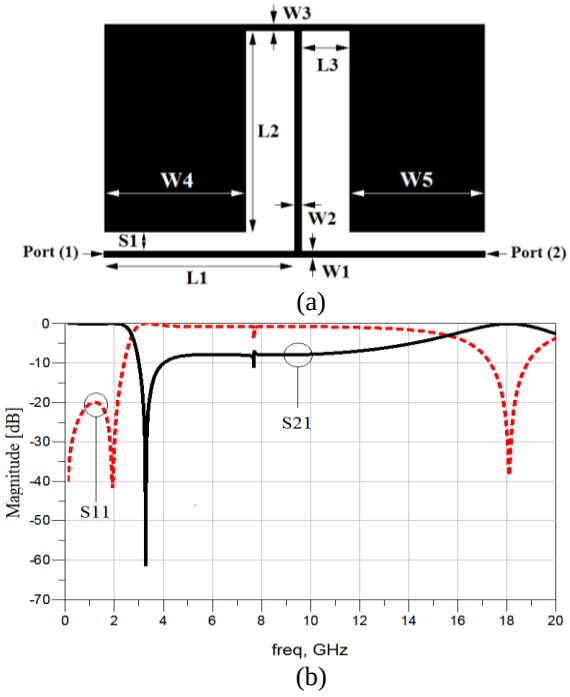

Fig. 1. (a) The basic structure of series LC tanks configuration, and (b) frequency response of the basic structure of series LC tanks configuration.

As it can be seen from the S-parameters, the operating frequency of this resonance cell is located on 2.4 GHz. According to the simulation results, the insertion and return losses in the pass band are 0.1 and rather greater than +20 dB, respectively. Moreover, the proposed cell creates a transition zero at 3.3 GHz with corresponding attenuation level of -61 dB bringing about a wide suppressing band of -7 dB. By changing the dimensions of the mentioned resonance cell the location of -3 dB operating frequency and also the transition zero can be controlled. To justify how it is possible, the simulated frequency response of the designed resonator against L2 and W2 is shown in Figs. 2 (a) and (b), respectively. As it is observed from Fig. 2 (a), by decreasing L2 from 3.1 to 2.3 mm with steps of 0.4 mm, because of reducing the value of capacitance of the low impedance line, the transmission zero in 3.3 GHz will move away from the lower frequencies. Similarly, in Fig. 2 (b), when W2 increases from 0.1 to 0.3 mm with steps of 0.1 mm, transmission zero will close to the upper frequency. Hence, the location of the transmission zero can be controlled by changing the length of L2 and the width of W2.

The equivalent LC circuit of the proposed cell and a comparison between the frequency responses of LC circuit and EM simulations have been shown in Figs. 3 (a) and (b), respectively. In the lumped circuit L1 and L2 represent the inductances of the transmission lines determined by W1 and W2, in Fig. 1 (a). L3, C4 and C5 model the inductance and capacitance of LC tank patch. C1, C2 and C3 account for the capacitance between the microstrip structure and the ground.

The values of inductances and capacitances are L1 = 2.9 nH, L2 = 3.4 nH, L3 = 0.75nH, C1 = 37 fF, C2 = 80 fF, C3 = 63 fF, C4 = 0.29 pF, C5 = 0.28 pF. Figure 4 indicates the main resonator utilizing primary resonance cell with series LC tanks patches where each of the employed primary resonance cell has the same dimension of that shown in Fig. 1 (a). As it is observed, two of the primary cells are placed on the both sides of the main transmission line. In Fig. 5, the frequency response of this resonator is illustrated.

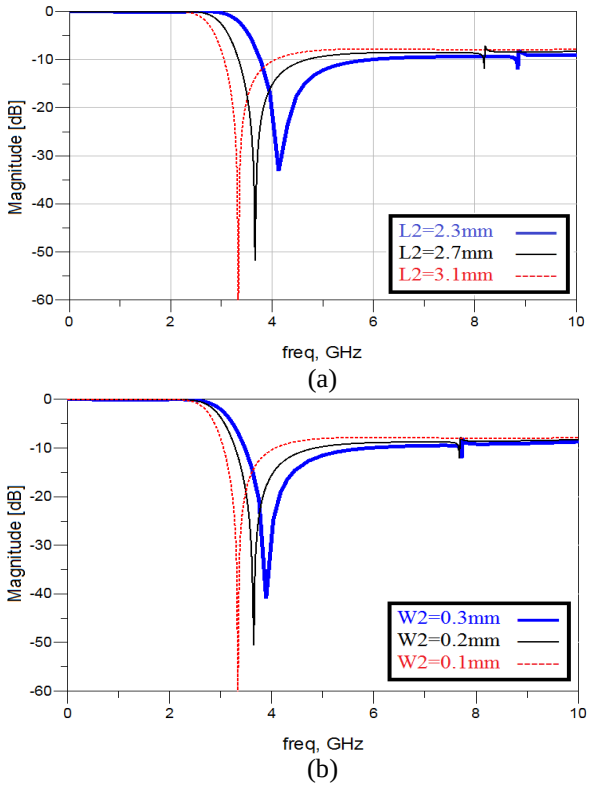

Fig. 2. (a) Magnitude of S_{21} versus changing the value of L2, and (b) magnitude of S_{21} versus changing the value of W2.

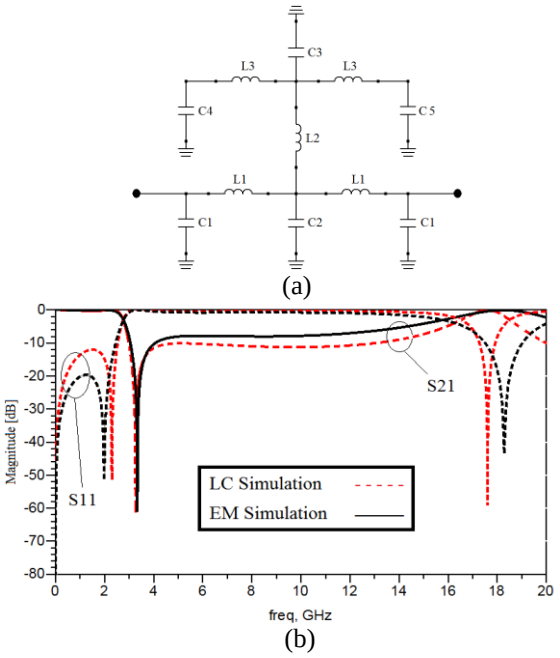

Fig. 3. (a) The equivalent LC circuit of the shown basic structure in Fig. 1 (a), and (b) the comparison between the frequency responses of LC circuit and EM simulations.

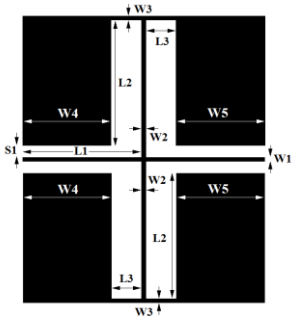

Fig. 4. The structure of the main resonator with the same dimensions as that shown in Fig. 1 (a).

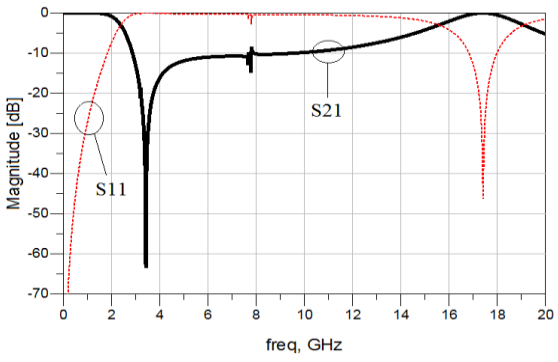

Fig. 5. The frequency response of the main resonator shown in Fig. 4.

According to the scattering parameters of the proposed resonator, it suffers from a low level of suppression in the whole stopband and a gradual transition band. To create some transmission zeros (TZs), several stages of the proposed resonator with different dimensions can be connected in series. The applied resonators to complete the operation of the main resonator are so-called completive resonance cells (S-CCRCs). Creating TZs at different frequencies not only improves the suppressing level of the rejection band but also leads to expanding the stopband region. However, setting several resonators in series increases the coupling effects, which causes to destroy the insertion loss in the passband region. Note that, the dimensions of S-CCRC must be chosen to achieve a higher -3 dB operating frequency than the main resonator having 2.4 GHz cut-off frequency, the lowest suppression in the pass band (to have no effect on the pass band of the main resonator) and high and wide stopband. The structure of S-CCRC having different dimensions in comparison to that shown in Fig. 4 and its equivalent LC circuit have been depicted in Figs. 6 (a) and (b), respectively. The dimensions of S-CCR are as follows: L4 = 2.3, L5 = 3, L6 = 0.4, W6 = 0.1, W7 = 0.1, W8 = 0.1, W9 = 1.9 and S2 = 0.3 (all in millimeter). The values of lumped elements are as follows: L4 = 1.66 nH, L5 = 2.45 nH, L6 = 0.3 nH, C6 = 30 fF, C7 = 104 fF, C8 = 63 fF, C9 = 0.32 pF. Actually, the proposed S-CCR has been designed to eliminate the defects of the frequency response of the main resonator. Figure 7 illustrates the frequency responses of LC circuit and EM simulation of S-CCR.

As shown in Figs. 8 (a) and (b) (S4 = 0.2 mm, S3 = 0.2 mm), by connecting two of S-CCRCs and the main resonator (see Fig. 8 (a)), the mentioned intents such as desired return loss (about +17 dB) and insertion loss (close to 0.1 dB) in whole pass band have been obtained. Moreover, the transition band from -3 up to -40 dB is 0.27 GHz and also, to some extent, an improved stopband is achieved.

Although the rejection band has been broadened, undesired poles over the frequency of 11 GHz do not let it to be expanded enough. To widen the stopband four high-low impedance resonators as suppressing cells are employed. The configuration of these cells and corresponding equivalent LC circuit are shown in Figs. 9 (a) and (b), respectively. In the LC circuit L7, L8, L9, L10 and L11 are the equivalent inductors of the transmission lines determined by L7, L8, L9, L10 and L11 in Fig. 9 (a). C10, C11, C12, C13 and C14 model the capacitance between the microstrip structure and the ground. C15 and C16 present the equivalent capacitances of the open stubs determined by L12 in the microstrip structure of suppressing cells. The coupling effects of two adjacent rectangular low impedance patches have been modeled by Cg1.

The dimensions of the proposed suppressing cell are: W10 = 0.3, L11 = 0.2, L10 = 3.2, L9 = 1.25, L8 = 2.1, L7 = 1, W16 = 1.1, W15 = 0.1, W14 = 0.95, W13 = 1, W12 = 0.1, W11 = 0.1 (all in millimetre), and the values of capacitances and inductors are as: L7 = 0.48 nH, L8 = 0.132 nH, L9 = 1.39 nH, L10 = 0.833 nH, L11 = 0.2 nH, C10 = 17 fF, C11 = 20 fF, C12 = 32 fF, C13 = 44 fF, C14 = 15 fF, C15 = 0.332 pF, C16 = 0.35 pF, Cg1 = 75 fF.

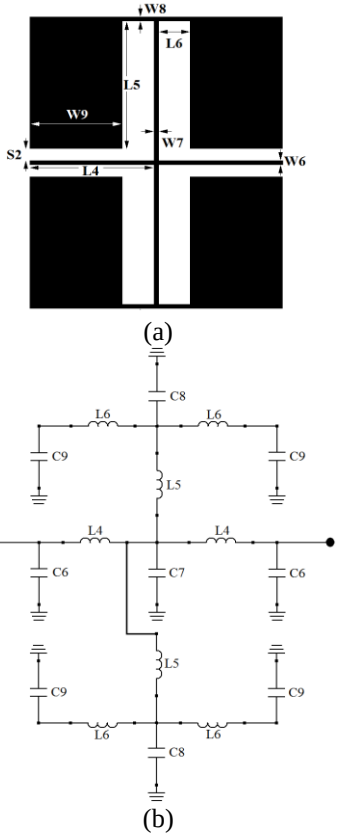

Fig. 6. (a) The configuration of completive resonance cells (S-CCRCs), and (b) the LC circuit of the completive resonance cells (S-CCRCs).

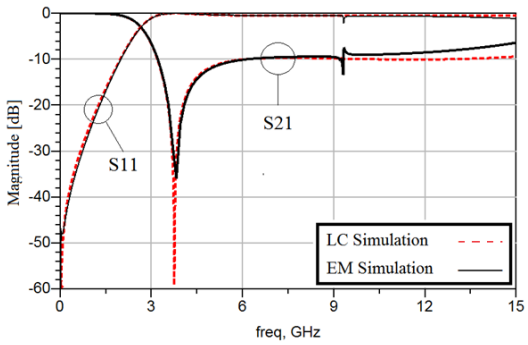

Fig. 7. The comparison between the frequency responses of LC circuit and EM simulations of S-CCRC.

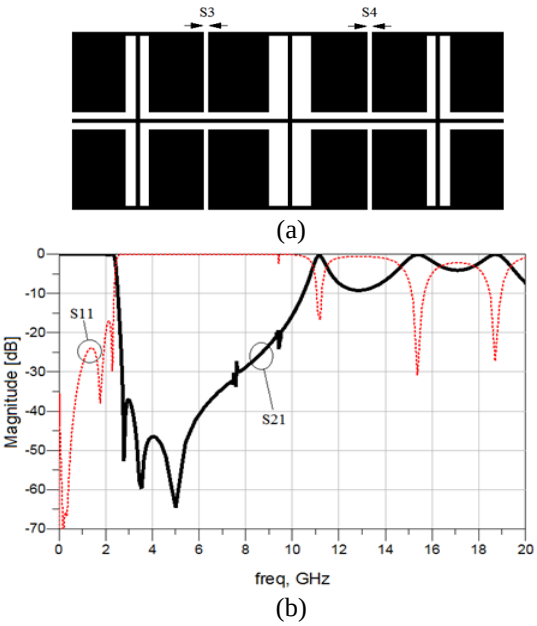

Fig. 8. (a) The configuration of connecting two of S-CCRCs and the main resonator, and (b) the frequency response of connecting two out of S-CCRCs and the main resonator.

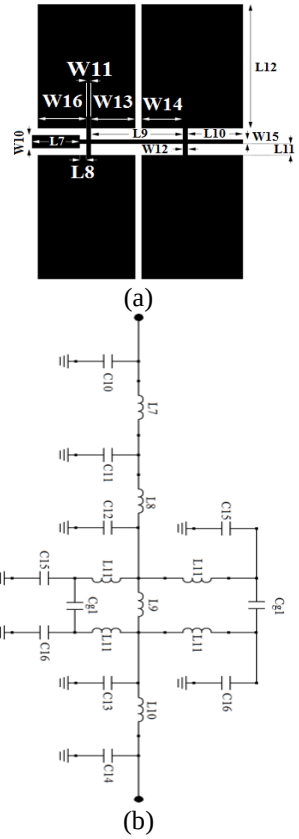

Fig. 9. (a) The configuration of suppressing cell, and (b) the equivalent LC circuit of suppressing cell.

The dimensions of the proposed suppressing cell are: W10 = 0.3, L11 = 0.2, L10 = 3.2, L9 = 1.25, L8 = 2.1, L7 = 1, W16 = 1.1, W15 = 0.1, W14 = 0.95, W13 = 1, W12 = 0.1, W11 = 0.1 (all in millimeter), and the values of capacitances and inductors are as: L7 = 0.48 nH, L8 = 0.132 nH, L9 = 1.39 nH, L10 = 0.833 nH, L11 = 0.2 nH, C10 = 17 fF, C11 = 20 fF, C12 = 32 fF, C13 = 44 fF, C14 = 15 fF, C15 = 0.332 pF, C16 = 0.35 pF, Cg1 = 75 fF. Figure 10 depicts the results of EM simulation and the frequency response of LC circuit, which are in good agreement. As it is observed, the designed suppressing cell creates two transmission zeros (TZs) at 9.1 and 20 GHz with corresponding attenuation levels of -56 and -64 dB, respectively. These TZs have created a wide stopband from 9 up to 23 GHz with a corresponding suppressing level of -20.5 dB. Finally, by connecting two out of this suppressing cells in the both side of the combination of the resonator and S-CCRCs a LPF with -3 dB cut-off frequency of 2.4 GHz is proposed. In Fig. 11, the configuration of the proposed LPF has been shown. The remained dimensions are as follows: Lf = 1.6, Wf = 1.56, S5 = 0.15 and S6 = 0.2 (all in millimeter). As the previous steps, the equivalent LC circuit of the proposed LPF and its frequency response are shown in Figs. 12 (a) and (b). The values of inductors and capacitors are as follows: L2 = 3.4 nH, L3 = 0.75 nH, L5 = 2.45 nH, L6 = 0.3 nH, L7 = 0.48 nH, L8 = 0.132 nH, L9 = 1.39 nH, L11 = 0.2 nH, L12 = 2.37 nH, L13 = 3.84 nH ,C3 = 63 fF, C4 = 0.29 pF, C5 = 0.28 pF, C8 = 63 fF, C9 = 0.32 pF, C10 = 17 fF, C11 = 20 fF, C12 = 32 fF, C15 = 0.332 pF, C16 = 0.35 pF, Cg1 = 75 fF, C17 = 72 fF, C18 = 157 fF, C19 = 180 fF, Cg1 = 75 fF, Cg2 = 10 fF, Cg3 = 25 fF**.** The frequency response of LC circuit of the proposed LPF and EM simulation are shown in Fig. 12 (b) and good agreement between them is clearly observed.

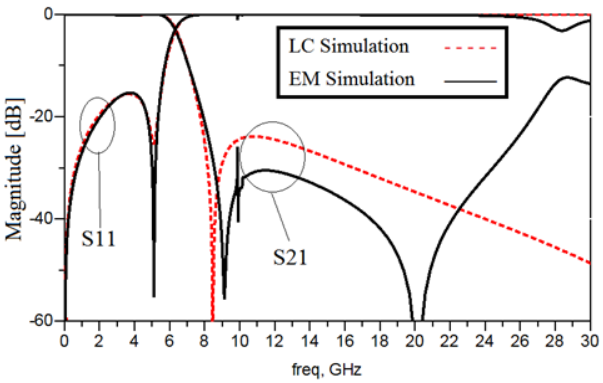

Fig. 10. EM simulation and the frequency response of LC circuit of the mentioned cells in Fig. 9.

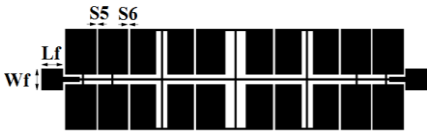

Fig. 11. The configuration of the proposed LPF.

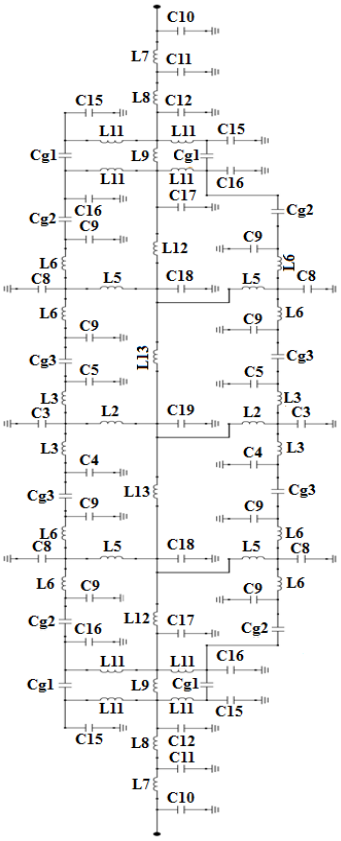

Fig. 12. (a) The equivalent LC circuit of the proposed LPF, and (b) EM and LC simulation of the proposed LPF.

III. MEASUREMENT AND SIMULATION RESULTS

The photograph of the proposed LPF is illustrated in Fig. 13. The proposed LPF has been designed, fabricated and tested. The implemented LPF has been constructed on RT/Duroid 5880 substrate with the thickness of 0.508 mm, the permittivity of 2.2 and the loss tangent of 0.0009. The simulation and measurement results of the designed LPF have been carried out by using an EM-simulator ADS based on the method of moments and a Rohde & Schwarz network analyzer ZVL13, respectively. Figure 14 shows the simulated and measured frequency responses of the proposed LPF. As it can be seen, -3 dB cut-off frequency of the filter has been located on 2.4 GHz. In the whole passband region the insertion loss is close to zero, which shows a flat response and also in this band the return loss is better than +35 dB. As it is observed, close to the operating frequency two transmission zeros (TZs) with attenuation levels of -50 and -60 are existed causing a sharp roll-off rate. Thanks to these TZs, a steep transition band about 0.27 GHz from 2.4 up to 2.67 GHz with corresponding attenuation levels of -3 and -40 dB, respectively, has been measured, which verify a desired skirt performance. The stopband region suppress spurious frequencies from 2.66 up to 23 GHz with corresponding rejection level of -35 dB. Moreover, in the rejection band a flat return loss close to zero has been obtained.

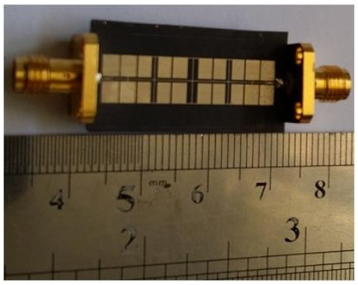

Fig. 13. The photograph of the proposed LPF.

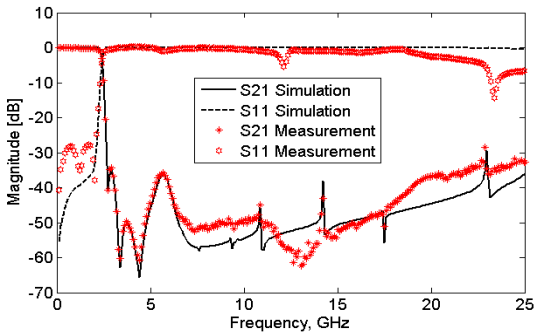

Fig. 14. The simulation and measurement results of the proposed LPF.

The occupied area of the proposed LPF is 25.5 mm × 7.1 mm. The simulation and measurement results are in good agreement, as it was expected. For comparison, Table 1 summarizes the performance of some published lowpass filters. In this table, the roll-off rate ξ is defined as:

$$\xi = \frac{\alpha_{\max} - \alpha_{\min}}{f_S - f_C} \quad (dB/GHz), \tag{1}$$

where α_{max} is the 40 dB attenuation point, α_{min} is the 3 dB attenuation point, f_s is the 40 dB stopband frequency, and f_c is the 3 dB Cut-off frequency. The relative stopband bandwidth (RSB) is given by:

$$\text{RSB} = \frac{\text{stop}-\text{band} \quad \text{bandwidth}\ (-20\text{dB})}{\text{stop}-\text{band} \quad \text{center} \quad \text{frequency}}. \tag{2}$$

The suppression factor (SF) is based on the SBW; for example, when the SBW is referred to 30 dB suppression, the corresponding SF is defined as 3. The normalized circuit size (NCS) can be derived as below:

$$\text{NCS} = \frac{\text{physical} \quad \text{size}(\text{length} \times \text{width})}{\lambda_g^2}. \tag{3}$$

Finally, the figure-of-merit (FOM), the overall index of a proposed filter, is given by:

$$FOM = \frac{\xi \times RSB \times SF}{NCS \times AF}. \tag{4}$$

Table 1: Comparison between the performance of the proposed lowpass filter and previous works

Ref.	Roll-off Rate (ζ)	RSB	SF	NCS	AF	FOM
[1]	36.3	1.323	1.5	0.0062	1	11543
[2]	37	1.15	2	0.021	1	3999
[3]	30	1.25	1.5	0.0064	1	8789
[4]	74	1.19	2	0.0119	1	14713
[5]	95	1.4	2	0.0222	1	11951
[6]	130	0.933	2	0.0202	2	6004
[7]	200	1.36	2	0.2995	1	1815.9
[8]	82	1.28	2.5	0.0242	1	10842
[9]	37	1.65	1.5	0.0101	1	9065
This Work	132	1.59	3.5	0.0152	1	48327

IV. CONCLUSION

In this article, by employing high-low impedance transmission lines, LC tank patches are designed to propose a LPF resonator. By connecting three of these resonators with different dimension in series, a sharp transition band has been obtained. To achieve a wide stopband eight suppressing cells are adopted. Combining the tripled resonators connected in series

and suppressing cells leads to implementing a LPF with sharp skirt performance and wide rejection band. The fabricated LPF has -3 dB cut-off frequency of 2.4 GHz.

REFERENCES

[1] J. Wang, L.-J. Xu, S. Zhao, Y.-X. Guo, and W. Wu, "Compact quasi-elliptic microstrip lowpass filter with wide stopband," *IEE Electron. Lett*., vol. 46, no. 20, pp. 1384-1385, 2010.

[2] S. Luo, L. Zhu, and S. Sun, "Stopband-expanded low-pass filters using microstrip coupled-line hairpin units," *IEEE Microw. Wireless Compon. Lett*., vol. 18, no. 8, pp. 506-508, Aug. 2008.

[3] X. B. Wei, P. Wang, M. Q. Liu, and Y. Shi, "Compact wide-stopband lowpass filter using stepped impedance hairpin resonator with radial stubs," *IEE Electron. Lett*., vol. 47, no. 15, pp. 862-863, July 2011.

[4] L. Li, Z.-F. Li, and J.-F. Mao, "Compact lowpass filters with sharp and expanded stopband using stepped impedance hairpin units," *IEEE Microw. Wireless Compon. Lett*., vol. 20, no. 6, pp. 310-312, June 2010.

[5] V. K. Velidi and S. Sanyal, "Sharp roll-off lowpass filter with wide stopband using stub-loaded coupled-line hairpin unit," *IEEE Microw. Wireless Compon. Lett*., vol. 21, no. 6, pp. 301-303, June 2011.

[6] M. K. Mandal, P. Mondal, S. Sanyal, and A. Chakrabarty, "Low insertion-loss, sharp rejection and compact microstrip lowpass filter," *IEEE Microw. Wireless Compon. Lett*., vol. 16, no. 11, pp. 600-602, 2006.

[7] R. Gomez-Garcia, M. A. Sanchez-Soriano, M. Sanchez Renedo, G. Torregrosa-Penalva, and E. Bronchalo, "Extended-stopband microstrip lowpass filter using rat-race directional couplers," *Electron. Lett*., vol. 49, no. 4, pp. 272-274, 2013.

[8] C.-J. Wang and C.-H. Lin, "Compact lowpass filter with sharp transition knee by utilising a quasi-π-slot resonator and open stubs," *IET Microw. Antennas Propag*., vol. 4, no. 4, pp. 512-517, 2010.

[9] J. Wang, H. Cui, and G. Zhang, "Design of compact microstrip lowpass filter with ultra-wide stopband," *IEE Electron. Lett*., vol. 48, no. 14, pp. 854-856, July 2012.

[10] J. S. Hong and M. J. Lancaster, *Microstrip Filters for RF/Microwave Applications*. John Wiley & Sons, Inc., 2001.

Ali Reza Nouritabar received the B.S. in Electronics Engineering, from Islamic Azad University, Kermanshah Branch, Kermanshah, Iran, in 2009 and M.S. degree from the K. N. Toosi University of Technology, Tehran, Iran, in 2012. His research interests include Microwave and millimeter wave devices and circuits.

Ashkan Abdipour received the B.S. in Electronics Engineering, from Islamic Azad University, Kermanshah Branch, Kermanshah, Iran, in 2009 and M.S. degree from the Razi University, Kermanshah, Iran, in 2013. His research interests include Microwave and millimeter wave devices and circuits.

Arash Abdipour received the B.S. in Electronics Engineering, from Islamic Azad University, Kermanshah Branch, Kermanshah, Iran, in 2009 and M.S. degree in Electronic Eng. at University of Science and Research, Kermanshah Branch, Kermanshah, Iran. His research interests include Microwave and millimeter wave devices and circuits.

Loop-based Flux Formulation for Three-dimensional Magnetostatic Problems

Yan-Lin Li [1], Sheng Sun [2], and Zu-Hui Ma [3]

[1] Department of Electrical and Electronic Engineering
The University of Hong Kong, Hong Kong, China

[2] School of Electric Engineering
University of Electronic Science and Technology of China, Sichuan, China
sunsheng@ieee.org

[3] School of Information Science and Engineering
Yunnan University, Yunnan, China

Abstract ─ In this paper, loop basis functions are introduced to expand the magnetic flux density and the magnetostatic subset of Maxwell's equations are solved in a compact and straightforward manner using finite element method. As linear combinations of div-conforming Schaubert-Wilton-Glisson basis functions in three-dimensional, loop basis functions are inherently divergence-free and originally constructed to represent solenoidal electric current density in the electric field integral equation. Sharing the same physical property with the solenoidal electric current density, the magnetic flux density can also be represented by the loop basis functions and thus, Gauss' law for magnetism is naturally satisfied; which is out of the capability of general Whitney elements. The relationship between the loop basis functions and Whitney elements, as well as the comparison between the proposed method and traditional method pertinent to magnetic vector potential are investigated.

Index Terms ─ Finite element method, flux formulation, loop basis function, magnetostatic problems.

I. INTRODUCTION

Magnetostatic boundary value problems (BVPs) are generally described by Ampère's law, Gauss' law for magnetism, and corresponding boundary conditions. For complex structures, various numerical methods, including finite element method (FEM), boundary element method (BEM) and finite difference method (FDM) are used to model the flow of magnetostatic fields. Various kinds of formulations are proposed, where the unknowns of the system might be different. As one of most popular methods, the magnetic vector potential **A** was introduced to construct a vector potential formulation, and several gauge conditions were applied to eliminate the nullspace of the resultant matrix system [1–4]. For ringlike current problems, the magnetic field **H** could be obtained from the total scalar potential and reduced scalar potential in different regions [5–7]. Mixed formulations with **H** or **B** being the principle unknown(s) [8–10], were proposed to overcome the computational drawbacks brought about by the aforementioned potential formulations, such as the numerical cancellation and weak enforcement of some physical laws. Although the potential formulations have been well developed in the past few decades, field oriented formulations are still attractive since they work directly with physically meaningful quantities and thus, the implementation is quite straightforward. However, the number of unknowns becomes relatively large because two sets of degrees of freedoms (DoFs) are involved, and specific techniques should be applied to solve the resultant indefinite matrix systems [8–10].

To alleviate the computational burden and complexity of the mixed formulations, one can think in the following ways: consider Gauss' law for magnetism as a gauge condition and incorporate it into Ampère's law, just like the Coulomb gauged vector potential formulation, and thus, only one of the two DoFs is necessary; or expand **B** by certain basis functions such that Gauss' law for magnetism is satisfied automatically and only Ampère's law needs to be solved. The former is unclear because it is difficult to find proper expansion basis functions for **H** or **B** as both the divergence and curl operators will act on it simultaneously; while the later is available, thanks to the successful application of loop basis functions in the electric field integral equation (EFIE) [11–14]. The loop basis functions are linear combinations of the Schaubert-Wilton-Glisson (SWG) basis functions [15] in three-dimensional (3D). The SWG basis functions are divergence-conforming, while loop basis functions are divergence-free, which is consistent with the physical nature of the solenoidal

Submitted On: February 17, 2015
Accepted On: July 4, 2016

current density $\mathbf{J}_{sol}$. Furthermore, the loop basis functions are defined with respect to edges of the geometrical meshes. Hence, the loop representation of $\mathbf{J}_{sol}$ greatly reduces the number of unknowns, in comparison with the SWG representation [14]. As **B** shares the same physical property with $\mathbf{J}_{sol}$, the introduction of the loop representation into finite element models pertinent to **B** is of great interest and importance.

In this paper, the application of the loop basis functions in finite element modeling is investigated and a novel flux formulation, which works solely with **B**, is proposed for solving 3D magnetostatic problems. By virtue of connection between Whitney elements [4, 16] and SWG basis functions, the space formed by the loop basis functions can be proved to be a subset of Whitney forms, from which one can further conclude that the proposed flux formulation is consistent with the vector potential formulation. In addition, since **H** is not accounted and the loop basis functions are associated to edges of the geometrical mesh, the number of unknowns of the proposed flux formulation is much less than that of the mixed formulations. In other words, the proposed flux formulation alleviates the computational burden and complexity, while retains the virtue of the mixed formulations.

The remainder of this paper is organized as follows. The loop basis functions are constructed and their connection to Whitney elements is demonstrated in Section 2. In Section 3, the proposed flux formulation is derived and compared with the vector potential formulation. In Section 4, numerical examples are presented to verify the accuracy and effectiveness of the proposed flux formulation. Finally, this paper is concluded by an overview of the proposed flux formulation in Section 5.

II. LOOP BASIS FUNCTIONS FOR 3D FINITE ELEMENT MODELING

In a 3D tetrahedral mesh, the loop basis functions are associated to edges. As shown in Fig. 1, the loop basis function with regard to edge $\vec{e}_{23}$ can be defined as [12]:

$$\boldsymbol{L}_{12}(\mathbf{r}) = \begin{cases} \dfrac{\mathbf{r}_{i2} - \mathbf{r}_{i1}}{V_i}, \ \mathbf{r} \in \Omega_i, \ i = 1, \ 2, \ 3, \ 4 \\ 0, \ \text{otherwise} \end{cases}, \tag{1}$$

with V_i the volume of Ω_i. $\mathbf{r}_{i2}$ and $\mathbf{r}_{i1}$ denote the positions corresponding to the ending and starting vertexes, respectively, of the edge opposite to $\vec{e}_{23}$. It is worthy to note that the loop basis function follows the right hand rule with regard to $\vec{e}_{23}$. $\boldsymbol{L}_{12}(\mathbf{r})$ can be written in the form of the SWG basis functions:

$$\boldsymbol{L}_{12}(\mathbf{r}) = 3\sum_{n=3}^{6} l_n \boldsymbol{f}_{12n}(\mathbf{r}), \tag{2}$$

where l_n is either 1 or −1, indicating a flux flowing out of or into Ω_i, respectively, and the subscripts denote the three vertices of a facet. Meanwhile, the curl of Whitney field element with regard to $\vec{e}_{23}$ can be expressed as [17]:

$$\nabla \times \vec{\omega}_{12}(\mathbf{r}) = \begin{cases} \dfrac{\mathbf{r}_{i2} - \mathbf{r}_{i1}}{3V_i}, \ \mathbf{r} \in \Omega_i, \ i = 1, \ 2, \ 3, \ 4 \\ 0, \ \text{otherwise} \end{cases}, \tag{3}$$

and the linear supposition of Whitney flux elements [16]:

$$\nabla \times \vec{\omega}_{12}(\mathbf{r}) = \sum_{n=3}^{6} l_n \vec{f}_{12n}(\mathbf{r}). \tag{4}$$

From (1), (3) and (4), it is straightforward to find:

$$\boldsymbol{L}_{12}(\mathbf{r}) = 3\nabla \times \vec{\omega}_{12}(\mathbf{r}) = 3\sum_{n=3}^{6} l_n \vec{f}_{12n}(\mathbf{r}), \tag{5}$$

which indicates that the loop basis functions are linear suppositions of Whitney flux elements as well. Furthermore, the 3D loop basis function is apparently divergence-free, i.e.:

$$\nabla \cdot \boldsymbol{L}_{12}(\mathbf{r}) = 3\nabla \cdot \nabla \times \vec{\omega}_{12}(\mathbf{r}) = 0. \tag{6}$$

The above derivation is applicable for every internal edge. For edges at the boundary, half loop basis functions [14] can be defined, which can be considered as full loop basis functions with virtual outside tetrahedra with relative permittivity μ_r = 1.0. Generally speaking, the loop basis functions include both full loops for the internal edges and half loops for those at the boundary.

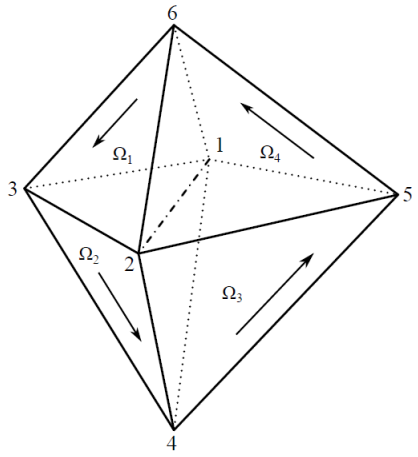

Fig. 1. The loop basis function defined for $\vec{e}_{23}$.

III. FLUX FORMULATION FOR MAGNETOSTATIC PROBLEMS

A. Governing equation

Consider a general 3D BVP as shown in Fig. 2. Assume that the structure is inhomogeneously composed of three bodies, Ω_0, Ω_1 and Ω_2, among which Ω_0 is bounded by Γ_D (solid line) and Γ_N (dash dotted line); Ω_1 and Ω_2 are bounded by Γ_1 and Γ_2, respectively. In

addition, the structure is excited by an impressed current source **J**. Thus, **B** satisfies the subset Maxwell's equations:

$$\nabla \times \frac{1}{\mu}\mathbf{B} = \mathbf{J}, \tag{7}$$

$$\nabla \cdot \mathbf{B} = 0, \tag{8}$$

with μ the magnetic permeability. In addition, two kinds of boundary conditions are imposed on Γ_D and Γ_N, respectively, i.e.:

$$\hat{n} \times \frac{1}{\mu}\mathbf{B}(\mathbf{r}) = \mathbf{K},\ \mathbf{r} \in \Gamma_N, \tag{9}$$

$$\hat{n} \cdot \mathbf{B}(\mathbf{r}) = b,\ \mathbf{r} \in \Gamma_D, \tag{10}$$

where $\hat{n}$ is the unit normal vector to the surface. b and **K** denote the normal component of **B** and surface current, respectively, which are of clear physical meaning. In the vector potential formulation, however, (7), (9) and (10) are rewritten as:

$$\nabla \times \frac{1}{\mu}\nabla \times \mathbf{A} = \mathbf{J}, \tag{11}$$

$$\hat{n} \times \frac{1}{\mu}\nabla \times \mathbf{A} = \mathbf{K},\ \mathbf{r} \in \Gamma_N, \tag{12}$$

$$\hat{n} \times \mathbf{A} = \boldsymbol{\alpha},\ \mathbf{r} \in \Gamma_D, \tag{13}$$

by assuming,

$$\mathbf{B} = \nabla \times \mathbf{A}, \tag{14}$$

$$\nabla \cdot \boldsymbol{\alpha} = b, \tag{15}$$

where the selection of $\boldsymbol{\alpha}$ is not evident [18].

Generally speaking, **B** is governed by (7-10), which are called the flux formulation and lead to an over determined system. To make the system solvable, an additional quantity, **H**, **A** or the reduced scalar potential φ, is introduced into the system for the mixed formulations. Hence, two unknown quantities are involved. Actually, the over determined problem can be solved by reducing the number of equations instead of adding more unknowns. As the loop basis functions are inherently divergence-free, (8) is automatically satisfied and hence, can be discarded if **B** is approximated by them. Similar strategy is applied in the vector potential formulation, where (8) is discarded due to (14).

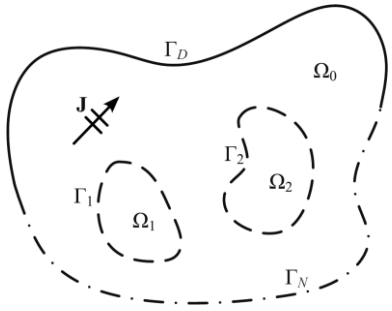

Fig. 2. A general 3D structure excited by an impressed current source **J**.

B. Finite element discretization

Expanding **B** with loop basis functions yields:

$$\mathbf{B} = \sum_{n=1}^{N_l} x_n \boldsymbol{L}_n(\mathbf{r}), \tag{16}$$

where N_l, the number of the loop basis functions, is equal to the number of edges of the geometrical mesh, which is also the number of expansion elements for the vector potential formulation; x_n is the corresponding unknown coefficient to be determined. Since (8) is automatically satisfied, Galerkin's technique can be directly applied to the BVP governed by (7, 9, 10). Testing (7) with $\vec{\omega}_m$ reads:

$$\int_\Omega \vec{\omega}_m \cdot \left(\nabla \times \frac{1}{\mu}\mathbf{B}\right) d\Omega = \int_\Omega \vec{\omega}_m \cdot \mathbf{J} d\Omega. \tag{17}$$

Integrating the left hand side of (17) by parts yields:

$$LHS = \int_\Omega \frac{1}{\mu}(\nabla \times \vec{\omega}_m) \cdot \mathbf{B} d\Omega - \int_\Gamma \vec{\omega}_m \cdot \left(\frac{1}{\mu}\mathbf{B} \times \hat{n}\right) d\Gamma. \tag{18}$$

For simplicity and without loss of generality, the homogeneous boundary conditions [3, 4], **K** = 0 in (9) and b = 0 in (10), are applied. Substituting (9, 10, 16, 18) into (17), one can obtain:

$$\sum_{n=1}^{N_l} x_n \int_\Omega \frac{1}{\mu} \boldsymbol{L}_m \cdot \boldsymbol{L}_n d\Omega = \int_\Omega \vec{\omega}_m \cdot \mathbf{J} d\Omega. \tag{19}$$

Note that the numbers of unknowns of the vector potential formulation, the mixed formulation (e.g., **H**-**B** formulation), and the proposed flux formulations are N_e, $N_e + N_f$ and N_e, respectively, where N_e and N_f are the numbers of edges and facets, respectively. Besides, it is interesting to find that the vector potential formulation and the proposed flux formulation are consistent in matrix condition. Specifically, **A** can be expanded by $\vec{\omega}(\mathbf{r})$, i.e.:

$$\mathbf{A} = \sum_{n=1}^{N_e} a_n \vec{\omega}_n(\mathbf{r}). \tag{20}$$

As implied in (5), the vector potential formulation and the proposed flux formulation should have the same solution space, with dimension $N_e - N_n + 1$ (N_n is the number of nodes), which lead to rank deficiency of the matrices. Fast convergence is achieved when the matrix systems are solved using iterative methods [2, 14]. However, the sign of $\nabla \times \vec{\omega}(\mathbf{r})$ in each tetrahedron is determined by the orientation of the tetrahedron [4], while the sign of $\boldsymbol{L}(\mathbf{r})$ in each tetrahedron is determined more straightforwardly by the right hand rule, as shown in Fig. 1.

In sum, the proposed flux formulation is consistent with the vector potential formulation. The former is advantageous in physical interpolation as well as numerical implementation of the boundary conditions over the later. At the same time, as **B** is traditionally expanded by Whitney-2 form (flux space) elements with dimension N_f, the number of unknowns can be greatly reduced if loop basis functions, with dimension N_e, are

applied to expand **B**, since N_e is generally much smaller than N_f.

IV. NUMERICAL VERIFICATION

As shown in Fig. 3, the IEEJ model [19, 20], which is proposed by the Institute of Electrical Engineers in Japan, is investigated to verify the proposed flux formulation. All the dimensions are in *mm*. As the structure is symmetrical, only the portion lying in the first quadrant, instead of the whole domain, is discretized.

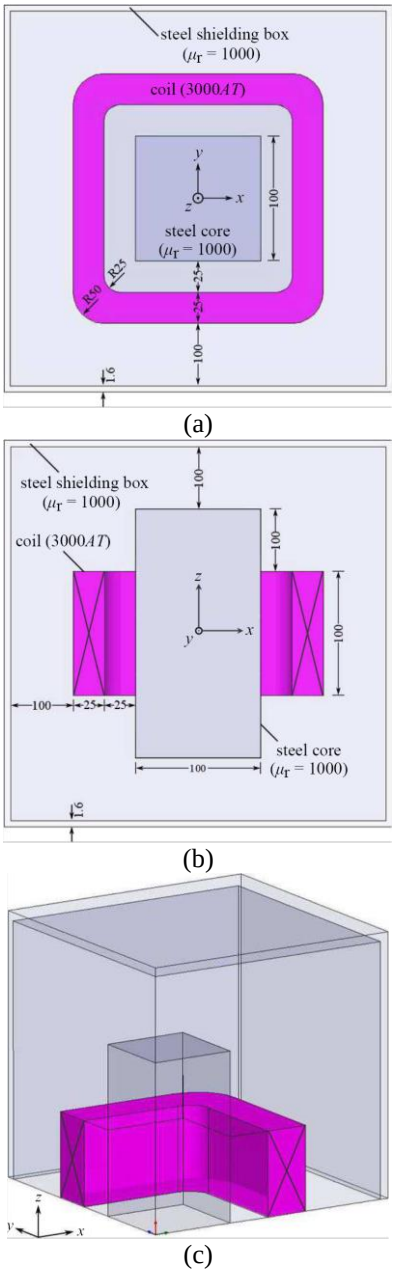

Fig. 3. IEEJ model, which contains a cubic iron core surrounded by a racetrack coil: (a) top view, (b) sectional view, and (c) 3D view of 1/8 domain.

As shown in Fig. 4, the variation of B_x and B_z along z axis obtained by the proposed flux formulation is compared with that obtained by the vector potential formulation. Also, |**B**| values at several sample points are listed, in contrast to the measurement [20], in Table 1. From Fig. 4 and Table 1, one can see that the results obtained by the two formulations agree with each other very well. Considerable but acceptable numerical error occurs at point #1, which might be caused by the quality of the mesh. Furthermore, field distributions of **B** are shown in Fig. 5 and the detailed statistics of the computational cost of the numerical methods is listed in Table 2, where Bi-CGSTAB iterative algorithm [21] is used and 10^{-6} accuracy is achieved. Obviously, the memory consumptions of the two formulations are almost the same, while the convergence of the proposed flux formulation is a little bit slower than that of the vector potential formulation.

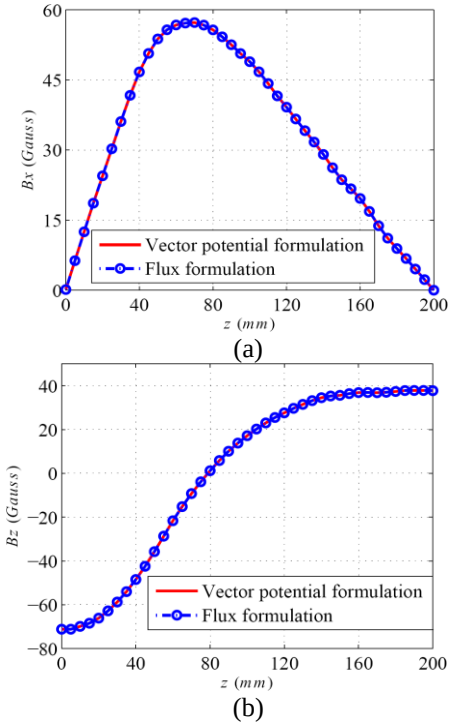

Fig. 4. Variation of (a) *Bx* and (b) *Bz* along *z* axis.

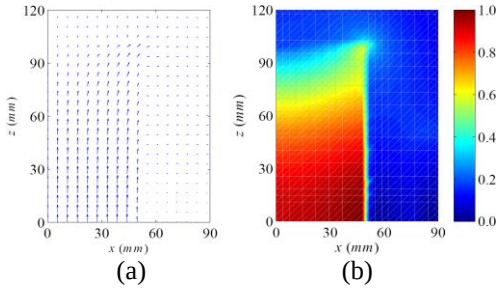

Fig. 5. (a) Vector and (b) magnitude distribution of **B**.

In sum, the proposed flux formulation exhibits a numerical performance as excellent as that of the vector potential formulation, while it is more straightforward since it works with physically meaningful quantity **B**. The application of the loop basis functions in finite element modeling of 3D magnetostatic problems is verified to be accurate and effective. The proposed flux formulation have some potential applications when the governing equations are pertinent to **B**, e.g., the **E**-**B** formulation for dynamic problems [22, 23], where the Whitney flux elements are applied and thus additional effort is needed to enforce the divergence-free condition of **B**. Fortunately, the divergence-free condition of **B** is guaranteed by definition and no more effort is needed if the loop basis functions are applied.

Table 1: Comparison of |**B**| values at sampled points

Coordinates of Sampled Points (*mm*)	|**B**| (*Gauss*)		
	Vector Potential Formulation	Flux Formulation	Measurement
#1 (0, 0, 110)	254.8656	254.8647	240.1
#2 (40, 0, 110)	306.3903	306.3896	298.1
#3 (40, 40, 110)	355.6713	355.6704	355.0

Table 2: Computational cost of the numerical methods

	Number of Unknowns	Matrix Sparsity[1]	Iterative Steps
Vector Potential Formulation	425428	3.49691×10^{-5}	339
Flux formulation	425428	3.49690×10^{-5}	365

[1] Defined as the ratio of the number of nonzero entries to the number of total entries.

V. CONCLUSION

The loop basis functions, which are originally proposed to expand solenoidal electric current density in EFIE, are proved to be in Whitney-2 form. They inherit the normal continuity of Whitney facet elements and are divergence-free. They have been applied to expand **B** in the finite element modeling of 3D magnetostatic problems. This implementation makes Gauss' law be satisfied naturally and thus leading to a compact and straightforward flux formulation, which solely works with **B**. This formulation retains the clear physical interpolation of the mixed formulation, while becomes more elegant and compact. At the same time, it can compete with the vector potential formulation in both accuracy and computational cost. This application of the loop basis functions provides a novel perspective to reconsider the BVPs and basis expansion of solenoidal quantities in the realm of FEM.

ACKNOWLEDGMENT

This work was supported in part by the Research Grants Council of Hong Kong (716713, 716112, and 17207114), in part by the University Grants Council of Hong Kong (Contract No. AoE/P-04/08) and Seed Funding (201209160031, 201211159076, and 201311159188).

The authors would like to thank Prof. W. C. Chew from University of Illinois at Urbana-Champaign for the valuable discussions.

REFERENCES

[1] J. B. Menges and Z. J. Cendes, "A generalized tree-cotree gauge for magnetic field computation," *IEEE Trans. Magn.*, vol. 31, pp. 1342-1347, 1995.

[2] O. Biro, K. Preis, and K. R. Richter, "On the use of the magnetic vector potential in the nodal and edge finite element analysis of 3D magnetostatic problems," *IEEE Trans. Magn.*, vol. 32, pp. 651-654, 1996.

[3] J.-M. Jin, *The Finite Element Method in Electromagnetics*. 2nd ed., New York: John Wiley & Sons Inc, 2002.

[4] Y. Zhu and A. C. Cangellaris, *Multigrid Finite Element Methods for Electromagnetic Field Modeling*. John Wiley & Sons, 2006.

[5] O. Biro, K. Preis, G. Vrisk, K. R. Richter, and I. Ticar, "Computation of 3D magnetostatic fields using a reduced scalar potential," *IEEE Trans. Magn.*, vol. 29, pp. 1329-1332, 1993.

[6] J. G. V. Bladel, *Electromagnetic Fields*. 2nd ed., New York: John Wiley & Sons Inc, 2007.

[7] A. Bermdez, R. Rodrłguez, and P. Salgado, "A finite element method for the magnetostatic problem in terms of scalar potentials," *SIAM J. Numer. Anal.*, vol. 46, pp. 1338-1363, 2008.

[8] P. Alotto and I. Perugia, "A field-based finite element method for magnetostatics derived from an error minimization approach," *Internat. J. Numer. Methods Engrg.*, vol. 49, pp. 573-598, 2000.

[9] L. Hamouda, B. Bandelier, and F. Rioux-Damidau, "A perturbation technique for mixed magnetostatic problem," *IEEE Trans. Magn.*, vol. 37, no. 5, pp. 3486-3489, 2001.

[10] B. Bandelier and F. Rioux-Damidau, "A mixed B-oriented finite element method for magnetostatics in unbounded domains," *IEEE Trans. Magn.*, vol. 38, no. 2, pp. 373-376, 2002.

[11] W. L. Wu, A. Glisson, and D. Kajfez, "A study of two numerical solution procedures for the electric field integral equation at low frequency," *ACES J.*, vol. 10, no. 3, 69-80, Nov. 1995.
[12] L. S. Mendes and S. A. Carvalho, "Scattering of EM waves by homogeneous dielectrics with the use of the method of moments and 3D solenoidal basis functions," *Micro. Opt. Tech. Lett.*, vol. 12, no. 6, 327-331, Aug. 1996.
[13] S. Kulkarni, R. Lemdiasov, R. Ludwig, and S. Makarov, "Comparison of two sets of low-order basis functions for tetrahedral VIE modeling," *IEEE Trans. Antennas Propagat.*, vol. 52, no. 10, 2789-2794, 2004.
[14] M.-K. Li and W. C. Chew, "Applying divergence-free condition in solving the volume integral equation," *Progress In Electromagnetics Research*, vol. 57, pp. 331-333, 2006.
[15] D. Schaubert, D. Wilton, and A. Glisson, "A tetrahedral modeling method for electromagnetic scattering by arbitrarily shaped inhomogeneous dielectric bodies," *IEEE Trans. Antennas Propagat.*, vol. 32, no. 1, pp. 77-85, Jan. 1984.
[16] A. Bossavit, "Whitney forms: A class of finite elements for three-dimensional computation in electromagnetics," *IEE Proceedings*, vol. 135, pt. A, pp. 493-500, 1988.
[17] M. L. Barton and Z. J. Cendes, "New vector finite elements for three-dimensional magnetic field computation," *J. AppL Phys.*, vol. 61, no. 8, pp. 3919-3921, 1987.
[18] O. Biro and K. R. Richter, *CAD in Electro-magnetism, in Series Advances in Electronics and Electron Physics*. Academic Press, New York, 82, 1991.
[19] "Calculation Techniques of 3-D Magnetostatic Fields," *Technical Report of IEE*, Japan, II-286, 1988.
[20] T. Nakata, N. Takahashi, K. Fujiwara, and T. Imai, "Effects of permeability of magnetic materials on errors of the T-Ω method," *IEEE Trans. Magn.*, vol. 26, pp. 698-701, 1990.
[21] H. A. Van der Vorst, "Bi-CGSTAB: A fast and smoothly converging variant of Bi-CG for the solution of nonsymmetric linear systems," *SIAM Journal on Scientific and Statistical Computing*, vol. 13, no. 2, pp. 631-644, 1992.
[22] N. Marais and D. B. Davidson, "A Comparison of some finite element time domain formulations in electromagnetics," *Electromagnetics in Advanced Applications, ICEAA 2007, International Conference on*, Torino, pp. 814-817, 2007.
[23] J. A. Ahmar, O. Farle, S. Wiese, and R. Dyczij-Edlinger, "An E-B mixed finite element method for axially uniform electromagnetic waveguides," *Electronic System-Integration Technology Conference (ESTC), 2012 4th*, Amsterdam, Netherlands, pp. 1-3, 2012.

Yan-Lin Li received the B.Eng. degree in Electronics from Beijing Jiaotong University (BJTU), Beijing, China, in 2007, M.S. degree in Physical Electronics from the University of Chinese Academy of Sciences (UCAS), Beijing, China, in 2010, and Ph.D. degree in Electrical and Electronic Engineering from the University of Hong Kong, Hong Kong, China, in 2015.

His research interests include numerical methods in computational electromagnetics, multi-physics modeling, and wireless power transfer.

Sheng Sun received the B.Eng. degree in Information Engineering from the Xi'an Jiaotong University, China, in 2001, and the Ph.D. degree in Electrical and Electronic Engineering from the Nanyang Technological University, Singapore, in 2006.

He was with the Institute of Microelectronics in Singapore (2005-2006), and with the NTU (2006-2008) as a Postdoc Research Fellow. He was also a Humboldt Research Fellow with the Institute of Microwave Techniques at the University of Ulm in Germany (2008-2010), and a Research Assistant Professor at The University of Hong Kong (2010-2015). Since 2015, he has been the Young Thousand Talents Plan Professor at The University of Electronic Science and Technology of China (UESTC). His research interests include electromagnetic theory and computational mathematics, multi-physics, numerical modeling of planar circuits and antennas, microwave passive and active devices, as well as the microwave and millimeter-wave communication systems. He has authored and co-authored one book, over 100 journal and conference publications. He received the Outstanding Reviewer Award for IEEE Microwave and Wireless Components Letters, in 2010. He was an Associate Editor for the IEICE Transactions on Electronics (2010-2014).

Sun was the recipient of the General Assembly Young Scientists Award from the International Union of Radio Science (URSI), in 2014. He also received the Hildegard Maier Research Fellowship of the Alexander Von Humboldt Foundation (Germany), in 2008, and the recipient of the ISAP Young Scientist Travel Grant (Japan), in 2004.

Zu-Hui Ma received the B.S. and M.S. degrees in Electromagnetics and Microwave Technology from the University of Electronic Science and Technology of China, and the Ph.D. degree in Electric and Electronic Engineering from the University of Hong Kong, in 2006, 2009 and 2013, respectively. He is now an Associate Professor in the School of Information Science and Engineering of the Yunnan University.

His research interests include numerical methods and fast algorithms in computational electromagnetics.

Amplitude Only Linear Array Synthesis with Desired Nulls Using Evolutionary Computing Technique

M. L. M. Lakshmi [1], K. Rajkamal [2], S. V. A. V. Prasad [3], and Md. Zia Ur Rahman [4]

[1,3] Dept. of Electronics and Communication Engineering, Lingaya's University, Faridabad, India

[2] Dept. of Electronics and Communication Engineering
K. L. University, Green Fields, Vaddeswaram-522502, Guntur, A.P., India

[4] Dept. of Electronics and Communication Engineering
KKR & KSR Institute of Technology and Science, Vinjanampadu, Guntur-522017, A.P., India

Abstract ─ Beamforming is a desirous technique in wireless communication by which the desired signal is filter spatially from the interference environment. In this paper, the Firefly algorithm (FFA) is used to demonstrate such beamforming characteristics in linear arrays using amplitude only technique. The amplitude only technique is effectively employed with the FFA to synthesize the linear arrays with desired radiation characteristics. The generated radiation patterns have single and multiple nulls with no constraint imposed on beam width or side-lobe level. The beam steering characteristics are also studied using the same methodology.

Index Terms ─ Beam width, direction of arrival, firefly algorithm, side lobe level.

I. INTRODUCTION

Multiple stationary elements collectively operate as a single element antenna there by concentrating the radiation to one direction which is desirable for many wireless applications. Earlier single element antennas with directivity much less than the required level are used for these applications. Later antenna arrays with excellent directivity characteristics have replaced these single element antennas [1-4].

Radiating elements for modern wireless communications needs to posses certain features like high directivity, good control on side-lobe level (SLL), control on beam width (BW) along with beam steering (BS) capabilities [5,6]. Single element antenna fails to achieve the above, as they exhibit poor directivity and no control on SLL and BW. Also, they require some additional circuitry to control the position of the main beam which makes the system more unwieldy. Moreover, the main problem with single element antenna is that they are highly frequency dependent. Any attempt to enhance the directivity would have a direct impact on the operating frequency of the antenna which is evident from the case of a simple fundamental is λ/2 (half wave length) dipole. The operating wavelength and the corresponding frequency gets modified when the length of the dipole is increased in order to increase its directivity. Hence, such antennas are not suitable for frequency dedicated applications. Therefore, the solution lies in enhancing the electrical length keeping the physical length constant. This is possible with the concept of antenna array where the electrical length is greater than the physical length of the each individual element constituting the array.

Antenna arrays are capable of controlling radiation pattern for desired main BW, half power BW and SLL with proper modifications of geometrical and electrical properties of the array.

An antenna array synthesis problem refers to determining weights for the geometrical properties like spacing (d) between elements or electrical properties like current excitation and phase excitation to produce desired radiation pattern. The choice of considering number of properties for synthesis depends on the type of synthesis problem. In general, the objectives of array synthesis include either SLL control or BW control or both to effectively produce desired shaped radiation pattern [7-14].

Interference suppression is the other reason for array synthesis which is not possible in the case of single element antennas. This is made possible by controlling the radiation in the unwanted direction and projecting the same in the desired direction. This concept in simple form known as beam-forming. The rejection of the undesired signal is carried out by simply placing the nulls in the direction of arrival (DOA) of the interference signal while the main beam is steered to the DOA of the desired direction.

Many conventional techniques like Schelkunoff and Taylor's methods are proposed to solve the problem of beamforming. Unfortunately these are time consuming

Submitted On: April 19, 2016
Accepted On: September 14, 2016

as well as prone to stick in the local minima. In order to overcome these hurdles, in the recent, past several evolutionary techniques are proposed. These techniques are quite efficient and often express the supremacy over traditional techniques.

In this paper, such an attempt is made by adopting Firefly algorithm (FFA) for such applications. FFA is effectively applied to the problem of null generation in linear arrays under non-beam steering and beam steering conditions. The procedure allows essential implementation of beamforming conditions.

The rest of the paper is organized as follows. Section II is dedicated to description the FFA. Problem statement and its formulation is given in Section III and the corresponding fitness evaluation and formulation is given in Section IV. Implementation of the FFA to the array synthesis problem is explained in Section V. The case wise presentations of results are given in Section VI which is followed by overall conclusion in Section VII.

II. FIREFLY ALGORITHM

FFA is a novel metaheuristic algorithm inspired by the behaviour of fireflies [15]. FFA is proposed by Yang. It is another swarm intelligence based algorithm which is inspired by the behaviour of fireflies and the phenomenon of bioluminescent communication.

The construction of FFA algorithm is based on the following set of rules

1. Fireflies (FF) are unisex and can attract any fellow FF.
2. Attractiveness depends on ones brightness.
3. The brightness or light intensity of a firefly is influenced by the landscape of fitness/cost function.

The structure of the FFA is as mentioned in Fig. 1.

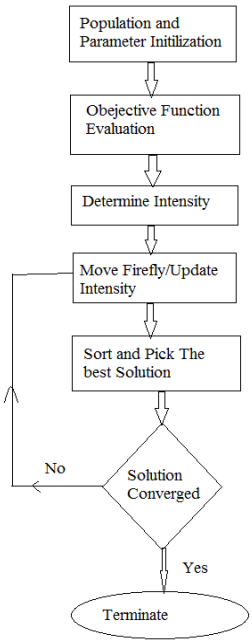

Fig. 1. Flow chart of FFA.

III. FORMULATION OF THE DESIGN PROBLEM

The geometry of the linear array with centre feed and symmetric distribution on either sides of the feed point is as shown in Fig. 2.

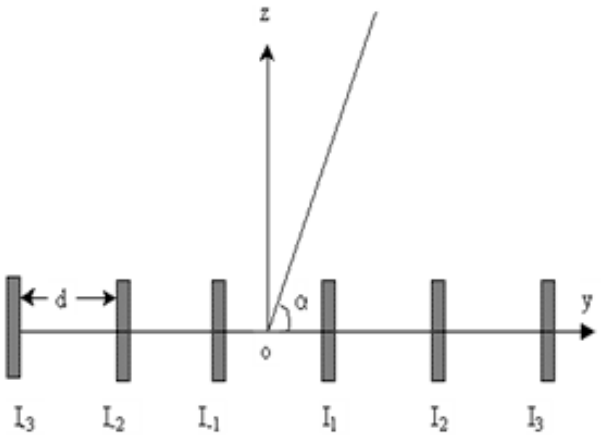

Fig. 2. Geometry of the linear array with symmetric distribution.

The number of elements in the array is given as N=2n and are oriented along X-axis along a straight line to depict a simple line array. Each element in the array is an antenna which is characterized by three parameters and are given as current excitation (I), phase of current excitation ($ø_n$) and spacing (d_{en}). The corresponding array factor that is used to draw the radiation pattern of the LA is a function of these three parameters. However, in this work it is already mentioned that the adopted technique is amplitude only. Hence, the remaining parameters, i.e., d and $ø_n$ are uniform and are assigned with values (0.5λ and 0^0 respectively). Accordingly, the array factor is simplified and given as:

$$AF(\theta) = 2\sum_{n=0}^{N-1} I_n \cos\left[\pi \cos\theta + \phi\right], \qquad (1)$$

where I_n is the nth element current excitation and θ is look angle.

IV. FORMULATION OF FITNESS FUNCTION

The Fitness Function formulation is according to the objective of the proposed work. Accordingly, is given as follows:

$$f = 60dB + E(\theta_{null}) \quad \text{if} \quad |E(\theta_{null})| < 60$$
$$= 0 \quad \text{Otherwise,}$$

where θ_{null} - null position in degrees, $E(\theta_{null})$ is the corresponding E-field magnitude at the desired null position and desired null depth of '60' is simply considered as the fitness value of the corresponding individual.

V. ARRAY DESIGN USING FIREFLY ALGORITHM

The implementation of the algorithm for the array design problem is explained in several steps as discussed below.

A. Population initialization

Like any other population based algorithm, the FFA also starts with initialization of random population in terms of P fireflies (FF) in a K dimensional search space. Each FF corresponds to a solution in the domain of search. Improvement in the solution is obvious with every progressive iteration. Implementation of the FFA for LA synthesis refers to interpretation of each FF as a vector of coefficients for the amplitudes of excitation of a LA. This is represented as:

$$x_i = [x_1, x_2, x_3 \ldots\ldots\ldots x_K]. \quad (2)$$

The corresponding population matrix is given as:

$$X = \begin{bmatrix} x_1 \\ x_2 \\ . \\ . \\ x_P \end{bmatrix} = \begin{bmatrix} x_{11}\, x_{12} \ldots . x_{1K} \\ x_{21}\, x_{22} \ldots . x_{2K} \\ . \; . \; . \; . \; . \; . \; . \\ . \; . \; . \; . \; . \; . \; . \\ x_{P1}\, x_{P2} \ldots . x_{PK} \end{bmatrix}. \quad (3)$$

The upper and lower bounds of the search variable is (x_{min}, x_{max}).

B.FF evaluation

FF evaluation refers to evaluation of the fitness for the corresponding amplitude distribution:

$$I_i = \text{ObjFunc}\,(x_i).$$

C. Attractiveness, distance and displacement

The calculation of the attractiveness of a FF is given by [15]:

$$\beta(r) = \beta_o * \exp\left(-\gamma r_{ij}^2\right). \quad (4)$$

Here, r is the distance between any two fireflies, β_o is the initial attractiveness at r=0 and γ is the absorption coefficient which controls the decrease of the light intensity. The distance between any two fireflies i and j at x_i and x_j respectively, can be defined as a Cartesian distance 'r_{ij}' using the following equation [15]:

$$r_{ij} = \left|x_i - x_j\right| = \sqrt{\sum_{k=1}^{n} \left(x_{ij} - x_{jk}\right)^2}. \quad (5)$$

The displacement of a firefly 'i' which is attracted by a more attractive (i.e., brighter) firefly 'j' is given by the following equation [15]:

$$x_i = x_i + \beta_o * \exp\left(-\gamma r_{ij}^2\right) * \left(x_j - x_i\right) + \alpha * (\text{rand} - 1/2). \quad (6)$$

The parameters used in the proposed FFA are shown in Table 1.

Table 1: Parameter used in the proposed FFA

Description	Parameter	Typical Value
Maximum attractiveness	β_0	1
Time varying algorithm parameter initial value	α	0.25
Absorption coefficient	γ	1
Swarm size	P	30
Number of iterations	Iter	250

VI. RESULTS AND DISCUSSION

The entire simulation based experimentation is divided in to four cases. Description of the problem statement and the corresponding radiation pattern plots are given case-wise in the following discussion. In every case the results are compared with those obtained using Genetic Algorithm. From Case 1 to Case 2, the number of desired nulls are incremented from 1 to 3. Whereas, in Case 4, the Case 3 objectives are repeated but, with the main beam steered in order to serve for DOA of 30^0. The last case significantly refers to the study of receiving a desired signal of interest, which is in the direction of $\Theta=30^0$ while the interference signals are in the direction of 20^0, 40^0 and 60^0.

The corresponding amplitude distribution for both GA and FFA are given in the respective column of Table 2 case-wise. In addition to the amplitude distribution, the computational time for each simulation based experimentation is also recorded in order to analyse the performance of the FFA when compared with GA.

A. Case-1

In this, a simple linear array is synthesised with desired nulls at one position, i.e., at 20^0. Due to the inherent symmetry, a similar null appears on the other side of the pattern at -20^0 also. The radiation pattern obtained for the amplitude distribution determined by the FFA is presented in the Fig. 3. A null at 20^0 with null depth of less than -80 dB can be observed.

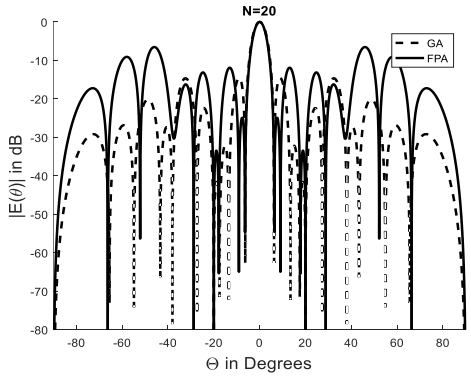

Fig. 3. Radiation pattern with null 20^0.

B. Case-2

In this case, multiple nulls are considered. The objective of this case involves in positioning the second null at 40^0 in addition to the earlier existing null. The validation and the effectiveness of the algorithm is evident with this kind of effort to generate the null which doesn't appear in the previous case protecting the existing null. The corresponding radiation pattern is as shown in the Fig. 4. The amplitude distribution is as mentioned in the Table 2. It is evident from the radiation pattern presented in Fig. 3 that, the magnitude of E-field at $\Theta=40^0$ is well above -30 dB, while the magnitude of E-field at the corresponding $\Theta=40^0$ is well below -80 dB.

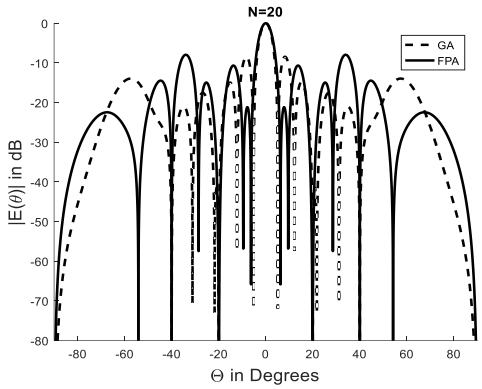

Fig. 4. Radiation pattern with nulls at 20^0 and 40^0.

C. Case-3

This case is similar to Case-2, but with enhanced number of nulls. Keeping the earlier two nulls in their position in the radiation patterns, an extra null is located at 60^0. This further helps in validating the efficiency of the algorithm in positioning the nulls in the desired directions as well as handling multiple nulls. This is demonstrated in Fig. 5, where the arrow marks show the position of the desired three nulls. The amplitude distribution obtained using the FFA is given in Table 2.

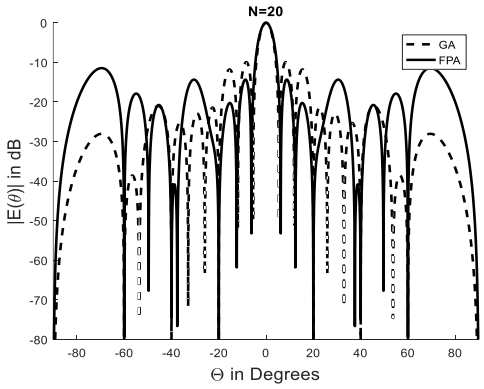

Fig. 5. Radiation pattern with nulls at 20^0, 40^0 and 60^0.

D. Case-4

Beam steering is one of the desired characteristics in beamforming. It is often desired to steer the main beam to the desired direction, which is the DOA of the actual signal. In addition to this, three nulls are also positioned as mentioned in the Case-3 which is considered as the DOA of the interference signals. This is shown in the Fig. 6, where the main beam is steered to an angle of 30^0 which is considered as the DOA of the desired signal. The corresponding amplitude distribution is as given in Table 2.

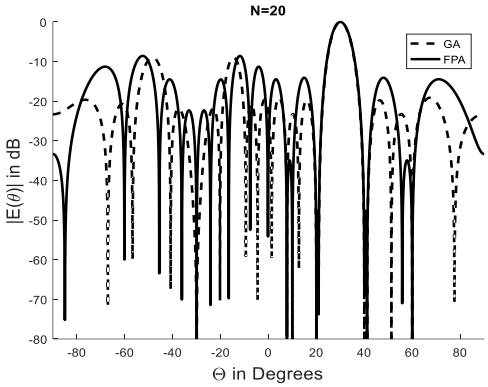

Fig. 6. Radiation pattern with nulls at 20^0, 40^0 and 60^0 with main beam scanned to DOA of 30^0.

Table 2: Amplitude distribution obtained using FFA for different cases

Case #	Algorithm	Normalised Amplitude Distribution	Computational Time (Sec)
1	FPA	0.698, 1, 0.267, 0,0.939, 0.078, 0.404, 0.524, 0, 1	0.56
	GA	0.558, 0.921, 0.714, 0.59, 0.817, 0.928, 0.777, 0.327, 0.402, 0.601	2
2	FPA	0.778, 0.868, 0.567, 0, 0.228, 1, 0.156, 0.211, 0.814, 0.534	1.02
	GA	0.615, 0.148, 0.629, 0.118, 0.898, 0.785, 0.668, 0.801, 0.719, 0.510	12.08
3	FPA	0.443, 0.949, 0.746, 0.519, 0.388, 0.985, 0.571, 0.848, 0.038, 0.622	9.89
	GA	0.625, 0.422, 0.493, 0.368, 0.473, 0.681, 0.737, 0.793, 0.776, 0.178	27.58
4	FPA	0.934, 0.602, 0.608, 0.379, 0.203, 0.860, 0.135, 0.004, 0.911, 0.082	10.08
	GA	0.637, 0.999, 0.33, 0.640, 0.638, 0.139, 0.667, 0.052, 0.265, 0.576	29.58

VII. CONCLUSION

The technique of generating nulls in the desired directions in order to suppress the interference signals is well demonstrated under unscanned and scanned conditions for beamforming characteristics. The novel algorithm has shown its efficiency and simplicity in terms of computation and complexity. When compared with GA, the FFA reported efficient synthesis results in terms of computational time. Instead of number of iterations, performance of the algorithm is evaluated in terms of computational time as the later would be an appropriate scale. Though the GA reported competitive results when compared with the FFA, the consumed time by the GA is at least three times higher than that of FFA. This appears to even worse when the number of elements or the design variable of the problem are considered in large arrays. The technique demonstrated in this paper can easily be extended to any multimodal problems with several constraints.

REFERENCES

[1] C. A. Balanis, *Antenna Theory: Analysis and Design*. John Wiley and Sons, Asia, 2003.

[2] I. M. Skolnik, *Radar Handbook*. McGraw-Hill, New York, 1990.

[3] R. S. Elliott, *Antenna Theory and Design*. Prentice Hall, Englewood Cliffs, NJ, 1981.

[4] S. A. Schelkunoff and H. T. Friis, *Antennas Theory and Practice*. JW & Sons Inc., London, 1952.

[5] K.-K. Yan and Y. Lu, "Sidelobe reduction in array-pattern synthesis using genetic algorithm," *IEEE Trans. Antennas Propagat*., vol. 45, no. 7, pp. 1117-1122, 1997.

[6] R. L. Haupt, "Phase-only adaptive nulling with a genetic algorithm," *IEEE Trans. Antennas Propagat.*, vol. 45, no. 6, pp. 1009-1015, 1997.

[7] D. Karaboga, K. Guney, and A. Akdagli, "Antenna array pattern nulling by controlling both the amplitude and the phase using modified touring ant colony optimisation algorithm," *Int. Journal of Electronics*, vol. 91, no. 4, pp. 241-251, Aug. 2006.

[8] V. V. S. S. S. Chakravarthy and P. M. Rao, "On the convergence characteristics of flower pollination algorithm for circular array synthesis," in *Electronics and Communication Systems, 2015 2nd International Conference on*, Coimbatore, pp. 485-489, Feb. 2015.

[9] V. V. S. S. S. Chakravarthy and P. M. Rao, "Amplitude-only null positioning in circular arrays using genetic algorithm," in *Electrical, Computer and Communication Technologies (ICECCT), 2015 IEEE International Conference on*, Coimbatore, pp. 1-5, Mar. 2015.

[10] K. D. Cheng, "Optimization techniques for antenna arrays," *Proceedings of the IEEE*, vol. 59, no. 12, pp. 1664-1674, 1971.

[11] V. S. S. S. ChakravarthyVedula, S. R. C. Paladuga, and P. M. Rao, "Synthesis of circular array antenna for sidelobe level and aperture size control using flower pollination algorithm," *International Journal of Antennas and Propagation*, vol. 2015, Article ID 819712, 9 pages, July 2015.

[12] L. Manica, P. Rocca, A. Martini, and A. Massa, "An innovative approach based on a tree-searching algorithm for the optimal matching of independently optimum sum and difference excitations," *IEEE Trans. Antennas Propag*., vol. 56, no. 1, pp. 58-66, Jan. 2008.

[13] M. Alvarez-Folgueiras, J. A. Rodriguez-Gonzalez, and F. Ares-Pena, "Synthesising Taylor and Bayliss linear distributions with common aperture tail," *Electron. Lett*., vol. 45, no. 11, pp. 18-19, Jan. 2009.

[14] V. V. S. S. S. Chakravarthy, K. N. Babu, S. Suresh, P. C. Devi, and P. M. Rao, "Linear array optimization using teaching learning based optimization," *Advances in Intelligent Systems and Computing*, vol. 338, pp. 183-187, 2015.

[15] X.-S. Yang, "Firefly algorithms for multimodal optimization," *in Stochastic Algorithms: Foundations and Applications: 5th International Symposium, SAGA 2009*, Sapporo, Japan, Oct. 2009.